London
South Bank
University

EST 1892

Characterising the Pore Space of Selected Sandstone Samples using Multiple Approaches

Marsha P. Maraj

A thesis submitted in partial fulfilment of the requirements of
London South Bank University
for the degree of Doctor of Philosophy

May 2019

ABSTRACT

A comprehensive knowledge of the porosity and pore size distribution (PSD) of hydrocarbon reservoirs is vital to several petroleum engineering disciplines including reserve estimation, reservoir characterisation, drilling operations and reservoir development planning. This work examines the three methods of Mercury Injection Capillary Pressure (MICP) Testing, Pore Network Modelling (PNM) and Nuclear Magnetic Resonance (NMR) which are currently used within the petroleum industry to determine representative measures of porosity and PSD.

Although MICP is a common method used within the petroleum industry, several factors impact its suitability for determining porosity and PSD. These are related to the destructive nature of the test which is challenging when samples are limited in quantity as well as the limitations of MICP to provide robust results for certain kinds of reservoir material, particularly for those that are unconsolidated and unconventional.

Recent advances in PNM and NMR have made these approaches attractive alternatives for pore evaluation studies which can enhance, supplement or replace the information derived from MICP testing. To examine the applicability of PNM and NMR methods to determine porosity and PSD, three sandstone core samples were used throughout this study. These were the Berea and Bentheimer core samples, which are consolidated and homogenous in nature allowing an opportunity for the benchmark testing of the PNM and NMR approaches and an Athabasca Oil Sand (AOS) sample, which is a prime example of unconsolidated material containing a very viscous in-situ fluid.

During the PNM process, micro-computed tomography (micro-CT) was used to obtain 2D contiguous images of a sample which were then compiled to produce a 3D representation of the pore space. Based on the literature, a 12-step comprehensive PNM approach was developed in this work and applied to the benchmark Berea and Bentheimer core samples to derive their porosity and PSD. This had a substantial processing time of over 100 hours (> 4 days) for each sample. The key findings from this comprehensive approach formed the basis of a simplified recommended PNM practice having only 9 steps and an anticipated processing time of 7 hours and 26 hours for homogenous and heterogeneous samples respectively. This simplified recommended PNM practice was then applied to the AOS sample with the porosity and PSD results showing a good agreement to that from the MICP and NMR testing.

The determination of porosity and PSD from NMR testing requires specific fluids to be contained in the pore space. This generally involves the removal and replacement of all original fluids with water (or brine) since the response of the low-viscosity water correlates well with surface measurements of the pore space. This typically precludes the testing of samples imbued with their original fluids which poses several restrictions for the NMR testing of unconsolidated and partially consolidated material.

The development of techniques which allow for the robust pore space testing of these kinds of materials without the cleaning or removal of their native fluids is therefore valuable to the petroleum industry. Based on these ideas, a novel empirical transform was developed which could allow the NMR testing of samples containing viscous fluids. This transform used the NMR response of glycerol (which is 1,412 times more viscous than water at 20°C) to develop a transform based on viscosity. The use of this transform showed great success in obtaining a robust PSD for the AOS sample containing its native bitumen which is comparable to the PSDs from the MICP and PNM approaches.

These results indicate that the PNM and NMR approaches can provide comparable results to conventional MICP testing, that they can be used as independent techniques for evaluating the pore space and that they can provide a robust measurement of the porosity and PSD for samples imbued with their native hydrocarbon fluids. When compared to MICP testing, these approaches might be preferred when testing a limited quantity of core samples, partially consolidated and unconsolidated samples and samples containing their original fluids.

Future work to strengthen these results include using a wider range of sandstone samples to test the developed recommended PNM practice and using a wider range of samples containing a greater variety of fluids to test the empirical transform.

DECLARATION

I declare that this thesis:

**Characterising the Pore Space of Selected Sandstone Samples
using Multiple Approaches**

is entirely my own research under the supervision of Dr Pedro Diaz and Dr Andrew Fergusson-Rees. The research was carried out in the Department of Chemical Engineering at London South Bank University. All published and unpublished material used in this thesis has been given full acknowledgement. None of this work has been previously submitted to this or any other academic institution for a degree or diploma, or any other qualification.

Marsha P. Maraj
PhD student
Department of Chemical and Petroleum Engineering
London South Bank University

DEDICATION

This thesis is dedicated to my parents, my sisters, my niece and Allan.

ACKNOWLEDGEMENTS

I would like to express my sincerest gratitude to my supervisor Dr Pedro Diaz for his support, patience and motivation over the last few years. His guidance throughout this research has been immeasurable and a source of constant inspiration during the writing of this thesis. He has been especially supportive of my career goals, encouraging me to pursue opportunities which I thought were too wide and he continues to be a wonderful mentor and trusted advisor. Thank you.

I would also like to thank the rest of my supervisory committee (both past and present): Dr Andrew Fergusson-Rees, Dr Julie Dee Bell, Dr David Roberts, Dr John Orrin and Dr Ali Qubian, for their help during the course of this work, for the procurement of core samples and other materials and for their insightful comments and encouragement.

I am also extremely grateful for the financial support and funding I received from the School of Engineering during my studies.

My sincere thanks also goes to Mr Nick Corps from the Bruker Corporation for his help, advice and support during the acquisition of the micro-CT images used in this work.

This thesis and research would also not be possible without the immense support and guidance of my friends, colleagues and the many academic and technical staff within the School of Engineering at LSBU who unfortunately, are too numerous to mention by name. Please know that I have treasured your advice and friendship and I very much look forward to continuing our journey.

Last but not the least, I would like to thank my family for their unconditional support, love and encouragement. Special thanks must go to my parents, particularly my mother. It is an eternal regret that you are not here to see the culmination of this work but I know you would be proud. I would also like to thank my sisters and niece for always sending words of love and encouragement across the big ocean that separates us, I could not have done this without you. Finally, I say heartfelt thanks to Allan – there are almost no words which can convey what you mean to me and I am indebted to you for your unwavering love and support, they have made all the difference.

Thank you all.

TABLE OF CONTENTS

List of Figures

List of Tables

List of Abbreviations and Acronyms

AOS	Athabasca Oil Sand/s
API	American Petroleum Institute
CPMG	Carr, Purcell, Meiboom and Gill sequence
EOR	Enhanced Oil Recovery
FIB-nt	Focused Ion Beam nano-tomography
FID	Free Induction Decay
MICP	Mercury Injection Capillary Pressure
Micro-CT	Micro-Computed Tomography
MROI	Maximum Region of Interest
NMR	Nuclear Magnetic Resonance
PNM	Pore Network Modelling
PSD	Pore Size Distribution
PSTD	Pore Throat Size Distribution
REV	Representative Elementary Volume
ROI	Region of Interest
TEM	Transmission Electron Microscopy

List of Symbols

A	amplitude value from NMR
B_o	externally applied magnetic field
B_1	pulsed oscillating magnetic field in a direction that is perpendicular to B_o
BV	bulk volume
D_o	diffusion coefficient of the bulk fluid;
	self-diffusion constant of the relaxing fluid'
	unrestricted diffusion coefficient (in bulk fluid)
D(t)	time dependent diffusion coefficient
f	Larmor frequency
F_s	geometric shape factor
G	strength of the field gradient
GV	grain volume
I	intensity of the transmitted radiation during micro-CT
I_o	intensity of the incident radiation during micro-CT
K_p	kurtosis
M(t)	longitudinal magnetisation at time *t*
M_o	bulk magnetisation; final and maximum magnetisation
M_{ox}	transverse magnetisation at $t = 0$ (the time at which the 90° pulse ceases)
$M_x(t)$	transverse magnetisation at time *t*
n	number of subdivisions of pore size
NE	Number of echoes
PV	pore volume
P_c	capillary pressure
r	pore radius
$r_{in\text{-}situ\ fluid}$	pore radius from in-situ fluid NMR testing
r_M	mean radius
r_t	pore throat radius
$r_{transformed}$	pore radius after applying the empirical NMR transform
S	surface area
$\overline{\left(\dfrac{S}{V}\right)}$	average surface area to volume ratio
S_p	pore sorting
Sk_p	skewness

t	time over which the hydrogen nuclei are exposed to magnetisation; observation time for diffusion
T1	longitudinal relaxation time
T2	transverse relaxation time
$\overline{T2}$	weighted harmonic mean of the T2 distribution
T2B	bulk fluid transverse relaxation time
T2D	diffusion transverse relaxation time
T2S	surface transverse relaxation time
$\overline{\left(\dfrac{1}{T2}\right)}$	inverse of the weighted harmonic mean of the T2 distribution
TE	inter-echo time
V	volume
x	distance of the radiation travelled through the material during micro-CT

Greek Symbols

δ	time over which B_1 is applied
ξ_i	volume fraction of pores with $\left(\dfrac{S}{V}\right)_i$ with relaxation time $T2_i$
ρ_2	surface relaxivity
φ	porosity
σ	interfacial tension between the fluid phases
θ	wettability angle; contact angle between the solid surface and the fluid-fluid interface; the angle through which the magnetisation is tipped from the longitudinal direction to a transverse plane
τ	de-phasing/re-phasing time
γ	gyro-magnetic ratio
μ	attenuation coefficient of the Lambert-Beer's Law; viscosity; micro (prefix)

List of Equations

CHAPTER 1

Introduction

Hydrocarbon recovery is strongly governed by the porosity and pore size distribution which exists in producing reservoirs (Ghous *et al.*, 2008). Obtaining robust measures of the pore space is therefore important towards influencing recoveries and this work examines the three methods of Mercury Injection Capillary Pressure (MICP) Testing, Pore Network Modelling (PNM) and Nuclear Magnetic Resonance (NMR) which are currently used within the petroleum industry to determine representative measures of porosity and pore size distribution. This chapter presents the relevant background information relating to the evaluation of porous media using these methods and outlines the rationale, broad objectives and deliverables of this work.

1.1 Characterising Porous Media

The use of porous media is prevalent for many scientific and industrial applications. A number of natural and synthetic substances such as ground-water aquifers, oil and gas reservoirs, biological tissues, food and construction materials are common examples of porous media.

A porous medium consists of a solid matrix in which pore spaces are distributed throughout. The connectivity of the pore space can allow for the flow of fluids through the material, and it is this potential for flow which typically underpins the importance of porous media for many applications.

The flow through a porous medium is strongly influenced by its microstructure and inherent pore geometry. Pore geometry refers to the shape, size and interconnectivity of the pores and pore throats (Bliefnick and Kaldi, 1996); these can be thought to comprise a pore network which traverses the material. For fluid-bearing media, the pores typically contain the fluids, and the pore throats allow for the passage of these fluids through the network. The size of the pores and pore throats and their distributions are therefore critical to fluid flow and impact a number of key parameters related to flow.

With specific reference to petroleum reservoirs, the flow of hydrocarbon fluids is greatly dependent upon the geometry and connectivity properties of the pore space (Dullien, 1991; Ghous *et al.*, 2008; Sok *et al.*, 2010). Reservoir material can contain a variety of pore dimensions which range from sub-micron to centimetres (Taud *et al.*, 2005; Tucker, 1991). Heterogeneity of the pore space and the lack of a firm understanding of the underlying pore system, particularly the way in which the porosity and pore size distribution are distributed throughout the material, are principal reasons which lead to inefficient hydrocarbon recovery (Song *et al.*, 2002).

1.2 Porosity and Pore Size Distribution (PSD)

There are a number of important properties which can be used to characterise porous media. These include porosity, pore size distribution, capillary pressure, permeability and the diffusion properties of liquids in pores. For petroleum reservoirs, porous media are most often characterised by their porosity and in particular, by how the pores and their sizes are distributed (Dullien, 1991; Song *et al.*, 2002).

Porosity is an important parameter for many petroleum engineering disciplines including reserve estimation, reservoir characterisation and drilling. It represents a measure of the amount of pore space occupied by hydrocarbon fluids and provides an early measure of the reservoir's economic potential as it is directly corresponds to the initial hydrocarbon amounts in place.

Although porosity provides useful information regarding the storage capacity, it does not provide an indication of how flow can be established. Pore size and its distribution are parameters which directly relate to the passage of fluids through the material (Song *et al.*, 2002). Pore networks approximate the porous medium as an interconnected system of pores and pore throats. At static conditions, the pores and throats typically contain the fluids. When pressure is applied, flow can be accomplished as fluid moves through both pores and pore throats. The size of the pores and throats are therefore important as they directly affect the amount of fluid which can be transmitted through the media.

Determining robust measures of the in-situ porosity and PSD and understanding how these vary across the reservoir can therefore help build comprehensive reservoir

characterisation models. These can identify the locations of highest productivity within the reservoir which can enhance reservoir development planning and influence the implementation of recovery schemes over the producing life of the reservoir.

Porosity and pore size distribution (PSD) can be obtained in a number of ways. Common methods used across several scientific and industrial disciplines include the microscopy of thin-sections, gas adsorption, mercury intrusion and small angle neutron scattering (SANS). Some of these are described in greater detail in later chapters of this thesis but an excellent review of these methods can be found in Aligizaki (2006).

1.3 Mercury Injection Capillary Pressure (MICP) Testing

For the petroleum industry, porosity and PSD information are usually obtained through core analysis which involves the physical measurement of material taken from the reservoir. Mercury Injection Capillary Pressure (MICP) testing is a common core testing procedure used to obtain porosity and PSD (Comisky *et al.*, 2007).

MICP testing involves the injection of mercury into a sample that has been cleaned of all original fluids and then subsequently dried and evacuated of all cleaning fluids. During the test, the sample is immersed in liquid mercury with pressure being increased progressively. Final injection pressures vary from 5,000 to 70,000 psi with higher pressures being used to access and characterise very small pores within the sample (Honarpour, 2004). Such large pressures generally require structurally competent samples which do not deform during the procedure.

The injection pressures provide a measure of the accessed pore throat radii and the results of the MICP test, although more accurately representing a pore throat size, are very often used to describe the pore (body) size distribution (Mao *et al.*, 2005; Vavra *et al.*, 1992; Volokitin *et al.*, 2001) since there is an assumed relationship between the radii of pore bodies and the radii of pore throats (Volokitin *et al.*, 2001)

Advantages of the MICP technique include the testing of small and irregularly shaped samples as well as rapid testing times. Limitations of the method include the destructive nature of the test as the intrusion of mercury renders the sample unusable for other kinds

of testing. This is challenging when samples are expensive to obtain and are limited in quantity. Other disadvantages involve the prerequisite cleaning and evacuation of in-situ fluids which is needed before the samples can be tested. This poses several restrictions for the MICP testing of unconsolidated and partially consolidated material.

1.4 Unconsolidated Porous Media

Reservoir material can be described as being either consolidated, partially consolidated (friable) or unconsolidated depending upon the amount of compaction and cementation that exists between the grains of the material (Ahmed, 2019). Unconsolidated rocks have little or no cement between their grains and are essentially compacted sediments (American Petroleum Institute, 1998).

A well-documented and prolific unconsolidated reservoir is the Athabasca Oil Sands of Canada. Rosen *et al.* (2007, para 1) state that 'unconsolidated sand is arguably the most difficult material to work with in core analysis'. Core testing on unconsolidated core samples are typically extensions of the techniques used for consolidated core samples. However, there is often debate regarding the reliability and accuracy of the results of these tests on unconsolidated core samples (Mattax *et al.*, 1975) particularly as the friable nature of unconsolidated material implies that any forceful handling and intrusion of fluids into the sample can deform the sample and irreversibly damage the inherent pore structure. This can severely hinder the use of MICP testing for these materials.

With specific reference to unconsolidated Athabasca oil sand material, the in-situ bitumen acts as a cohesive agent binding the grains together (Schmitt, 2005). Removal of this bitumen can lead to a rearrangement of the pore structure unless meticulous care is taken to preserve the pore integrity during the cleaning process. As such, core analytical techniques which require that samples be cleaned of original fluids may not readily provide consistent and robust pore information for these kinds of materials.

It therefore becomes important to investigate and develop alternative methods of characterising inherent pore structures for unconsolidated reservoir material, particularly as these structures govern efficient hydrocarbon recovery and exploitation.

1.5 Alternative Methods of Pore Characterisation

Recent advances in Pore Network Modelling (PNM) and Nuclear Magnetic Resonance (NMR) have provided attractive alternatives for pore characterisation which can enhance and supplement the information derived from conventional core testing.

1.5.1 Pore Network Modelling (PNM)

PNM has been used by many researchers to determine selected petrophysical properties (including porosity, capillary pressure and relative permeability) and to study multiphase flow in porous media (Balhoff and Wheeler, 2007; Blunt, 2001; Blunt *et al.*, 2013; Boek, 2010; Dong and Blunt, 2009; Golparvar *et al.*, 2018; Suicmez and Touati, 2008; Varloteaux *et al.*, 2013; Xiong *et al.*, 2016).

PNM uses image-based technology to characterise the porous medium. In PNM, micro-computed tomography (micro-CT) is used to obtain 2D contiguous images of the sample. These 2D images are then compiled to produce a 3D representation of the internal structure from which pore networks can be identified.

3D pore networks allow for the measurement of porosity and pore size distribution (PSD) by first extracting the topological skeleton running through the centre of the pore network and then identifying individual pore diameters by partitioning the skeleton and fitting ellipsoids into local minima. This typically provides a measurement of both the pore bodies and throats regardless of whether these are connected. This is different to MICP testing in which the pore throat radii of connected pores are obtained since the forced intrusion of mercury must take place through interconnected pores.

Although micro-CT scanning generally requires little to no prior sample preparation (Ketcham and Carlson, 2001) which makes it ideal for the testing of samples containing their in-situ fluids, several uncertainties associated with the PNM approach can impact the confidence of the results. These typically relate to the segmentation process and the identification of a Representative Elementary Volume (REV).

Segmentation involves identifying a *threshold value* which is used to label each part of 3D digital model as belonging to either the pore or to the solid (grain) phase (Iassonov *et al.*, 2009). This choice of threshold is significant as an 'incorrect' value has the

potential to reduce or amplify the pore space as well as blur, terminate or connect pore spaces which may not necessarily exist (Taud *et al.*, 2005). This can result in significant variations in porosity and PSD with only very small changes in the threshold (Sheppard *et al.*, 2004).

PNM approaches often involve significant quantities of data which require increasingly large processing times and computing power (Golparvar *et al.*, 2018; Iassonov *et al.*, 2009). The REV relates to the smallest size of the 3D model which adequately captures the majority of the sample's inherent features so as to be statistically representative of the entire sample (Gelb *et al.*, 2011) and is essentially the smallest amount of the 3D model which will be studied in order to provide representative characteristics.

The determination of the REV is dependent upon measuring changes in a property of interest as volumes are incremented. The process of incrementing these volumes as well as where these volumes are taken from within the sample (in terms of their location and orientation) has the potential to impact the REV and it becomes important to further investigate their influence in REV determination.

Additionally, porosity is prevalently chosen as the property of interest chosen during REV determination (Al-Raoush and Papadopoulos, 2010; Halisch, 2013) and it also becomes important to examine if an REV based on porosity will also hold true for other pore space measures like PSD. This is particularly interesting given that Bennion and Bachu (2006) have stated that there is no established correlation between porosity and pore size.

Robustly determining the REV by examining both the REV incremental process and the role of other pore space parameters like PSD can help refine and further reduce the amount of the 3D model needed to characterise the medium compared to traditional REV identification methods. This can reduce processing costs and times associated with the PNM approach.

1.5.2 Nuclear Magnetic Resonance (NMR)

NMR has been used extensively by a number of researchers to study the structure of porous media and to determine key petrophysical properties, including porosity, permeability, PSD and capillary pressure (Bryan *et al.*, 2008; Cabrera, 2008; Jin *et al.*, 2009; Mao *et al.*, 2005; Slijkerman and Hofman, 1998).

NMR measures the response of the hydrogen nuclei contained in the fluids of porous media that have been excited in a magnetic field and relates this response to porosity and PSD. PSD measurements using NMR testing are generally made on samples saturated with water or brine since the response to water and brine correlates well with surface measurements of the pore space (Sorland *et al.*, 2007). This requires that samples be cleaned of all in-situ fluids and replaced with either water or brine which reduces the use and value of NMR data for several NMR applications within the petroleum industry, notably that of NMR logging which is carried out on formations containing fluids which can be one or a combination of connate water, hydrocarbons and drilling mud (Shafer *et al.*, 1999).

The introduction of water or brine into the pore space must take place through interconnected pores and accordingly the PSD from NMR measurements typically reflect both the pore bodies and throats of connected pores which contain the hydrogen nuclei.

1.6 The Rationale and Scope of this thesis

MICP is a common method used within the petroleum engineering industry to study the pore structure of reservoir material (Comisky *et al.*, 2007). Although MICP has distinct advantages and represents an accepted route for the determination of porosity and pore size distribution (PSD), several factors impact the suitability of MICP as a testing method.

These centre upon the destructive nature of the test which is challenging when samples are expensive to obtain and are limited in quantity as well as the limitations of MICP to provide robust results for certain kinds of reservoir material, particularly for those that are unconsolidated and unconventional (Rosen *et al.*, 2007).

PNM and NMR methods have marked advantages over MICP testing which makes them desirable options for the determination of porosity and PSD. Both PNM and NMR are non-destructive allowing for the repeatability of measurements which is particularly useful when core material is limited. PNM can also test samples having their in-situ or native fluids and therefore involves minimal sample preparation which reduces the possibility of damage to the inherent pore structure leading to the likelihood of more representative results. Testing times for both methods are generally fast and the

equipment, although incurring a relatively high initial capital cost, has low maintenance and support expenses.

Although PNM and NMR offer attractive alternatives to MICP testing, it is important to note that these methods measure different aspects of the pore space to conventional MICP testing, namely the measurement of a pore throat (MICP) versus both pore body and throat sizes (PNM and NMR). This might imply that a convergence of the results across these approaches may not always be possible.

To examine the applicability of PNM and NMR methods to determine porosity and PSD, three sandstone core samples were used throughout this study. Two samples were taken from well-studied and consolidated reservoirs; these are the Berea and Bentheimer core samples. Berea and Bentheimer samples were chosen for this study as they are representative of typical reservoir material (Peng *et al.*, 2012). They are consolidated and homogenous in nature and as such, the investigation of these materials allows an opportunity for benchmark testing of the PNM and NMR approaches.

The third core sample is taken from an Athabasca Oil Sand (AOS) reservoir which is a prime example of unconsolidated material for which pore characterisation information is often limited.

1.7 Broad Objectives, Work-flows and Deliverables

The general objective of this work is to determine and compare the porosity and PSD of selected sandstone samples obtained from the three methods of MICP, PNM and NMR approaches. This is done in order: (1) to gauge whether the PNM and NMR approaches can provide comparable results to conventional MICP testing, (2) to assess the use of the PNM and NMR methods as stand-alone techniques for evaluating the pore space and (3) to determine whether PNM and NMR can provide a robust measurement of porosity and PSD for samples imbued with their native hydrocarbon fluids.

To achieve these broad objectives, the porosity and pore size distributions for all three samples were obtained through:

i. MICP testing which was done in accordance to API RP 40: Recommended Practices for Core Analysis (American Petroleum Institute, 1998).

ii. A PNM Approach which involved:
   a. Using the Berea and Bentheimer samples to investigate selected attributes of the PNM process related to the segmentation and REV processes in order to propose a Recommended PNM Practice;
   b. Applying this Recommended PNM Practice to the AOS sample.

iii. NMR Experimentation which involved:
   a. Saturating the Berea and Bentheimer samples with distilled water and then with glycerol in order to gauge the effect of changing fluid properties (specifically viscosity) on the NMR derivation of PSD;
   b. Using these results to develop a novel empirical transform which could be used to derive the PSD when viscous fluids are contained the pore space;
   c. Applying the developed empirical transform to the AOS sample to determine its PSD.

iv. A comparison and discussion of the results of all three testing methods to assess their use to evaluate porous media as stand-alone techniques and to gauge the applicability of these methods for unconsolidated samples imbued with their native hydrocarbon fluids.

1.8   Contribution to the Body of Knowledge

Based on the above objectives, the results of this work have contributed to the literature by adding important information regarding the use and applicability of the MICP, PNM and NMR methods for the testing of conventional and unconventional samples.

Two significant contributions have been made which include:
1. The development of a Recommended PNM Practice for Homogenous and Heterogenous samples which can reduce the uncertainties surrounding the segmentation and REV determination processes during PNM. This has been

shown to produce robust and comparable values of porosity and PSD results time-effective manner for both conventional and unconventional samples.

2. The development of a novel empirical transform which allow the NMR testing of samples containing viscous or in-situ fluids. This overcomes the limitations of the stipulated use of water or brine in the pore space during NMR testing. This transform has been shown to successfully obtain robust PSDs when two viscous fluids (bitumen and glycerol) are contained in the pore space.

Future work to strengthen these two contributions include:
1. Using a wider array of sandstone samples to test the Recommended PNM Practice for homogeneous and heterogeneous sandstone samples. This can result in a further refinement of steps leading to an even greater confidence in the results.

2. Testing the empirical transform with a wider range of samples containing a greater variety of fluids which would confirm the use of the empirical transform for a larger range of petroleum engineering applications.

1.9   Thesis Structure

This thesis contains the following seven (7) chapters:

Chapter 1: *Introduction*
This is the introductory chapter of the thesis and provides the background information, the rationale as well as the broad objectives and deliverables of this work.

Chapter 2: *Theoretical Background*
This chapter presents the fundamentals and relevant literature associated with the MICP, PNM and NMR approaches used in this work, particularly in the context of how these relate to the quantification of porosity and PSD.

Chapter 3: *Materials: The selection of samples in relation to the methods used*

Chapter 3 describes the three samples used in this work and in particular, examines how the nature of the Athabasca oil sand material impacts the analysis and interpretation of MICP and NMR data.

Chapter 4: *The Theoretical and Experimental Descriptions of the MICP, PNM and NMR Methods*

This chapter presents the theoretical descriptions and experimental design of the MICP, PNM and NMR tests used in this work, particularly in the context of how these relate to the quantification of porosity and pore size distribution.

Chapter 5: *The Application of the MICP, PNM and NMR Methods to the Berea and Bentheimer samples*

Chapter 5 provides the results when the MICP, PNM and NMR methods have been applied to the Berea and Bentheimer consolidated samples. It presents the porosity and PSDs values arising from each method which form the basis of the development of a Recommended Practice for PNM as well as an empirical transform for NMR PSD determination when selected viscous fluids are contained within the pore spaces of these samples.

Chapter 6: *The Application of the MICP, PNM and NMR Methods to the AOS Sample*

This chapter presents the results when MICP testing as well as the recommended PNM and NMR practices derived in Chapter 5 are applied to a selected Athabasca Oil Sand core sample.

Chapter 7: *Discussion and Conclusions*

This chapter integrates the findings from Chapters 5 and 6 and discusses the results of these methods to evaluate sandstone samples for a range of applications and conditions. It also summarises the key outcomes of this work providing a careful consideration of the objectives and the contributions to knowledge and the existing literature.

CHAPTER 2

Theoretical Background

The broad aim of this work is to evaluate the pore space of selected reservoir material using the three methods of Mercury Injection Capillary Pressure (MICP), Pore Network Modelling (PNM) and Nuclear Magnetic Resonance (NMR). This chapter presents the relevant theory and literature associated with these methods, particularly in the context of how these relate to the quantification of porosity and pore size distribution.

2.1 Porosity

Porosity is an important parameter for many petroleum engineering disciplines including reserve estimation, reservoir characterisation and drilling. It represents a measure of the amount of pore space occupied by hydrocarbon fluids or water and provides an early measure of the reservoir's economic potential as it directly relates to the initial hydrocarbon amounts in place. Porosity also impacts drilling operations and influences the rate of penetration and the quantities of drilling fluid lost to a formation by invasion. Furthermore, knowledge of porosity variations across the reservoir can assist in building robust reservoir characterisation models which can help identify the locations of highest productivity within the reservoir. This information can enhance reservoir development planning and influence the implementation of recovery schemes.

2.1.1 The Nature of Porous Media and its Relationship to Porosity

Brewer and Sleeman (1960) propose that the microstructure of porous media is comprised of two primary elements: the solid matrix and the pore spaces which encompass any in-situ fluids. With regards to this arrangement, the bulk volume (BV) of a porous medium can be thought to comprise of a pore volume (PV) and a grain or solid volume (GV). Porosity (φ) is defined as the ratio of the PV to BV.

$$\varphi = \frac{PV}{BV} \qquad [2\text{-}1]$$

The nature of the solid matrix influences the porosity. Grain size, packing, sorting and shape are textural parameters of the solid mass which directly affect porosities (Ahmed, 2019). Grain size is generally expressed as a function of length (typically as the diameter of the grain); sorting describes the distribution of the grain sizes. Packing refers to the arrangement of the grains which is influenced by their shape. A good example of this is grains that are flat and elongated are usually arranged with their flat surfaces together which tend to reduce pore space and lead to lower porosities.

The pore space is comprised of both pore bodies (pores) and pore throats. These can form an extensive network which traverses the medium and allow for the passage of fluids (Anovitz and Cole, 2015). The attributes of the pore space govern fluid flow and can be described as being either effective or isolated. Effective pore space indicates that the overall pore space is sufficiently interconnected allowing for the flow of fluid through the medium. Isolated or dead pore space can contain fluids but do not allow for these fluids to flow.

This degree of connectivity gives rise to two types of porosity: total porosity and effective porosity. Total or absolute porosity is the ratio of the total pore space to the total bulk volume. Effective porosity is the ratio of interconnected pore space to the bulk volume. For petroleum reservoirs, it is the effective porosity which is important towards the recovery of hydrocarbon fluids (Chen and Song, 2002).

2.1.2 The Scale of Pore Studies

Porous media can be studied at various scales which include the micro-, meso- or macro-scales. At the meso-scale, the overall dimension is of the order of 10 cm. This scale is also referred to as the lab or Darcy scale since Darcy's Law or its extensions generally describe the fluid flow at such dimensions (Peszyńska *et al.*, 2010). Darcy's Law is also applicable at the macro-scale, which is generally one order of magnitude longer than the meso-scale. Passage from meso-scale to macro-scale is known as *upscaling*.
.
At the micro- or pore-scale, pore dimensions are typically of the order of sub-micron to hundreds of microns (Taud *et al.*, 2005; Tucker, 1991). In order for pore-scale studies to be meaningful, the amount of material studied at the pore-scale must be representative of some larger volume of interest. This specific amount of material which must be studied is referred to as the *representative elementary volume* (REV).

The REV can be defined as the minimum volume of a sample from which a given parameter becomes independent of the size of the sample (Bear and Bachmat, 1990) and from which the majority of sample's inherent features are sufficiently and statistically captured for a high confidence in the results (Gelb *et al.*, 2011).

Many approaches have been proposed in the literature to determine the REV for porous media. Several notable works which include Al-Raoush and Papadopoulos (2010), Fernandes *et al.* (2012), Gelb *et al.* (2011), Halisch (2013) and Rozenbaum and Rolland du Roscoat (2014) are discussed below.

The most popular of these approaches focus on obtaining the REV deterministically by taking a small volume within the sample and then calculating a property of interest. The small volume chosen is called the region of interest (ROI) and porosity is the most common property of interest chosen (Al-Raoush and Papadopoulos, 2010; Halisch, 2013). The size of the ROI is then incrementally expanded in all directions and the property is recalculated at each incremental step. The REV is then identified as that particular volume across which the property remains constant.

Porosity is an average property determined over a representative elementary volume (REV) (Bear, 1972) as shown in Figure 2-1.
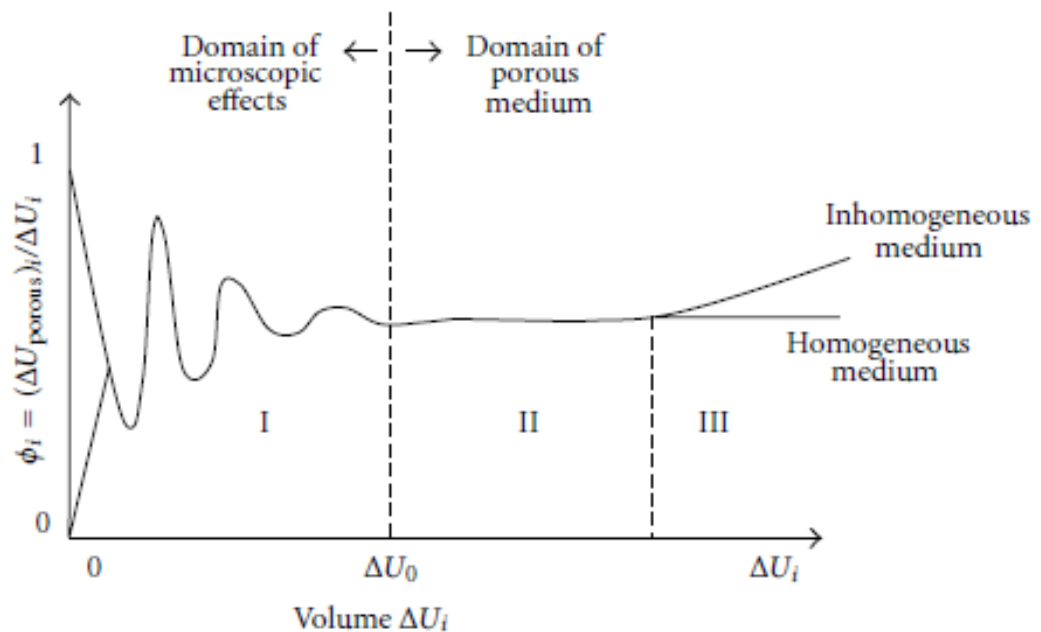
Figure 2-1: Representative elementary volume (REV, ΔU_o) for the porosity (ϕ). ΔU_i represents any volume in the porous media (after Bear, 1972).

For porosity to be meaningful, the volume of porous media studied must obey two criteria (Bear, 1972). The first is that the volume must exceed the size of a single pore and thus, the addition of more pores will maintain a representative statistical average. The second criterion is that the volume must be smaller than the heterogeneity of the entire flow domain (Figure 2-1). These two conditions define the REV and can be used to provide a uniform porosity for the total domain of the porous media.

2.1.3 Porosity Determination

The porosity of reservoir material can be determined via several methods. These include core analysis, interpretation of wireline logs, image analysis on thin-sections and micro-computed tomographic images, thermoporosimetry, crushing and well-testing (analysis of build-up tests) (Aligizaki, 2006). Of these, core analysis and well-logging are the most commonly practised within the petroleum industry (Jozanikohan *et al.*, 2014).

Wireline logging is generally carried out by lowering a *sonde* or probe into the borehole of a well, usually after a section of the well has been drilled. A log is a continuous recording of a particular geophysical parameter with depth. Porosities can be interpreted from electrical, nuclear, density or sonic signals acquired from the borehole. The principles of well-logging and well-log analysis have been extensively described elsewhere and excellent reviews of these methods can be found in Bateman (2012) and Krygowski (2004).

Porosity from core analysis can be obtained through several techniques which attempt to quantify bulk, grain or pore volumes. Common methods include intrusion by mercury or inert gas (e.g. helium), liquid saturation and fluid displacement. A comprehensive review of these methods is given by the American Petroleum Institute (1998).

The use of either core analysis or well-logging to provide a reliable measure of porosity is function of the method and interpretation of results. Both these techniques can yield accurate porosity measurements under favourable conditions. To be useful, results from core analysis must take into account the effects of core sample bias, sample frequency and volume (American Petroleum Institute, 1998). When core volumes are small, well-logs can typically provide better porosity information for heterogeneous reservoirs as logging tools can traverse large sections of the formation. However, the accuracy of well-logs depends upon applying the appropriate corrections for particular borehole

environment conditions (e.g. weight of mud fluids) and only then has a greater applicability when calibrated with porosities from core (Bateman, 2012).

2.2 Pore Size Distribution

Although porosity provides useful information regarding the storage capacity and hydrocarbon recovery, it does not provide an indication of how flow can be established. Pore size and its distribution however, are parameters which directly relate to the passage of fluids through the material (Song *et al.*, 2002). There is no established correlation between porosity and pore size and this is not surprising given that porosity is a measure of the volume (amount) of pores which exist and not of their size and size distribution (Bennion and Bachu, 2006).

Pore networks approximate the porous medium as an interconnected system of pores and pore throats. At static conditions, the pores and throats contain the fluids. When pressure is applied, flow can be accomplished as fluid moves through both pores and pore throats. The size of the pores and throats are therefore important as they directly affect the amount of fluid which can be transmitted through the media.

There are many ways to classify pore body and throat size. A popular terminology is the use of the terms: *micropore, mesopore* and *macropore*. Although in common use, there is a wide variation among researchers on the size of the pore radii which partition these three pore classes (Skalinski and Kenter, 2014). For example, the average pore throat radii of micropores are defined as being below 0.1 microns (Chekani and Kharrat, 2009), 0.2 microns (Porras and Campos, 2001), 0.3 microns (Marzouk *et al.*, 1995; Skalinski *et al.*, 2009), 0.5 microns (Arfi *et al.*, 2006) or 2 microns (Hulea and Nicholls, 2012).

In terms of pore bodies, Choquette and Pray (1970) studied carbonate reservoir material and defined the average diameters of micropores as being less 1/16 mm (62.5 microns), mesopores between 1/16 mm and 4 mm and macropores as being greater than 4 mm. Bell *et al.* (2012) and Rouquerol *et al.* (1994) classify the diameters of micropores as measuring less than 2 microns, mesopores between 2 and 50 microns and macropores as larger than 50 µm.

Information regarding the pore size distribution of reservoir material is generally acquired from either mercury injection capillary pressure (MICP) testing, image analysis of thin sections, pore network modelling or NMR studies. These techniques are described in subsequent sections on this chapter.

2.3 Capillary Pressure and its relationship to pore geometry

Capillary pressure is defined as the difference in pressure which exists at the interface between two immiscible fluids in the pores (capillaries) of the reservoir rock. It is dependent upon the 3D geometric and connectivity properties of the pore space and is a function of pore throat size, pore throat size distribution, fluid saturation, wettability and interfacial tension (Elshahawi *et al.*, 1999).

The distribution of pore throats in the porous medium determines the magnitude of capillary pressure (Volokitin *et al.*, 2001) and the fundamental equation governing P_c is the modified Young-Laplace equation given below:

$$P_c = \frac{2\sigma\cos\theta}{r_t} \qquad \text{[2-2]}$$

where P_c is the capillary pressure, r_t is the pore throat radius, σ is the interfacial tension between the fluid phases and θ is the contact angle between the solid surface and the fluid-fluid interface.

The contact angle, θ is controlled by the wettability which exists in the medium. Wettability can be defined as 'the tendency of one fluid to spread on or adhere to a solid surface in the presence of other immiscible fluids' (Craig, 1976). For a two-phase reservoir system consisting of oil and water, wettability is the preference of the solid matrix to be in direct contact with either a layer of oil or a layer of water. In this scenario, three further broad categories can exist: strongly water-wet, strongly oil-wet and intermediate wet. The variation in these three categories depends upon the contact angle made between the solid surface and the fluid-fluid interface.

Strongly water-wet media exhibit a contact angle close to zero when measured through the water phase whereas the angle is close to 180° for strongly oil-wet surfaces. If the surfaces are intermediate wetting, then no strong preference for either water or oil exists and the contact angles vary from 45° – 135° (Craig, 1976; Radke *et al.*, 1992).

Capillary pressure data provide important details regarding pore structure as pore throat size can be inferred from P_c at particular saturations (Jaya *et al.*, 2005). Equation 2-1 shows that the pressure at which a fluid enters a pore is determined by the surface tension at the fluid interface and the radius of a pore throat. It is assumed that fluid entering through a pore throat immediately fills most of the adjoining pore volume. As such, the capillary pressure curve can provide a cumulative *pore throat size distribution* (PTSD).

Traditionally, pore throat size distributions (PTSDs) have been measured using laboratory capillary (mercury injection) measurements on core (Mao *et al.*, 2005) where these measurements form part of the capillary pressure experiments conducted under SCAL. Once capillary pressure curves have been determined, these can be converted into PTSDs by rewriting equation 2-2 as shown below:

$$r_t = \frac{2\sigma \cos\theta}{P_c} \qquad \text{[2-3]}$$

It is important to note that the radius denoted to in this equation is sometimes incorrectly referred to as 'pore size' which describes the radius of a pore body. This radius however refers to the largest throat through which the pore body can be accessed (Vavra *et al.*, 1992).

2.3.1   Mercury Injection Capillary Pressure (MICP) Testing

Mercury injection capillary pressure (MICP) testing involves the injection of mercury into a sample that has been cleaned of all original fluids and then subsequently dried and evacuated of all cleaning fluids. The non-wetting phase is represented by the injected mercury and the wetting phase is the air that fills the evacuated sample. This requires conversion to reservoir conditions using contact angle and surface tension inputs (Comisky *et al.*, 2007). Given that mercury is strongly non-wetting, the resulting capillary pressure data represent primary drainage measurements (Pittman, 1992).

During the test, the sample is immersed in liquid mercury with pressure being increased progressively. The amount of mercury entering the sample is measured and converted to a non-wetting saturation. Pressures during the test can vary from 5,000 – 70,000 psi depending upon the sample where higher pressures can be used to access and characterise very small pores within the sample (Honarpour, 2004). The MICP test is able to provide direct measurements of porosities as the volume of mercury imbibed quantifies the amount of pore space. Pore throat radius can be inferred using equation 2-3.

Advantages of the MICP technique include relatively fast testing times as well as the capability of testing of small and irregularly shaped samples which becomes important when sample amounts are limited.

Disadvantages of the method include the prerequisite cleaning and evacuation needed before the samples can be tested. This can constrain the use of MICP for certain kinds of reservoir material; particularly for those that are unconsolidated and unconventional. Another important drawback is related to the lack of a true wetting phase during testing (Honarpour *et al.*, 2004). Given that mercury and air are not reservoir fluids, the method may not replicate reservoir displacement processes correctly (American Petroleum Institute, 1998).

Furthermore, there are challenges in interpreting PSDs from MICP measurements which understates the true nature of the material under study. A typical example of this is that mercury intrusion of larger pores may be hindered if these are accessed through smaller neighbouring pores which require larger injection pressures. When these larger pores are eventually accessed, they may be interpreted in the PSD incorrectly as an amplified quantity of smaller pores (Morrow and Heller, 1985).

2.4 Nuclear Magnetic Resonance (NMR) Fundamentals

NMR has been used extensively by a number of researchers to study the structure of porous media. These studies have included the determination of key fluid and petrophysical properties, including viscosity, porosity, permeability, pore-size distribution and capillary pressure (Adebayo *et al.*, 2017; Bryan *et al.*, 2003; Jin *et al.*, 2009;

Kleinberg, 1996; Lyu *et al.*, 2018; Mao *et al.*, 2005; Mitra *et al.*, 2003 and Volokitin *et al.*, 2001).

NMR analysis and interpretation rely upon a good understanding of several key concepts related to nuclear magnetism, polarization, relaxation times, spin echoes and pulse sequences. These concepts are presented briefly in Appendix I to provide a sufficient background. Excellent reviews and a more comprehensive framework of NMR physics can be found in Coates *et al.* (1999), Cowan (2005), Dunn *et al.* (2002) and Kimmich (2001).

NMR measurements are based upon the relaxation response of hydrogen nuclei to applied magnetic fields. Hydrogen is a primary component of the fluids present in petroleum reservoirs (water and hydrocarbons) and almost all NMR measurements related to the petroleum industry are based on the response of hydrogen nuclei (Coates *et al.*, 1999).

There are two relaxation times that can be measured during NMR experiments: longitudinal (T1) and transverse (T2) relaxation times. The T2 relaxation time is of particular importance to NMR core analysis and can provide key information regarding the structure and properties of porous media (Kleinberg, 1996; Mao *et al.*, 2009; Slijkerman and Hofman, 1998). Chapter 6 provides a more comprehensive outline of the related theory governing the T2 relaxation mechanism and how this is related the study of porous media.

The T2 relaxation time describes the NMR signal in the transverse plane with respect to the applied magnetic field. The contributions to the T2 relaxation time come from three terms (given in equation 2-4):

1. Bulk fluid relaxation (T2B) which is mainly due to dipole–dipole interactions between nuclei spins within the fluid.
2. Surface relaxation (T2S) which is associated with the interactions of nuclei at the pore-wall interface and the motion of a wetting fluid layer adjacent to the pore-wall interface (Banavar and Schwartz, 1989).
3. Diffusion (T2D) related relaxation due to presence of background magnetic field heterogeneities.

$$\frac{1}{T2} = \frac{1}{T2B} + \frac{1}{T2S} + \frac{1}{T2D} \qquad \text{[2-4]}$$

The relative contribution of each term to T2 is dependent upon a number of factors including the type of fluid in the porous medium, the pore size distribution and the nature of the pore-grain surface, specifically as relates to its wettability and pore surface area (Coates *et al.*, 1999; Niu *et al.*, 2008).

As an example, several researchers (Bryan *et al.*, 2003; Kantzas, 2009; Niu *et al.*, 2008) have shown that for selected water-wet media where brine is the major fluid contained in the pores, the T2 signal is dominated by the surface relaxation, T2S. When the fluid is changed to heavy oil or bitumen in the same water-wet pores, T2 is dictated by T2B. Bulk relaxation, T2B, results from the local diffusion of the fluid molecules as energy is exchanged between the spins of hydrogen nuclei. The rate at which this exchange takes place is limited by molecular motion (Brown and Gamson, 1960). The bulk relaxation rate of a fluid, T2B can be obtained by measuring the NMR response when a homogenous magnetic field is applied to a fluid that is placed in a large container whose dimensions are considered sufficiently sizeable to preclude the impact of surface relaxation.

T2B is directly proportional to its viscosity (Straley *et al.*, 1997). Low viscosity fluids are associated with a higher molecular mobility which results in slow relaxation rates and high values of relaxation times. Conversely, high viscosity fluids have a reduced molecular mobility and are associated with faster relaxation rates.

Water is generally considered a low viscosity fluid. The bulk relaxation rate of water is of the order of 2000 – 2500ms (Bryan *et al.*, 2003; Kantzas, 2009; Niu *et al.*, 2008). This rate is high when compared to higher viscosity fluids e.g. heavy oils and bitumen. Bitumen is very viscous and is defined as having an in-situ viscosity greater than 10,000 cP (Meyer *et al.*, 2007; World Energy Council, 2007). When compared to water, heavy oil and bulk bitumen typically relax at less than 10ms (Kantzas, 2009). This low rate is related to the restriction of the hydrogen nuclei in the high viscous bitumen mass which results in a very fast relaxation rate.

The diagram in Figure 2-2 shows the NMR spectra for a sample that contains 50% bitumen and 50% water and clearly indicates two peaks corresponding to the bitumen (T2B ~ 2ms) and water (T2B ~ 2000ms).

Bryan *et al.* (2008) have also conducted experiments which show that the relaxation times for bitumen generally occur at approximately the same T2 locations whether the

fluid exists in bulk or in porous media (shown in Figure 2-3). This is attributed to the high bitumen viscosity and implies that the relaxation due to surface effects for these oil sands is negligible.
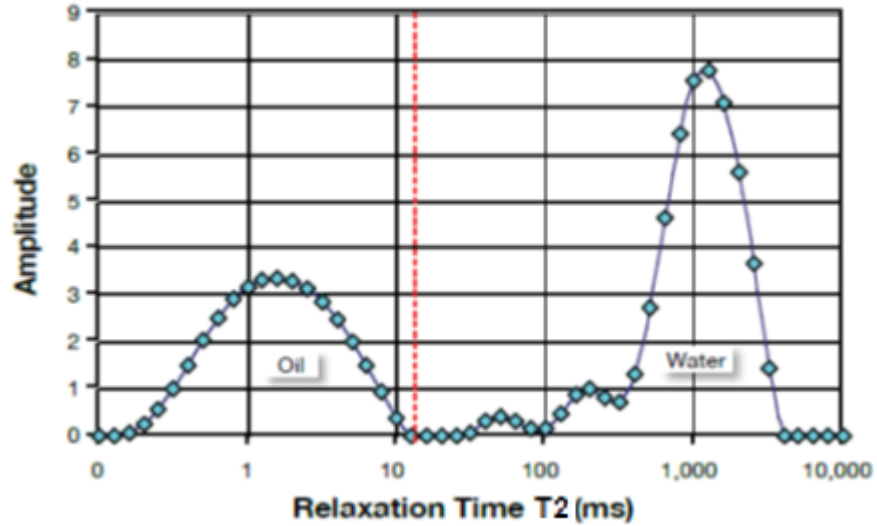
Figure 2-2: NMR spectrum of heavy oil and water mixture (after Kantzas, 2009)
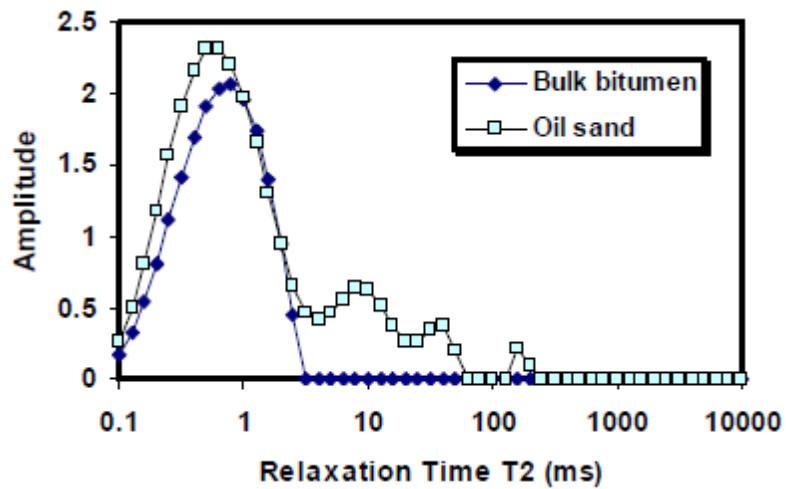
Figure 2-3: NMR spectrum of oil sand compared to bulk bitumen oil signal (after Bryan *et al.*, 2008)

Banavar and Schwartz (1989) go on to state that surface relaxation only occurs in a surface-wetting fluid and that when multiple fluids are present, a non-wetting fluid will only undergo bulk and diffusion-based relaxation. The material surfaces of the Athabasca Oil Sands are commonly accepted as being water-wet (Czarnecki *et al.*, 2005) with the presence of a 10 – 15 nm film of connate water surrounding the individual

sand grains signifying that no direct contact exists between the sand grain and bitumen (Takamura, 1982). Consequently, bitumen represents the non-wetting fluid will therefore only undergo bulk relaxation according to Banavar and Schwartz (1989). This would corroborate the findings of Bryan *et al.* (2008) (Figure 2-3) in which the overall T2 relaxation of the bituminous oil sands studied in his work is almost identical to the bulk bitumen relaxation signal. Some of these concepts are further explored in Chapters 6 and 7.

2.5 Pore Network Modelling (PNM)

Recent advances in imaging technologies have intensified the study of porous media at the micro- or pore-scale. This has given rise to an abundance of terms which are largely equivalent. Popular terminologies include: *Pore Network Modelling* (Dong and Blunt; 2009; Suicmez and Touati, 2008; Varloteaux *et al.*, 2013; Xiong *et al.*, 2016), *Digital Core Analysis* (Grachev, 2012; Zhou and Chen, 2017), *Digital Rock Physics* (Andra *et al.*, 2013; Kalam, 2012) and *Pore Scale Modelling* (Balhoff and Wheeler, 2007; Blunt *et al.*, 2013; Boek, 2010).

Regardless of the terminology, the general methodology and aims of these image-based techniques are the same. This work uses the term *pore network modelling* (PNM) to describe the derivation and analysis of realistic interpretations of the pore structure of porous media. Pore network models approximate the medium as an interconnected network of pores and pore throats and illustrate how pathways for fluid flow can be established. These networks can be derived in a number of ways but most involve first imaging the pore space and then using the resulting images to construct a 3D model.

2.5.1 Imaging Porous Media

Many efforts have been used to acquire pore network models through imaging methods (Amirtharaj *et al.*, 2011). Prior to the development of more sophisticated techniques such as backscatter scanning electron microscopy (Ioannidis *et al.*, 1996), micro-computed tomography (Dong and Blunt, 2009; Ghous *et al.*, 2008; Peng *et al.*, 2012) and focus ion beam nanotomography (Bera *et al.*, 2011), image analysis of porous media was limited to destructive methods such as thin-sectioning.

A thin section is a slice of material approximately 30 microns thick through a sample of interest (Passchier and Trouw, 2005). It consists of a basal glass plate, a slice of the sample material and a cover glass plate affixed together using appropriate gluing material. The procedure for obtaining pore network information involves cutting the sample into several slices, mounting these onto glass plates and using a light microscope to acquire selected 2D attributes of the pore space. The 2D information is then interpolated to construct a 3D model.

The use of thin sectioning however to derive 3D information has a number of limitations. The method is somewhat tedious and prone to errors since the sample can be altered during the cutting and mounting processes. In addition, the distance between slices is typically too large to preclude the loss of 3D information especially as relates to connectivity and permeability. An example of this is that pores that are isolated in 2D images could potentially be connected in a 3D model.

Recent advances in imaging technology have permitted the use of Nuclear Magnetic Resonance (NMR), Focused Ion Beam nanotomography (FIB-nt), Transmission Electron Microscopy (TEM) and Micro-Computed Tomography (micro-CT) to provide more robust 3D information. Excellent reviews of these methods are provided by Bera *et al.* (2011), Ioannidis *et al.* (1996), Ketcham and Carlson (2001) and Matrecano (2010).

The spatial resolution across these methods can vary considerably. This is often the rationale of selecting one method over another. For example, FIB-nt has a resolution of approximately 10 nm which is appropriate for use with materials whose pore spaces are within the nanometre range, such as shale (Peng *et al.*, 2012). Micro-CT, on the other hand, has a much lower resolution within the limit of 1.5 microns and higher and is better suited for investigating materials with larger pores above these dimensions.

This work focuses on acquiring images from micro-CT imaging since it is expected that the features of interest in this work will be sufficiently sampled at the resolutions micro-CT provides. In addition, among all the techniques listed above, micro-CT scanning is the most prevalent given that the technology is well-developed, highly commercialised, fast and non-destructive (Ketcham and Carlson, 2001; Matrecano, 2010).

2.5.2 Micro-computed Tomography (Micro-CT) Imaging

Micro-CT imaging uses the attenuation of X-rays to obtain 2D cross-sections of an object at various resolutions of several microns. During the process, the sample is mounted onto a platform positioned between the X-ray source and a detector. The sample is then rotated in a step-wise fashion while simultaneously subjected to X-ray beams. Owing to absorption, the X-ray beam is attenuated when it passes through the sample.

The degree of attenuation is dependent on a material's density which for a homogeneous medium, can be expressed by the Lambert-Beer's Law:

$$I = I_o e^{-\mu x} \qquad\qquad [2\text{-}5]$$

where I is the intensity of the transmitted radiation, I_o is the intensity of the incident radiation, μ is the attenuation coefficient and x is the distance travelled through the material. The principles governing micro-CT imaging are discussed comprehensively in the works of Ketcham and Carlson (2001), Keller (1998) and van Geet *et al.* (2000).
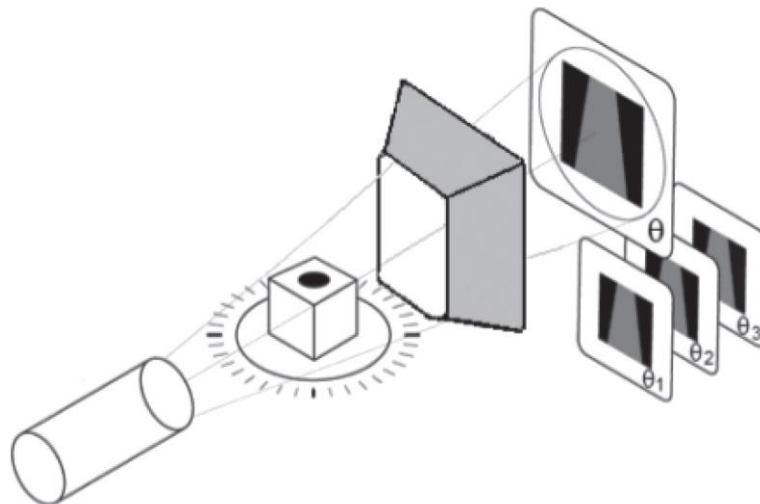
Figure 2-4: Micro-computed tomography operation principles
(after Fernandes *et al.*, 2012)

Measurements of the attenuation at prescribed angular steps can produce grey-level projection images or radiographs of the sample (see Figure 2-5). The intensity of the grey value at each location in the image corresponds to the change in intensity of the X-ray beam as it is attenuated. This suggests that if the principal elements comprising the sample have an adequate density variation - that is, if they attenuate the X-ray by

differing amounts - then these elements can be identified by their corresponding grey value. This is the reasoning behind which the pores (filled with either air or in-situ hydrocarbon fluids) can be distinguished from the solid mass.

2.5.3 Radiograph Reconstruction and Artefacts in Micro-CT Images

After the acquisition process, the projection images or radiographs need to be reconstructed to provide meaningful data. Reconstruction is the mathematical process of converting sonograms into 2D images. The most common reconstruction method uses a filtered back projection algorithm which is based on the work of Feldkamp. Comprehensive reviews of the Feldkamp algorithm are given by Feldkamp *et al.* (1984) and Ketcham and Carlson (2001). Figure 2-5 shows the raw data procured during micro-CT scanning and the final image after reconstruction.
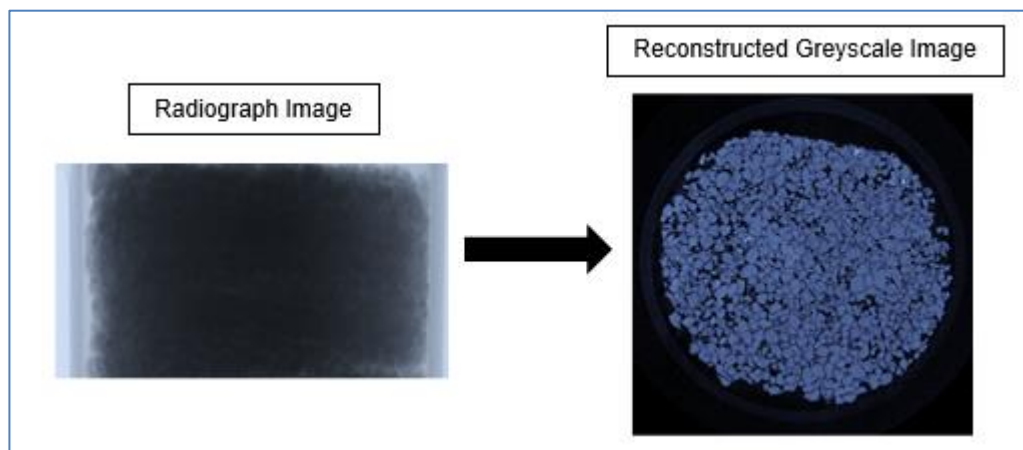
Figure 2-5: Reconstruction of a radiograph to 2D image

The intensity of the grey value at each location in the image corresponds to the change in intensity of the X-ray beam as it is attenuated which is related to the density of the material at that location. Generally, the pore space and solid mass of reservoir material possess an adequate density variation which allows the pores to appear as dark grey in colour which easily distinguishes them from the solid mass which appears as a lighter grey as indicated in the reconstructed greyscale image in Figure 2-5.

Micro-CT imaging however is prone to several limitations which tend to misrepresent the attenuation measurements and reduce the quality of the reconstructed 2D images. Common problems include high-frequency noise and the presence of artefacts in the radiographs. The most prevalent artefacts encountered include beam hardening and

ring artefacts. Ring artefacts manifest themselves as full or partial circles positioned on the rotational axis which are caused by variations in the output of the detectors (Ketcham and Carlson, 2001).

Beam hardening is caused by a variation in the energy of the X-ray beam, which for micro-CT scanners is polychromatic in nature (more than one wavelength). Selective absorption of low energy X-ray wavelengths from the polychromatic X-ray leaves the beam with a greater concentration of higher energy wavelengths. This results in the beam becoming increasingly more penetrating and causes the material at the edge of the sample to appear denser than at its centre (Ketcham and Carlson, 2001; Van Geet *et al.*, 2000; Wildenschild *et al.*, 2002). This manifests itself as a ring of bright pixels around the edge of the sample's 2D reconstructed image reducing to dark pixels at the centre.

To minimise the effects of beam hardening in the projection images, most micro-CT scanners employ built-in metallic filters (e.g. brass and aluminium) which attempt to reduce the absorption of low energy X-ray wavelengths. In addition, during the radiograph reconstruction process, beam hardening and ring artefact corrections are used to produce optimal quality 2D cross-sections.

2.5.4 3D Reconstruction

After radiograph processing is completed, the sequential 2D images can be now be compiled to provide a 3D model as shown in Figure 2-6 (Keehm and Lee, 2007). The smallest units of data in the 2D image and 3D model are termed pixels and voxels respectively and the size of these are governed by the resolution provided by the imaging technique. For example, a 2D image at a resolution of 5 microns implies that every pixel in the *x* and *y* directions have a length of 5 micron.

Moving from 2D images to a 3D model requires the use of specialised software employing advanced mathematical modelling techniques. Several commercially available software packages have been developed specifically for the analysis of porous media and geomaterials (Iassonov et al., 2009). These have been specifically designed to import 2D images and produce pore network models. The most common suites include Avizo^{TM} (http://www.tgs.com), ScanIP (http://www.simpleware.com), Amira® (http://www.amiravis.com), 3DMA-Rock (http://www.ams.sunysb.edu/~lindquis) and Blob3D (http://www.ctlab.geo.utexas.edu/software/).
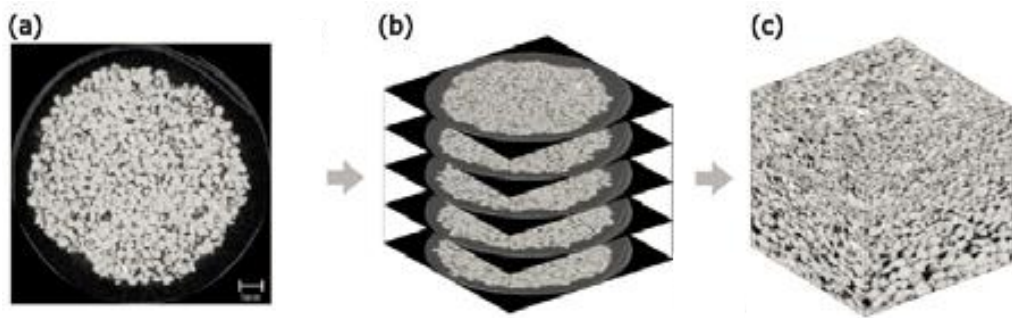
Figure 2-6: Compilation of 2D Images to produce a 3D Model

(after Keehm and Lee, 2007)

2.5.5 Noise Reduction and Filtering

Although the pore and solid mass phases are easily distinguished with the naked eye after radiograph reconstruction (Figure 2-5), direct measurements of the pore space are often not possible due to the presence of noise. Noise is a random variation of the brightness, contrast or colour information of a digital image and manifests itself as spots, blurring or greyscale speckling within the image.

Techniques to reduce noise involve the use of filtering methods which attempt to *clean* the image while minimising the loss of essential information. The most common filtering methods include mean filtering, median filtering and Gaussian smoothing. These methods have the effect of smoothing the image, especially in terms of contrast, which allows for a better distinction between phases by reducing spots and speckling and improving edge detection within the image (Rozenbaum and Rolland du Roscoat, 2014).

All three filtering techniques examine each voxel within the image and compares the voxel's greyscale value to that of the surrounding voxels in order to determine whether the voxel is representative of its surroundings. Mean filtering involves replacing each voxel greyscale value in an image with the mean or average value of its neighbours. This essentially eliminates voxels whose greyscale values are unrepresentative of their surroundings by replacing with the mean of surrounding voxels. Rather than replacing the voxel's greyscale value with the mean of the surrounding of voxels, the median filter changes it to the median of surroundings values. Gaussian smoothing or blur function uses a convolution method derived from the Gaussian (normal) function to examine each voxel in the image and replace its value to a weighted average of the surrounding voxels (Gonzales and Woods, 2001).

28

2.5.6 Segmentation

After filtering, it becomes possible to partition the greyscale voxels of the 3D image into distinct phases. Segmentation is the process of assigning a label to every voxel in a digital image so that voxels with the same label possess similar characteristics. In PNM, the goal of segmentation is to allow each voxel in the image to be labelled and identified as either belonging to a pore or the solid phase (Andra *et al.*, 2013).

There are numerous segmentation methods which are proposed in the literature. More common approaches include clustering, global thresholding, locally adaptive thresholding and region growing methods Iassonov *et al.* (2009). The principles of these techniques have been discussed extensively elsewhere and excellent reviews are presented in the work of Iassonov *et al.* (2009), Pal and Pal (1993) and Sezgin and Sankur (2004).

Global thresholding, however is the most commonly used technique for reservoir material and involves the identification of a single greyscale value or *threshold* which is used to distinguish the pores from the solid mass (Iassonov *et al.*, 2009). There are several techniques by which the threshold value can be identified but the most conventional method is through the use of a histogram approach which plots the grey level of each voxel against its frequency as shown in Figure 2-7. Once the threshold has been identified, the pore and solid mass are often distinguished from each other using either black to represent the solid mass or white to identify the pores or vice versa.

Determining the threshold is often one of the more difficult steps in PNM and there is sometimes significant uncertainty is the classification of voxels whose greyscale value are close to the threshold value (Verges *et al.*, 2011). This uncertainty has the potential to reduce or amplify pore space as well as blur, terminate or connect pore spaces which may not necessarily exist (Taud *et al.*, 2005). This can result in significant variations in porosity and other derived properties with only very small changes in the threshold parameter (Sheppard *et al.*, 2004).
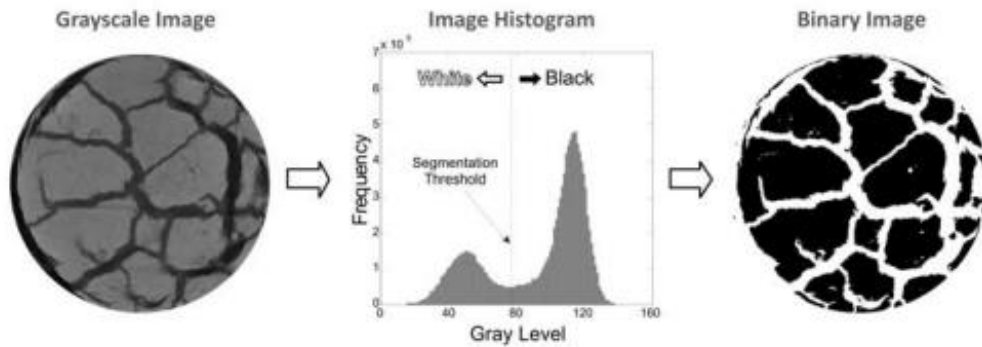
Figure 2-7: An illustration of the Histogram Thresholding Approach
(after Iassonov *et al.*, 2009)

2.5.7 Representative Elementary Volume (REV)

Common imaging techniques in PNM include Focused Ion Beam nanotomography (FIB-nt) and Micro-Computed Tomography (micro-CT). The spatial resolution across these methods differs. Generally as resolution increases, the amount of sample which can be viewed in the detectors becomes increasingly smaller due to technical limitations of imaging technique (Dufresne *et al.*, 2004).

Smaller samples raises questions regarding the representativity of the data to infer macroscopic characteristics based on microstructural data sets (Rozenbaum and Rolland du Roscoat, 2014). As such, microstructural studies of porous media often require the identification of a representative elementary volume (REV). The REV can be defined as the minimum volume of a sample from which a given parameter becomes independent of the size of the sample (Bear and Bachmat, 1990) and from which the majority of sample's inherent features are sufficiently and statistically captured for a high confidence in the results (Gelb *et al.*, 2011).

Obtaining the REV for microstructural studies is important for two main reasons. Firstly, the results of the study must be valid across the entire medium under consideration and as such, the REV has to be large enough to capture the inherent attributes of the material. Secondly, microstructural studies often involve the reconstruction, visualisation and characterisation of 3D images which is associated with large amounts of data and data handling. This generally requires high computing capacities and large processing times. Identifying the REV allows for the study of the smallest representative amount of sample which makes the most efficient use of time and computing resources.

Many approaches have been proposed in the literature to determine the REV for porous media. Notable works include Al-Raoush and Papadopoulos (2010), Fernandes *et al.* (2012), Gelb *et al.* (2011), Halisch (2013) and Rozenbaum and Rolland du Roscoat (2014).

The most common REV approach determines the REV deterministically by first taking a small volume from within the 3D mass and then calculating a property of interest. The small volume chosen is called the region of interest (ROI) and porosity is typically the common property of interest chosen (Al-Raoush and Papadopoulos, 2010; Halisch, 2013). The size of the ROI is then incrementally expanded in all directions and the property is recalculated. The REV is then identified as that particular volume across which the property remains constant as indicated in Figure 2-1.

2.5.8 Pore Network Extraction

The goal of PNM is to derive a 3D representation of the internal structure of the porous medium from which a pore network can be identified. This 3D pore network can provide useful information regarding the inherent pore attributes and be used to predict selected petrophysical properties without the need for conventional core testing.

There are two major methods of extracting the pore network from a 3D reconstructed model: the medial axis algorithm and the maximal ball algorithm (Sarker and Siddiqui, 2009). The medial axis algorithm works on the basis of producing a reduced representation of the pore space via the use of a thinning or burning algorithm. This acts as a topological skeleton running through the centre of the pore network. Partitioning of the pore space uses local minima along branches, and nodes to represent pore throats and pore bodies respectively. Disadvantages associated with this method include sensitivity to noise in the digital images which requires image processing to remove spurious data (Dong and Blunt, 2009; Lindquist *et al.*, 1996).

The maximal ball algorithm produces spheres around each voxel. The size of the sphere is increased until it is at a maximum when touching the boundary between the void space and the grains. Spheres that are considered to be inclusions of other spheres are then removed, leaving just the maximal balls in place. The largest maximal balls in the network represent pore bodies whereas the smallest maximal balls represent the pore throats (Silin *et al.*, 2003; Suicmez and Touati, 2008).

2.6 Comparing the MICP, PNM and NMR approaches

A broad aim of this work is to compare the porosity and pore size distributions determined independently from the MICP, PNM and NMR approaches. These methods generally measure varying aspects of the pore space with regards to the saturating fluids, pore dimension measurements (e.g. pore throat vs. pore body), the destructive nature of the test as well as the resolution and connectivity of the pore space.

In terms of the saturating fluids, both MICP and NMR require specific fluids to be contained in the pore space prior to testing. For MICP and NMR, these fluids are air and water (or brine) respectively. This generally precludes the MICP and NMR testing of samples imbued with their original fluids. Micro-CT scanning requires little to no prior sample preparation (Ketcham and Carlson, 2001) and so can be used when any fluid is contained within the pore space.

In terms of pore dimensions and connectivity, PNM derives porosity and PSD by first extracting the topological skeleton running through the centre of the pore network and then identifies individual pore diameters by partitioning the skeleton and fitting ellipsoids into local minima. This typically provides a measurement of both the pore bodies and throats regardless of whether these are connected which is different to the MICP testing in which only the pore throat radii of connected pores are measured since the forced intrusion of mercury must take place through interconnected pores. For NMR, the introduction of water (or brine) into the pore space prior to testing must take place through interconnected pores and accordingly the PSD from NMR measurements typically reflect both the pore bodies and throats of connected pores which contain the hydrogen nuclei.

In terms of resolution, micro-CT has the capability to identify pores having diameters within the limit of 1 - 1.5 microns and higher (Peng *et al.*, 2012). This is low when compared to a similar resolution from MICP testing which is capable of injecting mercury into samples at pressures up to 70,000 psi; this can characterise very small pores within the sample (Honarpour, 2004) within the sub-micron range. NMR can characterise pore dimensions to the sub-micron level, but this is dependent upon hydrogen nuclei being contained within those pores which requires high injection pressures of water or brine during the cleaning and saturation processes prior to NMR testing.

In terms of sample usability after testing, both PNM and NMR are non-destructive forms of testing which allows for the repeatability of measurements. The intrusion of mercury however renders the sample unusable for other kinds of testing which is challenging when samples are expensive to obtain and are limited in quantity. Table 2-1 summarises these findings.

Table 2-1: Comparing selected aspects of the MICP, PNM and NMR approaches

	MICP	PNM	NMR
Saturating Fluids: Requires the removal of in-situ fluids prior to testing?	**yes** (air is the wetting fluid)	**no**	**yes** (requires water of brine)
Pore Aspect Measured	pore throat	both pore throat and pore body	both pore throat and pore body
Type of porosity measured (connectivity of the pore space)	effective	total	effective
Resolution	sub-micron to cm	micron to mm	sub-micron to cm
Destructive or non-destructive?	destructive	non-destructive	non-destructive

2.7 Conclusion

Pore size and its distribution directly influence the hydrocarbon recovery and fluid flow properties of porous media. Information regarding the pore space can be obtained using three complementary methods: Mercury Injection Capillary Pressure (MICP), Pore Network Modelling (PNM) and Nuclear Magnetic Resonance (NMR). This chapter presented the fundamentals and relevant literature associated with these methods, particularly in the context of how these related to the quantification of porosity and pore size distribution.

CHAPTER 3

Materials:

The selection of samples in relation to the methods used

3.1 Introduction

The general objective of this work is to evaluate the pore space of selected sandstone samples using three complementary methods: Mercury Injection Capillary Pressure (MICP), Pore Network Modelling (PNM) and Nuclear Magnetic Resonance (NMR). The type of fluid contained within the pore space influences the robustness of the results for each method. Both MICP and NMR require specific fluids to be contained in the pore space prior to testing which generally requires the removal and replacement of all original fluids with air for MICP and with water (or brine) for the NMR method. This typically will preclude the testing of samples imbued with their original fluids using these methods. PNM requires little to no sample preparation prior to testing (Ketcham and Carlson, 2001) and so is ideal for studying samples containing their in-situ fluids.

Three sandstone core samples were used throughout this work. Two of these samples were taken from well-studied, consolidated reservoirs: these were the Berea and Bentheimer core samples which represent the benchmark materials for this study. The consolidated nature of these materials made them ideal for analysing the response and the influence of a number of selected fluids during NMR testing as they could be subjected to repeated fluid injection and removal without comprising or changing the inherent pore structure.

The third core sample is taken from an Athabasca Oil Sand (AOS) reservoir. This sample was chosen as it is a prime example of an unconsolidated material for which pore characterisation information is often difficult to obtain due in part to the nature of the oil sand material and the in-situ bitumen fluid. This chapter provides a brief description of the materials used in this project, the attributes of bituminous oil sands and the particular selection of these samples in relation to the methods used.

3.2   Berea and Bentheimer Core Samples

Berea and Bentheimer are well-studied materials within the petroleum engineering industry particularly as they are considered to be good representatives of typical reservoir material.   Their use for experimental work in various areas of petroleum engineering is prevalent (Chen and Song, 2002; Lindquist *et al.*, 1996; Prodanovic *et al.*, 2007).

Berea sandstone samples are taken from the Berea Quarry in Ohio, USA. This material is an uncemented, generally homogenous rock with ambient porosities which can range from 12 – 25% (Berea Sandstone Petroleum Cores, 2015). The pore size of Berea sandstone samples is generally small with the material being comprised of interconnected pores having an average radius of 2 – 5 microns (Bera *et al.*, 2011; Peng *et al.*, 2012).

Bentheimer sandstone samples are taken from the Lower Saxony Basin in Germany. This material is described as homogenous in nature with little or no structural clays. The porosity of Bentheimer sandstone typically ranges from 18 – 27% (Peksa *et al.*, 2015) with pore radii distributions generally lying within 2 – 40 microns (Wilson, 2004).

3.3   The Athabasca Oil Sand (AOS) Core Sample

Athabasca Oil Sands (AOS) are a very dense and un-cemented granular material in which the main mineral composition is quartz (Wong, 2005).   They are generally unconsolidated, high porosity and high permeability sand deposits in which the in-situ porosity tends to vary from 30 – 35% but can be as high as 45 – 47% (Wong *et al.*, 2004).

The ease of flow during production is therefore not a major concern in these reservoirs but rather it is the high viscosity associated with the bitumen which impedes its recovery. Bitumen is defined as having an API classification lower than 10° and an in-situ viscosity greater than 10,000 cP (World Energy Council, 2007).

3.3.1 The nature of AOS: Implications for Laboratory Characterisation

Several factors impact the length of testing time and the reliability of the laboratory characterisation of oil sand material. These include the unconsolidated nature of the material and the difficulty of cleaning the cores of their original fluids since the in-situ bitumen can act as a cementing agent holding the grains together (Schmitt, 2005).

Additionally, oil sand cores tend to expand when they are recovered from heavy oil formations (Wong, 2005). This is due to the pressure release and gas expansion (also termed *gas exsolution*) which occurs during the core retrieval process (Dusseault, 1980). Dusseault (1980) and Dusseault and van Domselaar (1982) contend that there is usually a significant quantity of gas dissolved in the fluid phase of oil sands. This gas is comprised predominantly of methane, carbon dioxide and nitrogen.

In the reservoir, the oil sands are in an undersaturated state and as such, do not contain any gas due to in-situ pressure conditions. However, when retrieved and brought to the surface, the solution gas *exsolves* or is liberated as discrete bubbles within the bitumen. Due to the viscous nature of the bitumen, these bubbles cannot escape or form a contiguous phase and so they expand within the pores. This leads to a considerable expansion which can dilate original volumes by almost 15% (Collins, 2005; Dusseault, 1980). Significant dilation can also result in a fracturing of the core material (Wong, 2005).

In addition to the disturbance caused by gas exsolution, the unconsolidated nature of the AOS makes it particularly difficult to avoid damage during the coring and retrieval process. Coring usually takes place using a PVC core liner within the core barrel. The liner's inner diameter is usually 5mm larger than the diameter of the core being cut so as to reduce frictional resistance as the core enters the liner (Collins, 2005). However due to the gas expansion, the core expands to fill the core liner permanently altering the pore structure.

The core is immediately frozen as soon as it has been retrieved at surface. Freezing is done to prevent further gas exsolution and to solidify the connate water. Freezing does not restore the cores to their initial state as once cores are disturbed, dilation of the pores and the subsequent the shift in grain structure prohibit a return to their original state (Collins, 2005; Wong, 2005). Cores are usually stored in a frozen state until needed when they are allowed to thaw which resumes gas exsolution. An excellent review of

the coring and retrieval of oil sand material can be found from American Petroleum Institute (1998).

3.3.2 A description of the AOS core sample used in this work

The oil sand core material used in this project was kindly donated by the University of Alberta and shipped to London South Bank University. It consisted of a sample taken from an exploration well on a lease site approximately 10 km north of Fort McMurray, Alberta which is located within the Athabasca oil sand region of northern Alberta (Figure 3-1).
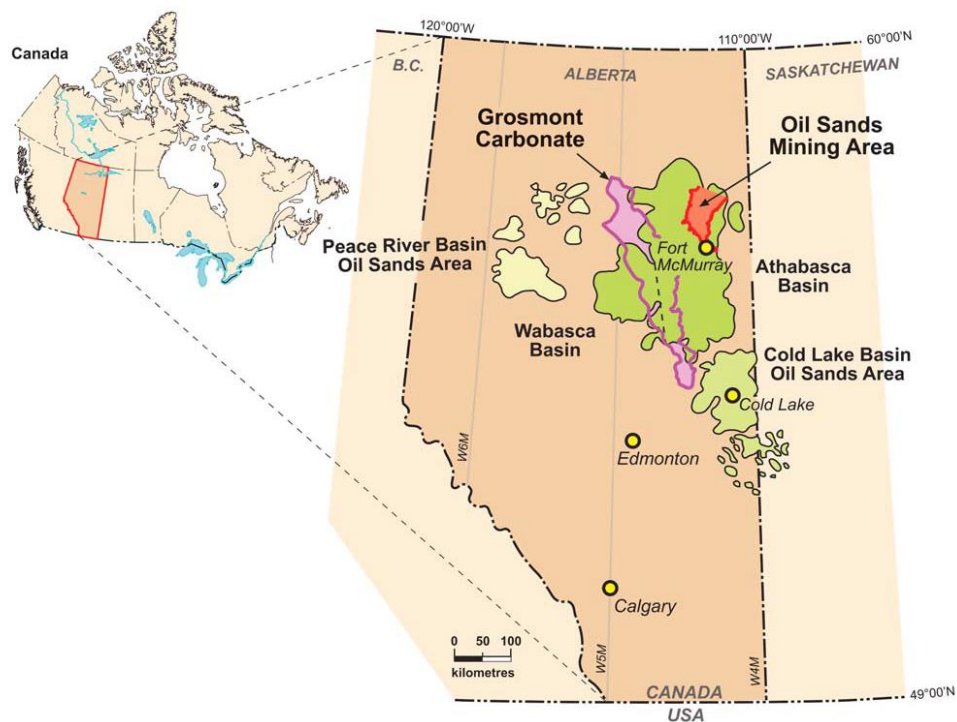
Figure 3-1: General Location Map showing the heavy oil deposits of Alberta
(after Peacock, 2010)

This sample came from the estuarine environment of the McMurray Formation at a depth of 81.4m, taken immediately below of a depositional environment transition. It is a medium-grained sand saturated with bitumen with fine grained laminae. The bitumen in the sample had a viscosity of 10870 cP at 25°C (Al-Wahaib, 2012) indicating its immobility at reservoir temperatures (< 10°C) (Fustic and Ahmed, 2006). Trace metal analysis for the bitumen shows that the Vanadium, Chromium, Iron and Nickel components were each less than 1 ppm (Al-Wahaib, 2012).

It is important to note that the AOS sample was received in an unfrozen state. This implied that the sample may have had a significant disturbance in its pore structure due to a prolonged expansion of gas. The consequence of this and its impact on the reliability of the results for the AOS sample is further explored in Section 3.4.1 below.

3.4 The selection of samples in relation to the methods used

The general objective of this work was to evaluate the pore space of selected reservoir material using three complementary methods: Mercury Injection Capillary Pressure (MICP), Pore Network Modelling (PNM) and Nuclear Magnetic Resonance (NMR). MICP is a common method used within the petroleum engineering industry to study the pore structure of reservoir material. Although MICP has distinct advantages and represents an accepted route for the determination of porosity and pore size distribution (PSD), several factors impact the suitability of MICP as a testing method.

Firstly, this test is destructive in nature which is challenging when samples are expensive to obtain and are limited in quantity. Secondly, the use of MICP can be constrained for certain kinds of reservoir material; particularly for those that are unconsolidated and unconventional. A good example of this limitation is when MICP is used to test oil sand material. MICP testing requires that samples be cleaned of original fluids so that air is the wetting fluid when mercury is imbibed. Athabasca Oil Sand material is an unconsolidated material in which the in-situ bitumen can be thought of as a binding agent holding the existing grains together. Removal of this bitumen causes the grains to become re-oriented leading to a rearrangement of the pore structure. This implies that the true pore structure cannot be derived from MICP testing for these materials since cleaning must be undertaken.

Furthermore, there are challenges in interpreting PSDs from MICP measurements which understates the true nature of the material under study. A typical example of this is that mercury intrusion of larger pores may be hindered if these are accessed through smaller neighbouring pores which require larger injection pressures. When these larger pores are eventually accessed, they may be interpreted in the PSD incorrectly as an amplified quantity of smaller pores (Morrow and Heller, 1985).

NMR and PNM offer attractive alternate means of studying porous media. There are many reasons why these methods represent attractive alternatives. Both NMR and PNM are non-destructive which allows for the repeatability of measurements which is particularly useful when core material is limited. The majority of samples can also be tested with in-situ native fluids. This implies that minimal sample preparation and processing is required and reduces the possibility of damage to the intrinsic pore structure thereby giving more representative results. Testing times for both methods are generally small and the equipment, although incurring a relatively high initial capital cost, has low maintenance and support expenses.

With regards to these advantages, the major aims of this study was to investigate the use of the PNM and NMR techniques as a means of: (i) enhancing the results obtained from MICP, (ii) assessing the use of these methods as stand-alone techniques for characterising porous media and (iii) gauging the applicability of these methods for unconsolidated samples imbued with their native hydrocarbon fluids.

Berea and Bentheimer core samples were chosen for this study as they are representative of typical reservoir material. They are consolidated and homogenous in nature and can undergo repeated cleaning and replacement of fluids within the pore space without comprising or changing the inherent pore structure. Given its prominent use within the petroleum industry, it was intended that the MICP results of the Berea and Bentheimer samples would act as a benchmark when comparing similar results from the NMR and PNM techniques. Furthermore, a good general agreement among the results from these three methods could therefore infer that any of these methods could be used to characterise porous media.

The AOS sample was also subjected to MICP Testing in accordance to the recommended practices for unconsolidated material. This involved the sample being cleaned of its in-situ bitumen using the Modified Dean-Stark method which is also known as the AOSI-3573 technique (Alberta Oil Sands Technology and Research Authority; 1974). This method is described in greater detail in Chapter 4 (Section 4.1.2).

The PNM and NMR testing of the AOS sample was however undertaken with its in-situ bitumen fluid. This is also described in greater detail in Chapter 6 (Sections 6.3 and 6.4). The results of the three methods will then be compared to assess the robustness of each method to obtain porosities and PSDs.

3.4.1 The order of testing and ensuring representative data

To compare equivalent data sets, it was imperative that the same sample be subjected to each of the testing methods. Given that MICP testing is destructive, it was essential that this test be carried out last. The order of testing used in this work took place by first performing micro-CT imaging (the initial step in PNM), followed by NMR experimentation and then finally MICP testing (which rendered the sample unusable).

For each material under study, only one sample was tested but this one sample was subjected to all three tests. A sample size of one for each material was deemed acceptable since the major goal of this work was to compare the use of three complementary methods and not to characterise the materials unequivocally. The nature of this project however allows for material characterisation but this will require a much larger sample size in order to make absolute conclusions for each material.

It is also important to note that the AOS sample was received in an unfrozen state which may have had a significant disturbance in its pore structure due to a prolonged expansion of gas. Although not ideal, this unfrozen sample was still subjected to the MICP, NMR and PNM techniques since the goal of this work was to compare the validity of the results from these three methods and not to characterise the material unequivocally. Indeed, an absolute characterisation of the AOS could not be possible as obtaining a representative sample of the formation would require either an extremely homogeneous reservoir or the testing a large number of samples in order to make absolute conclusions.

The Theoretical and Experimental Descriptions of the MICP, PNM AND NMR Methods

The broad aim of this work was to obtain the porosity and pore size distribution of three sandstone core samples using the three methods of Mercury Injection Capillary Pressure (MICP), Pore Network Modelling (PNM) and Nuclear Magnetic Resonance (NMR). This chapter presents the theoretical descriptions and experimental design associated with each these methods, particularly in the context of how these relate to the quantification of porosity and pore size distribution.

4.1 Mercury Injection Capillary Pressure (MICP) Testing

Mercury injection capillary pressure (MICP) testing is routinely used within the oil and gas industry to characterise the microstructure of reservoir material. The process involves the forced intrusion of mercury into the interconnected pore spaces of prepared samples. The injection pressures provide a measure of the accessed pore throat radii while the corresponding amounts of injected mercury are related to the distribution of the radii.

This section presents the method involved in obtaining the initial capillary pressure curves for the benchmark reservoir material: Berea and Bentheimer, the procedure for converting these into pore size distributions (PSDs), an analysis of the resulting data and the reliability and representativeness issues involved when interpreting the results.

4.1.1 Berea and Bentheimer Sample Preparation and Testing Procedure
MICP testing involves the injection of mercury into a sample that has been cleaned of all original fluids and then subsequently dried and evacuated of all cleaning fluids. All MICP tests reported in this thesis were performed by Core Laboratories U.K. Ltd using the MicroMeritics Porotech IV (MMP IV) apparatus.

Prior to testing, the Berea and Bentheimer samples were cleaned via Soxhlet-Extraction using a 50/50 solvent mixture of toluene and ethanol. The samples were then oven-dried for 48 hours at 250°F to remove moisture, then cooled to room temperature in a desiccator and weighed before the start of the MICP test.

Each sample was then placed into the penetrometer (a glass capillary tube of known diameter which holds the sample during testing) of the MMP IV apparatus. The penetrometer was then sealed and placed into the pressure vessel which was then evacuated to 50 μm Hg (0.000972 psi) using a vacuum pump. Evacuation is essential since all air and water vapour should be removed prior to the introduction of mercury as these additional substances will hinder the penetration of mercury into the pores of the sample. Figure 4-1 illustrates the layout of a typical MICP system.
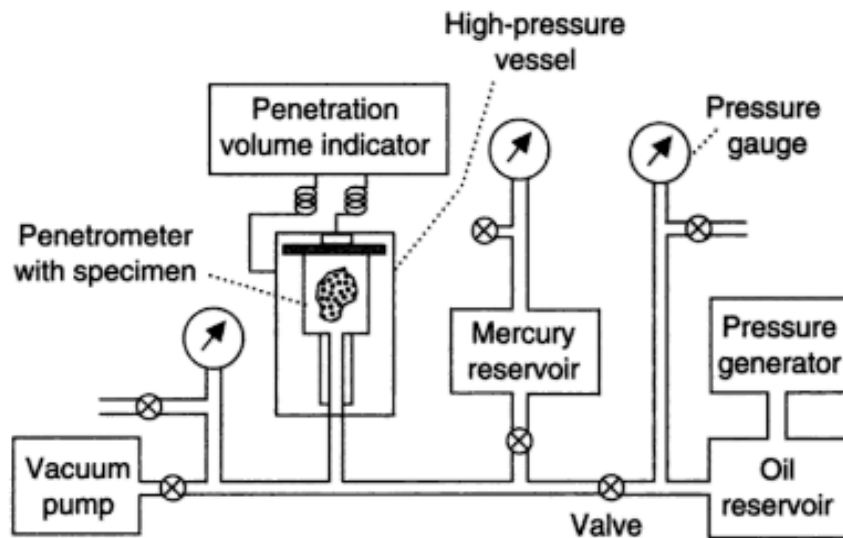
Figure 4-1: The layout of a typical MICP system (after Aligizaki, 2005)

The pressure vessel was then subjected to pressure increments in two stages: a low-pressure stage and a high-pressure stage. The low-pressure stage raises the pressure progressively from vacuum to a conformance pressure (0.58 psia). The conformance pressure is the pressure which allows the mercury to surround or *conform* to the sample's exterior without intruding into the pores. After reaching the conformance pressure, the pressure vessel was then subjected to increasingly higher pressures up to a maximum of 54952 psia (high-pressure stage). This pressure range typically provides coverage of the broad array of both saturations and capillary pressures for a wide variety of reservoir material, including not only high porosity-high permeability samples but also low porosity-tight sands (Comisky *et al.*, 2007).

42

In total, 85 pressure steps were recorded during testing with the equilibrium time (the minimum time to achieve a stable mercury reading before continuing to the next pressure) for the low-pressure stage being 20 seconds and 45 seconds for the high-pressure stage.

4.1.2 AOS Sample Preparation and Testing Procedure

MICP testing involves the injection of mercury into a sample that has been cleaned of all original fluids. The cleaning or removal of the in-situ bitumen from the AOS sample was performed by Core Laboratories U.K. Ltd using the Modified Dean-Stark method.

This method is also known as the AOSI-3573 technique (Alberta Oil Sands Technology and Research Authority, 1974) and requires that the sample be sleeved using a Teflon heat-shrink tube with screen wire mesh and platens at both ends to keep the sample intact since the in-situ bitumen can act as a cementing agent holding the grains together (Schmitt, 2005). The sample was then placed in a Dean-Stark (distillation extraction) apparatus using toluene as the cleaning solvent. The minimum heat rate to boil the toluene (boiling point 110.6°C) was then applied with the toluene being changed at regular intervals.

This process was carried out for approximately 7 – 10 days. The complete extraction of the bitumen from a sample is generally indicated by both the colour of the toluene (which should remain colourless) and through ultraviolent (UV) lighting under which selected oils have the tendency to fluoresce. Unfortunately, the samples were not subjected to fluorescent lighting. Instead, the cleanliness of the sample was only inferred through the colour change of the toluene. The American Petroleum Institute (1998, p. 3-7) however contends that '*the fact one solvent is clear after contact with the sample does not necessarily mean that oil has been completely removed from the sample*'.

The samples were then oven-dried for 48 hours at 250°F to remove moisture, then cooled to room temperature in a desiccator and weighed before the start of the MICP test which was performed by Core Laboratories U.K. Ltd using the MicroMeritics Porotech IV (MMP IV) apparatus following the same steps outlined in the previous section (Section 4.1.1).

43

4.1.3   Deriving Porosity and PSD from the MICP Test

MICP testing can provide measures of the porosity and PSD. Porosity is determined from the ratio of the total injected mercury volume to the bulk volume of the sample (Equation 2-1). The total injected mercury volume essentially represents the pore volume contacted by the mercury. It is important to note that the high injection pressures (up to a maximum of 54952 psia) are assumed to be sufficiently high to contact all of the pore space.

During MICP testing, mercury injection pressures are increased in a series of steps with the percentage of the pore volume saturated by the mercury at each step being recorded after allowing for a sufficient equilibrium time. The injection pressures are then plotted against corresponding mercury saturations (or equivalent water saturations) resulting in a capillary pressure curve.   MICP curves typically represent primary drainage measurements given that mercury is strongly non-wetting (Pittman, 1992).

Once a capillary pressure curve has been obtained, the pore throat size distribution can be obtained using the modified Young-Laplace equation (provided in Chapter 2 and also shown below):

$$r_t = \frac{2\sigma\cos\theta}{P_c} \qquad\qquad [2\text{-}3]$$

where r_t is the equivalent pore throat radius, σ is the interfacial tension between the fluid phases and θ is the contact angle between the solid surface and the fluid-fluid interface.

A key assumption in this equation is that all throats have a circular cross-section and cylindrical geometry. In real porous media, the pore and throats form a complex assortment of shapes and geometries. The assumption of cylindrical pores simplifies this complexity but may misrepresent the actual morphology which exists. To account for this assumption, the radii obtained from Equation 2-3 will be referred to as equivalent (cylindrical) pore radius in this thesis.

The contact angle, θ is controlled by the wettability.   The non-wetting phase is represented by the injected mercury and the wetting phase is the air that fills the evacuated sample. A contact angle of 140° and interfacial tension of 480 dynes/cm has been supplied by Core Laboratories U.K. Ltd. These values correspond to similar values in the literature (Vavra $et~al.$, 1992).

It is important to note that the radius denoted to in this equation is sometimes incorrectly referred to as 'pore size' which describes the radius of a pore body. This radius however refers to the largest throat through which the pore body can be accessed (Comisky *et al.*, 2007 and Vavra *et al.*, 1992). The results of the MICP test, although more accurately representing a pore throat size, however are very often used to describe the pore (body) size distribution (Mao *et al.*, 2005; Vavra *et al.*, 1992 and Volokitin *et al.*, 2001).

This assumption is often made for several reasons; one of which includes the existence of a relationship between the radii of pore bodies and the radii of pore throats. Volokitin *et al.* (2001) maintain that this relationship exists since the radius of the grains in a porous medium governs both the pore size and the pore throat size. It can then be assumed that if pore size is proportional to pore throat size, then two quantities reflect the same distribution.

Vavra *et al.*, 1992 go on to state that the fluid entering through a pore throat is assumed to immediately fill the adjoining pore body and as such the volumes accessed by both pore body and throat are proportional and echo similar distributions. In addition, the authors further contend that real pore throats have complex geometries which may not be well-reflected in Equation 2-3 (which hold only for cylindrical geometries) and which in turn, may lead to calculated values representing the effective size of both the pore throats and pore bodies.

Although it well recognised that the results of a MICP test is more relevant to describe pore throat size, based on the above arguments, it is assumed in this thesis that a MICP test provides a reliable and realistic estimate of pore (body) size.

4.1.4 Interpreting Pore Size Distribution (PSD): Statistical Measures
Pore size distribution data, like grain size distributions, are best described using selected statistical measures (Chilingarian *et al.*, 1992). These hinge on the characteristic statistical quantities related to measures of central tendency, dispersion, asymmetry and *peakedness*.

4.1.4.1 Measures of Central Tendency
The median radius (r_{50}) is the most often quoted central tendency measure which is used to describe pore size distribution (Aligzaki, 2006). This is the quantity which describes

50% of the pore volume and can be easily identified as middle-most member of the cumulative distribution. It reflects the overall pore size 'as influenced by the chemical or physical origin and any subsequent alteration' of the reservoir material (Chilingarian *et al.*, 1992).

The mean radius is usually taken as the weighted arithmetic average of the distribution function. This can be calculated using:

$$ r_M = \frac{\sum_{i=1}^{n}(PV_i)(r_i)}{\sum_{i=1}^{n}(PV_i)} \qquad \text{[4-1]} $$

where *PV* is the pore volume and *r* is the pore radius.

4.1.4.2 Measures of Dispersion

Pore sorting (S_p) is the standard deviation of the pore sizes in a sample (Folk and Ward, 1957) and indicates how the distribution varies from the mean. Lower values of S_p indicate that the data points tend to be close to the mean and are generally associated with narrow pore size distributions. With reference to a cumulative pore-radius curve, S_p is determined using:

$$ S_p = \frac{r_{84} - r_{16}}{4} + \frac{r_{95} - r_5}{6.6} \qquad \text{[4-2]} $$

4.1.4.3 Measures of Asymmetry

Skewness (Sk_p) measures the extent that the data distribution varies from a normal distribution (Folk and Ward, 1957). The limits of Sk_p range from -1 to +1. A normal distribution (which is symmetrical about the mean) has an Sk_p value of 0. Negative Sk_p values indicate that the distribution is skewed towards larger pores while positive values denote that the distribution has a *tail* in the small pores (Chilingarian *et al.*, 1992). With reference to the cumulative pore-radius curve, Sk_p is determined using:

$$ Sk_p = \left[\frac{r_{84} + r_{16} - 2r_{50}}{2(r_{84} - r_{16})} \right] + \left[\frac{r_{95} + r_5 - 2r_{50}}{2(r_{95} - r_5)} \right] \qquad \text{[4-3]} $$

4.1.4.4 Measures of Peakedness

Kurtosis (K_p) signifies the ratio between the spread of pore sizes in the tails to the pore sizes that are centrally located in the distribution (Folk and Ward, 1957). It is essentially a measure of the peakedness of the distribution. Normally distributed curves have K_p values of 1 while distributions having very narrow peaks may have K_p values ranging from 1.5 to 3 (Chilingarian *et al.*, 1992). Bimodal distributions tend to have low K_p value which may be as low as 0.6 (Folk and Ward, 1957).

With reference to the cumulative pore-radius curve, K_p is determined using:

$$K_p = \frac{r_{95} - r_5}{2.44(r_{75} - r_{25})} \qquad [4\text{-}4]$$

4.1.4.5 Pore Size Classification

Another popular means of representing pore size data involves the use of the terms: micropore, mesopore and macropore. There is however a wide variation among researchers on the size of the pore radii which partition these three pore classes (Skalinski and Kenter, 2014). This work uses the classification standard of Bell *et al.* (2012) and Rouquerol *et al.* (1994) who classify the radius of micropores as measuring less than 1 microns, mesopores between 1 and 25 microns and macropores as larger than 25 μm.

4.1.5   The Reliability and Challenges of using MICP Testing

Mercury injection capillary pressure (MICP) testing is routinely used within the petroleum industry to characterise the microstructure of reservoir material and to obtain robust estimates of pore size distribution (PSD). The reliability of the results from the MICP method is however dependent upon a number of key assumptions.

The first is that the pore throats have a cylindrical geometry. In real porous media, the pore and throats form a complex assortment of shapes and geometries. Assuming that all throats are cylindrical in nature and using this assumption to predict pore size distribution may misrepresent the actual morphology which exists.

The second is assumption that the results of the MICP test, although more accurately representing pore throat sizes, can be used to describe the pore (body) size distribution.

This assumption is often based on the existence of a relationship between the radii of pore bodies and the radii of pore throats where it is assumed that if the pore size is proportional to pore throat size, then these two quantities reflect the same distribution (Mao *et al.*, 2005; Vavra *et al.*, 1992 and Volokitin *et al.*, 2001).

The third is the contact angle used in the modified Young-Laplace equation. A contact angle of 140° is generally quoted in the literature and is used by many researchers and core analysts including the work in this thesis. However, a number of studies have highlighted that a wide range of contact angles exists between mercury and similar surfaces (Diamond, 1970; Gregg and Sing, 1983; Groen *et al.*, 2002). Variations in the contact angle will clearly impact the results of the PSD.

Furthermore, there are challenges in interpreting PSDs from MICP measurements which may understate the true nature of the material under study. A typical example of this is that mercury intrusion of larger pores may be hindered if these are accessed through smaller neighbouring pores which require larger injection pressures. When these larger pores are eventually accessed, they may be interpreted in the PSD incorrectly as an amplified quantity of smaller pores (Morrow and Heller, 1985).

A final assumption is related to the probing qualities of the MICP test which describes only the effective pore space since the forced intrusion of mercury must take place through interconnected pores. A number of alternative pore characterisation methods do not distinguish between the absolute and effective pore space. Nuclear Magnetic Resonance (NMR) and Pore Network Modelling (PNM) techniques are amongst these. For these two methods, the entire pore space comprised of both isolated and interconnected pores is considered. This implies that a convergence of the results between dissimilar approaches attempting to study the same characteristic may not always be possible. These concepts are discussed in greater detail in upcoming chapters of this thesis.

4.2   Pore Network Modelling (PNM)

Hydrocarbon recovery is strongly influenced by the microstructure and fluid properties which exist in producing reservoirs (Ghous *et al.*, 2008). At the micro-scale, the porous

medium can be represented as a solid skeleton permeated with pore spaces. This arrangement lends itself to the development of pore network models which show how pore spaces are connected and how pathways for fluid flow can be established.

Micro-computed tomography (micro-CT) imaging is capable of acquiring two dimensional (2D) images of the pore structure of reservoir material. Using appropriate software, these sequential 2D images can be processed to give a three dimensional (3D) model of the material imaged. In *pore network modelling* (PNM), 3D representations of the pore space are used to generate pore network models. These models attempt to approximate the porous medium as an interconnected network of pores and pore throats. Both 2D and 3D images have been used to obtain a range of morphological properties including pore and grain size distributions, sorting, hydraulic radii and tortuosity (Bauget *et al.*, 2005; Ghous *et al.*, 2008).

Pore size and its distribution directly influence the fluid transport properties of porous media. PNM has been used by the following researchers to first characterise the pore space and then use this information to study the flow in porous media and obtain particular fluid transport properties including porosity, relative permeability, wettability and capillary pressure for reservoir material: Andra *et al.* (2013), Balhoff and Wheeler (2007), Blunt (2001), Blunt *et al.* (2013), Boek (2010), Dong and Blunt (2009), Grachev (2012), Kalam (2012), Jerauld and Salter (1990), Suicmez and Touati (2008), Varloteaux *et al.* (2013), Xiong *et al.* (2016) and Zhou and Chen (2017).

The use of pore networks to obtain these properties can reduce the time and cost normally associated with the conventional experimental methods. In addition, pore networks provide the opportunity to model the relationships which may exist between pore geometry and macroscopic properties and can be used to show how such relationships impact the flow of fluid through the reservoir. This information can enhance current production methods and improve hydrocarbon recoveries.

4.2.1   The Pore Network Modelling (PNM) Approach

Although the study of porous media using PNM approaches has become increasingly prevalent, a review of the associated literature shows that there is no documented or standard procedure which govern these studies. This lack of a recommended practice is related to several factors which include:

49

- the variety of pore dimensions which range from sub-micron to centimetres (Taud *et al.*, 2005; Tucker, 1991) that affect resolution;

- the need to sample sufficient volumes in order to capture heterogeneities of the pore space which may exist due to anisotropy and obtain representative measurements;

- the influence of lithology on micro-CT image acquisition parameters where for example, sandstone formations may require different acquisition parameters to carbonates because of differing mineralogies;

- the continuous and rapid advances in computational approaches and their influence on the associated software; and

- the availability and affordability of prerequisite software.

Despite these factors however, researchers and practitioners tend to use similar methods to navigate from the initial input of sequential 2D images to a required output (Balhoff and Wheeler, 2007; Blunt, 2001; Blunt *et al.*, 2013; Boek, 2010; Dong and Blunt, 2009; Suicmez and Touati, 2008; Varloteaux *et al.*, 2013; Xiong *et al.*, 2016; Zhou and Chen, 2017).

This work builds upon and consolidates these methods to produce a comprehensive PNM approach to derive porosity and pore size distribution (PSD). The approach consists of four key stages as shown in Figure 4-2.
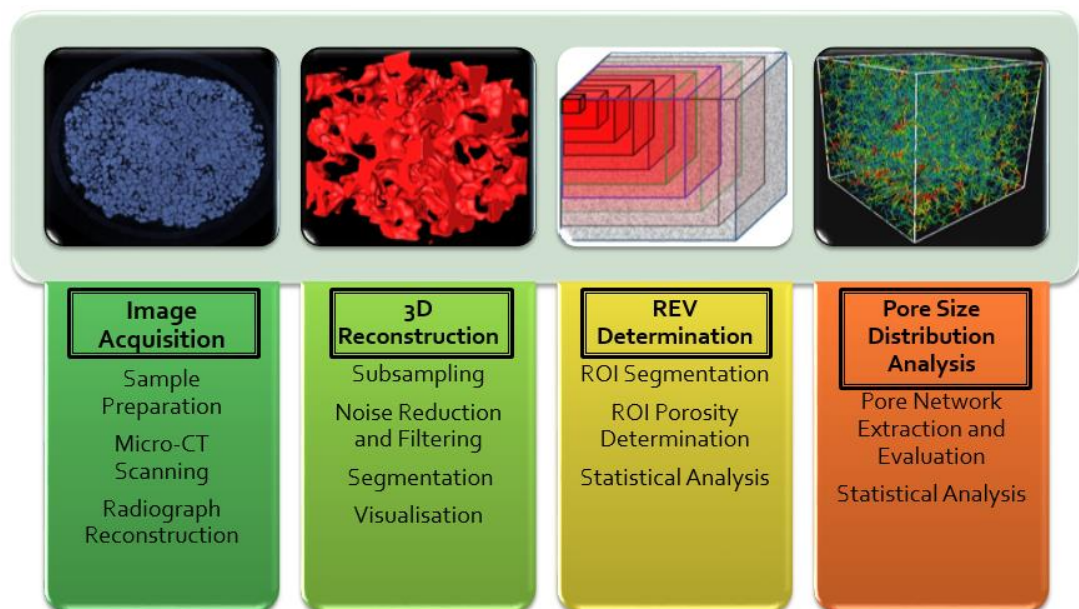
Figure 4-2: The Pore Network Modelling Approach used in this project

The first stage is termed Image Acquisition during which sequential digital 2D images of the samples from micro-CT imaging are obtained. The second stage involves compiling these sequential 2D images to provide a 3D model representative of the inherent microstructure. The third step entails obtaining the Representative Elementary Volume (REV) which is the smallest size of the 3D model which captures the majority of the sample's inherent features so as to be statistically representative of the entire sample (Gelb *et al.*, 2011). The last stage involves generating the pore network from which the pore size distribution (PSD) is obtained. These stages and well as the particular methodologies underlying each sub-stage are described in greater detail in the sections below.

4.2.2   Image Acquisition

Image acquisition involves three main sub-steps: sample preparation, micro-CT scanning and radiograph reconstruction. These are described in greater detail below.

4.2.2.1 Sample Preparation

Micro-CT scanning generally requires little to no prior sample preparation (Ketcham and Carlson, 2001). During the acquisition process however, it is important to ensure the sample does not move and that it fits within the view between the X-ray source and detector (please see Figure 2-11 for a general illustration). To ensure that these conditions were met, the samples were trimmed (final dimensions are provided in Table 4-1) and placed inside acrylic cylinders having a 1.0mm thickness.

4.2.2.2 Micro-CT Imaging

Micro-CT imaging uses the attenuation of X-rays to obtain 2D cross-sections of an object at varying resolutions of several microns. During the process, the sample is mounted onto a platform positioned between the X-ray source and a detector. The sample is then rotated in a step-wise fashion while simultaneously subjected to X-ray beams. Owing to its absorption, the X-ray beam is attenuated when it passes through the sample. Measurements of the attenuation at prescribed angular steps can produce grey-level projection images (radiographs) of the sample.

The intensity of the grey value at each location in the image corresponds to the change in intensity of the x-ray beam as it is attenuated. This suggests that if the principal

elements comprising the sample have an adequate density variation (that is, if they attenuate the X-ray by differing amounts), then these elements can be identified by their corresponding grey value. This is the reasoning behind which the pores (filled with either air or in-situ hydrocarbon fluids) can be distinguished from the solid mass.

The micro-CT scans used in this work were obtained using a Skyscan-Bruker 1172 model micro-tomography system which was located at a Bruker affiliated institution in Belgium. 2240 micro-CT images with a resolution of 5.0 microns/pixel for both samples were acquired in a time of 18 hours.

Table 4-1 below provides selected micro-CT parameters which were used to acquire the micro-CT images for the Berea, Bentheimer and AOS samples while Figure 4-3 shows a 2D image (slice) taken from the set of 2240 micro-CT images after radiograph reconstruction for the Berea and Bentheimer samples. A similar representative 2D slice for the AOS sample can be found in Section 6.3.1 (Figure 6-3).

Table 4-1: Micro-CT Scanning Parameters for All Samples

	Berea	Bentheimer	AOS
Scanning Attributes:			
Scanning Time [hours]	18	18	18
File Size [GB]	64.3	62.8	61.9
System Voltage [kV]	100	100	100
System Current [µA]	100	100	100
Rotation Step [degrees]	0.1	0.1	0.1
Image Attributes:			
Resolution [µm/pixel]	5.0	5.0	5.0
Total Number of Slices	2240	2240	2240
Image Dimensions:			
Total Height scanned [mm]	11.2	11.2	11.2
Scanned Sample Diameter [mm]	25.4	25.4	~ 25 (irregularly shaped)
Total Volume scanned [cm³]	5.7	5.7	~5.7

4.2.2.3 Radiograph Reconstruction

After the acquisition process, the projection images were reconstructed using the NRecon® [version 1.6.4.2] software to obtain 2D greyscale cross-sectional images (slices) of the sample. The NRecon® software uses a filtered back projection algorithm which is based on the work of Feldkamp. Excellent reviews of the Feldkamp algorithm are given by Feldkamp *et al.* (1984) and Ketcham and Carlson (2001).
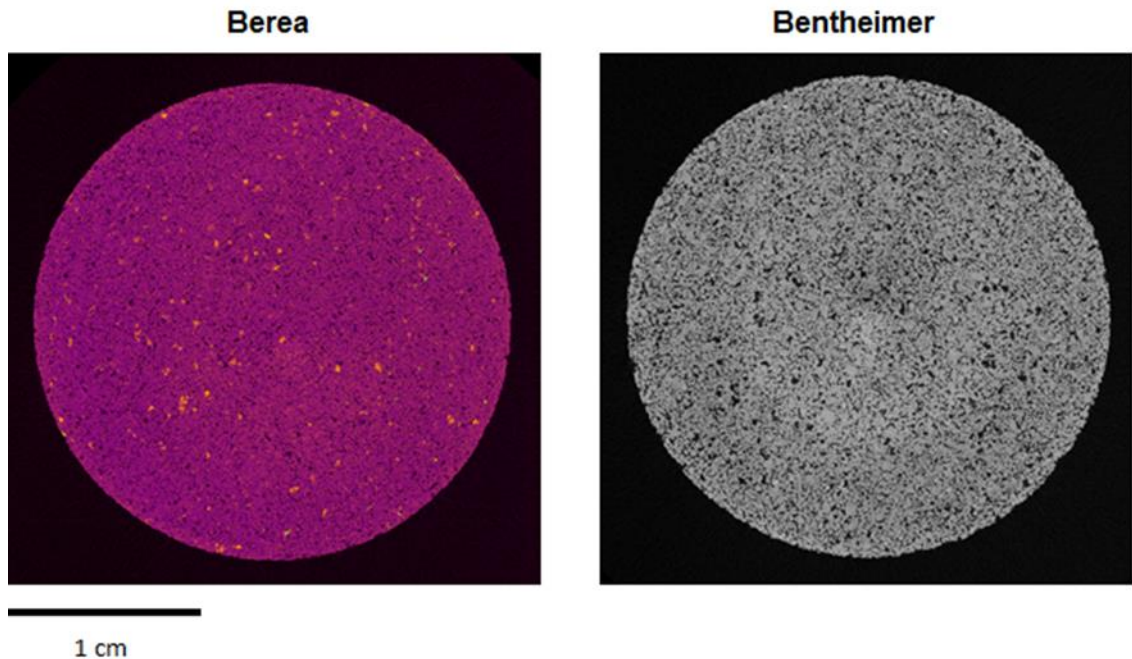
Figure 4-3: Berea and Bentheimer Sample Scans at Slice 1000

Figure 4-3 shows the Berea sample purposely in a false colour to highlight several bright spots (yellow) within the image. It is important to note that these bright spots are not solely noise related but are manifest due to a density difference of the various components making up the solid mass.

During the radiograph reconstruction process, the intensity of the grey value at each location in the image corresponds to the change in intensity of the X-ray beam as it is attenuated. This is related to the density of the material at that location. For reservoir material, if the solid mass - in this case, sandstone (therefore silicon-based) is interspersed with components having a significant density difference (e.g. heavy metal inclusions), then the components are manifest as bright spots due to the density differences (Langheinrich et al., 2009).

The reconstruction process is also predisposed to certain artefacts which reduce the quality of the reconstructed 2D images. The most common artefacts encountered in this work included beam hardening and ring artefacts. Ring artefacts manifest themselves as full or partial circles positioned on the rotational axis which are caused by variations in the output of the detectors (Ketcham and Carlson, 2001). Beam hardening is caused by a variation in the energy of the X-ray beam, which for micro-CT scanners is polychromatic in nature (more than one wavelength). Selective absorption of low energy X-ray wavelengths from the polychromatic X-ray leaves the beam with a greater concentration of higher energy wavelengths. This results in the beam becoming increasingly more penetrating and causes the material at the edge of the sample to appear denser than at its centre (Ketcham and Carlson, 2001; Van Geet *et al.*, 2000; Wildenschild *et al.*, 2002). This manifests itself as a ring of bright pixels around the edge of the sample's 2D reconstructed image reducing to dark pixels at the centre.

To minimise the effects of beam hardening in the projection images, the micro-CT scanner used in this work employed two metallic filters (brass and aluminium) which aimed to reduce the absorption of low energy X-ray wavelengths. During the reconstruction of the radiographs, the NRecon® software used a 25% beam hardening correction and a level 8 ring artefact correction to produce the optimal quality 2D cross-sections. These corrections were suggested and supplied by Nick Corps from the Bruker Corporation (Corps, 2013).

4.2.3 3D Reconstruction

The major aims of the 3D reconstruction process are to produce a 3D model which is the nearest representation of the material being studied and from which the pore spaces and matrix material can be clearly distinguished from each other. This 3D model forms the basis for all other analysis related to pore characterisation and property simulation and as such, it is important to produce a robust representative model. To do this, the following steps were undertaken: subsampling, noise reduction and filtering and segmentation. These are described in greater detail below.

4.2.3.1 Software and Subsampling

After radiograph processing, the sequential greyscale 2D images were compiled to provide a 3D model. Moving from 2D images to a 3D model requires the use of specialised software employing advanced mathematical modelling techniques. Several

commercially available software packages have been developed specifically for the analysis of porous media and geo-materials. An excellent review of these packages is provided by Iassonov *et al.* (2009).

This thesis uses the Avizo® Fire software which provides advanced 3D imaging workflows for scientists and engineers involved in the study of material properties from derived 3D structures, at any scale and size (FEI Company, 2013). The workflows used in this work focussed primarily on 3D image generation (stacking 2D slices), filtering, segmentation, and pore network extraction. These are further described in the sections below.

Due to the large amounts of data involved, subsampling was used to both improve processing times and to limit the effect of any disturbed areas within the sample (e.g. at the outer surfaces). A total of 2240 slices were obtained in the z-plane. Of these, 2000 slices (~ 1 cm in length) were subsampled. Each slice has a length of 1 pixel (= 5.0µm) and these 2000 slices represented approximately 90% of the scanned sample in z-plane. To complement this amount, 2000 pixels centred on the midpoint of the image were further chosen in both the x- and y-planes. This resulted in a sub-sample amount of approximately 20% of the scanned area (x-y plane).
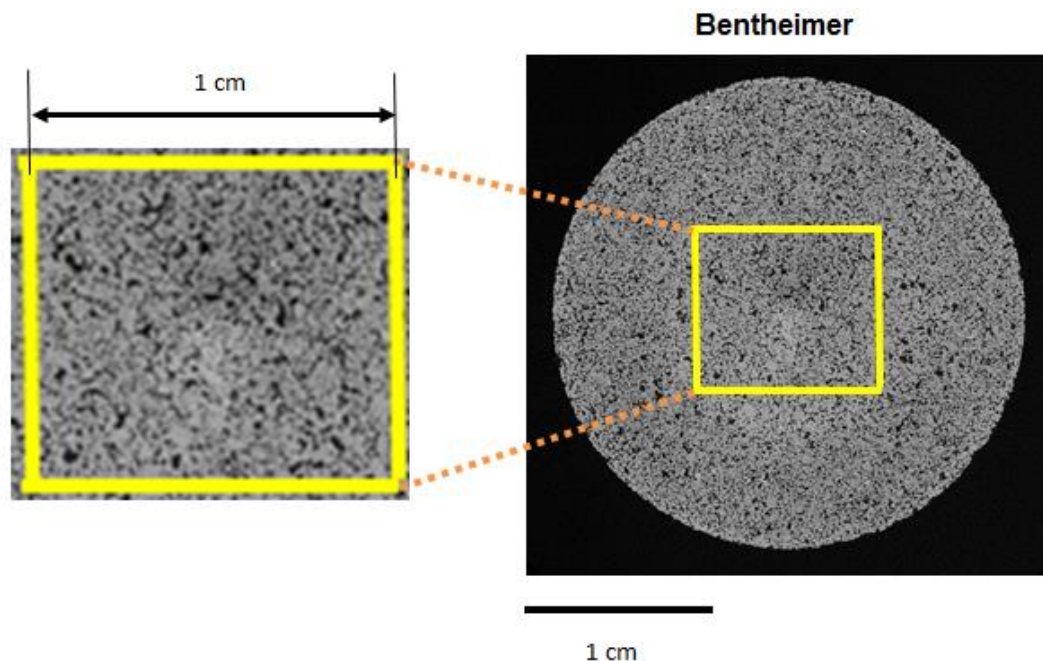
Figure 4-4: A Bentheimer Sample Scan at Slice 1000 showing the location of the subsampled ROI (2000 pixels) in the x-y plane

In total, the final volume analysed (termed the *Maximum Region of Interest*, MROI) comprised a cube of dimensions 2000 *x* 2000 *x* 2000 voxels which accounted for nearly 18% of the total scanned volume. At a resolution of 5.0μm per pixel, the volume of MROI was 1 cm^3. Table 4-2 and Figure 4-4 provide further information.

Table 4-2: Sub-sampled amounts which gave rise to the Maximum Region of Interest (MROI) Dimensions for all samples

	All samples
Total Volume scanned [cm³]	5.7
Subsampled MROI Attributes:	
Pixels (slices) in z-plane	2000
Percentage of the z plane sampled [%]	~ 90
Pixels in x-y plane	2000 x 2000
Percentage of the x-y plane sampled [%]	~ 20
MROI Volume [cm³]	1.013
Percentage of scanned volume [%]	18

4.2.3.2 Filtering

Noise is a random variation of the brightness, contrast or colour information of a digital image. It manifests itself as spots, blurring or greyscale speckling within the image. While the scanning process includes preventative measures to reduce these effects, the resulting images may in some cases still exhibit noise and *artefacts*. Artefacts are false structures within the final image that do not have a counterpart in the object being imaged (Kalender, 2011). Typical examples of artefacts in micro-CT images include ring and beam hardening artefact

Techniques to reduce noise and artefacts in the final images involve the use of filtering methods which attempt to *clean* the image while minimising the loss of essential information. The most common filtering methods include mean filtering, median filtering and Gaussian smoothing. These methods have the effect of smoothing the image, especially in terms of contrast, which allows for a better distinction between phases by reducing spots and speckling and improving edge detection within the image (Rozenbaum and Rolland du Roscoat, 2014).

This work used a median filtering process which involved replacing each voxel greyscale value in an image with the median of its neighbours. This essentially eliminated voxels whose greyscale values are unrepresentative of their surroundings by replacing with the median of surrounding voxels.

4.2.3.3 Segmentation

Figures 4-3 and 4-4 show that the pore and solid mass phases are easily distinguished with the naked eye after radiograph reconstruction. However, direct measurements of the pore space cannot generally be made until the filtering and segmentation processes on the images are completed.

A grey scale image appears to be black and white but is normally comprised of many shades of grey. The 3D images obtained from the radiograph processing were stored in an 8-bit file format (8 bits per voxel) in which each voxel is assigned an intensity which ranges from 0 to 255. A zero intensity represents black while a 255 intensity represents white. Any intensity between these represents varying shades of grey.

Segmentation is the process of assigning a label to every voxel in a digital image so that voxels with the same label possess similar characteristics. For reservoir material, the goal of segmentation is to allow each voxel in the image to be labelled and identified as either belonging to a pore or the solid phase (Andra *et al.*, 2013).

There are numerous segmentation methods proposed in the literature. An excellent review of the various methods is presented in the work of Iassonov *et al.* (2009), Pal and Pal (1993) and Sezgin and Sankur (2004). Global thresholding, however is a common technique used for reservoir material and involves the identification of a single greyscale value or *threshold* which is used to distinguish the pores from the solid mass (Iassonov *et al.*, 2009). The 3D images obtained from the radiograph processing were stored in an 8-bit file format (8 bits per voxel) in which each voxel is assigned an intensity which ranges from 0 to 255. A zero intensity represents black while a 255 intensity represents white. Any intensity between these represents varying shades of grey.

There are several techniques by which the threshold value can be identified. Jensen *et al.* (2014) and Abera *et al.* (2017) provide a good review of these techniques. Thresholding via the histogram approach is a popular approach for reservoir material

(Iassonov *et al.*, 2009; Sheppard *et al.*, 2004; Taud *et al.*, 2005; Verges *et al.*, 2011) where the frequency of the greyscale level of each voxel is plotted against a 0 to a 255 intensity range.

An *automatic threshold* (AT) value is then chosen either at the valley of the resultant bi-modal peaks or the bottom rim of a single peak (Figure 4-5). Each peak represents either the pores or the solid mass. This is usually referred to as the valley-emphasis method (Ng *et al.*, 2013). Image software packages like Avizo have built in functions which allows the automatic threshold to be identified from a greyscale histogram without the need for any user intervention.

Although there is an attempt to choose the AT at the boundary between pore and grain greyscale peaks, there is sometimes significant uncertainty is the classification of voxels whose greyscale value are close to the threshold value (Verges *et al.*, 2011). This can severely misrepresent the pore and grain space where for example, voxels which might belong to a pore might be incorrectly assigned to the grain mass. To combat this uncertainty, the threshold can also be selected using an interactive approach (termed *Interactive Thresholding*) which allows the user to control the choice of threshold based on visual measurements. An interactive threshold is entirely subjective based on the users' perception of the pore space and has been used by many researchers to characterise reservoir material (Verges *et al.*, 2011).

Figure 4-5: Optimal Threshold Identification from a Greyscale Histogram
(after Ng *et al.*, 2013)

The choice of threshold is of paramount importance when characterising the pore space as an '*incorrect*' value has the potential to reduce or amplify pore space as well as blur, terminate or connect pore spaces which may not necessarily exist (Taud *et al.*, 2005).

This can result in significant variations in porosity and other derived properties with only very small changes in the threshold parameter (Sheppard *et al.*, 2004).

To resist this effect and to examine how realistic changes in the threshold value might affect the pore space measurements, the automatic threshold value (software-suggested value based on the valley-emphasis histogram method) was first chosen.

To examine the influence of a user's subjective perception of the pore space, interactive thresholding was then used to study how a ±5% and ±10% change in the automatic threshold value affected the pore characterisation process. A maximum ±10% change was selected on the basis that sensitivities larger than ±10% would be discarded as unrealistic threshold values given that there would be obvious disparities between the original unsegmented and the final segmented images. This is examined in greater detail in Section 5.3.3.

4.2.4 Representative Elementary Volume (REV) Determination

Once segmentation is complete, the next step is to examine whether the Maximum Region of Interest (MROI) subsampled is representative of the entire sample and to gauge whether any measurements made from the MROI robustly characterises the entire pore space. Depending upon the resolution and initial volumes involved, the MROI chosen might be large in extent so that a much smaller volume from within the MROI can adequately capture the sample's intrinsic attributes.

This small volume is termed the *Representative Elementary Volume* (REV) and is defined as the minimum volume of a sample at which the sample's inherent features are sufficiently and statistically captured for a high confidence in the results (Gelb *et al.*, 2011).

Although the two volumes may coincide – in an ideal situation, the REV is less (and preferably very much less) than the MROI. However in some cases, the chosen MROI may not be sufficiently large enough and as such, the REV will lie outside the MROI as the volume studied is not large enough to capture the inherent attributes of the sample. In such cases, it is imperative to enlarge the MROI until the REV is encompassed.

The REV approach used in this project evaluates the REV deterministically by first taking a small volume within the 3D mass and then secondly, calculating a property of interest.

The small volume chosen is called the region of interest (ROI) and porosity is the common property of interest chosen (Al-Raoush and Papadopoulos, 2010; Halisch, 2013).

The size of the ROI is then incrementally expanded in all directions until the MROI is attained and the property is recalculated at each incremental step. The REV is then identified as that particular volume across which the property remains constant. Figure 4-6 outlines the methodology used in this work to determine the REV. Each step is discussed in greater detail in the sections below.
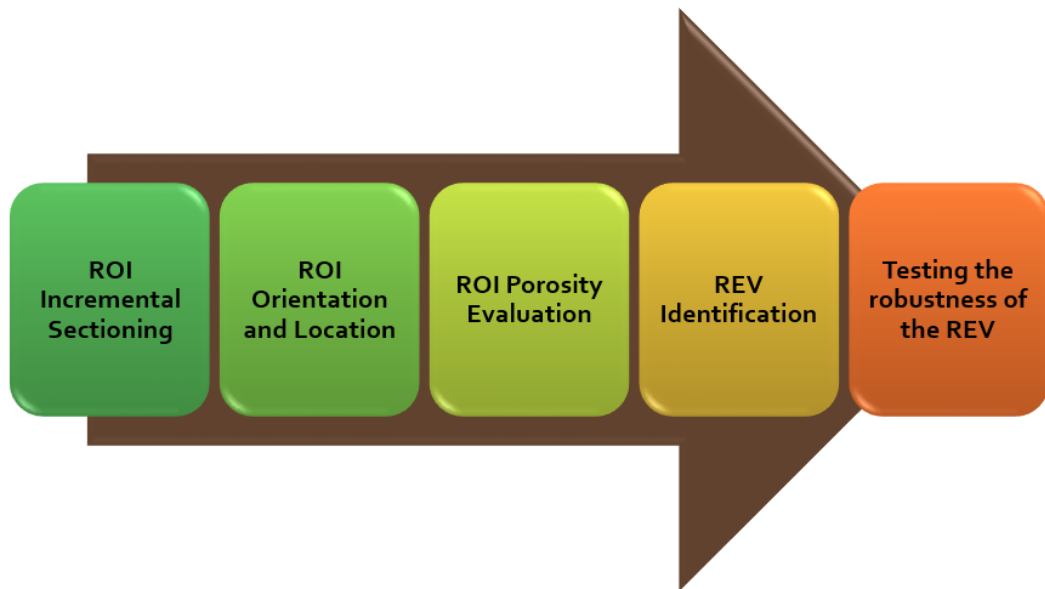
Figure 4-6: The REV Determination Approach used in this project

4.2.4.1 Region of Interest (ROI) Incremental Sectioning
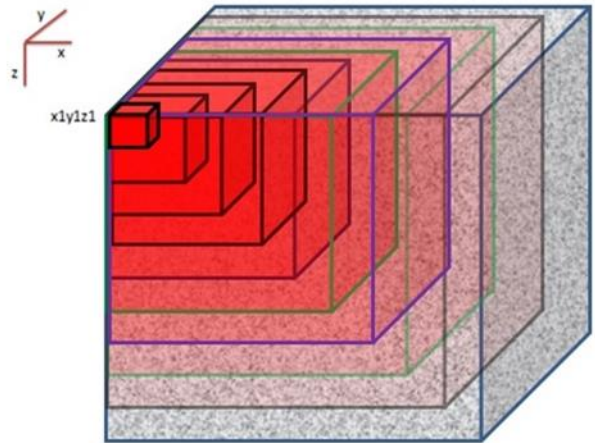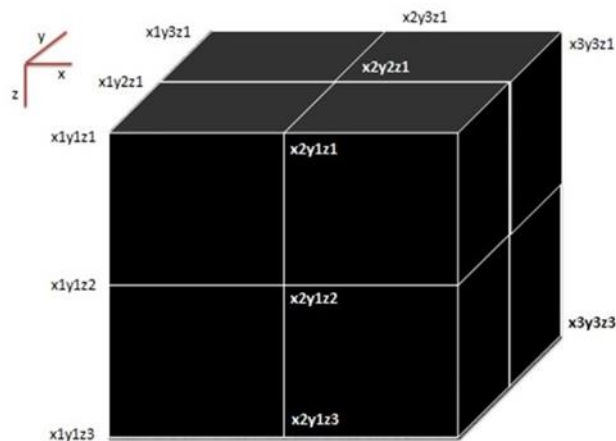
The Maximum Region of Interest (MROI) comprised a 2000 voxel cubic subsample of the initial 3D reconstructed volume. To help identify the REV, an initial cube of length 100 voxels (approximately 0.5 mm) was arbitrarily chosen as the first ROI from within the MROI. This volume was then increased in steps of 100 voxels in all directions until the MROI of length 2000 voxels (~ 10mm) was reached. This resulted in 20 ROIs being obtained from the initial starting position. A simplified illustration of this process is shown in Figure 4-7A. At each incremental step, the ROI porosity was calculated and recorded.
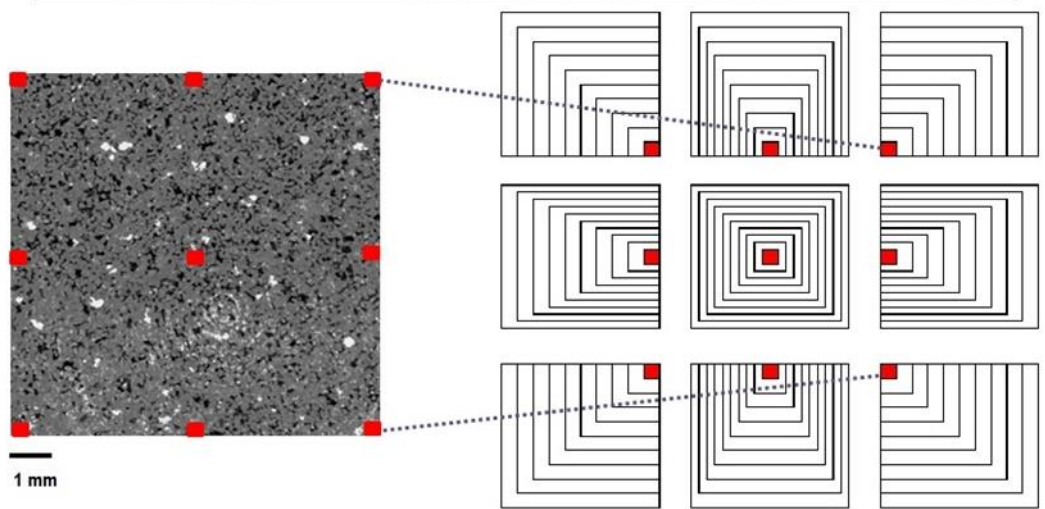
Figure 4-7: Exploring the ROI: Diagrams to illustrate the processes of Incremental
Expansion and Orientation and Origin Identification

4.2.4.2 Region of Interest (ROI) Orientation and Starting Positions

Increasing the incremental ROI and calculating the porosity at each step is essential towards obtaining the REV. However, it is important to recognise that the origin or starting location at which the ROI is initiated can also influence the REV outcome. Depending on the material's homogeneity, variations in the ROI starting points can have a significant impact on the porosities calculated.

To address these concerns, each x-y-z plane of the sample was subdivided into three planes. The corners, the midpoint of each plane as well as the midpoints of each plane-edge were identified as starting positions to expand the ROI from 100 voxels to the MROI (2000 voxels). These starting locations were identified in terms of xyz coordinates as shown in Figure 4-7B. An additional demonstration of the incremental ROI expansion process for the x-y plane is also shown in Figure 4-7C which indicates the starting locations of the ROI originating from that plane.

In total, the process outlined in Figure 4-7 resulted in 27 possible starting positions which are designated below. For each of these 27 orientations, 20 ROIs were generated - starting at a 100 voxel (~0.5 mm) cubic volume which was progressively increased by 100 voxels in each direction until the MROI (a 2000 voxel (~10 mm) cubic volume) was attained. This resulted in a total of 540 ROIs being generated and analysed for each sample.

The unique identifiers for each ROI origin were labelled in accordance to Figure 4-7B. For reference to other sections in this chapter, these were named:

x1y1z1	x2y1z1	x3y1z1	x1y2z1	x2y2z1	x3y2z1	x1y2z2	x2y2z2	x3y2z2
x1y2z3	x2y2z3	x3y2z3	x1y3z2	x2y3z2	x3y3z2	x1y3z3	x2y3z3	x3y3z3
x1y3z1	x2y3z1	x3y3z1	x1y1z2	x2y1z2	x3y1z2	x1y1z3	x2y1z3	x3y1z3

4.2.4.3 REV Determination

This REV identification applied in this work builds upon the approach used by VandenBygaart and Protz (1999) who investigated the representative elementary area (REA) of selected soil samples using digitised thin-sectioned images. These authors proposed a methodology whereby the REA would be attained in the area where a selected parameter quantity (porosity) in three successive areas of measurements did not change ±10% by relative to the next progressive area of measurement.

The VandenBygaart and Protz approach seems to use an arbitrary amount of the change (± 10%) of a given parameter between consecutive areas to identify the REA but the results presented by VandenBygaart and Protz (1999) illustrate that a ±10% change often results in very minute changes of porosity in the range of 0.05 porosity units. Changes of 0.05 porosity units between successive areas can be considered to be very minimal and fundamentally, imply that the area and any successive areas have a uniform porosity.

This approach was extended for use in this work and the REV was identified when the porosity percent change between consecutive ROI volumes became consistent within the range of a ±10% change.

The porosity percent change between each consecutive ROI volume was calculated using Equation 4-5:

$$Percentage\ Change_{from\ i\ to\ i+1} = \left[\frac{\emptyset_i - \emptyset_{i+1}}{\emptyset_i}\right] x100 \qquad [4\text{-}5]$$

where 'i' is the ROI number (from 1 to 20) for each of the 20 voxel cubic volumes.

4.2.4.4 Testing the robustness of the REV

As an alternative to automatic thresholding, the threshold value can also be chosen using an interactive approach (termed *Interactive Thresholding* as outlined in Section 4.2.3.3) which allows the user to control the choice of threshold based on visual measurements. An interactive threshold is entirely subjective based on the users' perception of the pore space and has been by many researchers to characterise reservoir material (Verges *et al.*, 2011). This method is often chosen when there is sometimes significant uncertainty is the classification of voxels whose greyscale value are close to the automatic threshold value.

It therefore became important to investigate how the REV changes when the threshold value was varied. This was done by using variations of ±5% and ±10% of the AT value to study the sensitivity of the REV to changing threshold parameters for both samples. For each variation in threshold, the same procedure used to determine the REV at the AT was followed. This involved:

a. Determining the ROI porosities at each of the 27 orientations identified in Figure 4-7 and at each incremental expansion (where 540 ROIs were generated and analysed for variation leading to a total 2160 measurements for each sample);

b. Obtaining the porosity percent change between successive ROI volume and choosing the REV accordingly (when the change became consistent in the range of a ±10%).

4.2.5   Pore Network Extraction

Pore networks approximate the porous medium as interconnected system of pores and pore throats. The goal of pore network extraction is to derive a 3D representation of the internal structure of the porous medium from which a pore network can be identified. Once the pore network has been acquired, measurements on the pore space can then provide a distribution of the pore size.

4.2.5.1 Method of Pore Network Extraction and obtaining the PSD

Avizo® Fire uses a medial axis algorithm to extract the pore network from a 3D reconstructed mode.   This algorithm works on the basis of producing a reduced representation of the pore space via the use of a thinning or burning algorithm (Dong and Blunt, 2009; Lindquist *et al.*, 1996). This produces a topological skeleton running through the centre of the pore network. Partitioning of the pore space uses local minima along branches where the minimum length of a fitted ellipsoid enclosing the pore is taken as the pore diameter.

The PSD using the Avizo® Fire software was obtained by using the '*AutoSkeleton'* command in the '*Image Morphology'* module to first extract the pore network and then using the '*Spatial Graph Statistics'* command in the '*Measure'* module to measure the pore radii.

4.2.5.2 Testing the Sensitivity of the PSD to changes in the Threshold Value

An REV measured using porosity changes may not necessarily be the same as an REV based on pore size since there is no established correlation between porosity and pore size (Bennion and Bachu, 2006). To examine whether an REV based on porosity is also applicable to pore size studies, the pore network was extracted at each of the 27 REV orientations identified in Figure 4-7 for Berea and Bentheimer samples.

To do this, REV threshold values were varied at ±5% and ±10% of the AT value with PSDs being obtained at each of the 27 orientations outlined in Figure 4-7B. The mean of these 27 PSDs was then obtained and compared to the PSD obtained from Automatic Thresholding. This resulted in a total of 108 pore network extractions being carried out for each sample from which the mean PSDs related to ±5% and ±10% of the AT value were obtained.

4.3   Nuclear Magnetic Resonance (NMR) Testing

Nuclear Magnetic Resonance (NMR) experiments measure the response of hydrogen nuclei which have been excited in a magnetic field. This response takes the form of an NMR signal whose amplitude is proportional to the amount of hydrogen nuclei present. The rate of decay of the NMR amplitude is related to a relaxation time of the nuclei back to equilibrium. There are two relaxation times that are usually performed during NMR experiments: a longitudinal (T1) and a transverse (T2) relaxation time. It is the T2 relaxation time which is important when determining pore size (Kleinberg, 1996; Mao *et al.*, 2009; Slijkerman and Hofman, 1998; Sorland *et al.*, 2007).

NMR laboratory measurements on core samples are generally made on samples saturated with distilled water or brine (Sorland *et al.*, 2007) since the T2 response to water and brine correlates well with surface measurements of the pore space. In contrast, NMR logging measurements are made on fluids in a reservoir environment which can be one or a combination of the following: connate water, hydrocarbons and drilling mud (Shafer *et al.*, 1999). The nature of the in-situ fluids influences the NMR response and it becomes worthwhile to study the NMR response (regardless of whether this is laboratory or field-acquired) when various fluids, other than water and brine are entrained in the pore space.

This section presents both the theory and method of obtaining NMR measurements for the Berea and Bentheimer samples when these are saturated with a variety of fluids as well as the procedure for converting these into porosity and pore size distributions (PSDs).

4.3.1 Theoretical Approach

During an NMR experiment, a saturated sample is placed in a magnetic field and excited with a series of radio frequency (RF) pulses. After each pulse, a small signal or echo is generated by the nuclei within the fluid. This is recorded as a train of echoes having a series of signal amplitudes which decay as the hydrogen nuclei start to randomly collide with each other (nuclei-nuclei interactions), collide with the pore walls (surface interactions) and diffuse through the porous media due to magnetic gradients (diffusion relaxation).

The raw data measured during a T2 NMR experiment is an echo train (a series of echo amplitudes) recorded as a function of time, usually at fixed time intervals termed the inter-echo time, TE. This raw data is then mathematically inverted by use of a best-fit curve which produces a T2 spectrum as shown in Figure 4-8.
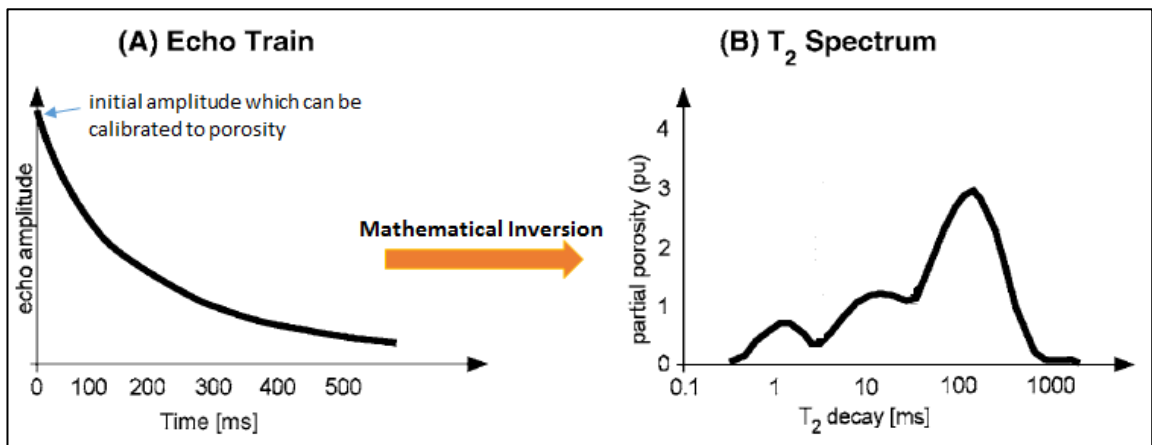
Figure 4-8: Diagram of an echo train (A) and transformation in a T2 spectrum (B) (after Westphal *et al.*, 2005)

The initial amplitude of the echo train (usually recorded in micro-volts [μV]) is a measure of the fluid-filled porosity as it is proportional to the number of hydrogen nuclei in the pores (Coates *et al.*, 1999). This amplitude can be calibrated to porosity units using the corresponding NMR signal from a known volume of the bulk fluid (Magritek, 2013). With proper calibration, the area under the T2 spectrum is equal to the porosity (Coates *et al.*, 1999). When the porous medium is saturated with water or brine, this distribution will correlate with pore-size distribution which is outlined below.

The T2 spectrum is comprised of three elements: (1) bulk fluid relaxations, T2B (nuclei-nuclei interactions), (2) surface relaxations, T2S (nuclei-pore wall interactions) and (3)

66

diffusion in the presence of varying magnetic field gradients, T2D. The relationship among these is given in Equation 4-6:

$$\frac{1}{T2} = \frac{1}{T2B} + \frac{1}{T2S} + \frac{1}{T2D} \qquad [4\text{-}6]$$

The relative contribution of each term in T2 is dependent upon a number of factors which include the type of fluid in the porous medium, the pore size distribution and the nature of the pore-grain surface (Coates *et al.*, 1999; Niu *et al.*, 2008).

The bulk fluid relaxation (T2B) is essentially the relaxation if the fluid were placed in a sufficiently large container within a homogeneous magnetic field so that the nuclei only interacted with themselves and not with the walls of the container. It is a property of the fluid and is directly proportional to its viscosity (Straley *et al.*, 1997). Low viscosity fluids are associated with a higher molecular mobility which results in slower relaxation rates and higher values of relaxation times. Conversely, high viscosity fluids generally have a reduced molecular mobility and are associated with faster relaxation rates.

The surface relaxation (T2S) describes the relaxation of the nuclei when they interact with the surface of the porous media. T2S is therefore strongly related to the surface morphology of porous media and is proportional to the surface to volume ratio $\left(\frac{S}{V}\right)$ of the pores which exists (Straley *et al.*, 1997). This relationship is given by Equation 4-7:

$$\frac{1}{T2S} = \rho_2\left(\frac{S}{V}\right) \qquad [4\text{-}7]$$

where S is the surface area of the pore and V is the pore volume. ρ_2 is the surface relaxivity which describes the rate at which a surface relaxes or attenuates the spins of the nuclei approaching the surface. It is essentially a proportionality constant between the surface relaxation rate and the pore size (Slijkerman and Hofman, 1998).

The diffusion relaxation rate can be obtained using the equation (Kenyon, 1997):

$$\frac{1}{T2_D} = \frac{D_o\gamma^2 G^2 TE^2}{12} \qquad [4\text{-}8]$$

in which γ is the gyro-magnetic ratio, D_o is the self-diffusion constant of the relaxing fluid, G is the strength of the field gradient and TE is the inter-echo time.

When the magnetic field is fixed and uniform and the TE is sufficiently short, diffusion effects become unimportant and can be ignored (Coates *et al.*, 1999; Mao *et al.*, 2005).

Manipulating the parameters which govern diffusion relaxation gives rise to two NMR experiments which when used in tandem can give a quantitative measure of the pore size. The first experiment measures the T2 response when the magnetic field is kept constant and the TE time is kept sufficiently short; this experiment is referred to as a T2 test. The second experiment varies the TE so that it is no longer considered short. This is called a Pulsed Field Gradient Stimulated Echo (PGSTE) experiment. The theory governing both experiments is further described below.

4.3.2 The T2 Test

In the particular case when the magnetic field is fixed and uniform TE is sufficiently short, the T2D term in Equation 4-6 can be ignored (Coates *et al.*, 1999; Mao *et al.*, 2005) which gives:

$$\frac{1}{T2} = \frac{1}{T2B} + \rho_2\left(\frac{S}{V}\right) \qquad [4\text{-}9]$$

For a low viscosity fluid such as water relaxing in a porous medium, the surface relaxation rate is significantly faster than the bulk relaxation rate (Cabrera, 2008). The bulk relaxation rate of the water is of the order of 2000 – 2500ms (Bryan *et al.*, 2003; Kantzas, 2009; Niu *et al.*, 2008). This means that when the porous medium is filled only with water or brine, the bulk water relaxation rate is sufficiently large when compared to the overall T2 signal, that the first term in Equation 4-9, $\left(\frac{1}{T2B}\right)$ becomes very small when compared to $\left(\frac{1}{T2}\right)$.

This implies that specifically for the case of brine contained within water-wet pores, bulk relaxation effects can be ignored given that *T*2B is usually much larger than T2 (Mao *et al.*, 2005) and results in:

$$\frac{1}{T2} = \rho_2\left(\frac{S}{V}\right) \qquad [4\text{-}10]$$

Equation 4-10 only applies in the fast diffusion limit when $\left(\dfrac{\rho_2 r}{D_o} < 1\right)$ (Jin *et al.*, 2009; Mitra *et al.*, 1993) where r denotes the pore radius and D_o is the self-diffusion coefficient of the bulk fluid (which is discussed later in Sections 4.3.3 and 5.4.2). Fast diffusion refers to the movement of the hydrogen nuclei in pores that are sufficiently small so that surface relaxation mechanisms take place at a sufficiently slow pace so that a hydrogen nucleus crosses the pore many times before it relaxes [Coates *et al.*, 1999]. This allows for an adequate measurement of the pore space from $\left(\dfrac{S}{V}\right)$ given that the hydrogen nuclei traverse the pore space many times before relaxing. Conversely, slower diffusion limits suggest that the nuclei do not make enough contact with the pore walls before relaxing to provide sufficient pore information (and that the relaxation is influenced more by the nuclei-to-nuclei interactions rather than the pore-to-nuclei interactions).

The surface area to volume term, $\left(\dfrac{S}{V}\right)$ in Equation 4-10 can provide a measure of the pore radius. For common geometric shapes, $\left(\dfrac{S}{V}\right)$ can be represented using a shape factor as shown in Table 4-3. This implies that Equation 4-10 can be re-written to include a shape factor as shown below:

$$\frac{1}{T2} = \rho_2 \left(\frac{S}{V}\right) = \rho_2 F_s \left(\frac{1}{r}\right) \qquad \text{[4-11]}$$

where F_s is the geometric shape factor and *r* is the pore radius.
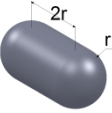
It is commonly accepted that the NMR spectra of porous media are essentially analogous to a measurement of the pore size distribution of the rock (Straley *et al.*, 1997). Equation 4-11 illustrates that each T2 value is associated with a unique pore radius and as such, a *T*2 distribution describes the existing pore-size distribution (although not in absolute units).

It is important to note that Equation 4-11 holds true for the specific case of porous media saturated with water or brine [Coates *et al.*, 1999; Mao *et al.*, 2005]. This is because water is a low viscous fluid and has a relatively large T2B relaxation time so that $\left(\dfrac{1}{T2B}\right)$

69

becomes very small when compared to $\left(\dfrac{1}{T2}\right)$ which allows the $\left(\dfrac{1}{T2B}\right)$ term to be ignored.

For more viscous fluids or for fluids having smaller T2B relaxation times, it may become unrealistic to ignore the $\left(\dfrac{1}{T2B}\right)$ term. This implies that the pore distribution is a function of both T2S and T2B. The effect of varying fluids in the pore space and their influence on determining the pore size distribution from NMR experiments will be investigated in later sections of this chapter.

Table 4-3: Shape Factor for several common geometric shapes

Pore Shape		Characteristic Length	Surface Area	Volume	$\dfrac{S}{V}$	Shape Factor, F_s
Sphere		Radius, r	$4\pi r^2$	$\dfrac{4}{3}\pi r^3$	$\dfrac{3}{r}$	3
Tube (Right Cylinder)		Radius, r Height = 2r	$4\pi r^2$	$2\pi r^3$	$\dfrac{2}{r}$	2
Cube (Right Cylinder)		Side, r	$6r^2$	r^3	$\dfrac{6}{r}$	6
Capsule		Radius, r Height = 2r	$8\pi r^2$	$\dfrac{10}{3}\pi r^3$	$\dfrac{12}{5r}$	$\dfrac{12}{5}$

4.3.3 The Pulsed Gradient Stimulated Echo (PGSTE) Test

When the magnetic field is fixed and uniform and the inter-echo time is sufficiently short, diffusion effects become unimportant and can be ignored (Coates *et al.*, 1999; Mao *et*

al., 2005) as outlined in Equation 4-9. However, diffusion effects can be enhanced when required for particular applications if an appropriate inter-echo spacing is selected.

One such application is the determination of D_o, the self-diffusion constant of the fluid confined in the porous medium. Diffusion may be restricted when fluids are confined in a small pore such as in porous media (Slijkerman and Hofman, 1998). For restricted diffusion, D is dependent on the diffusion time and tends to decrease with time.

NMR pulsed field gradient (PFG) diffusometry is a well-established method for measuring the self-diffusion coefficient, D_o, of fluids confined in porous media (Loskutov, 2012; Slijkerman and Hofman, 1998; Vogt *et al.*, 2002; Winklemann, 2017). To obtain *D*, a pulsed field gradient stimulated echo experiment (PGSTE) is carried out. This PGSTE experiment, developed by Cotts *et al.* (1989), comprises of 13 intervals as shown in Figure 4-9.
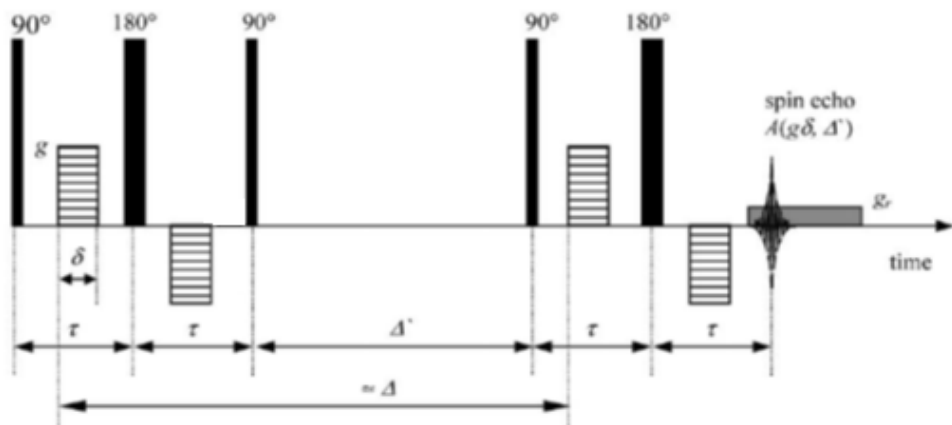
Figure 4-9: The 13-interval Pulsed Field Gradient Stimulated Echo (PGSTE) Experiment (after Cotts *et al.*, 1989)

Mitra *et al.* (1993) have shown that for exceedingly short diffusion times *t*, the restricted diffusion coefficient can be written as:

$$\frac{D(t)}{D_o} = 1 - \frac{4}{9\sqrt{\pi}}\sqrt{D_o t}\left(\frac{S}{V}\right) \qquad [4\text{-}12]$$

where *D(t)* is the time dependent diffusion coefficient, D_o is the unrestricted or self-diffusion coefficient (in bulk fluid) and *t* is the observation time for diffusion. This equation

becomes instrumental towards obtaining a value of $\left(\dfrac{S}{V}\right)$ for the porous media under study as outlined below.

Recall Equation 4-10 which states:

$$\frac{1}{T2} = \rho_2\left(\frac{S}{V}\right) \qquad [4\text{-}10]$$

This equation assumes that relationship between T2 to the surface to volume ratio and surface relaxivity holds true for any pore size (Sorland *et al.*, 2007). Porous media is often heterogeneous with respect to pore size distribution and as such, Equation 4-10 must hold true when pore size varies.

If ξ_i denotes the volume fraction of pores with $\left(\dfrac{S}{V}\right)_i$ with relaxation time T2$_i$ and *n* is the number of subdivisions of pore size, then Equation 4-10 can be rewritten in the form following Uh and Watson (2004):

$$\sum_{i=1}^{n}\xi_i\frac{1}{T2_i} = \sum_{i=1}^{n}\xi_i\rho_{2,i}\left(\frac{S}{V}\right)_i \qquad [4\text{-}13]$$

It can be assumed that the surface relaxivity is independent of pore size (Sorland *et al.*, 2007) and as such Equation 4-13 becomes:

$$\sum_{i=1}^{n}\xi_i\left(\frac{1}{T2_i}\right) = \sum_{i=1}^{n}\xi_i\overline{\left(\frac{1}{T2}\right)} \approx \rho_{2,i}\sum_{i=1}^{n}\xi_i\left(\frac{S}{V}\right)_i = \rho_2\overline{\left(\frac{S}{V}\right)}$$

$$\therefore \overline{\left(\frac{1}{T2}\right)} = \rho_2\overline{\left(\frac{S}{V}\right)} \qquad [4\text{-}14]$$

where $\overline{\left(\dfrac{1}{T2}\right)}$ is the inverse of the weighted harmonic mean of the T2 distribution and

$\overline{\left(\dfrac{S}{V}\right)}$ is the average surface area to volume ratio.

$\overline{\left(\dfrac{S}{V}\right)}$ can be found by performing a series of diffusion experiments at short diffusion in which the self-diffusion coefficient, D, is measured (Loskutov, 2012; Slijkerman and Hofman, 1998; Sorland et $al.$, 2007).

For a porous medium with varying pore sizes, Equation 4-14 can be expressed as:

$$\sum_i \xi_i \frac{D_i}{D_o} \approx \sum_i \xi_i \left[1 - \frac{4}{9\sqrt{\pi}} \sqrt{D_o t} \left(\frac{S}{V}\right)_i \right] = \left(1 - \frac{4}{9\sqrt{\pi}} \sqrt{D_o t} \overline{\left(\frac{S}{V}\right)} \right) \qquad [4\text{-}15]$$

Equation 4-15 shows that the average surface area to volume, $\overline{\left(\dfrac{S}{V}\right)}$ can be obtained from a linear fit of time-dependent restricted diffusion coefficients $D(t)$ plotted against the square root of time. This is further described in Section 5.4.2.2.

Once $\overline{\left(\dfrac{S}{V}\right)}$ has been determined, Equation 4-14 can be used to obtain the surface relaxivity, ρ_2 which is assumed to be independent of the pore size. With Equation 4-11, the T2 distribution can then be converted into a pore size distribution by modelling the pores as having defined geometric shapes.

4.3.4 The NMR-PSD Approach: Key Steps in deriving PSD from NMR Experiments

When combined, the T2 and PGSTE tests allow for the determination of PSDs through a 4-step process. These include:

Step 1: Running a T2 test to determine the T2 spectrum and obtain the inverse of the weighted harmonic mean $\overline{\left(\dfrac{1}{T2}\right)}$ of the T2 distribution

Step 2: a) Running a PGSTE experiment at selected diffusion times (t) and recording the values of $D(t)$

b) Plotting $D(t)$ vs $t^{1/2}$ and obtaining the average $\overline{\left(\dfrac{S}{V}\right)}$ ratio

Step 3: With known values of $\overline{\left(\dfrac{1}{T2}\right)}$ and $\overline{\left(\dfrac{S}{V}\right)}$ from steps 1 and 2, calculate the surface relaxivity, ρ_2 using Equation 4-14: $\overline{\left(\dfrac{1}{T2}\right)} = \rho_2\overline{\left(\dfrac{S}{V}\right)}$

Step 4: With this calculated value of ρ_2, T2 values can now be converted into pore radii using Equation 4-10: $\dfrac{1}{T2} = \rho_2\left(\dfrac{S}{V}\right)$

4.3.5 Berea and Bentheimer Sample Preparation and Testing Procedure

Prior to NMR testing, both samples were cleaned via Soxhlet-Extraction using a 50/50 solvent mixture of toluene and ethanol. The samples were then oven-dried for 48 hours at 250°F to remove moisture and then cooled to room temperature in a desiccator. They were then saturated with distilled water using a Vinci Technologies RC4500 centrifuge running at 2,000 rpm for 36 hours. The saturated samples were then wrapped in plastic film to avoid a loss of moisture after which, they were subjected to T2 and PGSTE NMR testing using a 2 MHz NMR Rock Core Analyzer Magritek instrument. All tests were performed at temperatures between 20 – 25°C.

A T2 test initially records an echo train (raw data) which is then converted to T2 spectrum using an appropriate mathematical inversion. T2 tests were carried out on both the saturated Berea and Bernheimer core samples as well as on a 25 mL volume of the bulk or saturating fluid (distilled water). The echo train of the bulk fluid is required in order to calibrate the porosity of the core samples. This is further discussed in Section 5.4.1. The acquisition parameters required for the T2 tests included the number of echoes and echo time. More information regarding these terms and the T2 test procedure used in this work can be found in Appendix 2.

The next step was to run a PGSTE experiment at selected diffusion times *(t)* to obtain the values of the self-diffusion coefficient, *D(t)*. The acquisition parameters needed for the PGSTE measurements included only the gradient separation time (diffusion time *(t)*). More information regarding these terms and the PGSTE test procedure used in this work can be found in Appendix 2.

4.3.6 Investigating the influence of viscous fluids on PSD determination from NMR Testing

The NMR-PSD method outlined in Section 4.3.4 is contingent upon carrying out NMR measurements of the pore space when it is saturated with either water or brine (or other suitably low viscous fluids). Low viscous fluids minimise the contribution of the bulk fluid relaxation term (T2B) in Equation 4-9 and lead to the T2 distribution being dependent only on the T2S surface relaxation as shown in Equation 4-10:

$$\frac{1}{T2} = \rho_2 \left(\frac{S}{V} \right) \qquad \text{[4-10]}$$

Obtaining NMR PSDs on formations and cores having their in-situ fluids (which may not necessarily be comprised of low viscous fluids) is valuable to the petroleum industry. Good examples of where these situations might occur include:

- the NMR logging of formations in which the in-situ fluids may be a combination of connate water, in-situ hydrocarbons and drilling mud (Shafer *et al.*, 1999). The capability of obtaining PSDs during NMR logging can identify sweet spots in real-time and provide pore information on material having a minimal drilling fluid invasion and formation damage.

- the testing of core samples which still have their in-situ fluids. With specific reference to unconsolidated Athabasca oil sand material, the in-situ bitumen acts as a cohesive agent binding the grains together. Removal of this bitumen can lead to a rearrangement of the pore structure unless meticulous care is taken to preserve the pore integrity during the cleaning process. As such, the use and development of robust techniques to test oil samples with their in-situ bitumen is helpful as alternate core analytical techniques which require that these samples be cleaned of original fluids may not readily provide consistent and reliable pore information for these kinds of materials.

It becomes important to therefore study the influence of fluid parameters which can affect the determination of PSD during NMR testing. The effect of using viscous fluid on NMR PSD determination was therefore also examined since many new exploits within the petroleum industry instead focus on heavy oil and bitumen (Hein, 2016).

The viscous fluid used is this work is glycerol. Glycerol ($C_3H_8O_3$) is a simple polyol compound which is colourless, odourless and highly soluble in water. It has a molecular

weight of 92.094 g/mol, a viscosity of 1,412 cp (1.412 Pa-s) at 20°C and a density of 1.261 g/cm³ at 20°C (Lide, 1994). In comparison, water has a viscosity of 1 cp (0.001 Pa-s) at 20°C.

After being saturated with distilled water (and therefore water-wet) as outlined in Section 4.3.5, Berea and Bentheimer samples were further saturated with glycerol using a Vinci Technologies RC4500 centrifuge running at 2,000 rpm for 36 hours in order to achieve an irreducible water saturation. The saturated samples were then wrapped in plastic film to avoid a loss of moisture after which, they were subjected to T2 and PGSTE NMR testing using a 2 MHz NMR Rock Core Analyzer Magritek instrument. All tests were performed at temperatures between 20 – 25°C.

4.3.7   AOS Sample Preparation and Testing Procedure

Section 4.3.6 outlined a modified approach for obtaining the PSDs of the Berea and Bentheimer samples which were saturated with fluids having viscosities higher than that of water. This attempted to extend the NMR-PSD approach provided in Section 4.3.4 which is limited to the use of low viscous fluids (like water and brine) since these minimise the contribution of the bulk fluid relaxation and simplify the overall T2 signal as a sole function of the surface relaxation.

Obtaining NMR PSDs on formations and cores that still contain their in-situ fluids (which may not necessarily be comprised of low viscous fluids) is valuable to the petroleum industry and particularly for NMR logging and other applications in which it is easier to test samples with their in-situ fluids such an unconsolidated oil sand material.

This formed the rationale for studying the AOS sample in as close to its native state as possible and as a result the AOS sample was subjected to NMR testing with its in-situ fluids. The sample was wrapped in plastic film and then subjected to T2 and PGSTE NMR testing using a 2 MHz NMR Rock Core Analyzer Magritek instrument. All tests were performed at temperatures between 20 – 25°C.

The Application of the MICP, PNM and NMR Methods to the Berea and Bentheimer samples

5.1   Introduction

The general objective of this work is to evaluate the pore space of selected sandstone samples using three complementary methods: Mercury Injection Capillary Pressure (MICP), Pore Network Modelling (PNM) and Nuclear Magnetic Resonance (NMR). Several attributes of these methods which relate to the kinds of fluids which should be present in the pore space often restrict these methods to the testing of certain kinds of material.   The Berea and Bentheimer samples were used in this work to explore a number of these attributes and they represent the benchmark materials for this study.

The consolidated nature of these samples made them ideal for analysing the response and the influence of a number of selected fluids during NMR testing as they could be subjected to repeated fluid injection and removal without comprising or changing the inherent pore structure. The type of fluid contained within the pore space influences the robustness of the results for each method. Both MICP and NMR require specific fluids to be contained in the pore space prior to testing which generally requires the removal and replacement of all original fluids with air for MICP and with water (or brine) for the NMR method. This typically will preclude the testing of samples imbued with their original fluids using these methods.   On the other hand, PNM requires little to no sample preparation prior to testing (Ketcham and Carlson, 2001) and so is ideal for studying samples containing their in-situ fluids.

This chapter provides the results of the applying the MICP, NMR and PNM approaches (outlined in Chapter 4) to the Berea and Bentheimer samples.

5.2 Mercury Injection Capillary Pressure (MICP) Test Results

MICP testing involves the injection of mercury into a sample that has been cleaned of all original fluids and then subsequently dried and evacuated of all cleaning fluids. The injection pressures provide a measure of the accessed pore throat radii while the corresponding amounts of injected mercury are related to the distribution of the radii.

MICP testing provide measures of the porosity and PSD. Porosity is related to the total injected mercury volume while PSDs can be inferred from the incremental injected mercury volume at each pressure step. These results of the MICP test are typically presented as a capillary pressure versus saturation curve (drainage capillary pressure curve). The magnitude of the capillary pressure at each saturation value represents a particular pore throat radius while the incremental mercury saturation denotes the proportion of that pore throat radius which has been accessed by the mercury. These concepts are further explored in this section.

5.2.1 Porosity Results

The MICP test provides direct measurements of effective porosity as the volume of mercury imbibed quantifies the amount of interconnected pore space. Using Equation 2-1, Table 5-1 provides the corresponding data for the Berea and Bentheimer samples.

Table 5-1: MICP Porosity Determination of the Berea and Bentheimer samples

	Berea	**Bentheimer**
MICP Injected Volumes:		
Injected Bulk Volume [cm^3]	7.010	8.093
Injected Pore Volume [cm^3]	0.955	1.471
Porosity from MICP Testing [%]	13.6	18.2

These results compare favourably with the range of porosities associated with the Berea (12 – 25%) and Bentheimer samples (18 – 27%) quoted in the literature (Berea Sandstone Petroleum Cores, 2015; Peksa *et al.*, 2015).

5.2.2 Capillary Pressure Results

During MICP testing, mercury injection pressures were increased in a series of steps with the percentage of the pore volume saturated by the mercury at each step being recorded after allowing for a sufficient equilibrium time. The injection pressures were then plotted against corresponding mercury saturations (or equivalent water saturations) resulting in a capillary pressure curve. MICP curves typically represent primary drainage measurements given that mercury is strongly non-wetting (Pittman, 1992).

The results of the MICP tests on the Berea and Bentheimer samples are shown in Figure 5-1 and highlight three key attributes which characterise capillary pressure curves. The first is the displacement pressure which is the minimum pressure required to force the non-wetting fluid (mercury) into the largest pores. The displacement pressures are 8.9 and 3.6 psia respectively for the Berea and Bentheimer samples. A lower displacement pressure indicates that larger pores are connected to the surface which generally implies higher permeability (Elshahawi *et al.*, 1999).

As the injection pressure increases, increasingly smaller pores are invaded which correspond to the middle or flat section of the curve. A lower flat section (i.e. lower capillary pressures) signifies that larger pores are being invaded and imply a higher permeability. The middle section of the Bentheimer sample is also lower than the Berea sample highlighting the Bentheimer's higher permeability.

The steepness of the curve over its middle section generally indicates the kind of reservoir quality which exists where a very steep curve that is nearly vertical over its middle section implies that the reservoir quality is poor with extremely fine grains, very poor sorting, low porosity and low permeability. A capillary pressure curve that remains essentially flat over its middle section indicates that the grains are well-sorted and the medium is fairly homogeneous (Elshahawi *et al.*, 1999).

It can be seen that the middle section of both samples are fairly flat indicating a good degree of homogeneity which is well-documented in the literature (Bera *et al.*, 2011; Peng *et al.*, 2012; Wilson, 2004). However, the middle section of the Berea curve is shorter than the Bentheimer's and becomes progressively steeper at around a 60% mercury saturation. This indicates that increasingly smaller pores are being accessed. Berea typically has a narrower pore size distribution than Bentheimer and as such, requires larger pressures early on to invade the smaller pores.
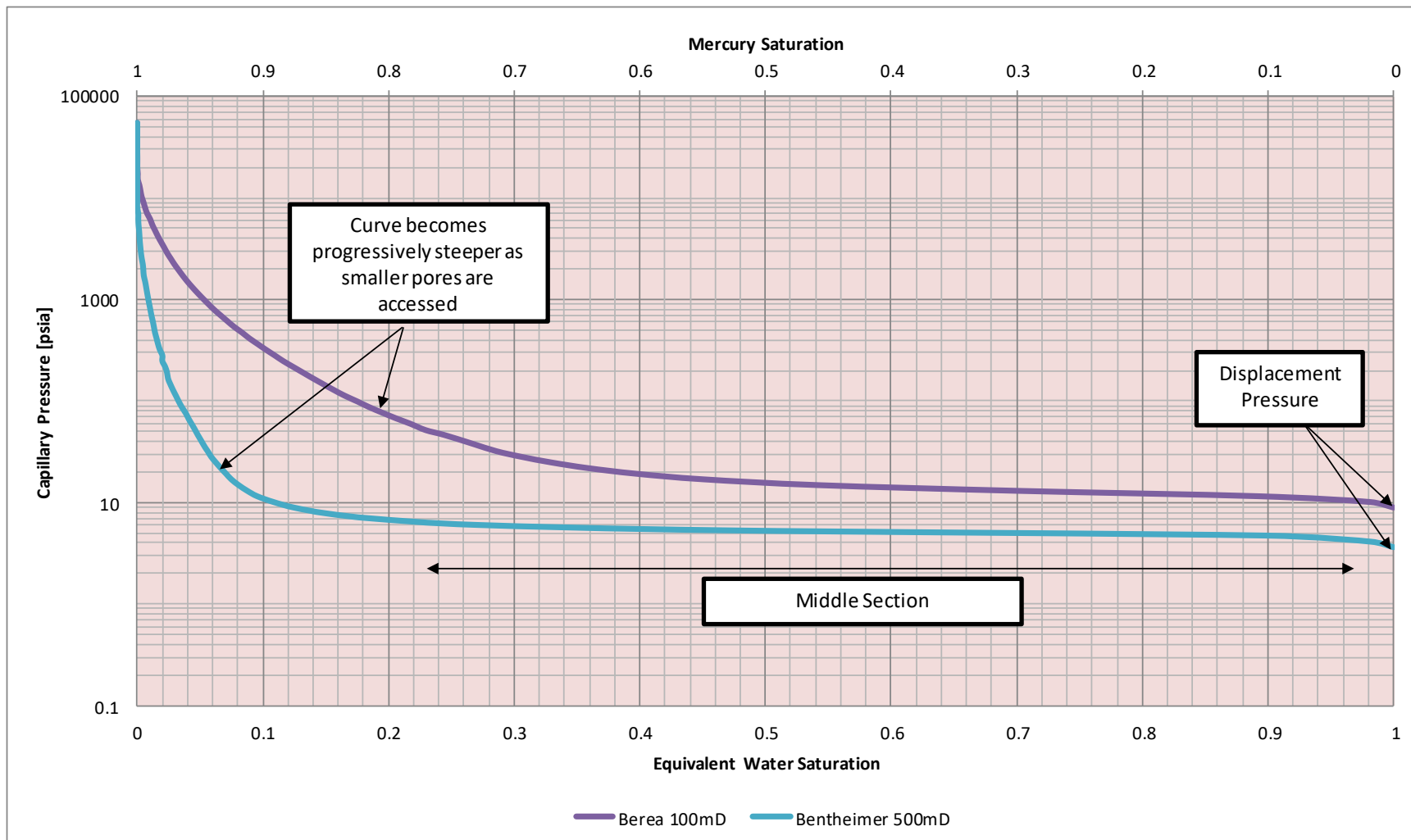
Figure 5-1: MICP Results for the Berea and Bentheimer Benchmark samples

After the middle section, the steepest part of the curve that tends towards infinite capillary pressure values commences which indicate that exceedingly larger pressures are required to enter the smallest pores.

5.2.3 Pore Size Distribution (PSD) Results

Once a capillary pressure curve has been obtained, the pore throat size distribution can be obtained using the modified Young-Laplace equation (provided in Chapter 2 and also shown below):

$$r_t = \frac{2\sigma \cos\theta}{P_c} \qquad \text{[2-3]}$$

where r_t is the equivalent pore throat radius, σ is the interfacial tension between the fluid phases and θ is the contact angle between the solid surface and the fluid-fluid interface.

By using Equation 2-3, the pore size distributions (PSDs) of the Berea and Bentheimer samples were obtained. There are several ways to present PSD information; the two most common approaches involve producing an incremental intruded pore volume vs radius diagram (which essentially a frequency distribution of the pore size) as well as a cumulative pore volume vs radius diagram. These diagrams are shown in Figures 5-2 and 5-3 for the Berea and Bentheimer samples.

These diagrams confirm that both materials are fairly homogenous being comprised of a relatively narrow pore size distribution which is well-documented in the literature (Bera *et al.*, 2011; Peng *et al.*, 2012; Wilson, 2004). The majority of the pore size radius of the Berea sandstone used in this work ranges 1 – 10 microns while similar data for the Bentheimer sample shows that the material is largely comprised of interconnected pores of 5 – 30 micron radius.

The data is best described using statistical measures outlined in Section 4.1.4.
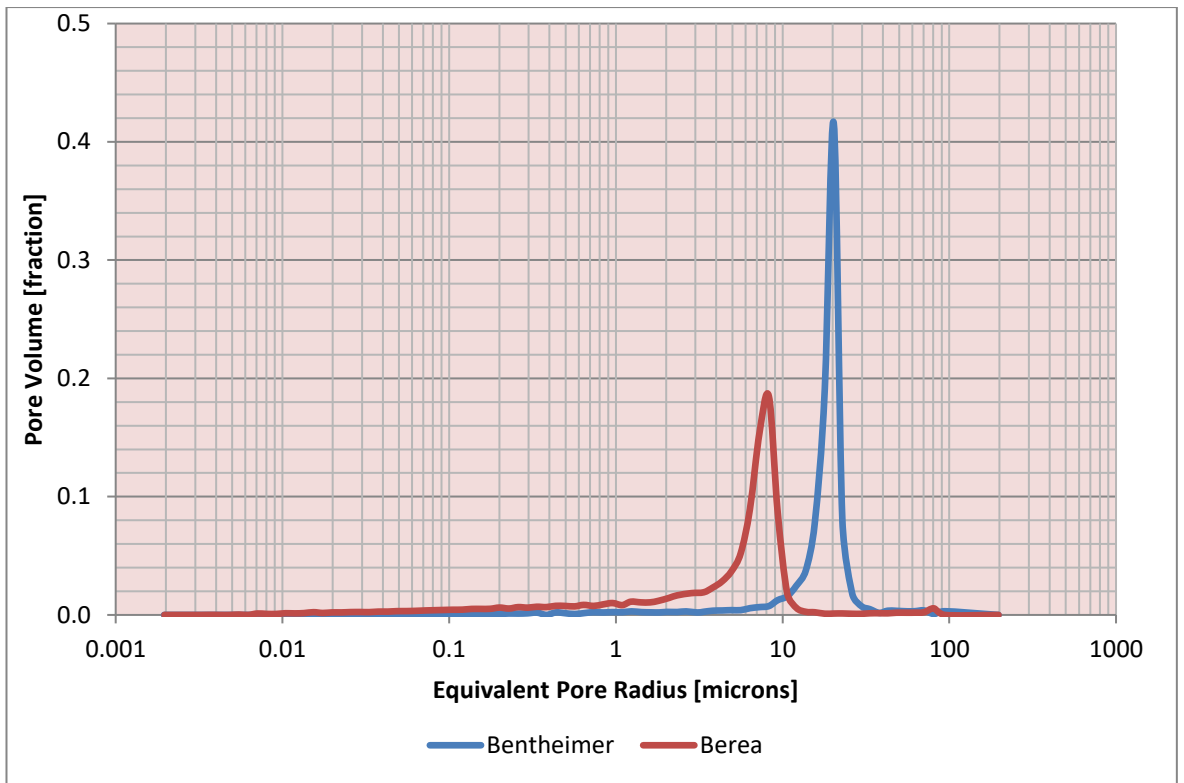
Figure 5-2: Pore Size (Frequency) Distribution for the Berea and Bentheimer
Benchmark samples
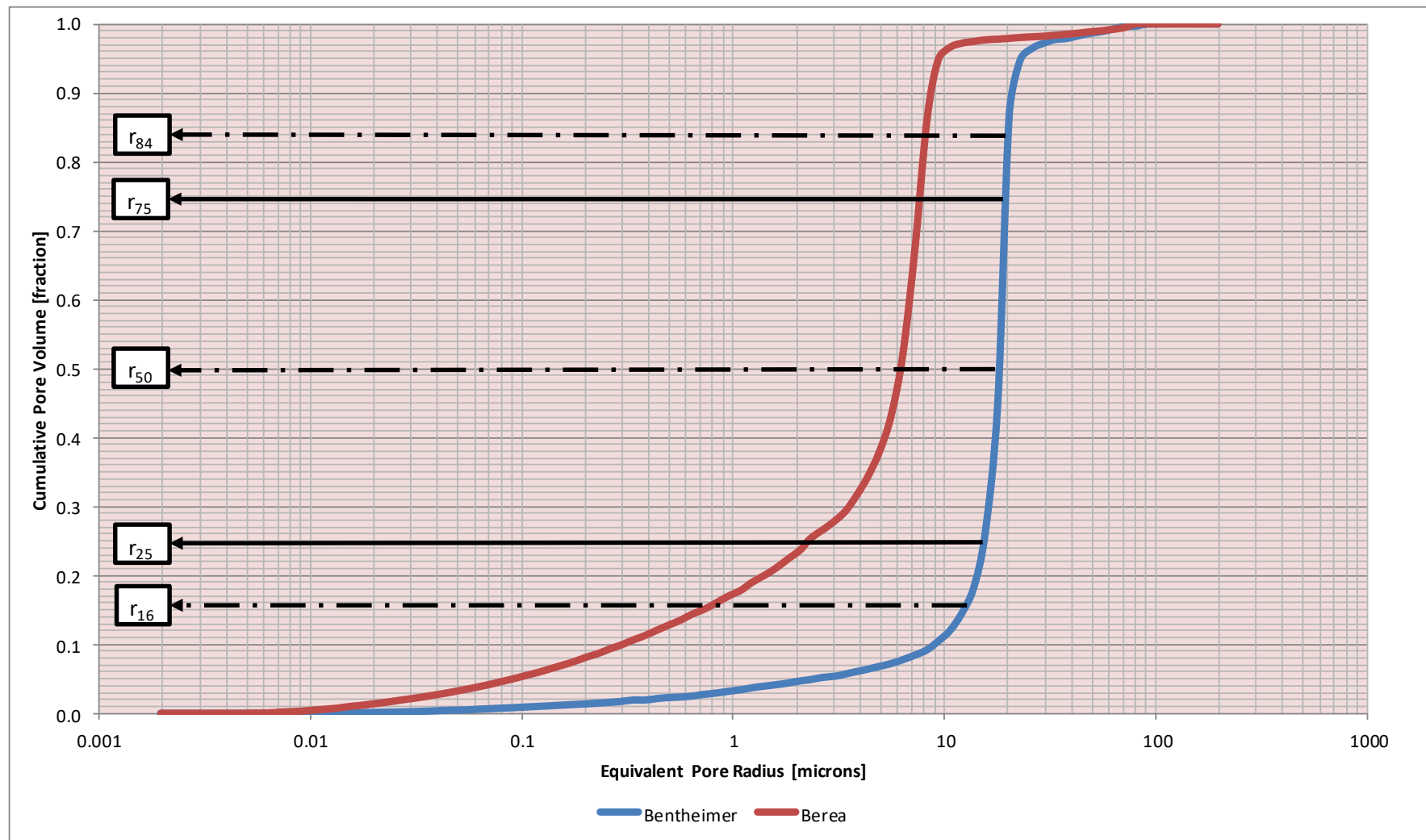
Figure 5-3: Cumulative Pore Size Distribution for the Berea and Bentheimer Benchmark samples

5.2.4 Statistical Analysis of the PSDs of the Berea and Bentheimer samples

Table 5-2 below outlines the statistical analysis of the Berea and Bentheimer samples using the approaches provided in Section 4.1.4 (after (Chilingarian *et al.*, 1992).

Table 5-2: Analysing the Pore Size Distributions of the Berea and Bentheimer samples from MICP Testing

	Berea	Bentheimer
r_5	0.09	2.6
r_{16}	0.82	12.2
r_{25}	2.15	16.1
r_{50}	6.1	18.2
r_{75}	7.61	19.5
r_{84}	8.1	20.1
r_{95}	9.3	22.1
Statistical Measures:		
Pore Size Range [µm]	0.003 - 100	0.015 - 200
Median (r_{50}) [µm]	6.1	18.2
Mean (r_m) [µm]	6.8	18.5
Pore Sorting (S_p)	3.2	4.9
Skewness (Sk_p)	-0.38	-0.56
Kurtosis (K_p)	0.69	2.35
Pore Classification:		
Micropore (≤ 1 µm) [%]	17	3
Mesopore (1 < r ≤ 25 µm) [%]	80	95
Macropore (> 25 µm) [%]	3	2

This table shows that the mean and median of both distributions are highly comparable which indicate that the data set is generally free of outliers (extreme values which differ significantly to other data values - the mean is more susceptible to the presence of anomalies or outliers in the data than the median).

For the Berea sample, the median pore size is 6.1 µm and the pore radius ranges from 0.003 – 100 µm. The sorting is 3.2 which is a relatively low value indicating that a majority of the pores are close to the 6.1 µm median and further highlights the narrowness of the pore size distribution. Although the pore size is narrow, the kurtosis

is approximately 0.7 indicating that the pore size is essentially bi-modal having two distinct range of pore sizes. This is confirmed by the pore classification where 17% of the pore distribution has a radius of 1 μm (micropores) or less and 80% are mesoporous in nature. This large number of mesopores influences the skewness of the distribution (-0.38) indicating that although a significant proportion of micropores exist, the distribution is essentially skewed towards larger pores.

The median pore radius of the Bentheimer sample is 18.2 μm with the pore radius ranging from 0.015 – 200 μm. The sorting is 4.9, which although still relatively low, is higher than the sorting for the Berea sample (3.2) indicating there is a larger dispersion of the data set from the median value. This difference is highlighted in the variations between the pore ranges of the two samples and the distinct narrowness of each pore size distribution.

This variation is further emphasised by the skewness (-0.56) which indicates that the distribution is predominantly influenced by the larger pores in the distribution which is evident in the pore classification where 95% of the pores are mesoporous in nature with only 3% residing in the micropore range.   This is further highlighted by the high kurtosis value (2.35) which indicates that the distribution is narrow where most of the pores (95%) lie in the relatively small 1 – 25 μm mesoporous range.

The above results confirm that both samples are fairly homogenous being comprised of a relatively narrow pore size distribution which is well-documented in the literature (Bera *et al.*, 2011; Peng *et al.*, 2012; Wilson, 2004). These results formed an initial baseline characterisation of the Berea and Bentheimer samples in terms of their porosity and PSD which was used to compare the results from the PNM and NMR methods (provided in the following sections).

5.3   Pore Network Modelling (PNM) Results

PNM can reduce the time and cost normally associated with the conventional experimental methods to derive porosity, PSD and other related reservoir properties. This work used the PNM approach outlined in Figure 4-2 which is comprised of 4 main stages. The first stage is termed Image Acquisition during which sequential

digital 2D images of the samples from micro-CT imaging are obtained (Section 4.2.2). The second stage involves compiling these sequential 2D images to provide a 3D model representative of the inherent microstructure (Section 4.2.3). The segmentation sub-stage within this step is particularly important as it involves identifying a *threshold value* which is used to label each part of 3D digital model as belonging to either the pore or to the solid (grain) phase (Iassonov *et al.*, 2009). This choice of threshold is significant as an 'incorrect' value has the potential to reduce or amplify pore space as well as blur, terminate or connect pore spaces which may not necessarily exist (Taud *et al.*, 2005). This can result in significant variations in porosity and PSD with only very small changes in the threshold (Sheppard *et al.*, 2004).

The third step (Section 4.2.4) entails obtaining the Representative Elementary Volume (REV) which is the smallest size of the 3D model which captures the majority of the sample's inherent features so as to be statistically representative of the entire sample (Gelb *et al.*, 2011). The determination of the REV is dependent upon measuring changes in a property of interest as volumes are incremented. The process of incrementing these volumes as well as where these volumes are taken within the sample (in terms of their location and orientation) has the potential to impact the REV and it becomes important to further investigate their roles in REV determination.

Porosity is prevalently chosen as the common property of interest chosen (Al-Raoush and Papadopoulos, 2010; Halisch, 2013) and has been used as the basis of determining the REV is this work. It becomes worthwhile however to examine if an REV based on porosity will hold true for other petrophysical variables like PSD. This is particularly interesting given that Bennion and Bachu (2006) have stated that there is no established correlation between porosity and pore size.

The last stage (Section 4.2.5) involves generating the pore network from which the pore size distribution (PSD) is obtained. These stages and well as the particular methodologies underlying each sub-stage are described in greater detail in the sections below. In addition, selected elements of the PNM Approach related to the concepts of segmentation, threshold value and REV are also examined in an attempt to further understand their influence on determining robust and representative measures of porosity and PSD.

These gave rise to the following research questions which are the focus of this work and which are further examined in the sections below.

i. How can the '*correct*' threshold value be robustly chosen?
ii. Does the REV based on porosity remain the same regardless of its orientation and location within the sample?
iii. How do changes in the threshold values affect the REV determination?
iv. Does an REV based on porosity also hold true for pore size (PSD)? Does the REV based on PSD remain the same regardless of its orientation and location within the sample?
v. How sensitive is the PSD to changes in the threshold value?

5.3.1 Choosing the 'correct' threshold value: Threshold Identification and Segmentation Results at the ROI for the Berea and Bentheimer Samples

Figures 4-3 and 4-4 show that the pore and solid mass phases are easily distinguished with the naked eye after radiograph reconstruction. However, direct measurements of the pore space cannot generally be made until segmentation processes on the images are completed.

Segmentation is the process of assigning a label to every voxel in a digital image so that voxels with the same label possess similar characteristics. For reservoir material, the goal of segmentation is to allow each voxel in the image to be labelled and identified as either belonging to a pore or the solid phase (Andra *et al.*, 2013).

There are numerous segmentation methods proposed in the literature. Global thresholding, however is a common technique used for reservoir material and involves the identification of a single greyscale value or *threshold* which is used to distinguish the pores from the solid mass (Iassonov *et al.*, 2009). The 3D images obtained from the radiograph processing were stored in an 8-bit file format (8 bits per voxel) in which each voxel is assigned an intensity which ranges from 0 to 255. A zero intensity represents black while a 255 intensity represents white. Any intensity between these represents varying shades of grey.

The greyscale histograms as well as the image results before and after segmentation are shown in the Figures 5-4 and 5-5 for the Berea and Bentheimer samples. It can be seen from Figure 5-4C that bi-modal peaks exist for in the Berea histogram

indicating that there is a clear distinction between the pores (black in colour) and the solid mass (blue in colour). The value at the valley of these bi-modal peaks provides the *automatic threshold* (AT) value which occurs at a greyscale intensity of 66. The greyscale ranges from 30 to 130 indicating that there are approximately 100 shades of grey in the image.

The unsegmented image for Berea (Figure 5-4A) also shows several bright spots within the image which as mentioned previously, is as a result of the grain structure being interspersed with components having a significant density difference (e.g. heavy metal inclusions). These components are manifest as bright spots (Langheinrich *et al.*, 2009) in the unsegmented image but can clearly be seen to be included in the solid mass (blue colour) in the final segmented image. This is expected since these form part of the solid matrix.

For the Bentheimer sample, the greyscale variation is much narrower than the Berea sample ranging from 5 to 55 indicating that there are approximately 50 shades of grey in the image. The histogram is unimodal and the AT was chosen at the bottom rim of the peak as shown in Figure 5-5C. The grey intensity of the AT is 24 and this value coincides with the start of an increase in the slope of the frequency curve towards the grain peak. To the left of the AT, the pore portion does not peak but flattens until the AT is reached indicating that the greyscale values associated with the pore space are generally of equal amounts.

Although there is an attempt to choose the AT at the boundary between pore and grain greyscale peaks, there is sometimes significant uncertainty is the classification of voxels whose greyscale value are close to the threshold value (Verges *et al.*, 2011). This can severely misrepresent the pore and grain space where for example, voxels which might belong to a pore might be incorrectly assigned to the grain mass. To combat this uncertainty, the threshold can also be selected using an interactive approach (termed *Interactive Thresholding*) which allows the user to control the choice of threshold based on visual measurements. An interactive threshold is entirely subjective based on the users' perception of the pore space and has been used by many researchers to characterise reservoir material (Verges *et al.*, 2011).

The choice of threshold is of paramount importance when characterising the pore space as an '*incorrect*' value has the potential to reduce or amplify pore space as well as blur, terminate or connect pore spaces which may not necessarily exist (Taud *et*

al., 2005). This can result in significant variations in porosity and other derived properties with only very small changes in the threshold parameter (Sheppard *et al.*, 2004).

To resist this effect and to examine how realistic changes in the threshold value might affect the pore space measurements, the automatic threshold value (software-suggested value based on the valley-emphasis histogram method) was first chosen.

To examine the influence of a user's subjective perception of the pore space, interactive thresholding was then used to study how a ±5% and ±10% change in the automatic threshold value affected the pore characterisation process. A maximum ±10% change was selected on the basis that sensitivities larger than ±10% would be discarded as unrealistic threshold values given that there would be obvious disparities between the original unsegmented and the final segmented images. This is examined in greater detail in Section 5.3.2.

The ATs for the Berea and Bentheimer samples from the software were found to be at greyscale intensities of 66 and 24 respectively. The approximate greyscale values corresponding to a ±5% and ±10% change in these ATs are presented in Table 5-3 and Figures 5-4D and 5-5D respectively.

Table 5-3: Greyscale Values at ±5% and ±10% change in the AT

	Berea	Bentheimer
Greyscale Range:	100	50
Minimum Greyscale Value	30	5
Maximum Greyscale Value	130	55
Greyscale Value at:		
Automatic Threshold, AT	66	24
-10% of AT	60	22
-5% of AT	63	23
AT	66	24
+5% of AT	69	25
+10% of AT	72	26

A. Filtered Image before Automatic Thresholding at selected 2D Slice No.1000 in the x-y plane
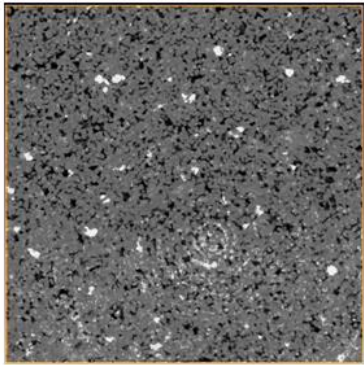
B. Image after Automatic Thresholding at selected 2D Slice No.1000 in the x-y plane
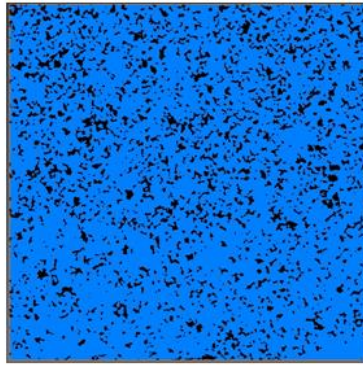
C. Histogram Approach to identify the Automatic Threshold (AT) value

BLACK COLOUR in segmented image

BLUE COLOUR in segmented image

PORES

Automatic Threshold (AT) Value occurs at the valley of the histogram at a greyscale value of 66

GRAINS/SOLID MASS
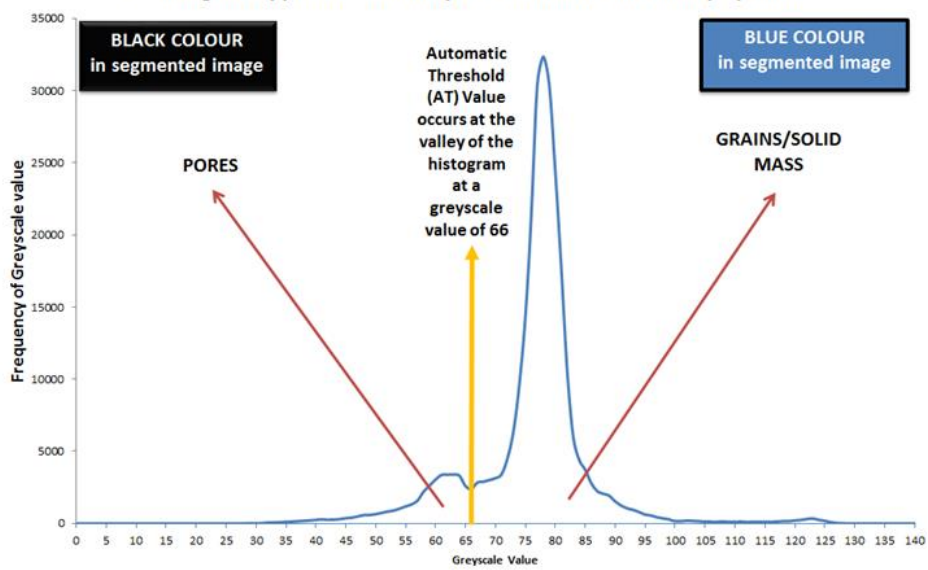
D. Identifying ± 5% and ±10% of the Automatic Threshold Value

Automatic Threshold (AT) Value occurs at the valley of the histogram at a greyscale value of 66

Threshold Value = 63
- 5% of AT Value (66)

Threshold Value = 69
+ 5% of AT Value (66)

Threshold Value = 60
- 10% of AT Value (66)

Threshold Value = 72
+ 10% of AT Value (66)
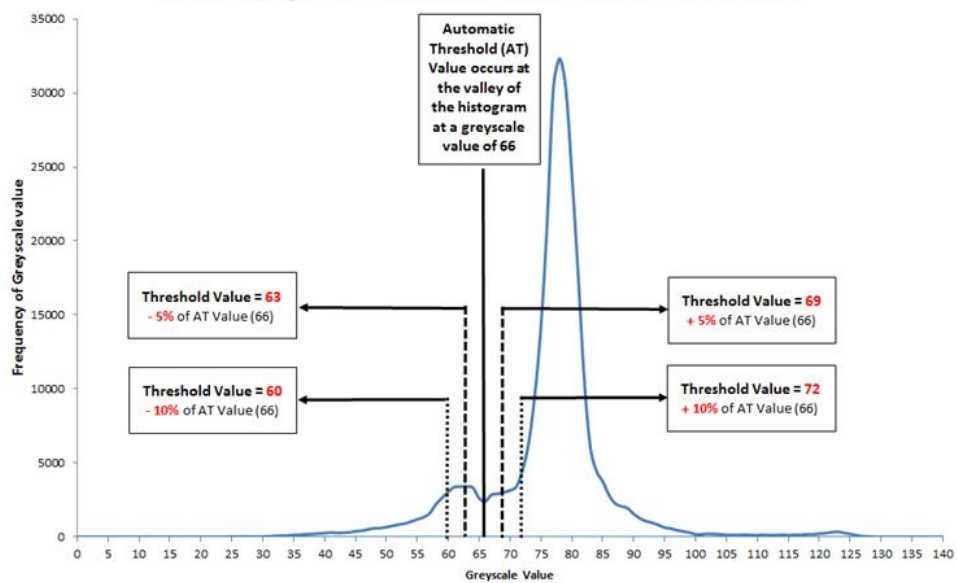
Figure 5-4: Threshold Identification and Segmentation Results at the MROI for the Berea Sample
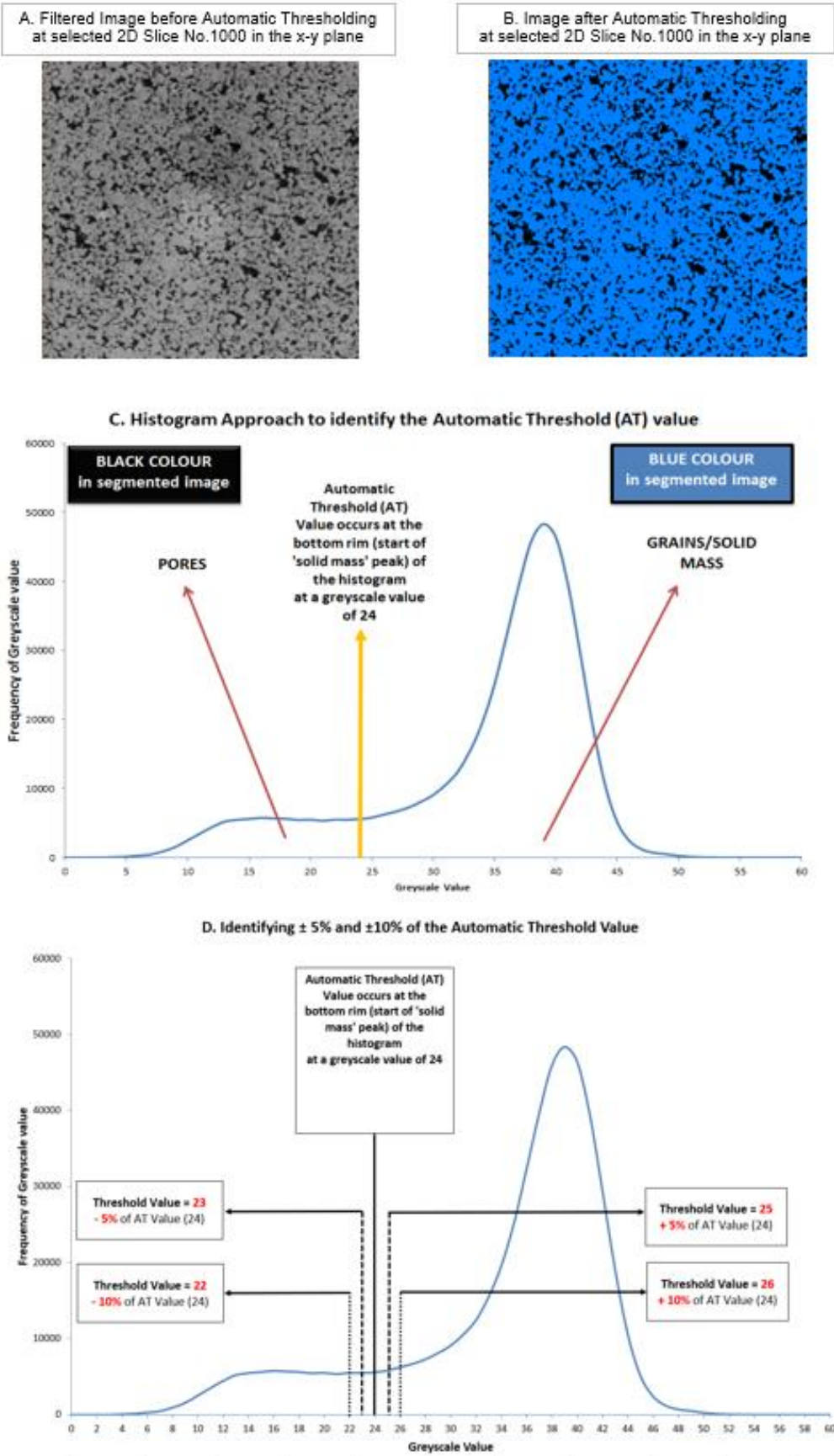
Figure 5-5: Threshold Identification and Segmentation Results at the MROI for the Bentheimer Sample
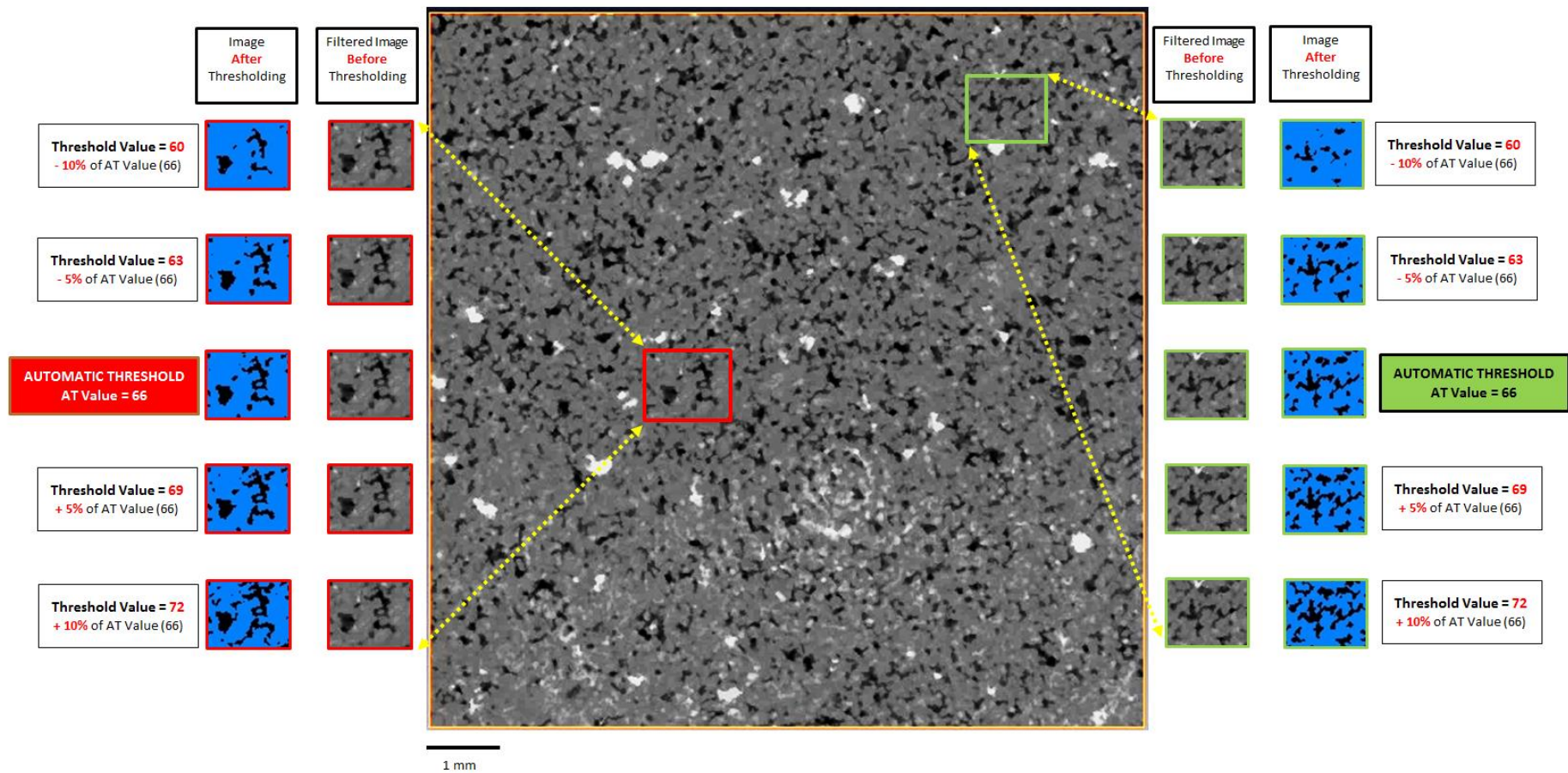
Figure 5-6: Testing the Sensitivity at ±5% and ±10% of the Automatic Threshold Value of the MROI for the Berea Sample at Slice 1000 in the x-y plane
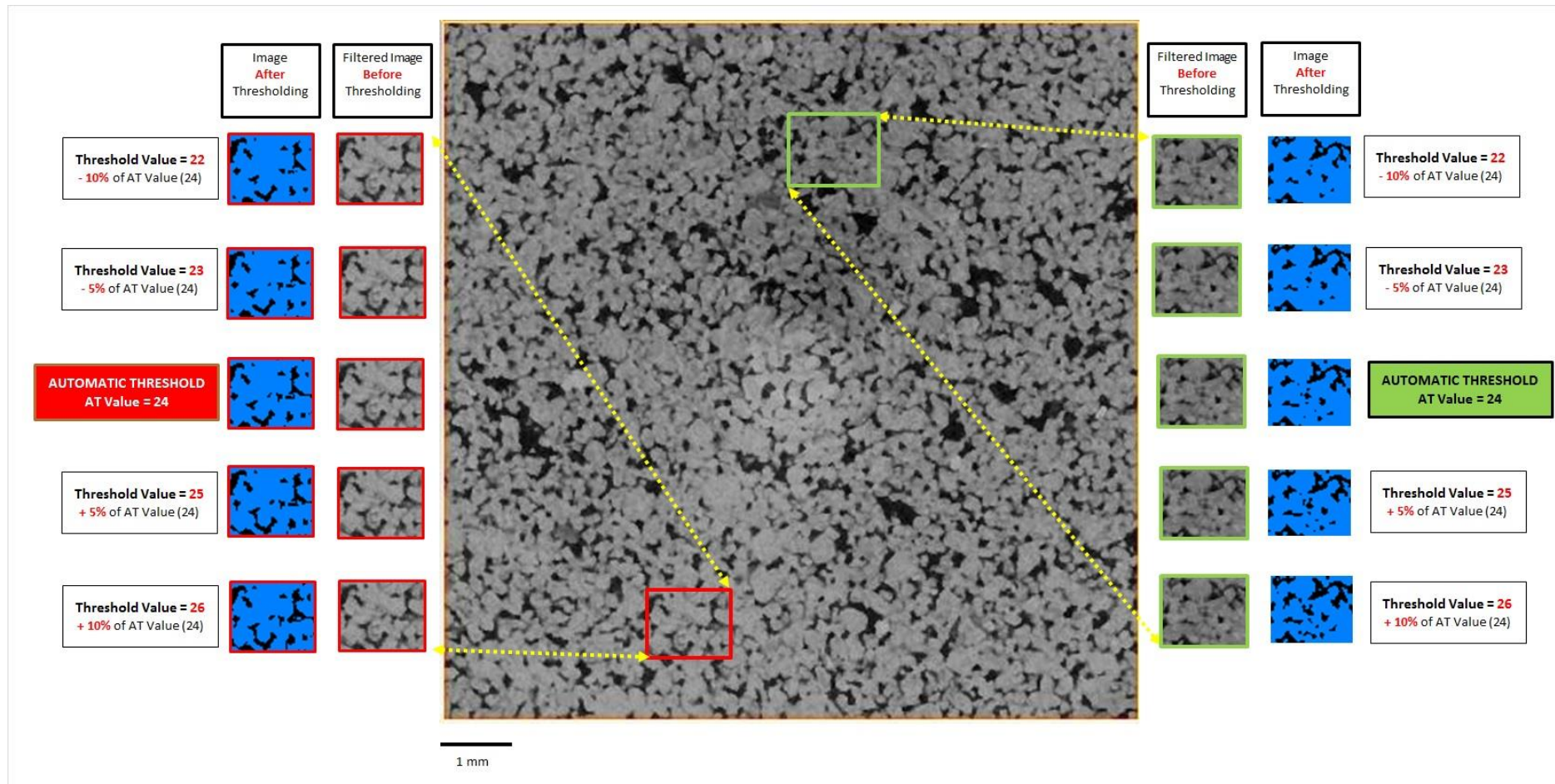
Figure 5-7: Testing the Sensitivity at ±5% and ±10% of the Automatic Threshold Value of the MROI for the Bentheimer Sample at Slice 1000 in the x-y plane

5.3.2 Testing the Sensitivity at ±5% and ±10% of the Automatic Threshold (AT)

Choosing the '*correct*' threshold is very important when characterising the pore space. A '*correct*' value is one which effectively represents the pore space and does not reduce or amplify pore space as well as blur, terminate or connect pore spaces which may not necessarily exist (Taud *et al.*, 2005). As significant variations in porosity and other derived properties can occur with only very small changes in the threshold parameter (Sheppard *et al.*, 2004), a part of this study examined the sensitivity of the pore measurements to changes (± 5% and ±10%) of the AT Value.

Figures 5-6 and 5-7 provide visual inspections of the pore space at ±5% and ±10% of the AT Value at selected sections of the filtered and segmented image. The diagrams show that as the threshold value is increased (to +5% and +10% of the AT), the pore space enlarges. This is because an increase in the greyscale value moves the pore peak of the greyscale histogram (Figures 5-4D and 5-5D) to the right, leading to a reduced grain/solid mass (or increased pore space). The opposite effect is therefore expected when the threshold value decreases (to -5% and -10% of the AT) due to more voxels being assigned to grain peak thereby increasing the grain/solid mass.

When compared to the original filtered (unsegmented) image for the Berea sample, Figure 5-6 shows that at a greyscale value of 60 (-10% of the AT), portions of the pore space are not adequately captured. Increasing the greyscale value to +10% of the AT, appeared to amplify the pore space unnecessarily and create pore linkages which are not inherent in the original image.

Similar findings were obtained with the Bentheimer sample where Figure 5-7 shows that as the greyscale value is decreased from the AT, the solid mass is overly amplified leading to portions of the pore space not being terminated. Increasing the greyscale value to +10% of the AT also increased the pore space excessively and created pore spaces which did not exist.

Based solely on visual inspection, the best segmentation appeared to come from the AT for both the Berea and Bentheimer samples where an excellent match between the pore features of both the original and segmented image existed.

5.3.3 Maximum Region of Interest (MROI) Porosity Evaluation

The Maximum Region of Interest (MROI) comprised a 2000 voxel cubic subsample of the initial 3D reconstructed volume which was subjected to segmentation via a global thresholding approach. Segmentation is used to differentiate the pore space from the solid mass. Once the pore space has been clearly identified, selected pore space attributes can be acquired in a straightforward manner. Porosity is one such attribute and is calculated by obtaining the volume of the pore space and dividing it by the bulk volume. To obtain the volume of the pore space, the '*volume3d*' command in the '*Quantification*' module of Avizo® Fire was used.

From the previous section, the automatic threshold (AT) was defined as the greyscale value corresponding to the valley of the greyscale frequency histogram. Users can further manipulate this threshold using interactive thresholding based on their perception of the pore space. A visual inspection of the effect of varying thresholds for ±5% and ±10% of the AT is shown in Figures 5-6 and 5-7.

In terms of a similar effect on porosities, the results of the porosities obtained when the threshold value is varied from ±5% and ±10% of the AT are presented in Table 5-4 and compared to the value obtained from the MICP testing.

Based on visual inspection, the best segmentation appeared to come from the AT for both the Berea and Bentheimer samples. Table 5-4 shows that the porosities obtained at the AT correspond agreeably to those attained from MICP testing with the AT porosities being greater for both samples. In terms of absolute porosity differences between the AT and MICP porosities, there is only a 1.4% and 0.9% difference (percentage changes of 9.3% and 4.7%) for Berea and Bentheimer respectively.

Although comparable, the AT porosities are higher than the MICP porosities but this is not unexpected given that a PNM approach process measures the total pore space (both connected and isolated) while MICP porosities are related to pores invaded by mercury (effective porosity). This could infer that approximately 1.4% and 0.9% of the total respective Berea and Bentheimer volumes represent either isolated pores which could not be accessed by the invading mercury during MICP testing or pores which were too small to be invaded due to a lack of sufficient pressure applied during MICP.

Table 5-4: Porosity Values at ±5% and ±10% change in the Automatic Threshold

	BEREA		BENTHEIMER	
	Porosity [%]	Percentage Change compared to AT Porosity [%]	Porosity [%]	Percentage Change compared to AT Porosity [%]
MICP Testing	13.6	-9.3	18.2	-4.7
Pore Network Modelling at:				
Automatic Threshold, AT	15.0		19.1	
-10% of AT	7.0	-53.3	16.7	-12.6
-5% of AT	12.4	-17.3	17.9	-6.3
AT	15.0	0	19.1	0
+5% of AT	18.2	21.3	20.4	6.8
+10% of AT	22.0	46.7	21.9	14.7

Table 5-4 also shows that the porosity decreases for both samples when threshold values are decreased (-10% and -5% of the AT) since portions of the pore space are not expected to be adequately captured due to an overestimation of the grain space. In the case of Berea, a -10% change in threshold value from the AT notably reduces the porosity by almost 50%. A -10% change in threshold is not as significant for the Bentheimer sample resulting in only a 12% percentage decrease in porosity.

Correspondingly, this effect is reversed when threshold values are increased (+5% and +10% of the AT) due to an exaggeration of the pore space. A -10% change in threshold value from the AT for Berea increases the porosity by 46% but this change is not as marked for Bentheimer, where a -10% change in threshold results in only a 14% percentage increase in porosity.

The above shows that small changes in the threshold value can significantly affect PNM derived porosities which in turn might have severe repercussions for other successively derived properties. This effect can be moderated when compared to other complementary methods e.g. using MICP and Porosimetry to regulate PNM porosity measurements. However, it becomes important when using stand-alone PNM techniques to ensure that any derived properties are tested to sensitivities in

the threshold and that these sensitivities are taken into account when deriving subsequent properties.

Table 5-4 also highlights that as the AT derived porosity value is smaller for Bentheimer than Berea, the percent changes in ±5% and ±10% of the AT (when compared to the AT) result in much smaller porosity changes for Bentheimer than Berea. This shows that the Bentheimer sample is more homogenous with respect to porosity than Berea. These results are also shown in Figure 5-8 and further demonstrate that the porosity increases are more pronounced for Berea than Bentheimer sample.
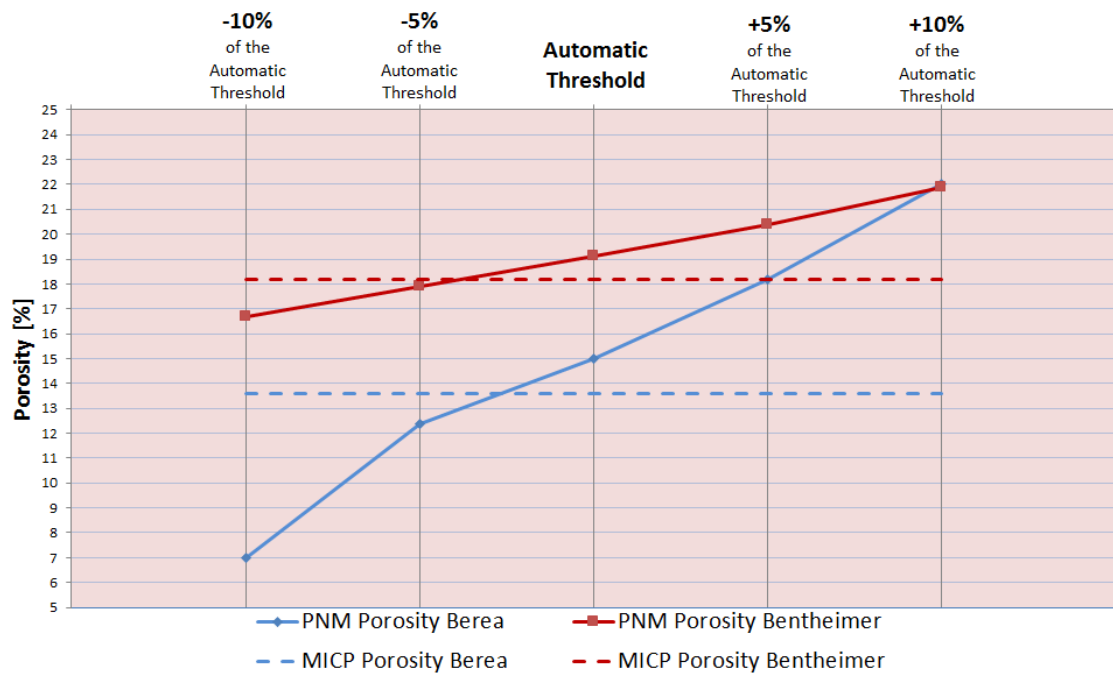
Figure 5-8: Testing the Sensitivity of Porosities at ±5% and ±10% of the AT for Berea and Bentheimer

5.3.4 3D Visualisation

The final pore and grain space arrangements at the Automatic Threshold (AT) are shown in Figure 5-9.

3D model visualisation of the Berea and Bentheimer samples showing (from left to right) a surface generation of skeletal material (A & D), a volume rendering of pore space (B & E) and an amalgamation of overall microstructure (C & F).

The diagrams illustrate a cube of length 200 voxels (~ 1 mm).
The total voume represented is approximately 1 mm^3.
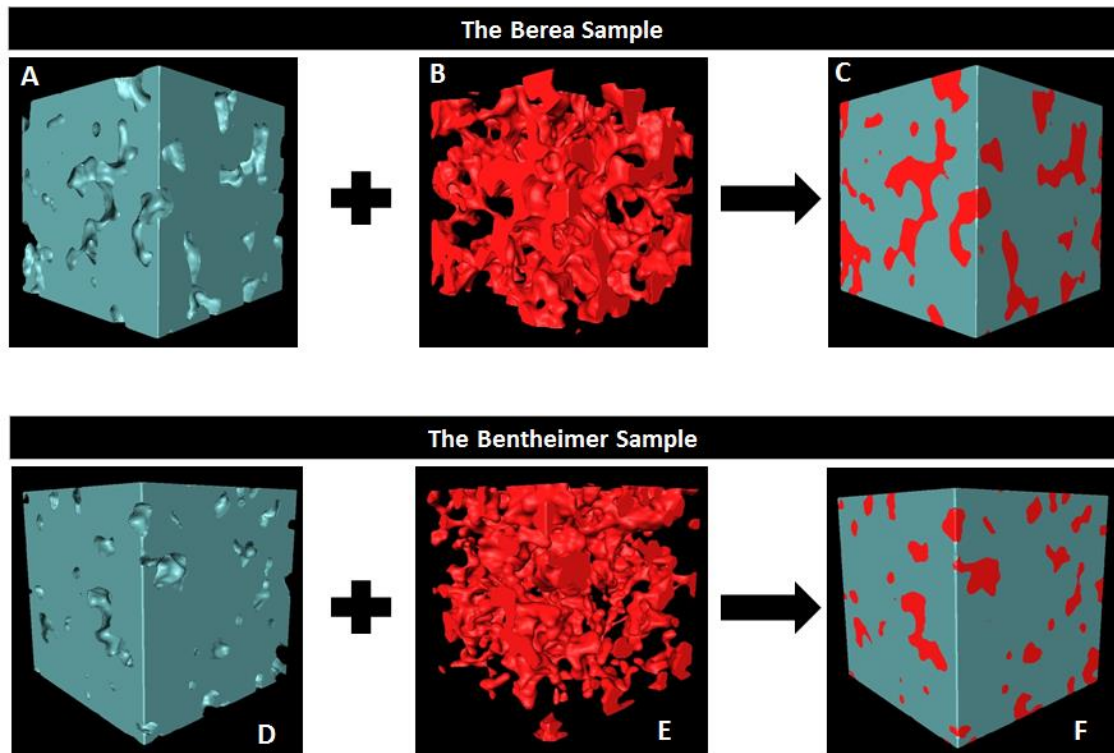
Figure 5-9: 3D Visualisation of the Pore and Grain Space Arrangements for Berea and Bentheimer

5.3.5 Representative Elementary Volume (REV) Determination

Once segmentation is complete, the next step is to examine whether the Maximum Region of Interest (MROI) subsampled is representative of the entire sample and to gauge whether any measurements made from the MROI robustly characterises the entire pore space. Depending upon the resolution and initial volumes involved, the MROI chosen might be large in extent so that a much smaller volume from within the MROI can adequately capture the sample's intrinsic attributes.

This small volume is termed the *Representative Elementary Volume* (REV) and is defined as the minimum volume of a sample at which the sample's inherent features are sufficiently and statistically captured for a high confidence in the results (Gelb *et al.*, 2011).

Although the two volumes may coincide – in an ideal situation, the REV is less (and preferably very much less) than the MROI. However in some cases, the chosen MROI may not be sufficiently large enough and as such, the REV will lie outside the MROI as the volume studied is not large enough to capture the inherent attributes of the sample. In such cases, it is imperative to enlarge the MROI until the REV is encompassed.

The Maximum Region of Interest (MROI) comprised a 2000 voxel cubic subsample of the initial 3D reconstructed volume. The REV approach used in this project is outlined in Section 4.2.4 and involves selecting an initial cube of length 100 voxels (approximately 0.5 mm) as the first ROI from within the MROI at each of 27 possible starting positions. For each of these 27 orientations, 20 ROIs were generated - starting at a 100 voxel (~0.5 mm) cubic volume which was progressively increased by 100 voxels in each direction until the MROI (a 2000 voxel (~10 mm) cubic volume) was attained. This resulted in a total of 540 ROIs being generated and analysed for each sample.

5.3.5.1 ROI Porosity Evaluation at the Automatic Threshold (AT)

The ROI porosities at each orientation and at each incremental expansion for both samples were then calculated (Section 4.2.4 and Figure 4-7). These 540 results are presented graphically in Figures 5-10 and 5-11 for the Berea and Bentheimer samples.
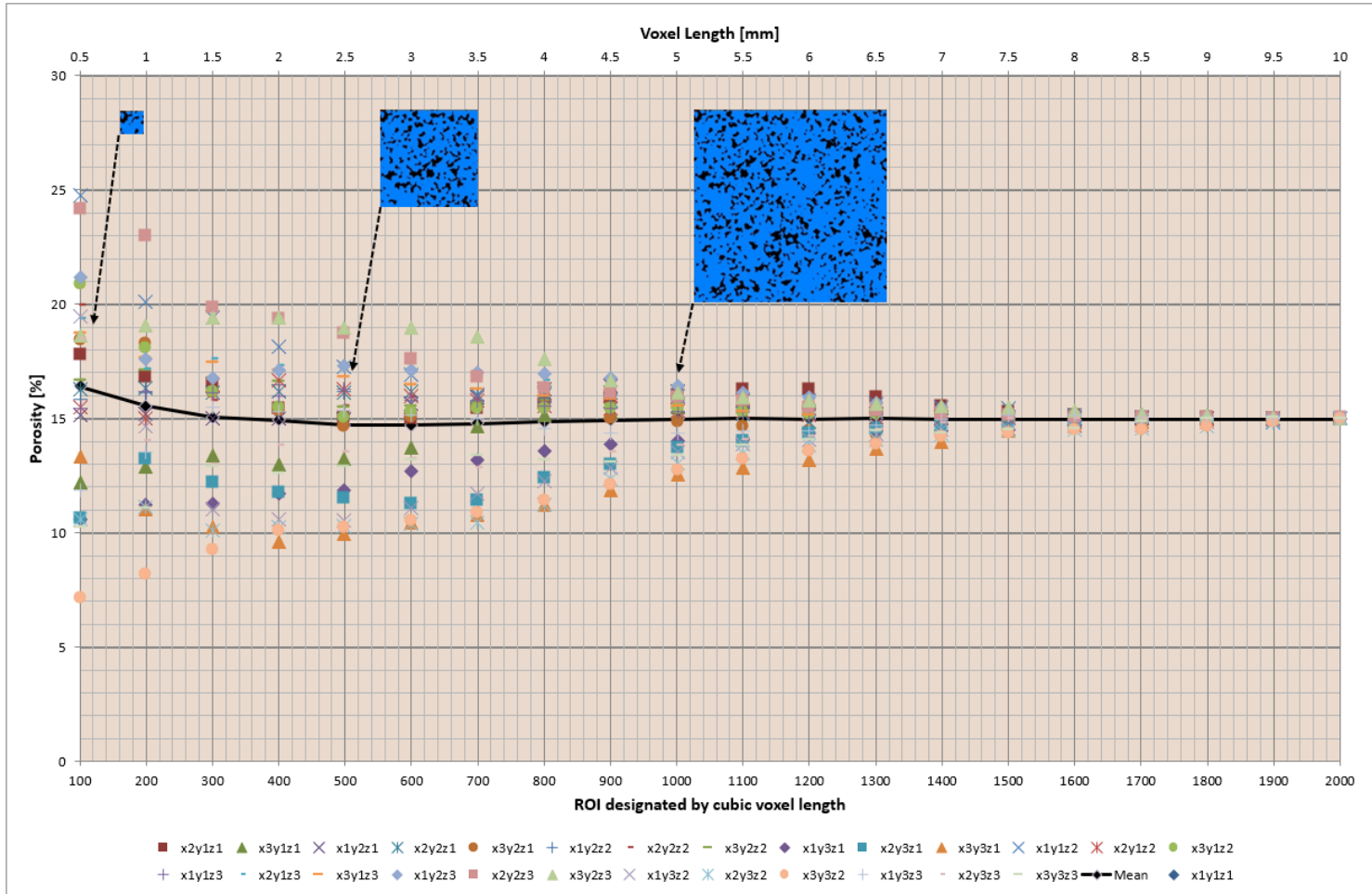
Figure 5-10: ROI Porosity Evaluation for the Berea Sample at the Automatic Threshold (AT)
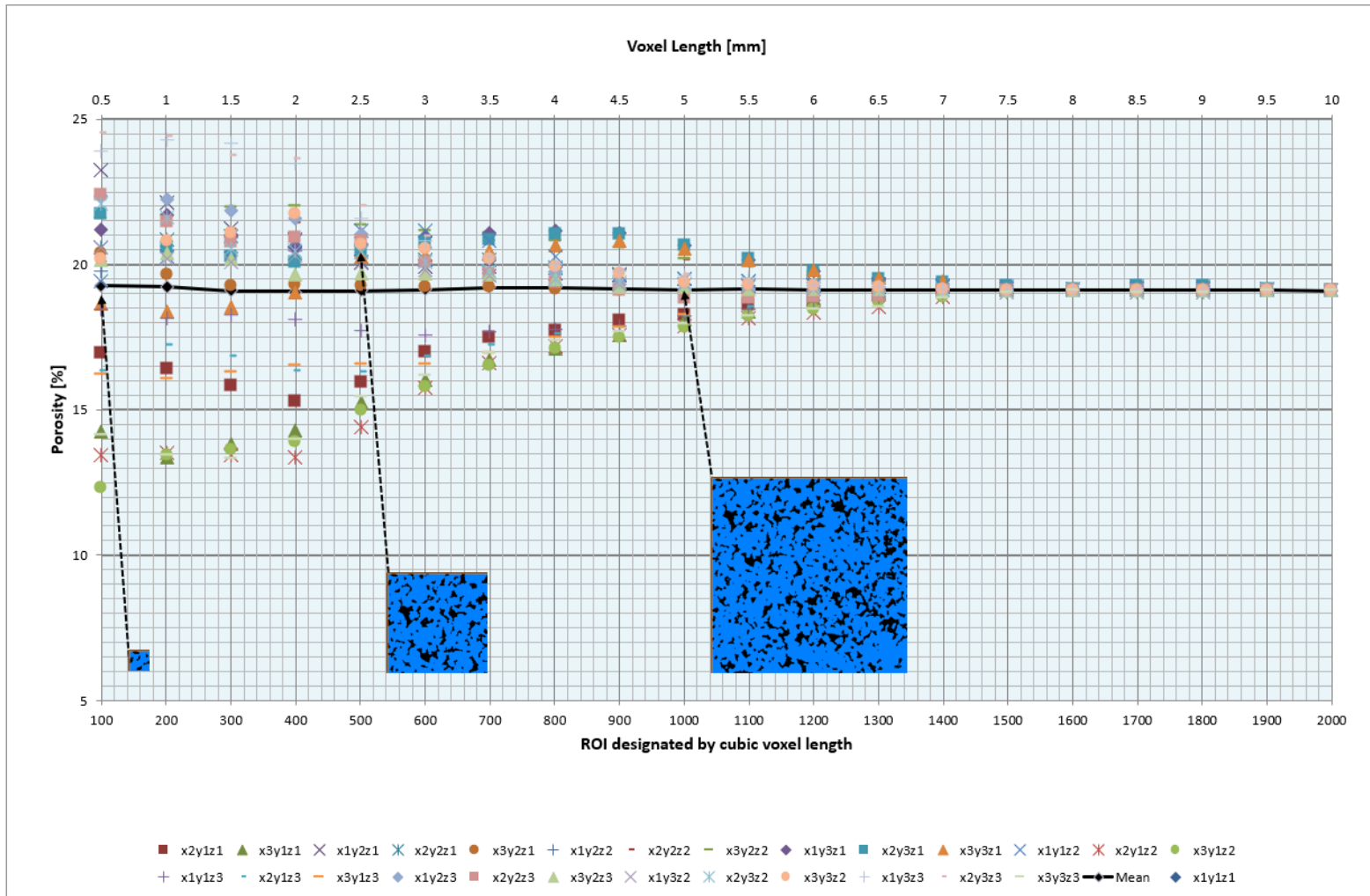
Figure 5-11: ROI Porosity Evaluation for the Bentheimer Sample at the Automatic Threshold (AT)

5.3.5.2 Obtaining the REV for the Berea and Bentheimer samples

Figures 5-10 and 5-11 show that within each ROI, porosity is randomly distributed but the variation in porosity becomes progressively smaller as the ROI increases and converges towards a consistent value at relatively large volumes (around 1500 voxel cube ~ 7.5 mm). This implies that the REV lies within the Maximum Region of Interest (MROI) subsampled and that no further increases in the MROI were needed.

Although the porosities attenuate and become consistent at progressive ROI volumes, Figures 5-10 and 5-11 do not provide a reliable means of identifying the REV. The REV can be defined as the minimum volume of a sample from which a given parameter becomes independent of the size of the sample (Bear and Bachmat, 1990). The identification of the REV is not generally presented robustly in the literature where in some cases, the REV has been identified based on an arbitrary visual '*minimal*' change of a given parameter from diagrams similar to the one presented in Figures 5-10 and 5-11 (Halisch, 2013).

This REV identification applied in this work builds upon the approach used by VandenBygaart and Protz (1999) who investigated the representative elementary area (REA) of selected soil samples using digitised thin-sectioned images. These authors proposed a methodology whereby the REA would be attained in the area where a selected parameter quantity (porosity) in three successive areas of measurements did not change ±10% by relative to the next progressive area of measurement.

The VandenBygaart and Protz approach seems to use an arbitrary amount of the change (± 10%) of a given parameter between consecutive areas to identify the REA but the results presented by VandenBygaart and Protz (1999) illustrate that a ±10% change often results in very minute changes of porosity in the range of 0.05 porosity units. Changes of 0.05 porosity units between successive areas can be considered to be very minimal and fundamentally, imply that the area and any successive areas have a uniform porosity.

This approach was extended for use in this work where porosity percent changes between consecutive ROI volumes were measured and the REV was identified when changes became minimal. Figures 5-12 and 5-13 illustrate these concepts.

Figure 5-12: Identifying the REV at the Automatic Threshold Value for the Berea Sample using a Percent Change Approach
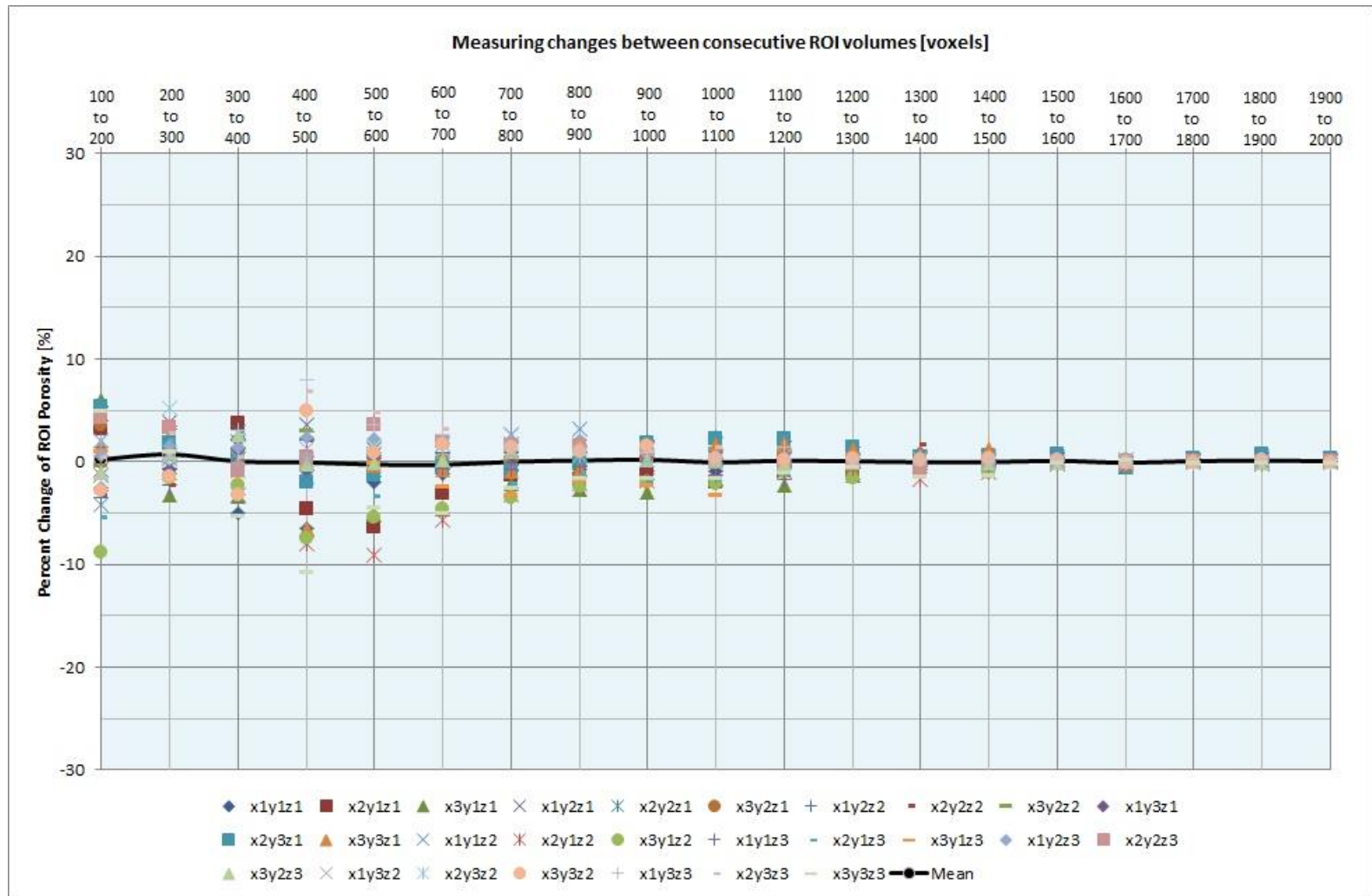
Figure 5-13: Identifying the REV at the Automatic Threshold Value for the Bentheimer Sample using a Percent Change Approach

Figure 5-12 shows that the maximum variation in porosity percent change (~ ±25%) occurs when the ROI is expanded from an initial 100 voxel volume to 200 voxel volume. It also shows that from an ROI of 300 voxels (~1.5 mm length cube) onwards, the changes in porosity for all 27 orientations lie within a ±10% range. Berea is generally considered to be homogenous in nature (Bera *et al.*, 2011; Peng *et al.*, 2012) and consequently starts to show uniform tendencies in porosity at very small sample volumes (~1.5 mm length cube). Although somewhat conservative, the REV for Berea in this work was identified when the percentage change in ROI porosity became consistent at a very small amount of ±5% (±0.05 porosity units). The REV for Berea was therefore taken to be at an ROI of 1000 voxels (~5 mm length cube).

The image resolution for the Berea and Bentheimer samples was 5 microns/voxel. At this resolution, an ROI volume of 1000 voxels is relatively small and allows for a relatively manageable computer processing time when further work is carried out to measure pore size (described in Section 5.3.7.1). Had the REV at a ±5% porosity percent change occurred at larger ROI volumes, this might have led to a much larger porosity percent change (up to maximum of ±10%) being chosen in order to improve processing times. Choosing a REV based on a larger porosity percent change means that the REV volumes will be reduced. The sensitivity of changing this amount is examined in Section 5.3.5.3.

Similar results for the Bentheimer sample show that from the onset (100 voxels ~ 0.5mm), the changes in porosity lie within a ±10% range. This is not entirely unexpected given that Figure 5-8 showed that the Bentheimer sample was more homogenous with respect to porosity than Berea. As with the Berea sample, the REV for Bentheimer was chosen when the changes in porosity became uniform at a very small amount of ±5% (±0.05 porosity units). The REV for Bentheimer was therefore taken to be at an ROI of 700 voxels (~3.2 mm length cube).

5.3.5.3 Testing the robustness of the REV

To determine the REV, 27 ROI orientations were examined as shown in Figure 4-7. Figures 5-10 to 5-13 show that at the Automatic Threshold (AT) value, the REV remains the same regardless of orientation. This is attributed to the homogeneity of the Berea and Bentheimer samples and implies that the materials are isotropic with respect to porosity. This may not necessarily be the case for other materials with show directional variations in porosity. It also becomes important to examine whether an REV based on porosity also holds true for other measured properties. This is further examined Section 5.3.6.3.

In addition to the above, it also became important to investigate how the REV changes when the threshold is varied. As an alternative to automatic thresholding, the threshold value can also be chosen using an interactive approach (termed *Interactive Thresholding*) which allows the user to control the choice of threshold based on visual measurements. An interactive threshold is entirely subjective based on the users' perception of the pore space and has been by many researchers to characterise reservoir material (Verges *et al.*, 2011). This method is often chosen when there is sometimes significant uncertainty is the classification of voxels whose greyscale value are close to the automatic threshold value.

Variations of ±5% and ±10% of the AT value were used to study the sensitivity of the REV to changing threshold parameters for both samples. For each variation in threshold, the same procedure used to determine the REV at the AT was followed. This involved:

  a. Determining the ROI porosities at each of the 27 orientations identified in Figure 4-7 and at each incremental expansion (540 ROIs were generated and analysed for variation leading to a total 2160 measurements for each sample);
  b. Obtaining the porosity percent change between successive ROI volume and choosing the REV accordingly

The results are presented in Figures 5-14 to 5-17 for both samples.
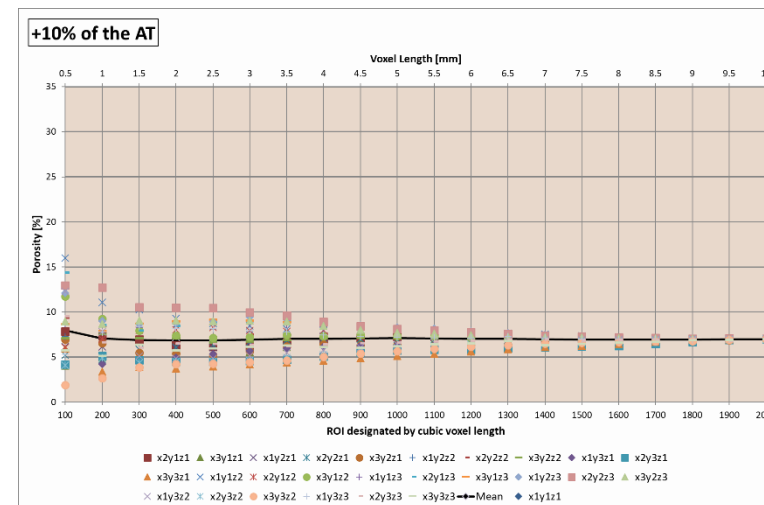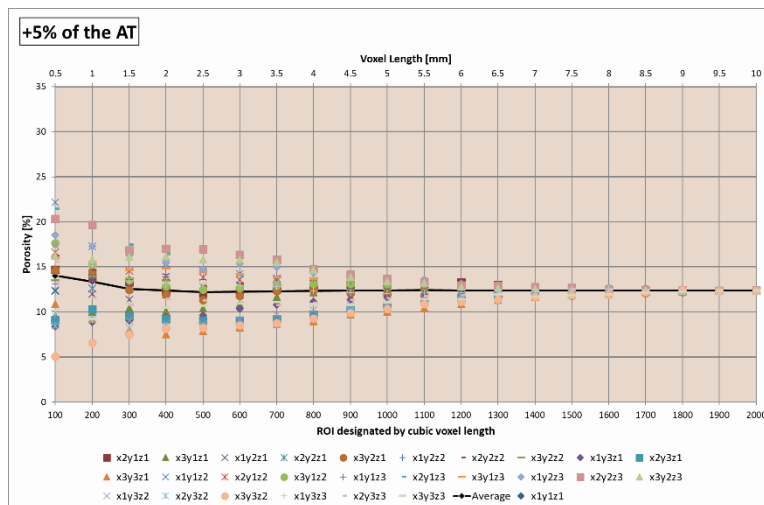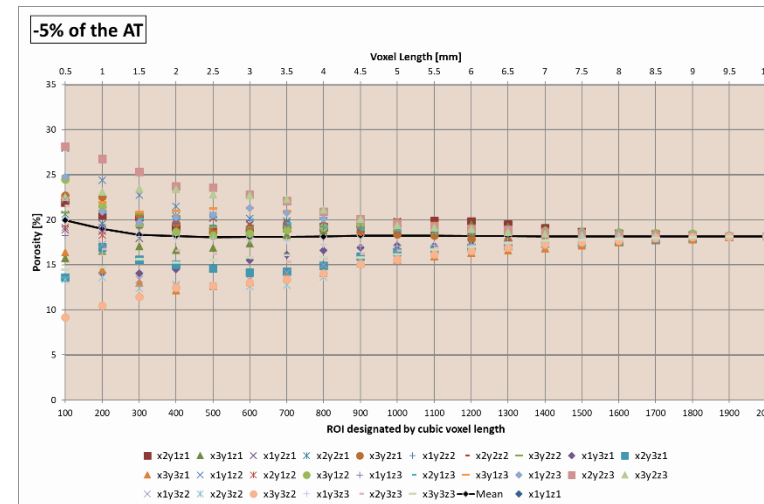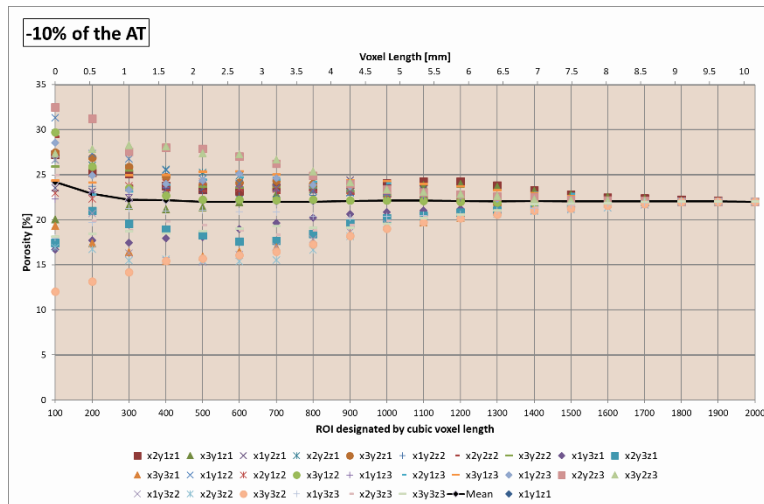
Figure 5-14: ROI Porosity Evaluation for the Berea Sample at varying threshold values (±5% and ±10% of Automatic Threshold)
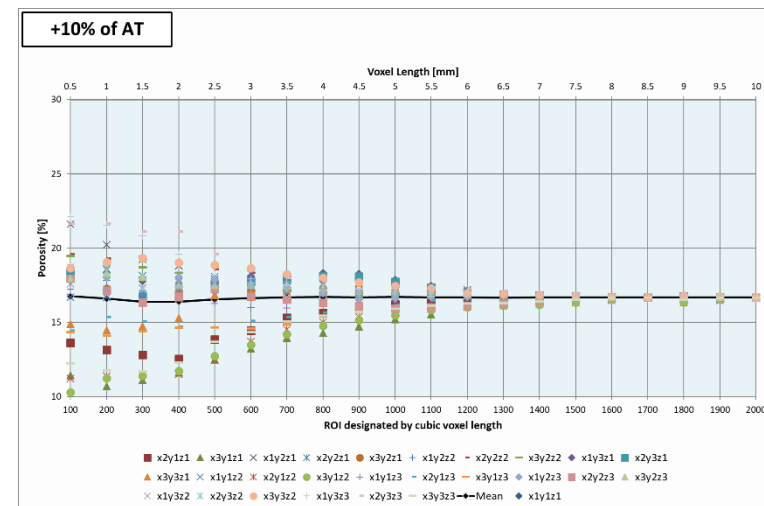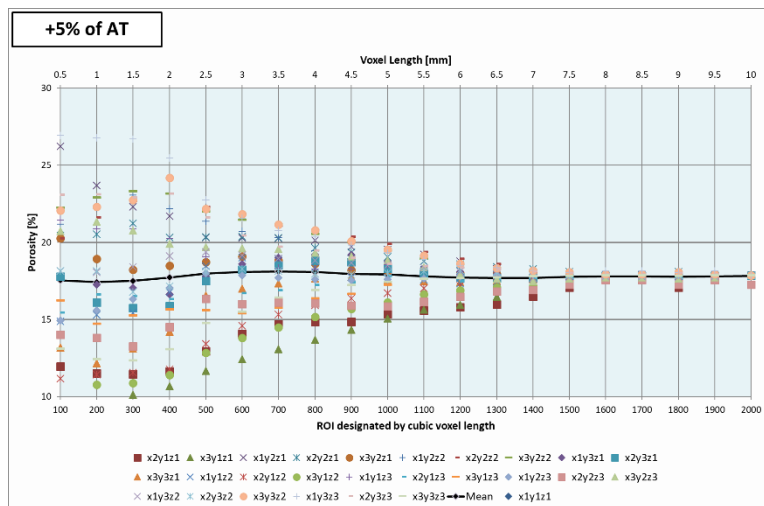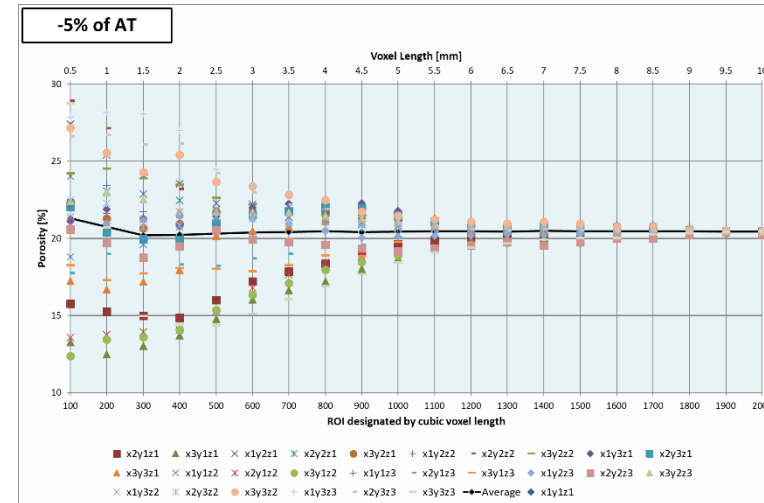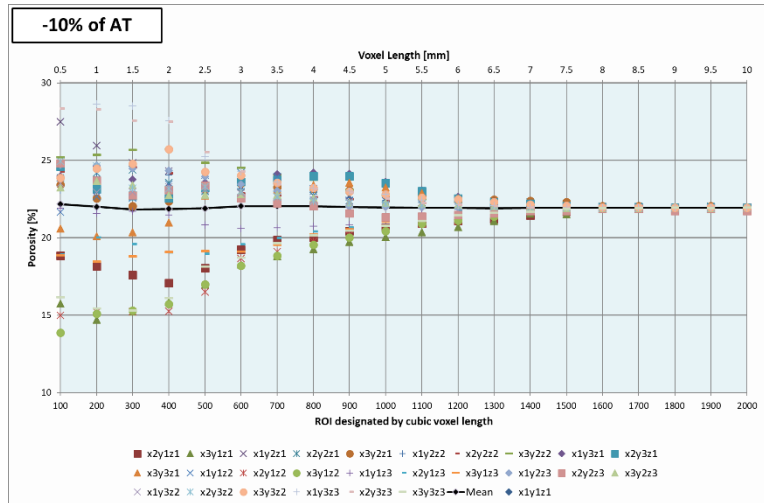
Figure 5-15: ROI Porosity Evaluation for the Bentheimer Sample at varying threshold values (±5% and ±10% of Automatic Threshold)
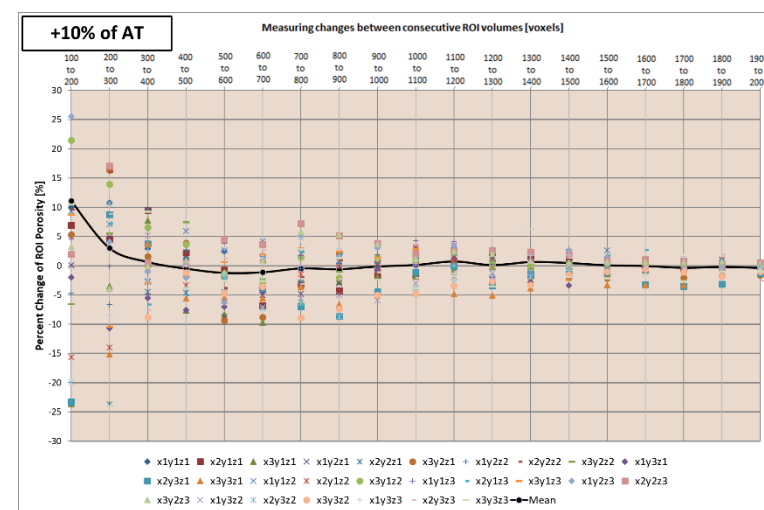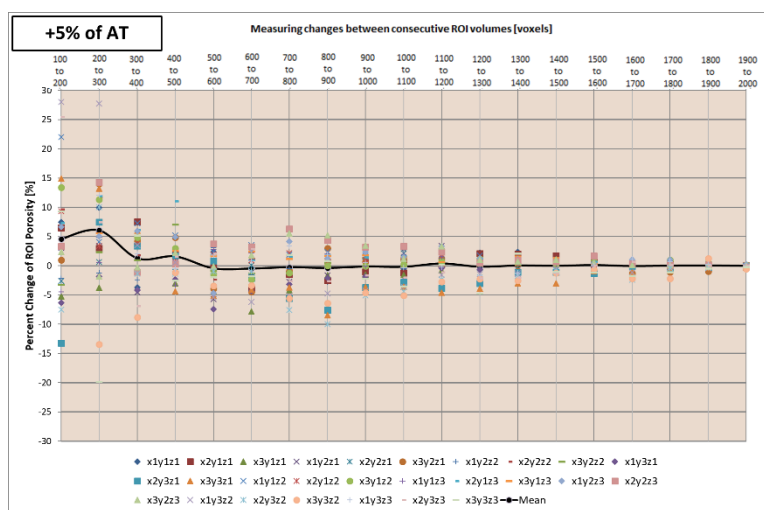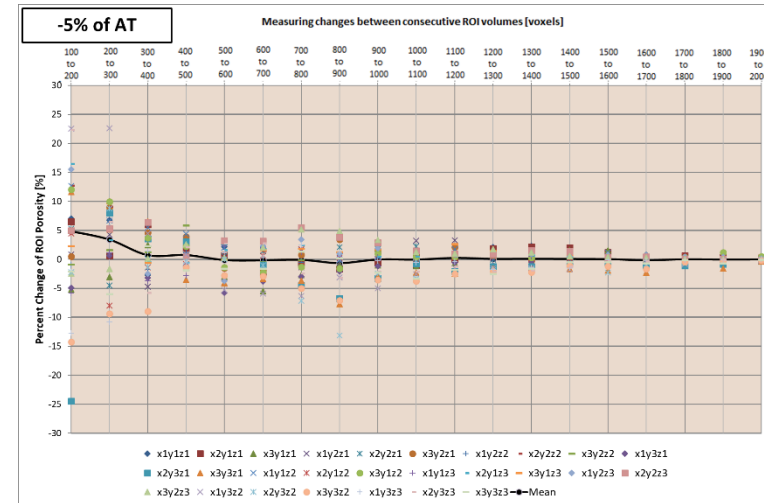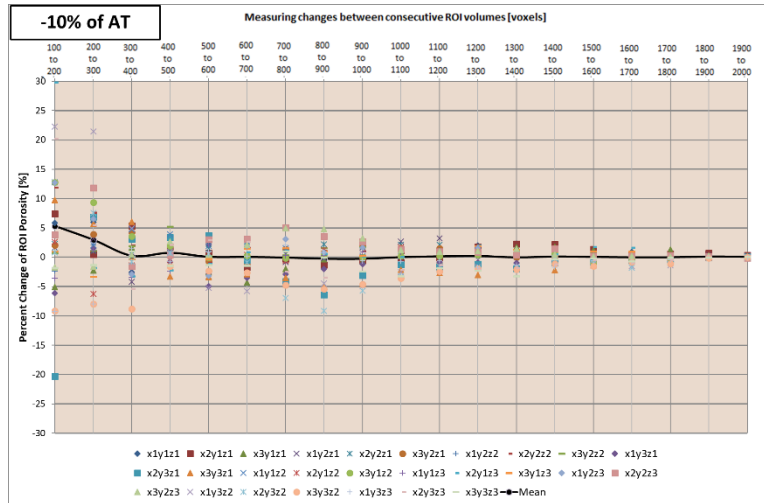
Figure 5-16: Identifying the REV at the Varying Threshold Values for the Berea Sample using a Percent Change Approach
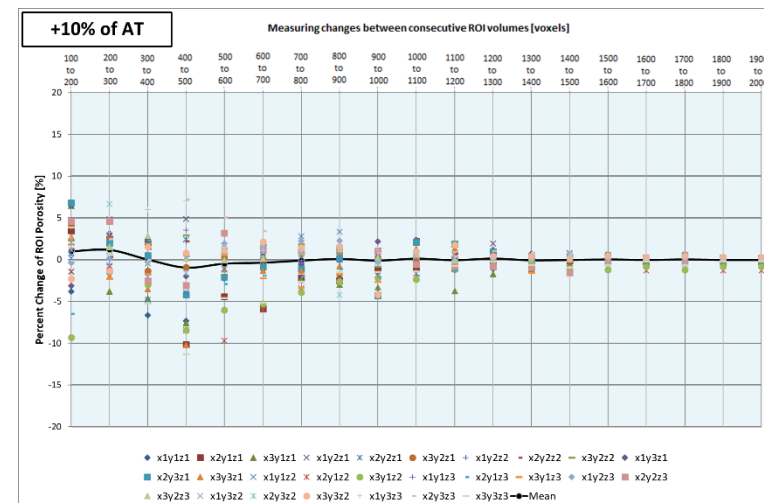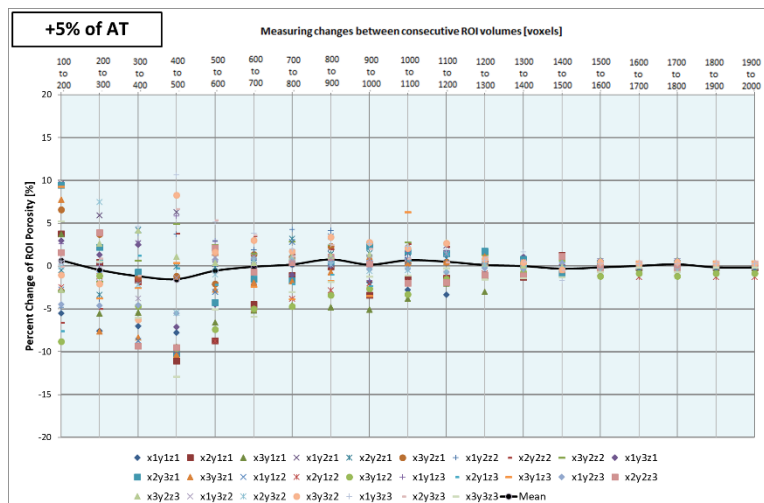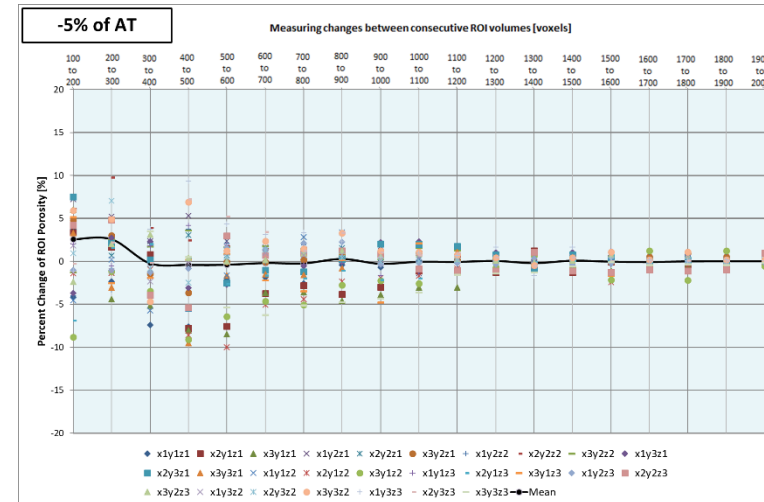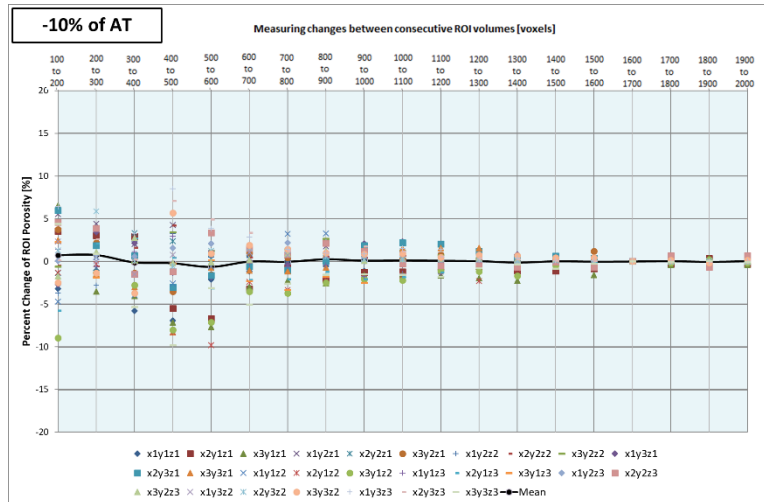
Figure 5-17: Identifying the REV at the Varying Threshold Values for the Bentheimer Sample using a Percent Change Approach

Table 5-4 shows the changes in porosity when the threshold values are varied from ±5% and ±10% of the AT. For the Berea sample, porosity values ranged from 7 – 22% when a ±5% and ±10% of the AT in threshold value was applied. Although porosity values change, Figures 5 -14 and 5-16 show that the REV for Berea remains fairly consistent at an ROI volume of 1000 voxels for all threshold values. The REV is chosen when the porosity percent change is ±5% between successive volumes. Similar results are obtained for the Bentheimer sample where the REV is obtained at around ROI volumes of 700 voxels (Figures 5-15 and 5-17).

This indicates that an REV based on porosity is independent of threshold value and as such, an interactive threshold (based entirely on the users' perception of the pore space) can adequately describe the pore space with respect to porosity. Although the porosity remains consistent once the REV has been attained, it does not imply that the pore size (radius) becomes uniform within the REV. There is no established correlation between porosity and pore size and this is not unexpected given that porosity is a measure of the volume (amount) of pores which exist and not of their size and distribution (Bennion and Bachu, 2006).

It therefore becomes important to examine whether an REV based on porosity also holds true for pore size and robustly provides a measure of pore size distribution. This is examined in further sections of this chapter.

5.3.6 Pore Network Extraction

Pore networks approximate the porous medium as interconnected system of pores and pore throats. The goal of pore network extraction is to derive a 3D representation of the internal structure of the porous medium from which a pore network can be identified. Once the pore network has been acquired, measurements on the pore space can then provide a distribution of the pore size.

Avizo® Fire uses a medial axis algorithm to extract the pore network from a 3D reconstructed mode. This algorithm works on the basis of producing a reduced representation of the pore space via the use of a thinning or burning algorithm (Dong and Blunt, 2009; Lindquist *et al.*, 1996). This produces a topological skeleton running through the centre of the pore network. Partitioning of the pore space uses local minima along branches where the minimum length of a fitted ellipsoid enclosing the pore is taken as the pore diameter.

The PSD using the Avizo® Fire software was obtained by using the '*AutoSkeleton*' command in the '*Image Morphology*' module to first extract the pore network and then using the '*Spatial Graph Statistics*' command in the '*Measure*' module to measure the pore radii.

5.3.6.1 Pore Size Distribution (PSD) Results

Figures 5-10 to 5-13 show that an REV based on porosity remains the same regardless of orientation at the Automatic Threshold (AT) value. An REV measured by porosity may not necessarily be the same as an REV based on pore size since there is no established correlation between porosity and pore size (Bennion and Bachu, 2006). To examine whether an REV based on porosity is also applicable to pore size studies, the pore network was extracted at each of the 27 REV orientations identified in Figure 4-7 for Berea and Bentheimer. The results are presented in the following figures.

Figures 5-18B and 5-19B show the cumulative pore size distribution (PSD) for the Berea and Bentheimer samples at all 27 orientations based on REVs of 1000 and 700 voxels respectively at the Automatic Threshold. The number of pores analysed at these REVs vary significantly. For the Berea sample, the number of pores analysed at each of the 27 orientations ranged from 84,600 to 135,650. Similar data for the Bentheimer give pore numbers which range from 28,550 to 68,250.

The PSDs for all 27 orientations appear to be statistically similarly. The r_{50} values (median) for the Berea sample ranges from 8.0 – 9.6 μm while 25% and 75% of the distribution have a radius of 5.4 – 6.6 μm (r_{25}) and 11.2 – 12.9 μm (r_{75}) respectively. Figure 5-19B show similar results for Bentheimer where the r_{50} values lie between 12.5 – 14.3 μm with 25% and 75% of the distribution having a radius of 9.8 – 11.3 μm (r_{25}) and 15.6 – 17.8 μm (r_{75}) respectively. The r_{25}, r_{50} and r_{75} values for both samples are all normally distributed. These results imply that an REV based on porosity statistically captures the inherent PSD sufficiently for a high confidence in the results.

A. The 3D visualisation of the Pore Network Model for Berea
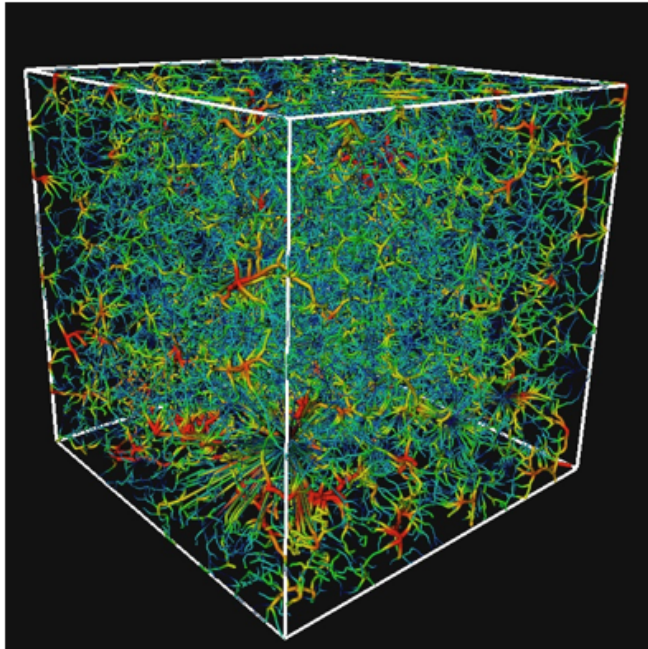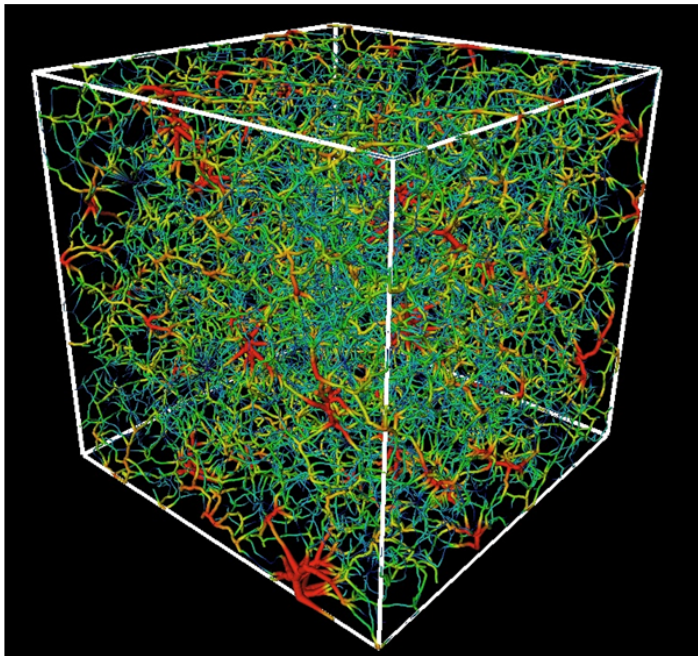
The sample shown is cubic of length 500 voxels (0.25 mm). The total voume is approximately 15.6 mm³.

Pore diameters are represented by tube thickness and a colour gradient. Red indicates larger pore sizes (15 - 30um diameter), blue represents the smaller pore sizes (<5um diameter) and colour grading between.

B. The cumulative Pore Size Distribution for Berea at 27 REV orientations

Figure 5-18: Extracting and Analysing the Pore Size Distribution (PSD) for Berea
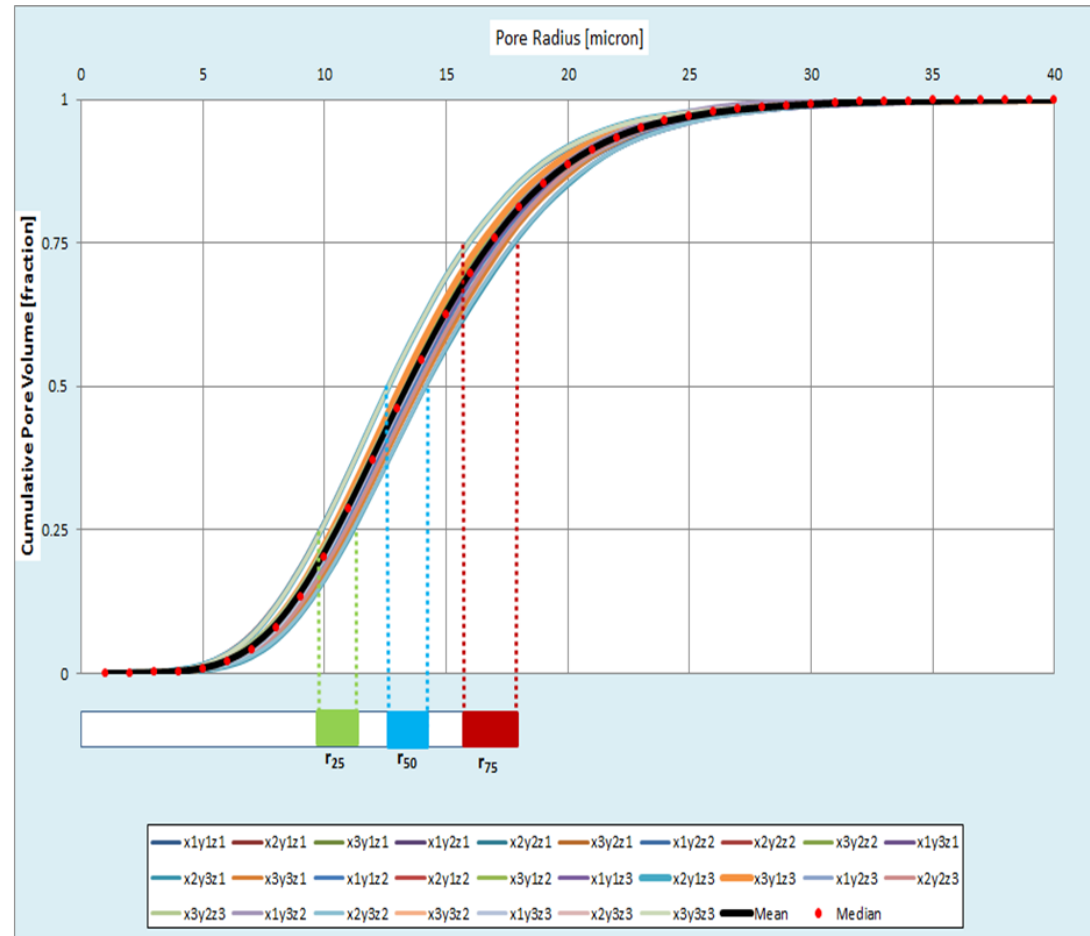
Figure 5-19: Extracting and Analysing the Pore Size Distribution (PSD) for Bentheimer

5.3.6.2 Statistical Analysis of the PSDs of the Berea and Bentheimer samples

Figures 5-18B and 5-19B show that consistent PSDs are obtained for both the Berea and Bentheimer samples regardless of the orientation when using an REV based on porosity. This consistency suggests that these 27 PSDs might be taken from a population which has a mean PSD that is comparable to the sample mean of 27 PSDs. This would indicate that the mean PSD (shown in black in Figures 5-18B and 5-19B) would effectively represent the PSDs of the Berea and Bentheimer samples resulting from the PNM process.

To provide suitable evidence to support this, the Friedman statistical test was used examine the statistical similarity of the 27 PSDs from the Berea and Bentheimer samples. The Friedman test is a non-parametric test that is widely used to compare two or more related samples in which the goal is to determine whether there are significant differences among the means of the samples (Eisinga *et al.*, 2017).

The test ranks the values of matched sets of data from low to high (Corder and Foreman, 2014); a matched set for the PSD data refers to the individual radii ranges comprising the cumulative distribution e.g. pores falling within 1 – 2 micron range for each of 27 PSDs is a matched data set. For the PSD data, there were 50 matched data sets corresponding to the pore size which ranged from 0 - 50 microns.

The Friedman test was suitable for this work because it could appropriately gauge the statistical similarity of the 27 PSDs by comparing their means, it allowed for an easy use of existing data formats given that the PSD data represented in Figures 5-18B and 5-19B were already in the form of blocks or matched sets and it could be used with large samples.

There are several test outputs which are usually reported when using the Friedman test (Corder and Foreman, 2014, p. 101). These include:
- the number of samples (k) which for this work was 27 given that there were 27 PSDs.
- the number of matched data sets (n) which was 50 for this work as there were 50 pore size matched data sets ranging from 0 - 50 microns.
- the Friedman test statistic (F_r) which is measure of the statistical similarity between the mean ranks. It is 0 when the mean ranks are exactly equal and becomes progressively larger as the difference among them increase.

- the degrees of freedom (df) associated with the test statistic which is equal to the number of samples compared minus 1. For 27 PSDs, the df is equal to k - 1 = 27 – 1 = 26 degrees of freedom.
- the p-value which is the significance level or probability of the sample differences occurring if the population distributions are equal.
- the alpha value (α) is the pre-chosen level of significance. Alpha values are frequently set to 0.05 (which is also the value used in this work) which indicates that there is a 95% probability that any observed statistical difference will be real and not due to chance (Corder and Foreman, 2014).

The p-value in relation to α is used to determine whether the samples are statistically similar; the F_r value provides a measure of the extent of that similarity. If the p-value < α, then there is a large statistical difference among the means of the 27 PSDs and suggests that the 27 PSDs do not come from the same population. For this work, a p-value < α will indicate that the mean PSD (shown in black in Figures 5-18B and 5-19B) will not effectively represent the PSDs of the Berea and Bentheimer samples from the PNM process.

IBM® SPSS version 25 was used to carry out the Friedman test and the results are shown in Table 5-5.

Table 5-5: The results of the Friedman test for the PSDs obtained at the 27 REV orientations for the Berea and Bentheimer samples

	Berea	Bentheimer
k	27	27
n	50	50
F_r	33.1	27.3
df	26	26
p-value	0.394	0.157
α	0.05	0.05

Table 5-5 shows the p-values for both the Berea and Bentheimer samples are greater than α, which indicate that all 27 PSDs are statistically similar and indicate that the mean PSDs (shown in black in Figures 5-18B and 5-19B) effectively represent the PSDs of the Berea and Bentheimer samples. These mean PSDs were therefore taken as the final PSD culminating from PNM process. These were then subjected

to further statistical analysis using the approaches outlined in Section 4.1.4. with the results shown in Table 5-6.

Table 5-6 shows that for the Berea sample, the mean and median of the PNM PSD are comparable and indicate that the data set is generally free of outliers. The median pore size is 8.7 µm and the pore radius has a narrow range of 0 – 40 µm. The sorting is 4.8 which is a relatively low value indicating that a majority of the pores are close to the 8.7 µm median and further highlights the narrowness of the pore size distribution.

Although the pore size is narrow, the kurtosis is approximately 1.1 indicating that the pore size is normally distributed having an even spread of pore sizes in the tails to the pore sizes that are centrally located in the distribution. This is confirmed by the pore classification where the PNM PSD shows that the medium is essentially mesoporous in nature being only comprised of 3% micropores (≤ 1 µm radii) and 1% macropores (>25 µm radii) respectively. This is highlighted by the skewness which is less than 0.13 indicating that the distribution is normally distributed symmetrical about the mean.

Similar results for the Bentheimer sample show that the mean and median of the PNM PSD are comparable being 14.3 and 13.3 µm respectively. The pore radius also has a narrow range of 0 – 50 µm. The sorting is 4.7 indicating that a majority of the pores are close to the median and further emphasises the narrowness of the pore size distribution. The kurtosis is approximately 1 indicating that the pore size is normally distributed which is highlighted by the skewness (0.18) indicating that the distribution is symmetrical about the mean. The PNM PSD also shows that the medium is essentially mesoporous in nature having negligible amount of both micropores (≤ 1 µm radii) and macropores (>25 µm radii).

The above results confirm that both materials are fairly homogenous and are comprised of a pore size distribution which is similar to that from the literature (Bera *et al.*, 2011; Peng *et al.*, 2012; Wilson, 2004) as well as to the MICP Testing carried out in Section 5.2. A more detailed comparison of how these results compare to the values quoted in the literature and to the results of the MICP Testing is provided in Chapter 7.

Table 5-6: Analysis of the PSDs of the Berea and Bentheimer samples from PNM

	Berea	Bentheimer
Average number of pores comprising PSD	110,520	55,230
r_5	1.6	7.2
r_{16}	4.5	9.3
r_{25}	5.8	10.5
r_{50}	8.7	13.3
r_{75}	11.9	16.8
r_{84}	13.8	18.6
r_{95}	18	22.8
Statistical Measures:		
Pore Size Range [μm]	0 - 40	0 - 50
Median (r_{50}) [μm]	8.7	13.3
Mean (r_m) [μm]	9.6	14.3
Pore Sorting (S_p)	4.8	4.7
Skewness (Sk_p)	0.13	0.18
Kurtosis (K_p)	1.1	1.0
Pore Classification:		
Micropore (≤ 1 μm) [%]	3	0
Mesopore (1 < r ≤ 25 μm) [%]	96	97
Macropore (> 25 μm) [%]	1	3
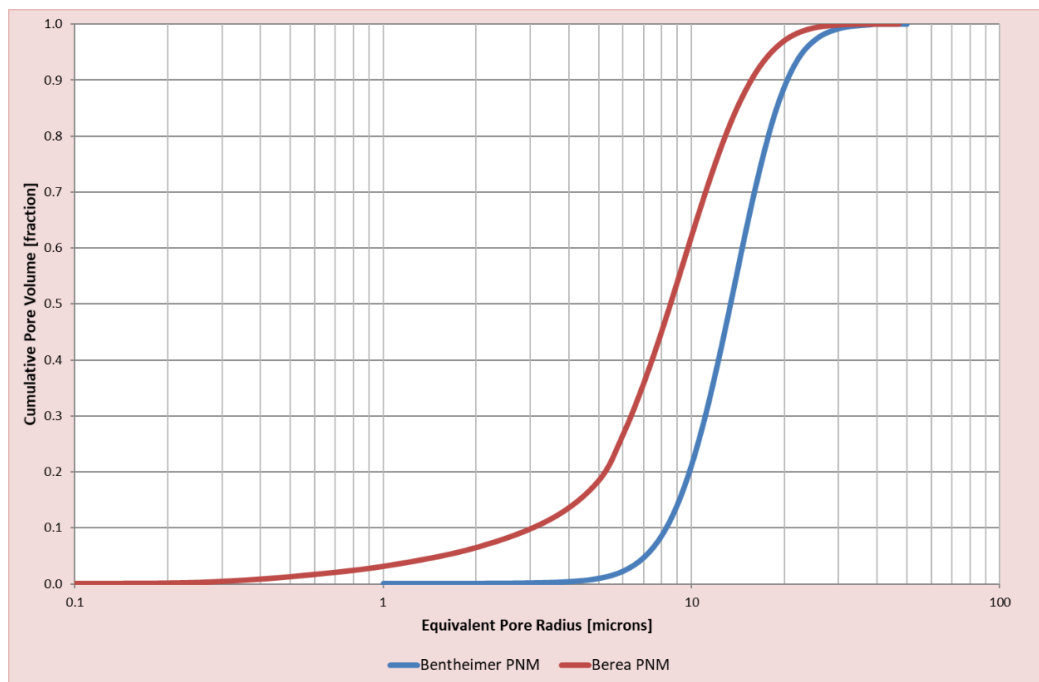
Figure 5-20: Cumulative PSDs of the Berea and Bentheimer samples from PNM

5.3.6.3 Testing the Sensitivity of the PSD to changes in the Threshold Value

The PNM PSD derived above was obtained from analysis on the REV at the Automatic Threshold (AT) value. Based on visual perceptions of the pore space, users may instead choose an interactive threshold to partition the pore space. Previous sections of this chapter have investigated the effect of changing the threshold value by ±5% and ±10% of the AT value when determining the REV and have shown that the REV remains constant regardless of threshold value.

At this point, it becomes useful to also gauge how the PSD is affected by changes in the threshold value. To do this, REV threshold values were varied at ±5% and ±10% of the AT value with PSDs being obtained at each of the 27 orientations outlined in Figure 4-7B. The mean of these 27 PSDs was then obtained and compared to the PSD obtained from Automatic Thresholding. This resulted in a total of 108 pore network extractions being carried out for each sample from which the mean PSDs related to ±5% and ±10% of the AT value were obtained. The results are shown in Figures 5-21 and 5-22.

Statistical analysis of the PSDs is provided in Tables 5-7 and 5-8 for both samples. The kurtosis and skewness variables for all PSDs show that the distributions are normal in nature with the pore sorting (ranging from 4.5 to 5) indicating that the data points tend to be close to the mean which is characteristic of narrow pore size distributions. Across all PSDs, r_{50} values for the Berea and Bentheimer sample range between 7.8 - 9.7 µm and 13.2 – 14.1 µm respectively which correlate well with the results of the MICP testing.

It is useful to recall that as the threshold value is decreased (at -5% and -10% of the AT), the pore space enlarges leading to an increase in porosity (Table 5-4). This is because a decrease in the threshold value assigns more greyscale voxels to the pore space leading to a reduced grain/solid mass (or increased pore space). The opposite effect is therefore expected when the threshold value increases (at +5% and +10% of the AT).

Although the porosity increases with increasing threshold value, there is no established correlation between porosity and pore size. As such, increases in threshold value (which are positively correlated to porosity) do not show a defined relationship for PSD as illustrated in Figures 5-21 and 5-22. This is not unexpected

119

given that porosity is a measure of the pore volumes which exist and not of their size and distribution (Bennion and Bachu, 2006).

These results also show that the pore size changes only marginally with increases in threshold value. This implies that although significant increases in porosity exist with decreasing threshold value, a -5% and -10% of the AT changes the PSD minimally and suggests that within these limits, the choice of threshold value become unimportant. This assumption may not necessarily hold true for volumes smaller than the REV.

Table 5-7: Testing the Sensitivity of the PSD for the Berea sample at varying threshold values (±5% and ±10% of Automatic Threshold)

	-10% of AT	-5% of AT	AT	+5% of AT	+10% of AT
Porosity [%] from Pore Network Modelling	22.0	18.2	15.0	12.4	7.0
Statistical Measures:					
Pore Size Range [µm]	0 - 40	0 - 40	0 - 40	0 - 40	0 - 40
Median (r_{50}) [µm]	8.2	9.7	8.7	9.1	7.8
Mean (r_m) [µm]	9.3	11	9.6	10.2	8.3
Pore Sorting (S_p)	4.8	5.0	4.8	5.0	4.5
Skewness (Sk_p)	0.14	0.19	0.13	0.18	0.10
Kurtosis (K_p)	1.11	1.11	1.1	1.11	1.10

Table 5-8: Testing the Sensitivity of the PSD for the Bentheimer sample at varying threshold values (±5% and ±10% of Automatic Threshold)

	-10% of AT	-5% of AT	AT	+5% of AT	+10% of AT
Porosity [%] from Pore Network Modelling	21.9	20.4	19.1	17.9	16.7
Statistical Measures:					
Pore Size Range [µm]	0 - 40	0 - 50	0 - 50	0 - 40	0 - 40
Median (r_{50}) [µm]	14.6	14.1	13.3	14.7	13.5
Mean (r_m) [µm]	13.8	13.2	14.3	14.1	12.7
Pore Sorting (S_p)	4.6	4.7	4.7	4.5	4.4
Skewness (Sk_p)	0.15	0.16	0.18	0.15	0.14
Kurtosis (K_p)	0.99	1.04	1.0	1.0	1.04
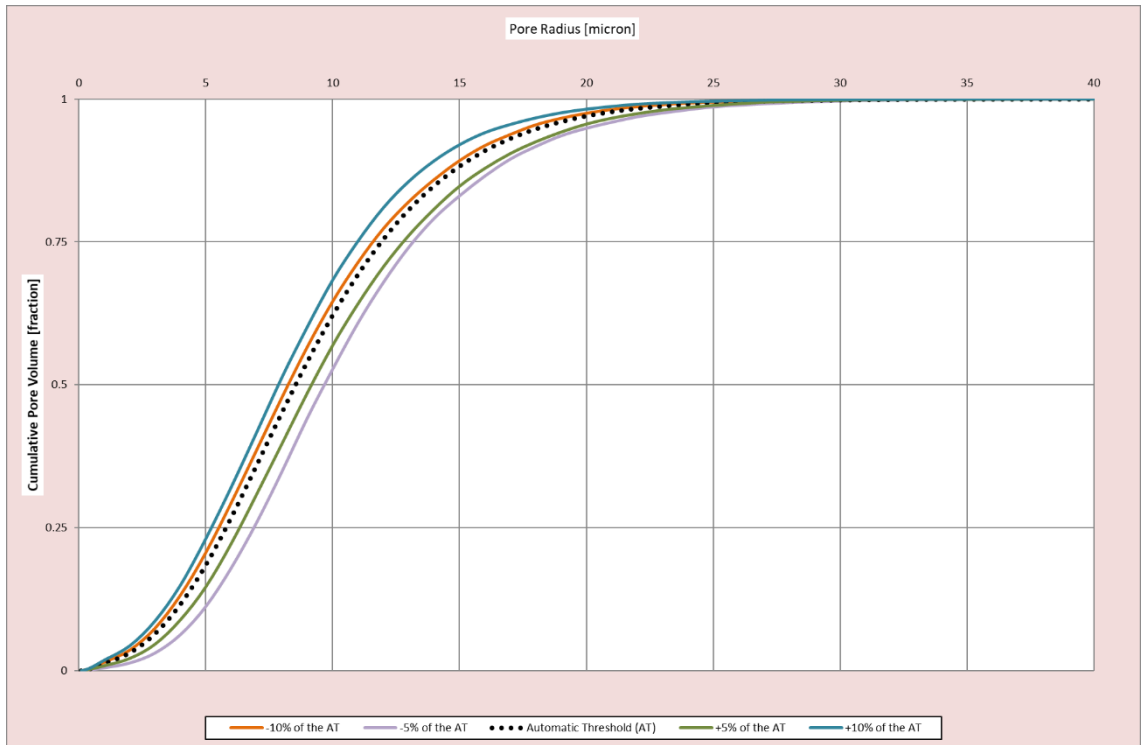
Figure 5-21: PSD Analysis for the Berea Sample at varying threshold values
(±5% and ±10% of Automatic Threshold)
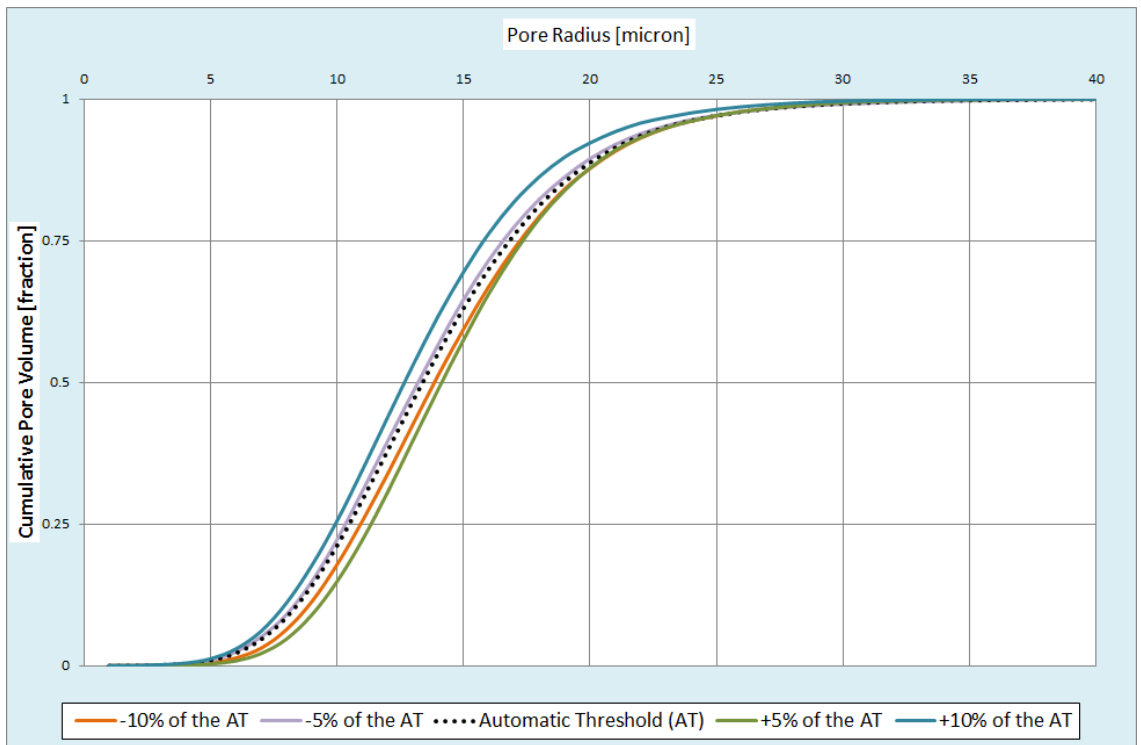
Figure 5-22: PSD Analysis for the Bentheimer Sample at varying threshold values
(±5% and ±10% of Automatic Threshold)

5.3.7 Revising the Pore Network Modelling Approach

Figure 4-2 outlines the general methodology of the PNM approach used in this work which has been applied to selected sandstone samples. The major stages include Image Acquisition, 3D Reconstruction, REV Determination and Pore Size Distribution (PSD) Analysis.

Following the Image Acquisition stage, Table 5-9 shows the broad steps within each stage which were undertaken during this work to complete the remaining 3 stages of 3D Reconstruction, REV Determination and PSD Analysis. These broad steps included investigating selected PNM elements related to the concepts of segmentation, threshold value and REV to further understand their influence on determining robust and representative measures of porosity and PSD.

This resulted in a comprehensive PNM procedure which is provided in Table 5-9. Several key findings which arise from selected steps are also shown in Table 5-9; these can potentially serve to simplify the overall method which is examined in the following sections.

Table 5-9: The PNM steps used to investigate porosity and PSD in this work

Step	Description	Key Findings
1	Subsample at either 2000 voxels or 20% of the total scanned volume (whichever is larger) to produce the Maximum Region of Interest (MROI) as shown in Figure 4-4.	
2	Filter if necessary using an appropriate filtering process.	
3	Segment using a Thresholding Approach where an Automatic Threshold (AT) value based on the valley-emphasis method is chosen as the default as shown in Figures 5-4 and 5-5.	
4	Visually compare the segmented and original images as shown in Figures 5-6 and 5-7. If the segmented and original images visually compare well (based on user's perception), then proceed to Step 5. Else vary the threshold value (Interactive Thresholding) until a favourable comparison is obtained and then proceed to Step 5.	

5	Incrementally section the volume in 100 voxels up to the MROI at the 27 orientations as shown in Figure 4-7.	
6	Determine and plot the porosity at each ROI increment for each orientation as shown in Figures 5-10 and 5-11.	The porosity is randomly distributed across each ROI
7	Calculate and plot the percent porosity change at each ROI increment for each orientation as shown in Figures 5-12 and 5-13.	The variation in porosity attenuates as the ROI increases and converges towards the MROI's porosity
8	Choose the REV where the percent porosity change is consistent at ±5% for successive ROIs (Figures 5-13 and 5-14).	Within a ±5% percent porosity change, the REV should remain the same regardless of orientation for homogeneous samples.
9	Due to the subjective nature of choosing the threshold value, test the sensitivity of the REV to changes in threshold value by varying the threshold value by ±5% and ±10% of the value chosen in Step 4 as shown in Figures 5-14 to 5-17.	The REV should remain the same regardless of threshold chosen.
10	Extract the pore network and obtain the pore size distribution for the REV at each of the 27 orientations (outlined in Figure 4-7) as shown in Figures 5-18 and 5-19.	
11	Use an appropriate statistical test (Friedman test) to determine the statistical similarity of the 27 PSDs obtained at each orientation. Ideally these 27 PSDs should be statistically similar which will lend support of choosing the mean PSD from all 27 PSD orientations to represent the PSD for the sample. If the results show that the 27 PSDs are statistically different, the mean PSD from the 27 PSDs can still be used but it will be important to note the level of statistical dissimilarity as this will impact the confidence of using the mean PSD.	The REV is commonly chosen based on porosity. Statistically similar PSDs will show that the PSD is also a rationale choice for REV determination.

12	Test the sensitivity of the PSD to changes in threshold value by varying the threshold value by ±5% and ±10% of the value chosen in Step 4 as shown in Figures 5-21 and 5-22.	The mean PSD at the threshold value chosen in Step 4 is statistically equivalent to the PSDs obtained when threshold values are changed by ±5% and ±10% (of the value chosen in Step 4).

Table 5-9: The PNM steps used to investigate porosity and PSD in this work

5.3.7.1 Work-flow and Processing Times

Table 5-9 provides a comprehensive procedure for obtaining both porosity and PSD using the PNM approach outlined in Figure 4-2. The consideration of several key findings show that it may be possible to simplify selected steps for homogeneous sandstone samples. This becomes particularly important given that for a PNM approach to be a viable means of pore characterisation, it should be relatively simple to perform, require low processing times and resources when compared to similar pore evaluation techniques (like MICP testing).

The processing times are related to computer processing speeds. Using an AMD FX-8120 eight-core processor with 3.1 GHz processing power and 32GB of RAM, Table 5-10 provides the details and average processing times incurred for one sample at each of the steps identified above. More advanced computers can reduce these times.

Table 5-10 shows that the average processing time for each sample is substantial and it becomes valuable to consider ways of reducing these times using the key findings outlined in Table 5-9. This is further discussed in the following section.

Table 5-10: The Average Processing Times for each step of the PNM Approach

	No. of Computations Involved	Average Processing Times [hr]
Step 1: Subsampling	1	0.2
Step 2: Filtering	1	2
Step 3: Segmentation via a Thresholding Approach	1	0.5
Step 4: Choosing the best threshold	1	0.2
Step 5: ROI Increment Sectioning	20 x 27 = 540	3
Step 6: Determine and plot ROI Porosity	20 x 27 = 540	15
Step 7: Plot porosity percent change vs ROI	20 x 27 = 540	5
Step 8: Choose REV at a ±5% porosity change	1	0.1
Step 9: Test the REV to changing threshold value Porosity Determination at a ±5% and ±10% threshold	4 x 20 x 27 =2160	25
Step 10: Pore Network Extraction at REV	27	15
Step 11: Statistical analysis on the median radii	27	2
Step 12: Test the PSD to changing threshold value PSD Determination at a ±5% and ±10% threshold	4 x 27 = 108	32
TOTAL		**~ 100**

5.3.7.2 A Condensed Recommended Practice for the Pore Network Modelling of homogeneous and heterogeneous sandstone samples

During this work, selected elements of the general PNM approach outlined in Figure 4-2 have been examined to answer specific questions relating to their influence on the robustness of porosity and PSD determination. These included:

1. How can the '*correct*' threshold value be robustly chosen?
2. Does the REV based on porosity remain the same regardless of its orientation and location within the sample?
3. How do changes in the threshold values affect the REV determination?
4. Does an REV based on porosity also hold true for pore size (PSD)? Does the REV based on PSD remain the same regardless of its orientation and location within the sample?
5. How sensitive is the PSD to changes in the threshold value?

These questions have arisen due to uncertainties regarding sample heterogeneity and threshold identification and investigating them resulted in a comprehensive

(although time-consuming) procedure for PNM as outlined in Table 5-9. A comprehensive approach which follows the steps in Table 5-9 is best when there are considerable uncertainties surrounding the heterogeneity and anisotropy of the pore space as well as the identification of an appropriate threshold value. These uncertainties can hinder the acquisition of representative pore measures leading to a low confidence in PNM results.

The Berea and Bentheimer sandstone samples used in this work have been found to be relatively homogeneous (which is particularly emphasised in Figures 5-10 to 5-13 and 5-18 to 5-20). For these homogeneous samples, a consideration of the key findings highlighted in Table 5-9 indicates that the PNM approach does not necessarily have to be as comprehensive as outlined in Table 5-9. This has the potential to reduce or eliminate several steps which can significantly reduce processing times. Against this backdrop and in relation to the above questions, the following is observed:

1. The automatic threshold (AT) value determined from the valley-emphasis method can provide an appropriate and robust threshold value when compared to a ±5% and ±10% change in AT value.

2. The REV based on porosity remains the same regardless of orientation and location (Section 5.3.5, Figures 5-12 and 5-13) and therefore only one orientation/location needs to be chosen. This results in a significant reduction in the number of computations required for Steps 5 – 12.

3. The REV was found to remain the same regardless of changes in threshold values (±5% and ±10% change in AT value); this implies that Step 9 can be eliminated.

4. An REV based on porosity was found to be the same as the REV based on PSD. The REV based on PSD remains the same regardless of orientation and location (Section 5.3.6.3, Figures 5-18 and 5-19) and therefore the PSD at only one orientation/location can appropriately represent the sample's PSD. This indicates that Steps 9 and 11 can be eliminated.

5. Given that the mean PSD (or from point 4 above, that the PSD at any one orientation/location) is comparable to the PSDs obtained when threshold values are changed, Step 12 can be eliminated.

These findings significantly reduce several steps found in Table 5-9 and forms the basis of a simplified recommended practice which can be used as an initial guide to

the PNM of both homogeneous and heterogenous sandstone samples. Table 5-11 outlines this recommended practice.

5.3.8 Discussion of the PNM Approach used in this work

The use of PNM approaches to characterise and evaluate the pore space of reservoir material has become increasingly prevalent as these can reduce the time and cost normally associated with similar conventional methods like MICP Testing.

This work builds upon the common practice of conducting PNM studies used by several researchers and culminates in a comprehensive PNM approach for obtaining the pore size distribution of sandstone samples which is outlined in Table 5-9. This comprehensive approach can minimise the uncertainties surrounding the heterogeneity and anisotropy of the pore space and lead to the identification of an appropriate threshold value. When considerable uncertainties exist, the PNM approach outlined in Table 5-9 (consisting of 12 steps minus image acquisition) can help provide representative measures leading to a high confidence in PSD results. Although there is a high confidence in the results, the approach has a substantial processing time which for a highly heterogeneous sample can be in excess of 100 hours (> 4 days).

For relatively homogeneous samples however, a consideration of the key findings of this work (highlighted in Table 5-9) shows that the approach can be reduced to just 9 steps which have a total processing time of roughly 7 hours. This represents a 93% reduction in processing time and may lead to reduced costs.

For well-studied materials like Berea and Bentheimer, it is easy to recognise that these are relatively homogeneous at the onset of PNM testing since this is prevalent in the literature (Bera *et al.*, 2011; Peng *et al.*, 2012; Wilson, 2004) and the condensed approach outlined in Table 5-11 can be adopted.

For materials with unknown heterogeneities and anisotropies, Table 5-11 for also provides a condensed approach for heterogeneous samples. which can be used as an initial guide to PNM PSD. This can provide an initial analysis of PNM PSD data in roughly 26 hours which represents an almost 75% reduction in processing time when compared to the comprehensive method in Table 5-9. This initial analysis can provide an initial measure of PSD which can then be compared with similar data from other

testing methods like MICP Testing. If significant findings exist, then the approach outlined in Table 5-9 should be used for these materials as this will lead to a higher confidence in the PNM results.

It is important here to note that the approaches outlined in both Tables 5-9 and 5-11 only include the 3D Reconstruction, REV Determination and PSD Analysis stages. These are the last three stages of the general PNM methodology from Figure 4-2. The first stage (Image Acquisition) is not included in the average processing times quoted in Tables 5-9 and 5-11 since this stage is dependent upon:

- the lithology (for example, the differences among shales, sandstone, carbonates and their in situ minerals may require varying PNM parameters to adequately capture pore information;
- the required resolution which is linked to the variety of pore dimensions in reservoir material which range from sub-micron to centimetres (Taud *et al.*, 2005; Tucker, 1991).

Table 5-1 shows that for the Berea and Bentheimer sandstone samples which have pore sizes ranging from 0 – 100 microns, a scanning time of approximately 18 hours was needed to acquire samples at a resolution of 5 microns per pixel. This scanning time is strongly related to the required resolution where for smaller resolutions, larger (and sometimes significantly larger) scanning times may be required.

Although there are reservations and uncertainties related to heterogeneity, segmentation and resolution which impact processing times, the above results show that the PNM approach used in this work can robustly model the pore space and provide excellent measures of pore size distribution comparable to that from the literature (Bera *et al.*, 2011; Peng *et al.*, 2012; Wilson, 2004) as well as to the MICP Testing carried out in Chapter 4 (Figures 4-3 and 4-4). A more detailed comparison of how these results compare to the values quoted in the literature and to the results of the MICP Testing is provided in Chapter 7.

Table 5-11: A Recommended Practice for the Pore Network Modelling of homogeneous and heterogeneous sandstone samples

Step	Description	Before PNM Process Refinement		After PNM Process Refinement leading to the Condensed Recommended Practice			
				Homogeneous Samples		Heterogeneous Samples	
		No. of Computations Involved	Average Processing Times [hr]	No. of Computations Involved	Average Processing Times [hr]	No. of Computations Involved	Average Processing Times [hr]
1	Subsample at either 2000 voxels or 20% of the total scanned volume (whichever is larger) to produce the Maximum Region of Interest (MROI).	1	0.2	1	0.2	1	0.2
2	Filter if necessary using an appropriate filtering process.	1	2	1	2	1	2
3	Segment using a Thresholding Approach where an Automatic Threshold (AT) value based on the valley-emphasis method is chosen as the default.	1	0.5	1	0.5	1	0.5
4	Visually compare the segmented and original images. If the segmented and original images visually compare well (based on user's perception), then proceed to Step 5. Else vary the threshold value (Interactive Thresholding) until a favourable comparison is obtained and then proceed to Step 5.	1	0.2	1	0.2	1	0.2
5	Incrementally section the volume in 100 voxels up to the MROI at *A) any orientation if homogeneous* or *B) at the 27 orientations identified in Figure 4-7B is heterogeneous*	20 x 27 = 540	3	20	2	20 x 27 = 540	3
6	Determine the porosity at each ROI increment identified in Step 5.	20 x 27 = 540	15	20	0.5	20 x 27 = 540	15
7	Calculate the percent porosity change at each ROI increment identified in Step 5.	20 x 27 = 540	5	1	1	20 x 27 = 540	5

129

8	Choose the REV where the percent porosity change is consistent at ±5% for successive ROIs.	1	0.1	1	0.1	1	0.1
9	Test the REV by changing the threshold value and determine the porosity at a ±5% and ±10% threshold value.	4 x 20 x 27 = 2160	25	0	0	0	0
10	Extract the pore network and obtain the pore size distribution for the REV.	27	15	1	0.5	1	0.5
11	Use an appropriate statistical test to determine the statistical similarity of the PSDs obtained at each orientation.	27	2	0	0	0	0
12	Test the PSD by changing the threshold value and determine the PSD at a ±5% and ±10% threshold value.	4 x 27 =108	32	0	0	0	0
	TOTAL		~100		7		26.5

Table

5-11: A Recommended Practice for the Pore Network Modelling of homogeneous and heterogeneous sandstone samples

5.4   Nuclear Magnetic Resonance (NMR) Test Results

Nuclear Magnetic Resonance (NMR) experiments measure the response of hydrogen nuclei which have been excited in a magnetic field. This chapter presents the NMR porosity and pore size distributions results for the Berea and Bentheimer samples when these are saturated with a variety of fluids as outlined in Section 4.3.

5.4.1   Porosity Determination from NMR Testing

The initial amplitude of the echo train of a saturated sample is proportional to the number of hydrogen nuclei that have been polarised in the pores (Coates *et al.*, 1999). This amplitude can therefore provide a measure of the pore volume once an appropriate calibration is used.   For NMR studies, this calibration comes from measuring the NMR amplitude for a specific volume of the saturating fluid.   Pore volumes can then be converted to porosities using the bulk volume of the saturated samples.

In this study, 25mL of water (bulk fluid) was subjected to T2 testing but any amount of fluid can be used given that the Magritek NMR system has a highly linear relationship between the measured amplitude and the sample volume and therefore requires only a single point for accurate calibration (Magritek, 2013).

Figure 5-23 shows the echo trains for the Berea, Bentheimer and bulk fluid (water) samples. This shows that the initial amplitude of the bulk water signal was 1.038µV. Given that a linear relationship exists between this amplitude and the sample volume (Magritek, 2013), a porosity calibration value of 1.038µV = 25mL was used to convert the initial amplitudes of the Berea and Bentheimer samples to pore volumes and then to porosities using the bulk volumes provided in Table 5-12. A sample calculation is shown below for the Berea sample.

For bulk water, the initial amplitude of 1.038µV corresponds to 25mL.

$$\text{Therefore, } 1\mu V = \left(\frac{25}{1.038} \right) mL \qquad \text{[5-1]}$$

From Figure 5-23, the initial amplitude from the Berea echo train = 0.262µV. Using the porosity calibration value of 1.038µV = 25mL, this gives a pore volume of

$$0.262 x \left(\frac{25}{1.038} \right) mL = 6.31mL.$$

From Table 5-12, the bulk volume of the Berea sample is 49.6mL.

Therefore, the porosity of the Berea sample = $\left(\frac{PV}{BV} \right) = \left(\frac{6.31}{49.6} \right) = 0.128 = 12.8\%$

Similar values for the Bentheimer sample can be seen below in Table 5-12.
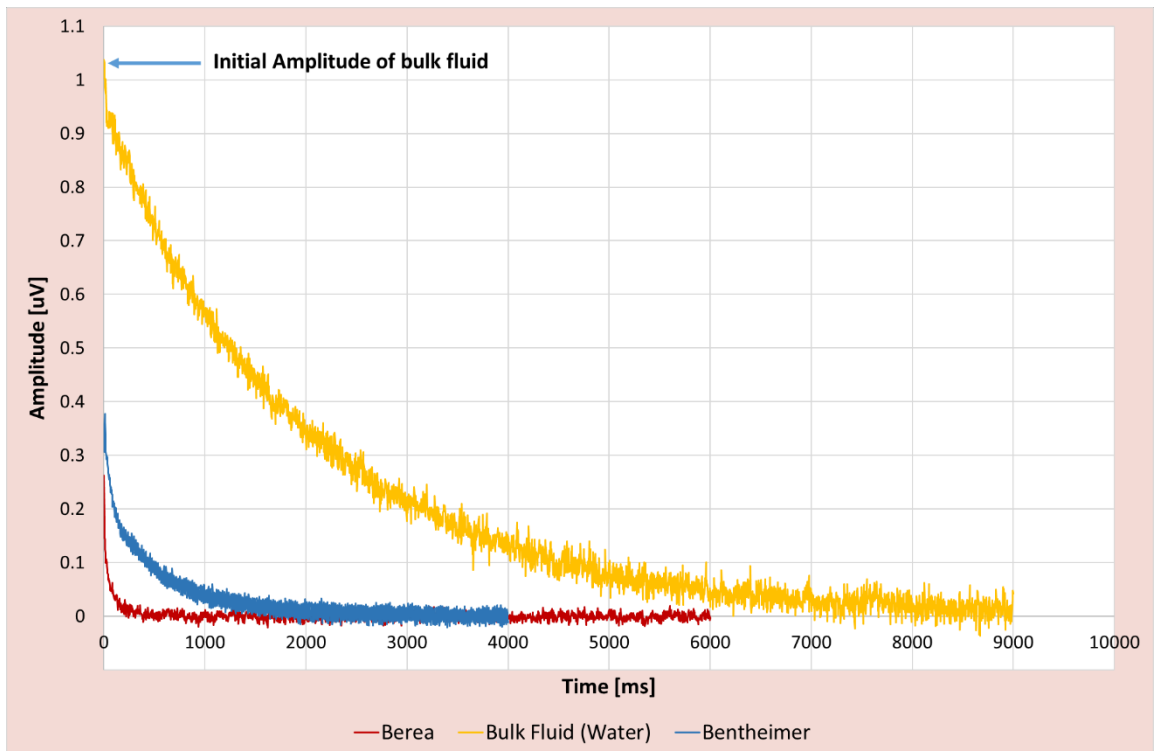
Figure 5-23: Echo trains (raw data) for the Berea, Bentheimer and bulk fluid (water) samples

Table 5-12: NMR Porosity Calculations for the Berea and Bentheimer samples

	Bulk Fluid (distilled water)	Berea	Bentheimer
Sample Dimensions			
Length [cm]	-	10.11	10.14
Diameter [cm]	-	2.50	2.49
Bulk Volume, BV [cm^3 or mL]	25	49.6	49.4
Initial Amplitude from echo train [µV]	1.038	0.262	0.377
Pore volume (PV) using the calibration given in Equation 5-1 [mL]	-	6.32	9.08
NMR Porosity [%]	-	12.8	18.5

The NMR porosities for Berea (12.8%) and Bentheimer (18.5%) shown in Table 5-12 are comparable those from the MICP and PNM testing (Table 5-4). A further comparison of these values is provided in Chapter 8. Figure 5-23 also shows that the signal amplitudes of the Berea and Bentheimer samples decay much more rapidly than the bulk fluid signal. This decay is due to the relaxation of the hydrogen nuclei when they interact with the surfaces of the pore walls. This provides the basis for determining the pore size which is further described in the Section 5.4.2.

5.4.2   Pore Size Distribution (PSD) from NMR Testing

Section 4.3.4 outlines the method of determining the PSD from NMR testing using a 4-step process that combines the results of the T2 and PGSTE testing. The first step converts the echo trains (raw T2 test data shown in Figure 5-23) into T2 spectra from which the inverse of the weighted harmonic mean of the T2 distribution $\overline{\left(\dfrac{1}{T2}\right)}$ can be found. The second step involves running a PGSTE experiment at selected diffusion times (t) and plotting the resulting D(t) values against t$^{1/2}$ to obtain the average $\overline{\left(\dfrac{S}{V}\right)}$

ratio. The third step uses the values of $\overline{\left(\dfrac{1}{T2}\right)}$ and $\overline{\left(\dfrac{S}{V}\right)}$ from steps 1 and 2 to calculate surface relaxivity (ρ_2) which can then be used to convert the T2 distribution into corresponding pore radii using Equation 4-11.

The rest of section examines and provides the results for each of these steps.

5.4.2.1 Step 1 of the NMR-PSD Approach: Obtaining the T2 Spectra and Weighted Harmonic Means

Figure 5-23 shows the echo trains for the Berea, Bentheimer and bulk water samples used in this work. These echo trains represent the raw data measured during a T2 NMR test (as shown in Figure 4-8). To obtain the classic T2 spectra associated with T2 NMR testing, the echo trains need to be mathematically inverted using a best-fit curve. Several mathematical inversions are commonly used with the Lexus and modified-NNLS methods being popular choices (Coates *et al.*, 1999; Testamantia and Rezaee, 2018; Washburn *et al.*, 2015).

This work used the Lexus module found within the Prospa® software package which is part of the Rock Core Analyzer Magritek instrument used to test the Berea and Bentheimer samples. This technique has been used as a preferred method in many NMR studies (Washburn *et al.*, 2015) and provides logarithmic binning on data points allowing both short and long relaxation times to be appropriately extracted (Butler *et al.*, 1981). Figure 5-24 shows the T2 spectra after using the Lexus mathematical inversion for the Berea and Bentheimer samples.
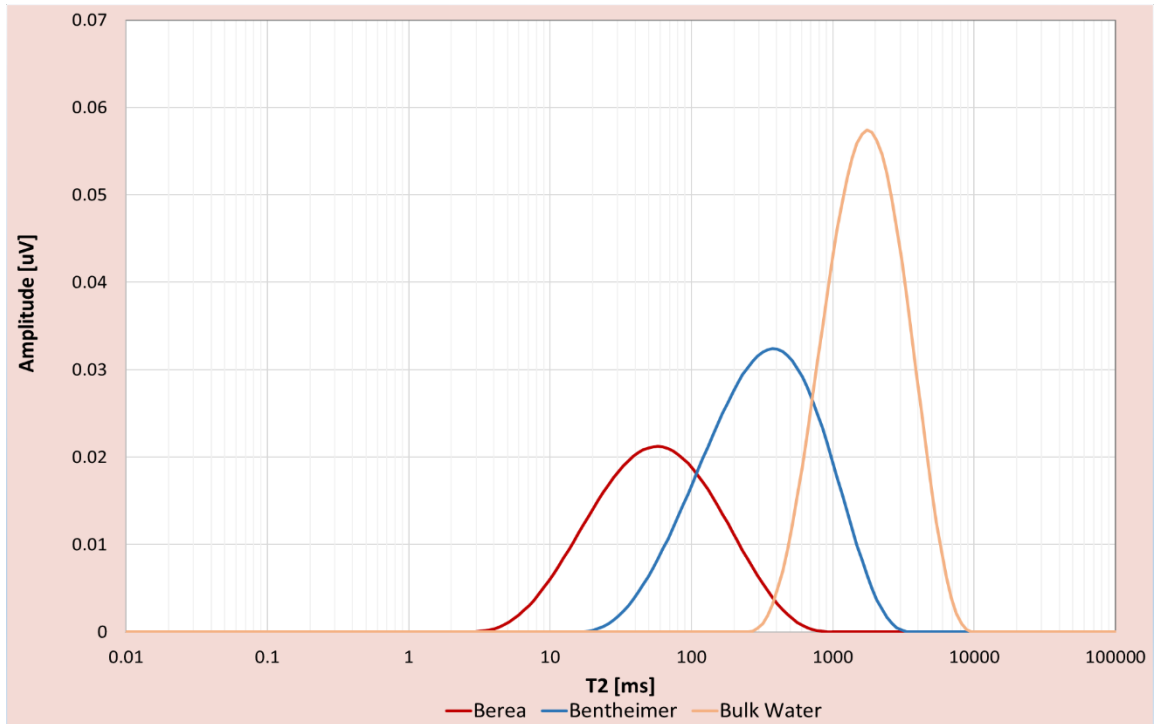
Figure 5-24: The T2 spectra after mathematical inversion for the Berea and Bentheimer samples

It is commonly accepted that T2 spectra of porous media are analogous to a measurement of the pore size distribution of the rock (Straley *et al.*, 1997). Equation 4-11 illustrates that each T2 value is associated with a unique pore radius and as such, a T2 distribution describes the existing pore-size distribution (although not in absolute units).

Figure 5-24 shows that Berea sample has a shorter T2 response than that for Bentheimer. These samples have been saturated with distilled water (Section 4.3.5). For the case of distilled water contained within water-wet pores, Equation 4-11 shows that the T2 response can be considered as a measure of the pore radii with smaller T2 values representing smaller radii.

The smaller T2 response for Berea indicates that this sample is comprised of a smaller set of pores to that of Bentheimer. Smaller pores have shorter T2 relaxation times as the excited hydrogen nuclei will interact more with each other and with the pore walls within the confines of a smaller pore space thereby relaxing faster. The converse is true for larger pores in which the hydrogen nuclei will have to travel longer distances to interact with each other and the pore space which leads to a slower loss of energy or a longer relaxation time.

The T2 response between the Berea and Bentheimer samples show that Berea sample is comprised of smaller pores than the Bentheimer sample which has been confirmed in the literature (Bera *et al.*, 2011; Peng *et al.*, 2012; Wilson, 2004) as well as from the MICP Testing (Figures 5-2 and 5-3) and PNM Approach (Figure 5-20). A more detailed comparison of these results is provided in Chapter 7.

The bulk relaxation rate of the 25 mL sample of distilled water (the saturating fluid) is also shown in Figure 5-24. Bulk relaxation rates are obtained by measuring the NMR response of a fluid that is placed in a large container whose dimensions are considered sufficiently sizeable to preclude the impact of surface relaxation. The T2 response for the bulk water in Figure 5-24 is comparable to that from the literature (Chapter 2, Figure 2-7) being within the order of 2000 – 2500ms (Bryan *et al.*, 2003; Kantzas, 2009; Niu *et al.*, 2008). This relatively high response is a result of the water's low viscosity (Straley *et al.*, 1997) where low viscosity fluids are associated with a higher molecular mobility which results in high values of relaxation times. Conversely, high viscosity fluids have a reduced molecular mobility and are associated with faster relaxation rates.

Step 1 of the NMR-PSD Approach also provides a measure of the weighted harmonic mean of the T2 distribution which is calculated using:

$$\overline{(T2)} = \frac{\sum_i A_i}{\sum_i \frac{A_i}{T2_i}} \qquad [5\text{-}2]$$

where A_i is the amplitude value corresponding to a specific relaxation time $T2_i$.

The $\overline{(T2)}$ of a distribution leans strongly toward the least elements of the data set and is commonly used to mitigate the impact of large outliers in the distribution and augment the impact of small ones (Gaze and Wagner, 2009).

The values of $\overline{(T2)}$ for the Berea and Bentheimer samples were found to be 86.7 ms and 311 ms respectively. These are further described in Table 5-14.

5.4.2.2 Step 2 of the NMR-PSD Approach: Obtaining the average surface area to volume ratio

Equation 4-14 is given below.

$$\overline{\left(\frac{1}{T2}\right)} = \rho_2 \overline{\left(\frac{S}{V}\right)} \qquad [4\text{-}14]$$

This shows that once the values of the inverse of the weighted harmonic mean $\overline{\left(\frac{1}{T2}\right)}$ and the average surface area to volume ratio $\overline{\left(\frac{S}{V}\right)}$ are known, a value of surface relaxivity (ρ_2) can be found which can then be used to convert the T2 distribution into a corresponding pore size distribution (PSD) using Equation 4-11.

$\overline{\left(\frac{S}{V}\right)}$ can be found by performing a series of pulsed field gradient stimulated echo (PGSTE) experiments at short diffusion (Loskutov, 2012; Slijkerman and Hofman, 1998; Sorland $et\ al.$, 2007). These experiments measure the time dependent restricted diffusion coefficient [$D(t)$] when the observation time for diffusion [t] is varied.

Equation 4-15 shows that the time-dependent restricted diffusion coefficient can be rewritten as:

$$\sum_i \xi_i \frac{D_i}{D_o} \approx \sum_i \xi_i \left[1 - \frac{4}{9\sqrt{\pi}} \sqrt{D_o t} \overline{\left(\frac{S}{V}\right)_i}\right] = \left(1 - \frac{4}{9\sqrt{\pi}} \sqrt{D_o t} \overline{\left(\frac{S}{V}\right)}\right) \qquad [4\text{-}15]$$

$$\therefore \frac{D(t)}{D_o} = \left(1 - \frac{4}{9\sqrt{\pi}} \sqrt{D_o t} \overline{\left(\frac{S}{V}\right)}\right) \qquad [5\text{-}3A]$$

$$\therefore D(t) = D_o - \frac{4}{9\sqrt{\pi}} (D_o)^{\frac{3}{2}} \sqrt{t} \overline{\left(\frac{S}{V}\right)} \qquad [5\text{-}3B]$$

Equation 5-3B is in the form of a straight line when D(t) is plotted against $t^{1/2}$ as shown in Figure 5-25. $\overline{\left(\frac{S}{V}\right)}$ can then be obtained from the gradient of this plot.
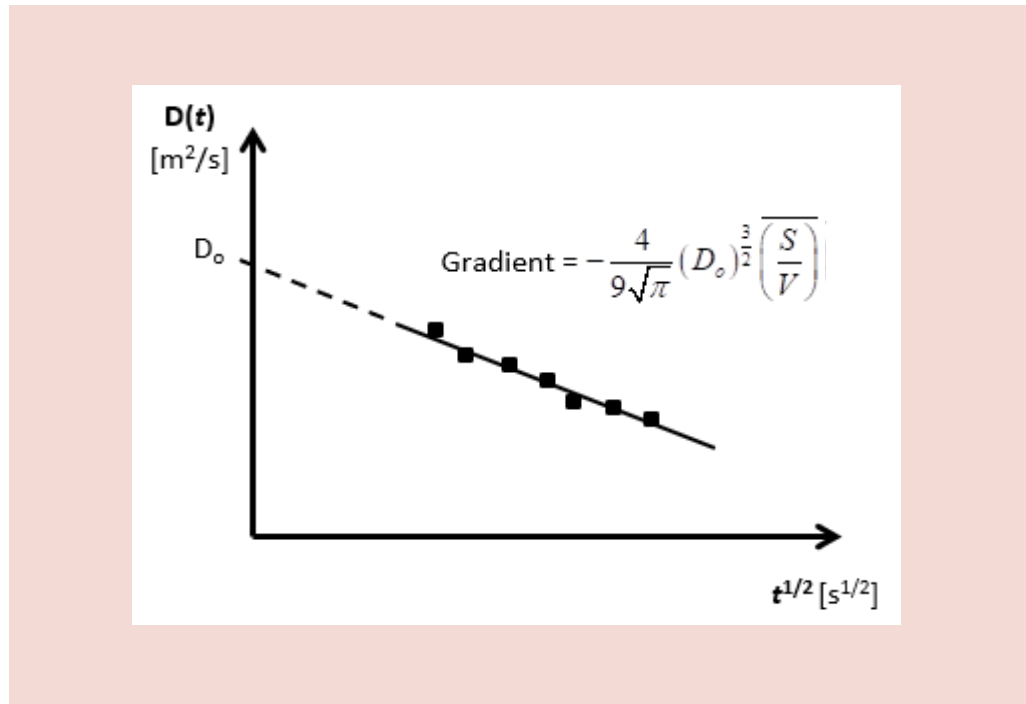
Figure 5-25: Determining $\overline{\left(\dfrac{S}{V}\right)}$ from a linear plot of D(t) against $t^{1/2}$

The results of the PGSTE Testing for the Berea and Bentheimer samples are shown below in Table 5-13 and Figure 5-26.

Table 5-13: Restricted Diffusion Coefficients from PGSTE Testing

		Berea	Bentheimer
Observed diffusion time, t [s]	$t^{1/2}$ [s$^{1/2}$]	**D(t)** [x 10^{-10} m^2/s]	**D(t)** [x 10^{-9} m^2/s]
16	0.126	8.50	-
20	0.141	5.00	-
24	0.155	4.50	1.55
32	0.179	1.50	1.20
36	0.190	1.00	1.09
48	0.219	-	1.05
64	0.253	-	0.90

D_o is the unrestricted or self-diffusion coefficient of the saturating fluid. Unrestricted here means movement of the hydrogen nuclei take place by *self-diffusion* and are not significantly influenced by interactions with the pore walls.

D_o is strongly temperature-dependent (Gillen *et al.*, 1972; Mills, 1973) and values for water typically lie between 1.756 – 2.317 x 10^{-9} m^2/s when the temperature varies from 15 – 25°C (Tofts *et al.*, 2000). The PGSTE experiments in this work were carried out at temperatures between 20 and 25°C. At these temperatures, it is expected that D_o values would lie between is given as 2.02 – 2.317 x 10^{-9} m^2/s (Tofts *et al.*, 2000).

Figure 5-26 shows the linear plots of D(t) against $t^{1/2}$ for the Berea and Bentheimer samples. The important parameters from this plot are D_o and numerical gradient values. Rearranging the gradient formula in Figure 5-26 gives the following equation from which $\overline{\left(\dfrac{S}{V}\right)}$ can be calculated. These values are provided in Table 5-14.

$$\overline{\left(\frac{S}{V}\right)} = -\frac{Gradient}{\frac{4}{9\sqrt{\pi}}\left(D_o\right)^{\frac{3}{2}}} \qquad [5-4]$$
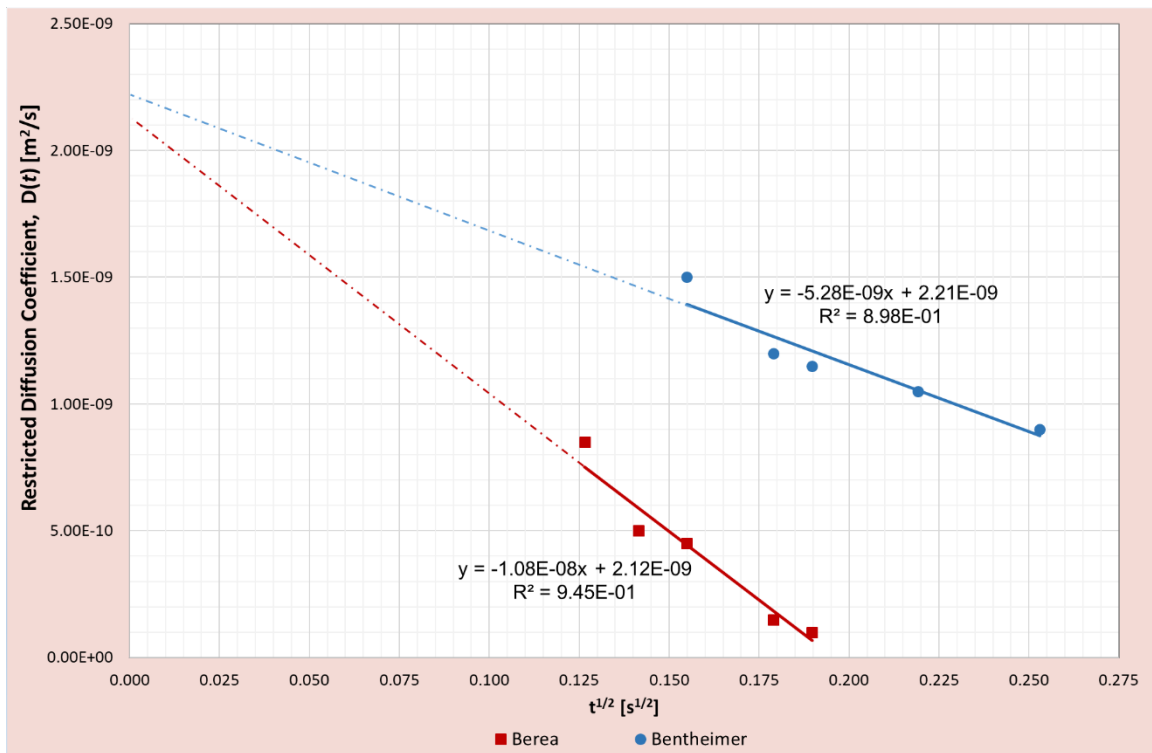
Figure 5-26: The linear plots of D(t) vs $t^{1/2}$ for the Berea and Bentheimer samples from the PGSTE Testing

Table 5-14: The average surface area to volume for the Berea and Bentheimer samples from the PGSTE Testing

	Berea	Bentheimer
Gradient [x 10^{-9}]	-10.8	-5.28
D_o [x 10^{-9} m^2/s]	2.12	2.21
From Equation 5-4: $\overline{\left(\dfrac{S}{V}\right)}$ [1/m]	443,129	202,717

While the T2 and PGSTE tests do not provide the number of pores within the sample, the resulting $\overline{\left(\dfrac{S}{V}\right)}$ values in Table 5-14 as well as the corresponding NMR porosities from Table 5-12 show that the Berea sample on average contains smaller pores than the Bentheimer sample. This confirms the findings from the T2 test in Figure 5-24 in which the Berea sample had a faster T2 relaxation time than the Bentheimer sample indicating the prevalence of smaller pores.

Although the Berea and Bentheimer samples have varying pore sizes, the extrapolation back to zero observation time produces an unrestricted diffusion coefficient of water D_o that ranges from 2.12 to 2.21 $\times 10^{-9}$ m^2/s. The PGSTE experiments in this work were carried out at temperatures between 20 and 25°C. At these temperatures, the D_o values of 2.12 to 2.21 $\times 10^{-9}$ m^2/s compare well with those available in the literature (2.02 – 2.317 x 10^{-9} m^2/s) (Tofts *et al.*, 2000).

This leads to a high confidence in the PGSTE testing since the use of Equations 4-10 to 4-15 which provide the basis of the $\overline{\left(\dfrac{S}{V}\right)}$ calculations are only valid for exceedingly short or fast diffusion times (*t*) (Jin *et al.*, 2009; Mitra *et al.*, 1993). Given that the extrapolation of the restricted diffusion coefficient [D(*t*)] back to a zero-observation time does not deviate significantly from the unrestricted or bulk diffusion coefficient of the water, the use of Equations 4-10 to 4-15 and their results can be assumed to be valid.

5.4.2.3 Step 3 of the NMR-PSD Approach: Obtaining the surface relaxivity (ρ_2)

The surface relaxivity (ρ_2) of a material is related to the rate at which the surfaces of that material relax or attenuate the spins of the nuclei approaching the surface. It is dependent upon the mineralogical composition of the material (Kleinberg, 1996) but independent upon changes in temperature and pressure (Coates *et al.*, 1999).

The surface relaxivities of sandstone material have been shown to vary from 6.4 to 46 µm/s (Dunn *et al.*, 2002; Lonnes *et al.*, 2003; Marschall *et al.*, 1995). Lonnes *et al.* (2003) contend that the range of surface relaxivities for use within the petroleum industry should lie between 7 and 30 µm/s since this will ensure that the surface relaxations governed by Equation 4-10 will lie within the fast diffusion limit as described in Section 4.3.2.

Using the values obtained for $\overline{\left(\dfrac{1}{T2}\right)}$ and $\overline{\left(\dfrac{S}{V}\right)}$ from steps 1 and 2, the surface relaxivities for the Berea and Bentheimer samples can be calculated using Equation 4-14. These are given in Table 5-15.

Table 5-15: The calculated surface relaxivities for the Berea and Bentheimer samples

	Berea	**Bentheimer**
$\overline{(T2)}$ [ms]	86.7	311
$\overline{\left(\dfrac{1}{T2}\right)}$ [1/s]	11.5	3.22
$\overline{\left(\dfrac{S}{V}\right)}$ [1/m]	443,129	202,717
From Equation 4-14: ρ_2 [µm/s]	26.0	15.9

The calculated values for the surface relaxivities for the Berea and Bentheimer samples from Table 5-15 show that these compare well to similar values quoted in the literature (Dunn *et al.*, 2002; Lonnes *et al.*, 2003; Marschall *et al.*, 1995) and that these fall within the range of acceptable values of 7 - 30 μm/s (Lonnes *et al.*, 2003) which ensure that the surface relaxations lie within the fast diffusion limit.

5.4.2.4 Step 4 of the NMR-PSD Approach: Obtaining the pore size distribution

The final step of the NMR-PSD approach involves converting the T2 distribution into a pores size distribution (PSD) using Equation 4-11.

$$\frac{1}{T2} = \rho_2 \left(\frac{S}{V} \right) = \rho_2 F_s \left(\frac{1}{r} \right) \qquad [4-11]$$

This requires the use of a shape factor (F_s). When no other information is available, pores are commonly assumed to be spherical (Anovitz and Cole, 2015; Brownstein and Tarr, 1979; Coates *et al.*, 1999) resulting in the use of a shape factor of 3 as shown in Table 4-3. It is important to note however, that porous media can comprise a complex assortment of shapes and geometries. The assumption of a spherical geometry may simplify this complexity and tend to misrepresent the actual morphology which exists (Vavra *et al.*, 1992). This is further examined in Section 5.4.3 below.

For spherical pores, Equation 4-11 can be therefore rewritten to give:

$$\frac{1}{T2} = \rho_2 \left(\frac{3}{r} \right) \qquad [5-5]$$

With the calculated value of surface relaxivity (ρ_2) from Table 5-15, Equation 5-5 can be used to convert each T2 value of the T2 spectrum into a unique pore radius with the corresponding amplitude of the T2 spectrum representing the quantity of pores having that unique radius. The final PSDs resulting from NMR Testing for the Berea and Bentheimer samples are shown in Figure 5-27.

Figure 5-27 shows that the Berea sample has a range of smaller pores than the Bentheimer sample. This is similar to what has been published in the literature (Bera *et al.*, 2011; Peng *et al.*, 2012; Wilson, 2004) as well as the results of the MICP Testing (Figures 5-2 and 5-3) and the PNM Approach (Figure 5-20). The curves in Figure 5-

27 were then subjected to statistical analysis using the approaches outlined in Section 4.1.4 with the results shown in Table 5-16.
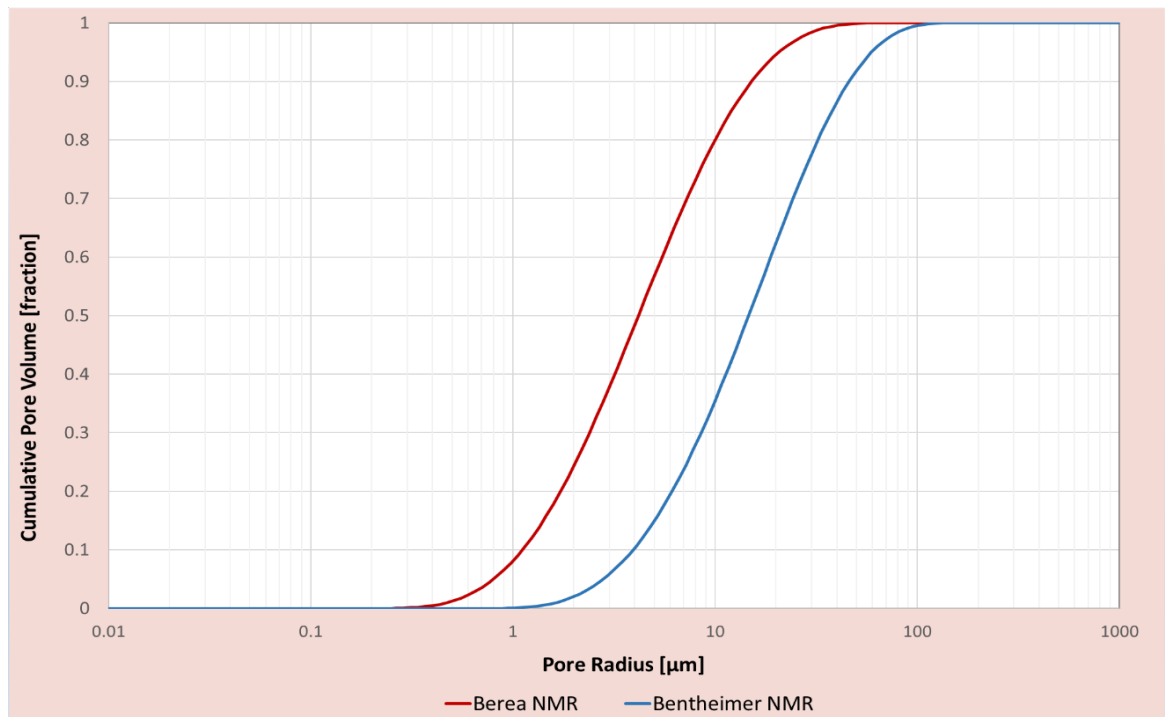
Figure 5-27: The Cumulative PSDs of the Berea and Bentheimer samples from NMR

Table 5-16 shows that for the Berea sample, the mean and median of the NMR PSD are comparable and indicate that the data set is generally free of outliers. The median pore size is 4.2 μm and the pore radius has a range of 0.3 – 100 μm. The sorting is 5.7 which is a relatively low value indicating that a majority of the pores are close to the 4.2 μm median. This is confirmed by the pore classification where the NMR PSD shows that the medium is contain a majority of mesopores (89%) with the remaining pores being comprised of 8% micropores (≤ 1 μm radii) and 3% macropores (>25 μm radii).

This is highlighted by the skewness which is 0.6 indicating that the distribution follows a normal distribution with the majority of the pore size symmetrical about the mean. The kurtosis (1.3) further supports the above distribution of pores among micropores, mesopores and macropores and indicates that the pore size has a somewhat even spread of pore sizes in the tails to those that are centrally located in the distribution.

Similar results for the Bentheimer sample show that the mean and median of the PNM PSD are particularly comparable being 14.6 and 14.8 μm respectively. The pore radius ranges from 1 - 120 μm with mesopores and macropores accounting for 70% and 30% respectively. It is interesting to note that the NMR PSD for Bentheimer contained no micropores which is consistent with the findings from the PNM PSD and MICP PSD.

The sorting is 16.3 indicating that there is wide variation of pore size compared to the median which further highlights the existence of the two mesopore and macropore populations (70% and 30% respectively) within the Bentheimer sample. Although these two classes of pore size exist, the kurtosis is 1.1 indicating that the pore sizes are normally distributed which is highlighted by the skewness (0.5) which further show that the distribution is symmetrical about the mean.

Table 5-16: Analysis of the PSDs of the Berea and Bentheimer samples from NMR

	Berea	Bentheimer
r_5	0.8	2.8
r_{16}	1.48	5.3
r_{25}	2.1	7.3
r_{50}	4.2	14.8
r_{75}	8.7	28.1
r_{84}	12.1	36.3
r_{95}	21.1	59.1
Statistical Measures:		
Pore Size Range [μm]	0.2 - 100	1 - 120
Median (r_{50}) [μm]	4.2	14.8
Mean (r_m) [μm]	4.3	14.6
Pore Sorting (S_p)	5.7	16.3
Skewness (Sk_p)	0.6	0.5
Kurtosis (K_p)	1.3	1.1
Pore Classification:		
Micropore (≤ 1 μm) [%]	8	0
Mesopore ($1 < r \leq 25$ μm) [%]	89	70
Macropore (> 25 μm) [%]	3	30

A more detailed comparison of how these results compare to the values quoted in the literature and to the results of the MICP Testing and PNM Testing is provided in Chapter 7.

5.4.3 Opportunities for improving the NMR PSD using Micro-CT, PNM and Pore Shape Characterisation

Although a more detailed comparison of the NMR PSD method with the MICP Testing and PNM approach is provided in Chapter 7, an initial review shows that these methods compare somewhat favourably in terms of mean pore size and pore size range.

This lends support for the use of NMR testing as an independent method for deriving robust PSDs for sandstone samples. One opportunity to strengthen this approach lies in the identification of a more representative pore shape factor. When no other information is available, pores are commonly assumed to be spherical (Anovitz and Cole, 2015; Brownstein and Tarr, 1979; Coates *et al.*, 1999) resulting in the use of a generic shape factor of 3 during NMR testing.

In real porous media, the pore networks can comprise a complex assortment of shapes and geometries (Vavra *et al.*, 1992). The assumption of a spherical geometry can therefore simplify this complexity and tend to misrepresent the actual morphology which exists.

The use of micro-CT and PNM approaches presents a viable means of exploring more realistic shape factors. As described in Sections 4. 2 and 5.3, PNM uses micro-CT imaging to obtain a 3D representation of the pore space from which pore network models can be derived. In this work, the medial axis algorithm of the Avizo® Fire software was first used to extract the topological skeleton running through the centre of the pore network (as described in Section 5.3.6). Individual pores were then identified by partitioning the skeleton and fitting ellipsoids into local minima whose minimum length was taken as the pore diameter.

For the representative elementary volumes (REVs) identified in Section 5.3.5, Table 5-6 shows that and average of 110,520 and 55,230 pores were contained in the 1000 REV ($5mm^3$) and 700 REV ($3.5mm^3$) respectively for the Berea and Bentheimer

samples. Figure 5-28 shows some of these pores within a small section of the REV for the Berea sample.

Figure 5-28: Identification of selected pores within the REV for the Berea sample

Once the individual pores have been identified, a number of measurements relating to their shape and size can be made. The pore shape measures which are useful for improving the NMR PSD relate to the pore dimensions of surface area, volume and minimum and maximum Feret diameters. Table 5-17 describes these in more detail (Krumbein, 1941; Wadell, 1932) and provides the associated Avizo® algorithms used to measure them.

Table 5-17: Selected Pore Shape Descriptors

	Description	Avizo® Measure
Surface Area	The surface area is the sum of an object's surface boundary	*Area3d*
Volume	Volume of the object based on length, width and height	*Volume3d*
Feret Diameter	Feret diameter (or caliper diameter) is a measure of an object's size along a specified direction. It is defined as the distance between the two parallel planes restricting the object perpendicular to that direction (Krumbein, 1941; Wadell, 1932)	
	Minimum Feret Diameter (***pore diameter***)	*Width3d*
	Maximum Feret Diameter	*Length3d*

The PNM approach can strengthen and inform the NMR PSD approach in two main ways. The first is the identification of a representative shape factor (F_s) shown in Equation 4-11 which is required to convert the T2 distribution into a PSD in terms of absolute units.

$$\frac{1}{T2} = \rho_2\left(\frac{S}{V}\right) = \rho_2 F_s\left(\frac{1}{r}\right) \qquad \text{[4-11]}$$

The second is obtaining an average surface area to volume $\overline{\left(\frac{S}{V}\right)}$ value which is needed during the PGSTE testing in order to obtain the surface relaxivity (ρ_2) as shown in Equation 4-14.

$$\therefore \overline{\left(\frac{1}{T2}\right)} = \rho_2 \overline{\left(\frac{S}{V}\right)} \qquad \text{[4-14]}$$

Table 5-17 shows that the surface area and volume of individual pores can be obtained from the Avizo® algorithms of *Area3d* and *Volume 3d*. The $\overline{\left(\frac{S}{V}\right)}$ term in Equation 4-14 can easily be found by calculating the surface area to volume ratio ($\frac{Area3d}{Volume3d}$) for each pore identified and then finding the average value across all the pores.

In terms of the shape factor (F_s), Equation 4-11 shows that:

$$\left(\frac{S}{V}\right) = F_s\left(\frac{1}{r}\right)$$

$$\therefore F_s = r\left(\frac{S}{V}\right) \qquad \text{[5-6]}$$

where *r* is the pore radius ($= \frac{Width3d}{2}$) and where *S* and *V* are *Area3d* and *Volume3d* measures from Avizo®.

147

5.4.3.1 Obtaining pore shape factors from the PNM Approach

Using Equation 5-6, an analysis of the shape factors of the pores identified in 1000 REV and 700 REV volumes respectively for the Berea and Bentheimer samples is shown in Figure 5-29. These factors ranged from 1 – 12 for the Berea sample and from 2 – 11 for the Bentheimer sample. Table 4-3 shows selected shape factors for common shapes where for example, F_s = 3 for a spherical, F_s = 2 for a tube pore and F_s = 6 for a cube pore. As the F_s increases, the shape becomes more polyhedral and complex.
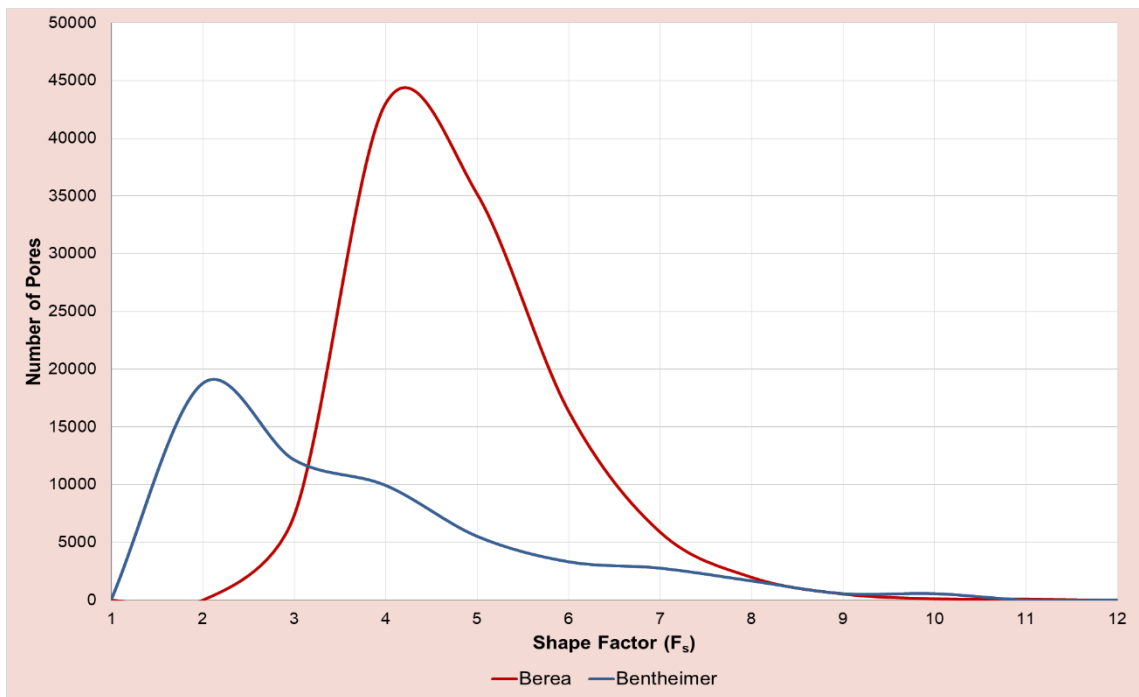
Figure 5-29: Shape Factor Analysis of the pores within the REVs for the Berea and Bentheimer samples

The average weighted shape factor for the Berea and Bentheimer samples were found to be 4.3 and 2.4 respectively. This implies that many of the pores with the Berea sample may be cubic in shape with rounded corners and that the pores of the Bentheimer sample tend to be either tubular or capsular in shape (Table 4-3).

This allows Equations 4-11 and 5-5 to be refined as shown below for the Berea and Bentheimer samples and use a more realistic and representative pore shape factor to derive the PSD.

NMR PSD Equation for the Berea sample:
$$\frac{1}{T2} = \rho_2 \left(\frac{4.3}{r} \right)$$
[5-7A]

NMR PSD Equation for the Bentheimer sample: $\quad \dfrac{1}{T2} = \rho_2 \left(\dfrac{2.4}{r} \right)$ $\qquad$ [5-7B]

The use of Equations 5-7A and 5-7B can be used to derive more representative PSD for the Berea and Bentheimer samples is further discussed in Chapter 7.

5.4.3.2 Obtaining the average surface area to volume ratio from PNM

The surface area and volume of individual pores can be obtained from the Avizo® algorithms of *Area3d* and *Volume 3d*. This allows the surface area to volume ratio ($\dfrac{S}{V} = \dfrac{Area3d}{Volume3d}$) for each pore to be calculated. Figure 5-30 shows the distribution of the $\left(\dfrac{S}{V} \right)$ of the pores identified in 1000 REV and 700 REV volumes respectively for the Berea and Bentheimer samples.
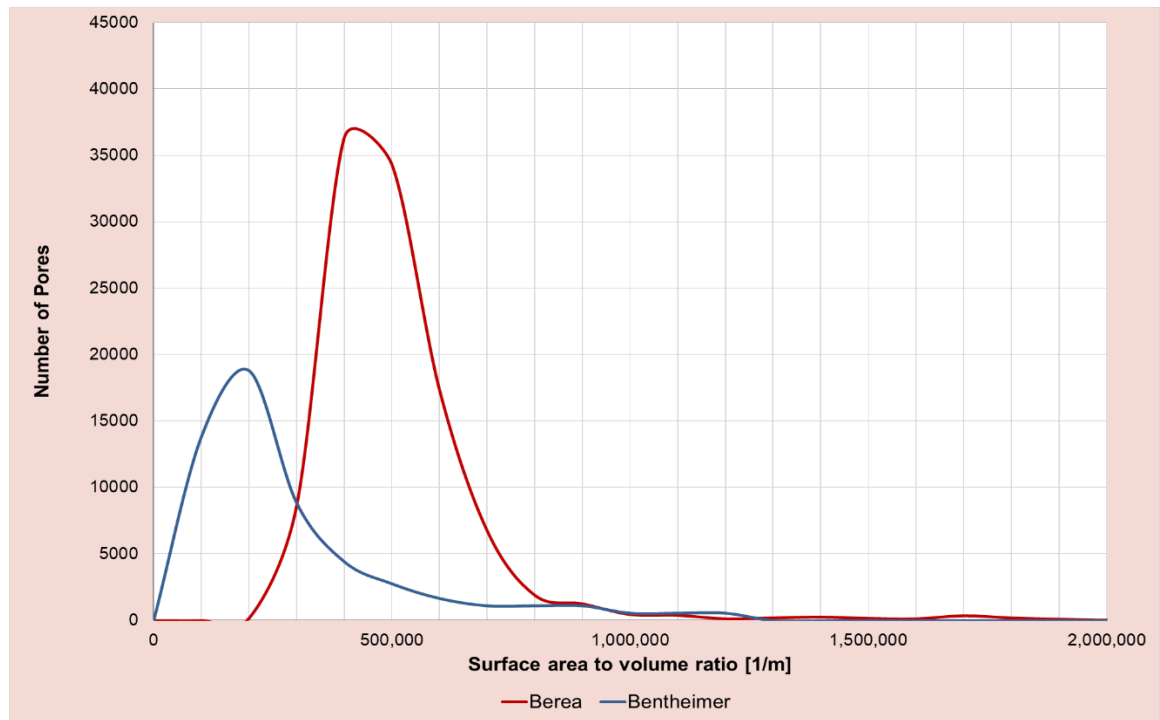
Figure 5-30: The distribution of the surface area to volume ratio of the pores within the REVs for the Berea and Bentheimer samples

The average surface area to volume ratio of the pores within the REV of the Berea and Bentheimer samples were found to be 472,964 m^{-1} and 192,806 m^{-1} respectively.

These values compare well to those obtained from the PGSTE testing which were found to be 443,129 m^{-1} and 202,717 m^{-1} respectively for the Berea and Bentheimer samples (Table 5-14). Table 5-18 shows the calculation and compares the values of surface relaxivity (ρ_2) obtained from the PGSTE and PNM approaches. These values compare well and suggest that the PNM can provide an alternate means of acquiring the $\overline{\left(\dfrac{S}{V}\right)}$ and ρ_2.

Table 5-18: Comparison of the surface relaxivities from PGSTE and PNM testing

	Berea	Bentheimer
Values from PGSTE Testing (Table 5-14)		
$\overline{\left(\dfrac{1}{T2}\right)}$ [1/s]	11.5	3.22
$\overline{\left(\dfrac{S}{V}\right)}$ [1/m]	443,129	202,717
$\boldsymbol{\rho_2}$ from PGSTE Testing[μm/s]	26.0	15.9
Values from PNM		
Number of pores	110,520	55,230
$\overline{\left(\dfrac{S}{V}\right)}$ [1/m]	472,964	192,806
Using $\overline{\left(\dfrac{1}{T2}\right)}$ from above with Equation 4-14: $\boldsymbol{\rho_2}$ from PNM [μm/s]	24.3	16.7

An alternative method for determining $\overline{\left(\dfrac{S}{V}\right)}$ and ρ_2 becomes valuable in situations when PGSTE Testing cannot be performed. An example of this is during NMR logging in which T2 data is widely obtained but where PGSTE testing is not carried out. Another example is when cores, still having their in-situ fluids, are subjected to laboratory NMR testing without the pre-requisite cleaning and saturation of water or

brine. Although PGSTE can be performed, the nature of the fluids in the pore space

may preclude and affect a robust   determination of $\overline{\left(\dfrac{S}{V}\right)}$ and during PGSTE testing.

The capacity to obtain these values through an alternate means like PNM is therefore beneficial. This is further explored in Chapter 7.

5.4.4 Investigating the influence of viscous fluids on PSD determination from NMR Testing

The NMR-PSD method outlined in Section 4.3.4 is contingent upon carrying out NMR measurements of the pore space when it is saturated with either water or brine (or other suitably low viscous fluids). Low viscous fluids minimise the contribution of the bulk fluid relaxation term (T2B) in Equation 4-9 and lead to the T2 distribution being dependent only on the T2S surface relaxation as shown in Equation 4-10:

$$\frac{1}{T2} = \rho_2 \left(\frac{S}{V}\right) \qquad \text{[4-10]}$$

Obtaining NMR PSDs on formations and cores having their in-situ fluids (which may not necessarily be comprised of low viscous fluids) is valuable to the petroleum industry. Good examples of where these situations might occur include:

- the NMR logging of formations in which the in-situ fluids may be a combination of connate water, in-situ hydrocarbons and drilling mud (Shafer *et al.*, 1999). The capability of obtaining PSDs during NMR logging can identify sweet spots in real-time and provide pore information on material having a minimal drilling fluid invasion and formation damage.

- the testing of core samples which still have their in-situ fluids. With specific reference to unconsolidated Athabasca oil sand material, the in-situ bitumen acts as a cohesive agent binding the grains together. Removal of this bitumen can lead to a rearrangement of the pore structure unless meticulous care is taken to preserve the pore integrity during the cleaning process. As such, the use and development of robust techniques to test oil samples with their in-situ bitumen is helpful as alternate core analytical techniques which require that these samples be cleaned of original fluids may not readily provide consistent and reliable pore information for these kinds of materials.

It becomes important to therefore study the influence of fluid parameters which can affect the determination of PSD during NMR testing. The section looks specifically at examining the effect of a viscous fluid on NMR PSD tests since Equation 4-10 is dependent upon the use of low viscous fluids and many new exploits within the petroleum industry instead focus on heavy oil and bitumen (Hein, 2016).

The viscous fluid used is this work is glycerol. Glycerol ($C_3H_8O_3$) is a simple polyol compound which is colourless, odourless and highly soluble in water. It has a molecular weight of 92.094 g/mol, a viscosity of 1,412 cP (1.412 Pa-s) at 20°C and a density of 1.261 g/cm^3 at 20°C (Lide, 1994). In comparison, water has a viscosity of 1 cP (0.001 Pa-s) at 20°C.

After being saturated with distilled water (and therefore water-wet) as outlined in Section 4.3.5, Berea and Bentheimer samples were further saturated with glycerol using a Vinci Technologies RC4500 centrifuge running at 2,000 rpm for 36 hours in order to achieve an irreducible water saturation. The saturated samples were then wrapped in plastic film to avoid a loss of moisture after which, they were subjected to T2 and PGSTE NMR testing using a 2 MHz NMR Rock Core Analyzer Magritek instrument. All tests were performed at temperatures between 20 – 25°C.

5.4.4.1 The NMR-PSD Testing on glycerol-saturated Berea and Bentheimer samples

As outlined in Section 4.3.4, the NMR-PSD approach comprises of 4 main steps. The first step produces the T2 distribution from which the inverse of the weighted harmonic mean of the T2 distribution $\overline{\left(\dfrac{1}{T2}\right)}$ can be found.
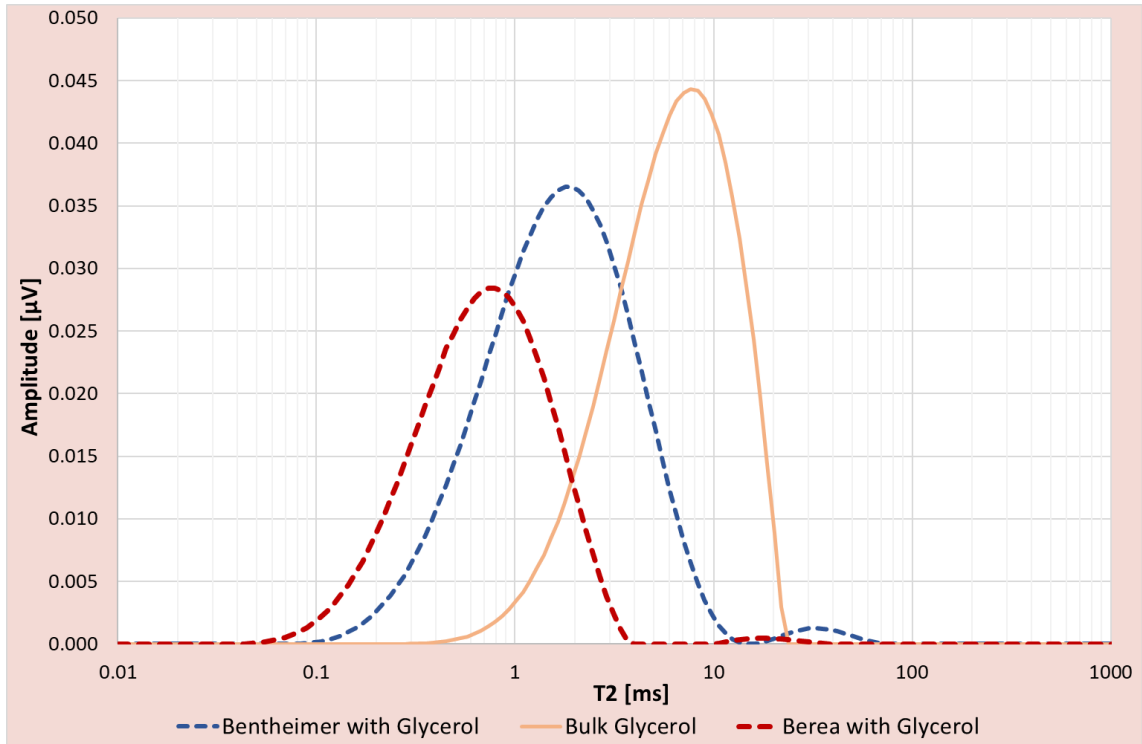
Figure 5-31: The T2 distribution of glycerol-saturated Berea and Bentheimer samples

When water fills the pore space, T2 is essentially a function of only the surface relaxation (T2S) since the bulk relaxation (T2B) can be ignored. This is due to water being a low viscous fluid which is associated with a higher molecular mobility and results in slow relaxation rates and high values of relaxation times.

Figure 5-31 shows that the average bulk relaxation time for glycerol is around 8 -10ms which is comparable to similar values from the literature (Yang *et al.*, 2018). This is expected since glycerol can be considered as a relatively high viscous fluid (1,412 cP at 20°C) which typically tend to have a reduced molecular mobility related to the restriction of the hydrogen nuclei in the high viscous glycerol mass which results in a very fast relaxation rate and therefore faster relaxation rates (lower relaxation times).

Figure 5-31 shows that there are two peaks associated with the NMR relaxation of the Berea and Bentheimer samples. The first peak relaxes before 2ms and 10ms for the Berea and Bentheimer respectively while the smaller second peak relaxes between 10 – 100ms for both samples. The presence of these two peaks indicates that there are two fluid subgroups within the sample having different viscosities.

The portion of the spectra that takes place before 2ms and 10ms for the Berea and Bentheimer respectively is attributed to the relaxation of glycerol which undergoes a very fast relaxation due to both surface relaxation and bulk relaxation (as a result of its higher viscosity). The second peak is attributed to a water signal arising from irreducible water in the pores which tend to have larger relaxation times.

Figure 5-31 also shows that when saturated with glycerol, the Berea sample has a shorter T2 response than that for the Bentheimer sample. This is not unexpected given that the Berea sample has been shown to be comprised of series of smaller pores than the Bentheimer sample. This implies that the shorter T2 response in Berea is a combination of both the high viscous fluid (T2B response) as well as the hydrogen nuclei interacting with the pore walls (T2S response). The Bentheimer has a similar T2 response however it has larger T2 relaxation times when compared to the Berea sample indicating that there are the larger pores within Bentheimer in which the hydrogen nuclei must travel longer distances to interact with the pore walls.

Step 1 of the NMR-PSD Approach also provides a measure of the weighted harmonic mean of the T2 distribution which is calculated using Equation 5-2. The values of $\overline{(T2)}$ for the Berea and Bentheimer samples were found to be 0.68ms and 1.65ms respectively.

The second step involves running a PGSTE experiment at selected diffusion times (t) and plotting the resulting D(t) values against $t^{1/2}$ to obtain the average $\overline{\left(\dfrac{S}{V}\right)}$ ratio using Equation 5-4.

Figure 5-32 shows the linear plots of D(t) against $t^{1/2}$ for the glycerol-saturated Berea and Bentheimer samples while Table 5-19 provides the relevant parameters leading to the calculation of $\overline{\left(\dfrac{S}{V}\right)}$ for the glycerol-saturated Berea and Bentheimer samples.
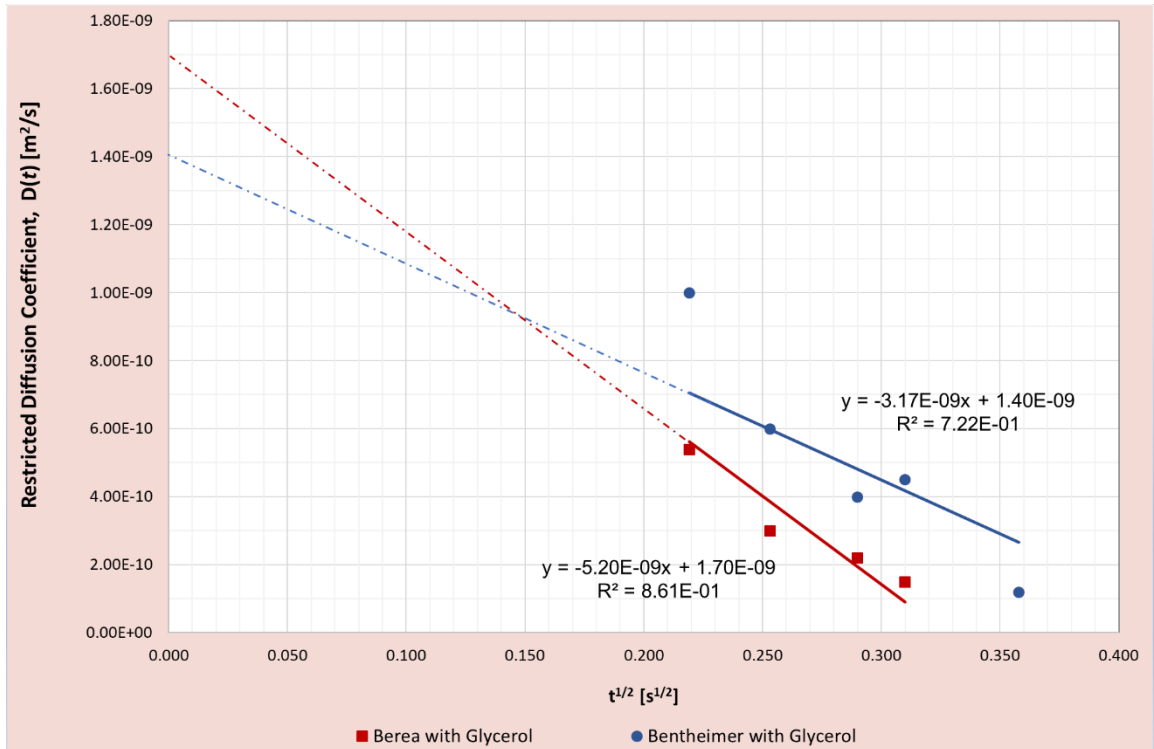
Figure 5-32: The linear plots of D(t) vs $t^{1/2}$ for the glycerol-saturated Berea and Bentheimer samples from the PGSTE Testing

Table 5-19: The average surface area to volume for the glycerol-saturated Berea and Bentheimer samples from the PGSTE Testing

	Berea	Bentheimer
Values from Glycerol-saturated PGSTE Testing		
Gradient [x 10^{-9}]	-5.20	-3.17
D$_o$ [x 10^{-9} m^2/s]	1.4	1.7
$\overline{\left(\dfrac{S}{V}\right)}$ [1/m]	287,441	241,538
Values from Water-saturated PGSTE Testing (Table 5-14)		
$\overline{\left(\dfrac{S}{V}\right)}$ [1/m]	443,129	202,717
Values from PNM		
$\overline{\left(\dfrac{S}{V}\right)}$ [1/m]	472,964	192,806

Table 5-19 presents the $\overline{\left(\dfrac{S}{V}\right)}$ results of the glycerol-saturated PGSTE testing as well

as the related $\overline{\left(\dfrac{S}{V}\right)}$ results from the PGSTE testing of water-saturated samples and

from the PNM. These results show that a wide disparity between the glycerol-saturated PGSTE testing to those obtained from the PGSTE testing of water-saturated samples and from the PNM. This suggests that the glycerol-saturated PGSTE testing should not be used given that they lead to values of surface relaxivity (shown in Table 5-20) which do not robustly reflect the sample characteristics.

Although glycerol-saturated PGSTE testing provide questionable results, the extrapolation back to zero observation time produces an unrestricted diffusion coefficient of glycerol ($D_{o,glycerol}$) that ranges from 1.4 to 1.7 $\times 10^{-9}$ m^2/s which compare well with those available in the literature ($0.8 - 2.0 \times 10^{-9}$ m^2/s) (Tomlinson, 1972).

Using the values obtained for $\overline{\left(\dfrac{1}{T2}\right)}$ and $\overline{\left(\dfrac{S}{V}\right)}$ from Figure 5-32 and Table 5-19, the

surface relaxivities for the glycerol-saturated Berea and Bentheimer samples can be calculated using Equation 4-14. These are given in Table 5-20.

The surface relaxivities (ρ_2) of sandstone material have been shown to vary from 6.4 to 46 μm/s (Dunn *et al.*, 2002; Lonnes *et al.*, 2003; Marschall *et al.*, 1995). These values from the PNM and the water-saturated PGSTE testing fall compare well with these values. However, the ρ_2 values from the glycerol-saturated PGSTE testing are

significantly lower and this is a consequence of both lower $\overline{(T2)}$ values as well as

mismatched $\overline{\left(\dfrac{S}{V}\right)}$ values resulting from the glycerol-saturated PGSTE testing.

As a robust and representative value of ρ_2 is needed to convert the T2 distribution into a PSD, it becomes important to assume a reflective ρ_2 value other than the one resulting from the glycerol-saturated PGSTE testing.

Several options exist for obtaining a more representative ρ_2 value. The easiest and first option will be assuming a ρ_2 value from literature or choosing either the ρ_2 value from the water-saturated PGSTE testing or from the PNM approach given that both

these values are particularly comparable as shown in Section 5-4.3.2 and Table 5-20.

A second viable option is to use the $\overline{(T2)}$ value from the glycerol-saturated T2 test with the $\overline{\left(\dfrac{S}{V}\right)}$ value from the PNM approach to calculate a new ρ_2 value using Equation 4-14. This option is particularly attractive for applications when T2 testing is carried out but when PGSTE is not possible, such as in the case of NMR logging.

Of these two options, the second option was chosen since this approach would be more useful to the remainder of this work (as shown in the Section 6.4). A new ρ_2 value was therefore calculated from the $\overline{(T2)}$ value from the glycerol-saturated T2 test with the $\overline{\left(\dfrac{S}{V}\right)}$ value from the PNM as shown in Table 5-20.

It is important to note that Equation 4-10 (and therefore Equation 4-14 on which the ρ_2 value is based) only applies in the fast diffusion limit when $\left(\dfrac{\rho_2 r}{D_o} < 1\right)$ (Jin *et al.*, 2009; Mitra *et al.*, 1993). Fast diffusion refers to the movement of the hydrogen nuclei in pores that are sufficiently small so that surface relaxation mechanisms take place at a sufficiently slow pace so that a hydrogen nucleus crosses the pore many times before it relaxes [Coates *et al.*, 1999] which increases the probability of the pore being characterised completely. Surface relaxation dominates the overall T2 signal when a nucleus crosses the pore many times before it relaxes which indicates a negligible the bulk relaxation term.

The $\overline{(T2)}$ value from the glycerol-saturated T2 test is however comprised of both surface and bulk relaxations and may therefore lie within a slower diffusion limit suggesting that the nuclei do not make enough contact with the pore walls before relaxing to provide complete pore information. This results in newly calculated ρ_2 values which are significantly lower (~5,000 – 7000 less) than those from the literature as well as the water-saturated PGSTE and PNM approaches as shown in Table 5-20.

Table 5-20: The calculated surface relaxivities for the glycerol-saturated Berea and Bentheimer samples

	Berea	Bentheimer
Values from Glycerol-saturated PGSTE Testing		
$\overline{(T2)}$ [ms]	0.68	1.65
$\overline{\left(\dfrac{1}{T2}\right)}$ [1/s]	1.48	0.61
$\overline{\left(\dfrac{S}{V}\right)}$ [1/m]	287,441	241,538
ρ_2 [µm/s]	0.0051	0.0025
Values from Water-saturated PGSTE Testing (Table 5-15)		
$\overline{(T2)}$ [ms]	86.7	311
$\overline{\left(\dfrac{S}{V}\right)}$ [1/m]	443,129	202,717
ρ_2 from PGSTE Testing [µm/s]	26.0	15.9
Values from PNM (Table 5-18)		
$\overline{\left(\dfrac{S}{V}\right)}$ [1/m]	472,964	192,806
ρ_2 from PNM [µm/s]	24.3	16.7
Values from the combined glycerol-saturated T2 and PNM approaches		
$\overline{(T2)}$ [ms]	0.68	1.65
$\overline{\left(\dfrac{S}{V}\right)}$ [1/m]	472,964	192,806
ρ_2 from combined approach [µm/s]	0.0031	0.0032

Although the newly calculated ρ_2 values are significantly low, these have been used with Equation 4-10 to convert the T2 distribution of the glycerol-saturated Berea and Bentheimer samples into PSDs. Figure 5-33 shows that these PSDs are considerably smaller in pore size from the benchmark water-saturated PSDs owing to the very small ρ_2 values used in Table 5-20. Despite the considerable difference in pore size, there is a substantial agreement in the shape between the glycerol-saturated and water-saturated PSDs.

This similarity in shape suggests that perhaps shifting the glycerol-saturated PSDs to the right would result in more representative PSDs (that is, closer to the values obtained from the water-saturated PSDs). This idea prompted the development of an empirical NMR Transform which would be capable of obtaining more representative PSDs of samples saturated with fluids more viscous than that of water.
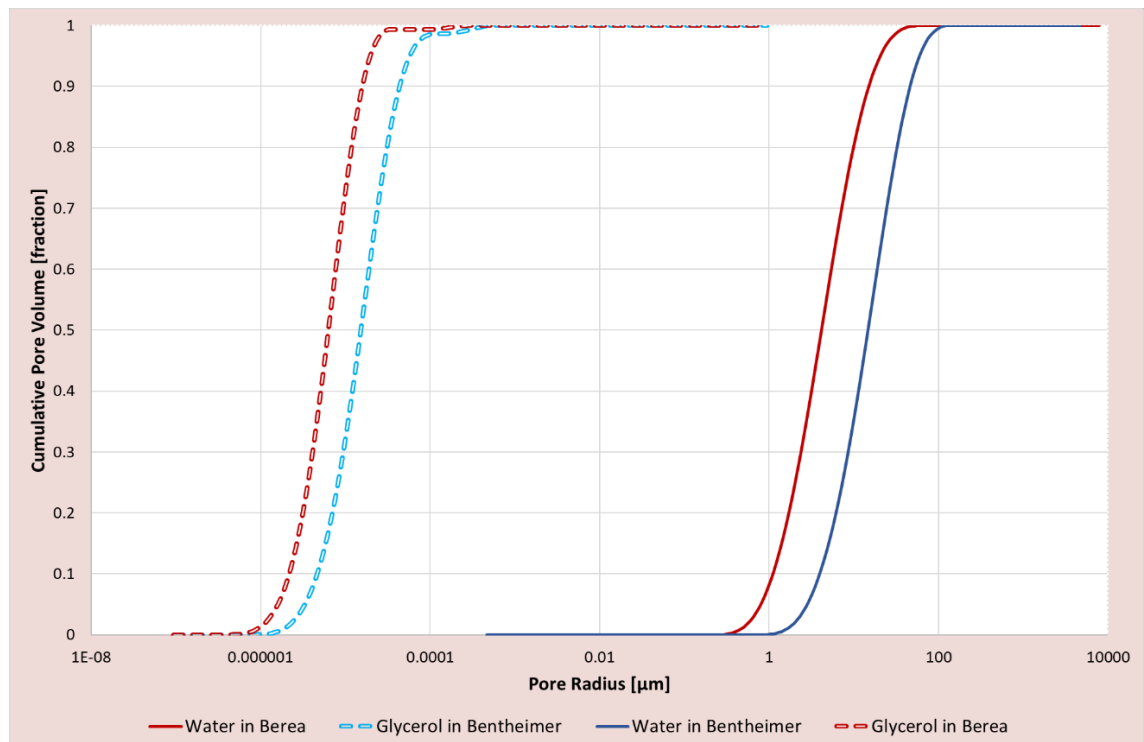
Figure 5-33: The Cumulative PSDs of the glycerol-saturated Berea and Bentheimer samples

A number of NMR parameters and fluid properties (viscosity, density, molecular weight and hydrogen index) were considered during the development of the NMR Transform and after numerous iterations the following empirical NMR Transform based on fluid viscosity and $\overline{(T2)}$ was developed.

$$\textbf{\textit{Empirical NMR Transform}} = 16.5\mu^{1.5}\overline{T2} - 550,000 \qquad [5\text{-}8]$$

where µ is the viscosity of the fluid [cP] and $\overline{(T2)}$ is the weighted harmonic mean of the T2 distribution [ms].

When multiplied by the pore radius, this empirical transform is capable of shifting PSDs (to the right) as shown in Equation 5-9.

$$r_{transformed} = \left(\textit{Empirical NMR Transform}\right) x \; r_{in-situ\; fluid}$$

$$\therefore r_{transformed} = \left(16.5\mu^{1.5}\overline{T2} - 550,000\right) x \; r_{in-situ\; fluid} \qquad [5\text{-}9]$$

With the values of $\overline{(T2)}$ from Table 5-20 and the viscosity of glycerol being 1,412 cP (at 20ºC), the empirical NMR transforms for the glycerol-saturated Berea and Bentheimer samples were calculated to be 41,810 and 891,006 respectively. These values were then used to transform the PSDs of the glycerol-saturated Berea and Bentheimer samples which are shown in Figure 5-34.

Figure 5-34 shows that the empirical transform can result in robust PSDs which are exceptionally comparable to the benchmark water-saturated PSDs. This information is particularly useful for NMR logging and for other applications in which it is easier to test samples with their in-situ fluids which may not necessarily have low viscosities.

Although the empirical transform has been successful in shifting the glycerol-saturated PSDs towards the more representative water-saturated PSDs, it is important to recognise that this transform has been developed under the limited conditions of one fluid type and one viscosity and therefore may not be applicable to samples having varying fluid characteristics. This is examined in further detail in Chapter 6 (Section 6.4).
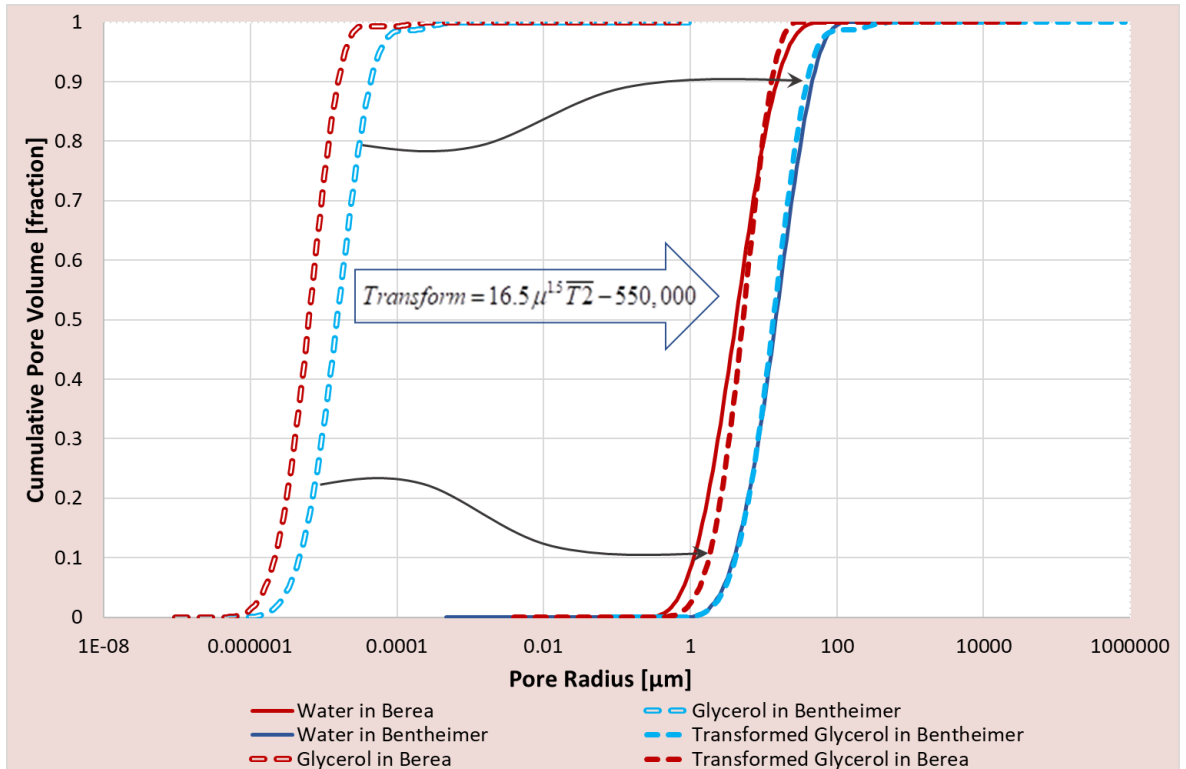
Figure 5-34: The Cumulative PSDs of the ***transformed*** glycerol-saturated Berea and Bentheimer samples

5.4.5 Discussion of the NMR Approach used in this work

NMR measurements has been shown to obtain robust measure of the pore size (Kleinberg, 1996; Mao *et al.*, 2009; Slijkerman and Hofman, 1998; Sorland *et al.*, 2007). These measurements are typically made on core samples saturated with distilled water or brine (Sorland *et al.*, 2007) since the T2 response to water and brine correlates well with surface measurements of the pore space.

Although a more detailed discussion is provided in Chapter 8, an initial review of the NMR findings on the water-saturated Berea and Bentheimer samples indicate that these results compare well to the values quoted in the literature and to the results of the MICP Testing (Section 5.2) and PNM Testing (Section 5.3) and lead to a high confidence of the results as a robust method of PSD determination.

One opportunity to strengthen this approach lies in the identification of a more representative pore shape factor. When no other information is available, pores are commonly assumed to be spherical which may simplify the complex assortment of

shapes and geometries found in real porous media (Vavra *et al.*, 1992) and tend to misrepresent the actual morphology which exists.

Dedicated pore shape factors can be found using selected algorithms of image acquisition software like Avizo® Fire. An examination of the pore space using PNM approaches shows that the average shape factor for the Berea and Bentheimer samples are 4.3 and 2.4 respectively. This implies that many of the pores with the Berea sample tend to be cubic in shape with rounded corners and that the pores of the Bentheimer sample tend to be either tubular or capsular in shape. This can affect the robustness of the NMR-PSD approach which is further discussed in Chapter 7.

The NMR-PSD approach is also limited to the use of low viscous fluids since these minimise the contribution of the bulk fluid relaxation and simplify the overall T2 signal as a sole function of the surface relaxation. This reduces the use and value of NMR data for many applications within the petroleum industry, notably that of NMR logging and in other applications in which it is easier to test samples with their in-situ fluids such an unconsolidated oil sand material.

The development and successful trial of an empirical NMR transform in this work overcomes several of these limitations and is therefore valuable to the petroleum industry. Although a number of NMR parameters and fluid properties (related to viscosity, density, molecular weight and hydrogen index) were considered when developing the transform, the most appropriate form was found to be a function of only the fluid viscosity and the weighted-harmonic mean of the T2 as shown in Equation 5-8.

Despite being based on a limited set of conditions related to fluid type and viscosity, this transform has been effective in shifting the glycerol-saturated PSDs of Berea and Bentheimer towards the more representative water-saturated PSDs. Further work to investigate the potential of similar success with the Athabasca Oil Sand material is examined in further detail in Section 6.4.

CHAPTER 6

The Application of the MICP, PNM and NMR Methods to the AOS Sample

6.1 Introduction

The results and analysis when the MICP, PNM and NMR approaches were applied to the well-studied Berea and Bentheimer sandstone materials are presented in Chapter 5. Given that these materials are consolidated and generally homogeneous in nature (Bera *et al.*, 2011; Peng *et al.*, 2012; Wilson, 2004), they help serve as a benchmark which can lead to a refinement of the PNM and NMR methods allowing them to be applied robustly to a wider range of materials.

A good example of this refinement is the development and successful trial of an empirical NMR transform which overcomes the limitations of using only water and brine to determine the PSD from NMR testing. Although not developed on a wide range of materials and fluids, this transform can produce a robust PSD for the Berea and Bentheimer samples when they are saturated with a relatively high viscosity fluid. This chapter applies the use of this transform to an Athabasca Oil Sand (AOS) sample containing its original high-viscous bitumen fluid. The successful use of this transform to derive the PSD of the AOS sample will be valuable to the petroleum industry, particularly in the areas of NMR logging and in-situ fluid core analysis.

Another example of where the benchmark testing of the Berea and Bentheimer samples has proved useful is the development of a recommended PNM practice for homogenous and heterogeneous materials. This was developed based on key findings which show that the REV for porosity also holds true for PSD and that small changes in the threshold value (within the range of ±10%) do not significantly affect the PSD.

These outcomes allow a wider range of materials to be studied in a robust and timely manner and this chapter attempts to investigate the effectiveness of the modified PNM and NMR approaches described above towards obtaining the porosity and PSD of an Athabasca Oil Sand (AOS) core sample.

6.2   MICP Testing of the AOS sample

MICP testing involves the injection of mercury into a sample that has been cleaned of all original fluids. The cleaning and MICP testing were performed by Core Laboratories U.K. Ltd using the MicroMeritics Porotech IV (MMP IV) apparatus. The samples were cleaned using the Modified Dean-Stark method which is also known as the AOSI-3573 technique (Alberta Oil Sands Technology and Research Authority, 1974) as outlined in Section 4.1.2.

6.2.1   MICP Results: Porosity and Capillary Pressure

The MICP test provides a measure of effective porosity as the volume of mercury imbibed quantifies the amount of interconnected pore space. Table 6-1 provides the corresponding data for the AOS samples tested:

Table 6-1: MICP Porosity Determination of the AOS sample

	AOS Sample
MICP Injected Volumes:	
Injected Bulk Volume [cm^3]	3.724
Injected Pore Volume [cm^3]	1.192
Porosity from MICP Testing [%]	32.0

As mentioned previously, it is important to note that the AOS sample was received in an unfrozen state and as such, may have undergone a prolonged gas expansion possibly leading to severely dilated pore volumes.   The MICP porosities in Table 6-1 however compare favourably to the values quoted in the literature (Bell *et al.*, 2012; Collins, 2005; Dusseault, 1980; Wong *et al.*, 2004; Wong, 2005) where the average in-situ porosity of AOS varies from 30 – 35%.

The results of the MICP test on the AOS sample are shown in Figure 6-1. It can be seen that the displacement pressures (which are the minimum pressures required to force the mercury into the largest pores) are in the vicinity of 0.5 psia. This value is within the 0.6 – 2.0 psia range for unconsolidated sands quoted by Shafer and Neasham (2000).

These authors state that such low displacement pressures are because of the general high permeabilities which exist.

The middle section of the curve is generally flat ranging from 1 – 10 psia indicating that the grains are well-sorted and the samples are fairly homogeneous (Elshahawi *et al.*, 1999). The curve however becomes progressively steeper at around an 8% mercury saturation which indicates that increasingly smaller pores are being accessed. The curve is also a smooth progression having a sharp pressure rise as it tends towards infinity. This is probably due to the reduced integrity of the grain matrix as the high pressure exceeds the material's strength.
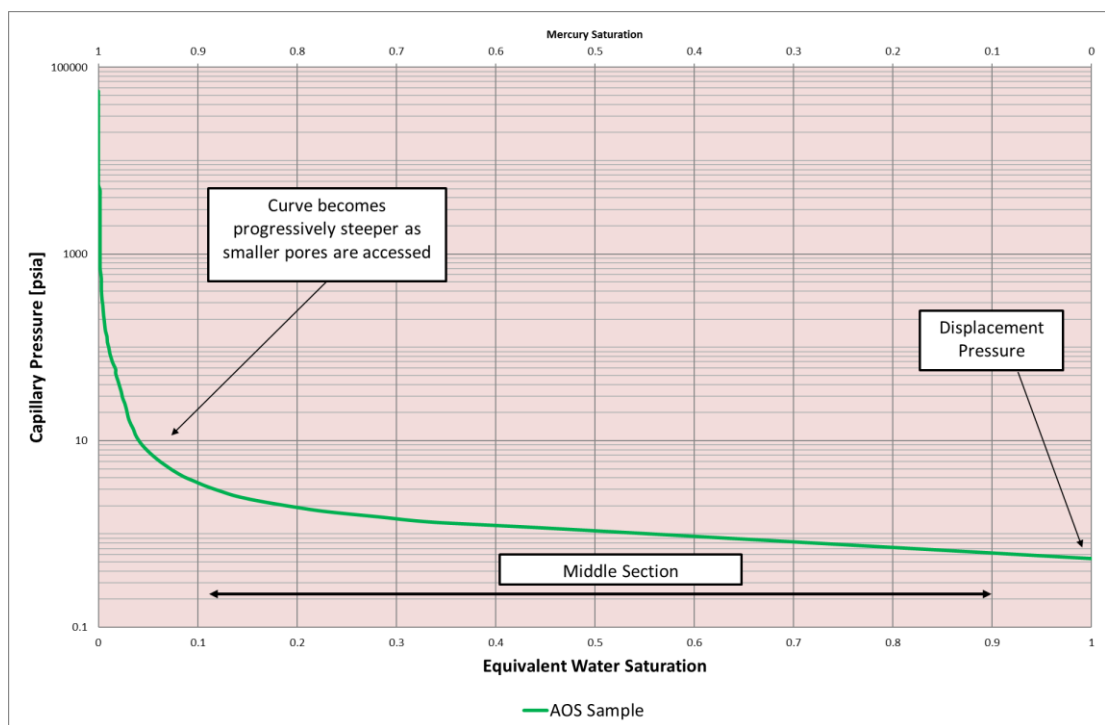
Figure 6-1: MICP Capillary Pressure Results for the AOS Sample

6.2.2 Pore Size Distribution

As outlined in Section 4.1.3, Equation 2-3 can be used to obtain the equivalent (cylindrical) pore radius:

$$r_t = \frac{2\sigma\cos\theta}{P_c} \qquad [2\text{-}3]$$

A contact angle of 140° and an interfacial tension of 480 dynes/cm was used since it was assumed that all of the in-situ bitumen had been removed resulting in air and mercury

being the wetting and non-wetting fluids respectively (Vavra *et al.*, 1992). The results of the pore size distribution (PSD) are shown in Figure 6-2.

Further statistical analysis of this PSD is provided in Chapter 7 (Section 7.2) which also presents the PSD results of the NMR and PNM Testing of the AOS sample. The NMR and PNM Testing of the AOS sample are described in Sections 6.3 and 6.4 below.
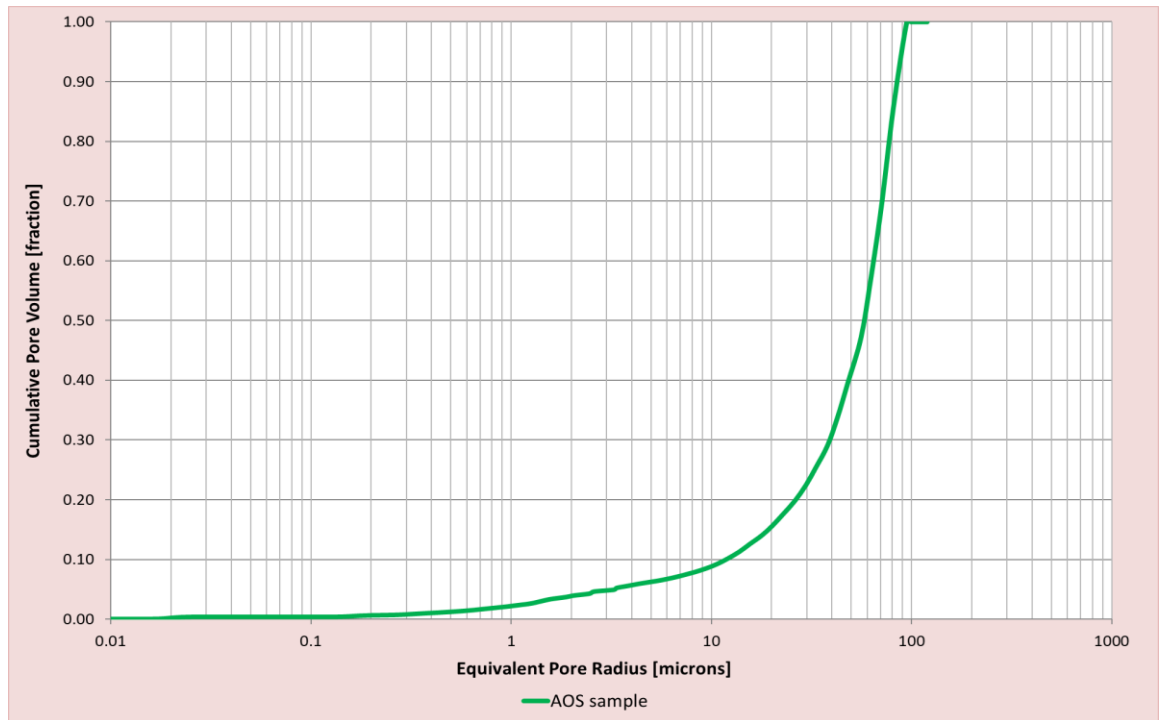
Figure 6-2: The Cumulative PSD from the MICP Testing for the AOS sample

6.3   Pore Network Modelling of the AOS sample

Micro-CT scanning generally requires little to no prior sample preparation (Ketcham and Carlson, 2001) and so is ideal to the testing of samples containing their in-situ fluids. Although bitumen is immobile at temperatures between 20 – 25°C (the temperatures at which the PNM was carried out), it was important that the fluids did not leak from the sample and so the sample was wrapped in plastic film. These were then placed inside acrylic cylinders having a 1.0mm thickness and subjected to micro-CT testing using a Skyscan-Bruker 1172 model micro-tomography system.

2240 micro-CT images were acquired in a time of 10 hours having a resolution of 5 microns/pixel. Once these images had been acquired, PNM of the AOS sample was then carried out using the Recommended Practice for Heterogeneous Samples as outlined in Table 5-11. The heterogeneous method was chosen as no related information was obtained from the University of Alberta regarding the sample's homogeneity.

6.3.1 Pore Size Distribution of the AOS sample from PNM

Step 1 of the Recommended Practice for the PNM of Heterogeneous Samples requires a subsampling at either 2000 voxels or 20% of the total scanned volume (whichever is larger) to produce the Maximum Region of Interest (MROI). Figure 6-3 shows the subsampling of 2000 pixels from a micro-CT scan (in false colour) at Slice 1000.
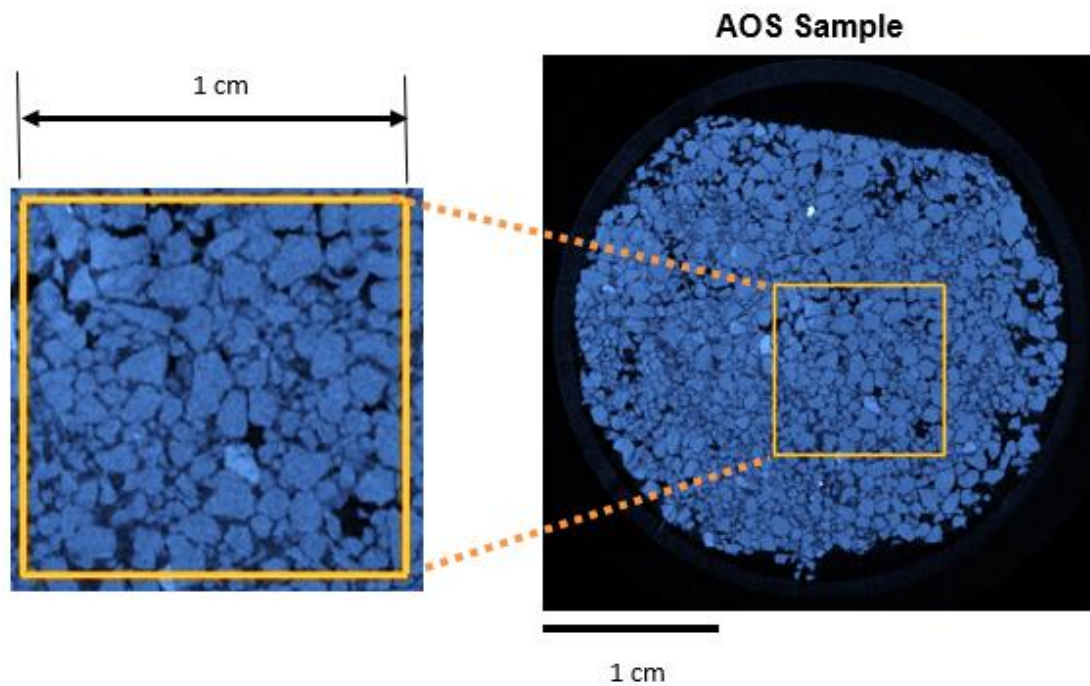
Figure 6-3: An AOS Sample Scan at Slice 1000 showing the location of the subsampled ROI (2000 pixels) in the x-y plane

Steps 2 and 3 involve filtering the image to remove noise and then segmenting using a Thresholding Approach to identify the Automatic Threshold (AT) value based on the valley-emphasis method outlined in Section 4.2.3.3. Step 4 involves a visual comparison of the segmented and original images. If the segmented and original images compare well (based on the user's perception), then the AT is accepted. Otherwise, the threshold value is varied using Interactive Thresholding until a favourable comparison is obtained.

Figures 6-4A and 6-4B show that the pore space is adequately captured at the AT which corresponds to a greyscale value of 86. This threshold was then used to segment the MROI on which the REV analysis in Steps 5 - 8 was performed.
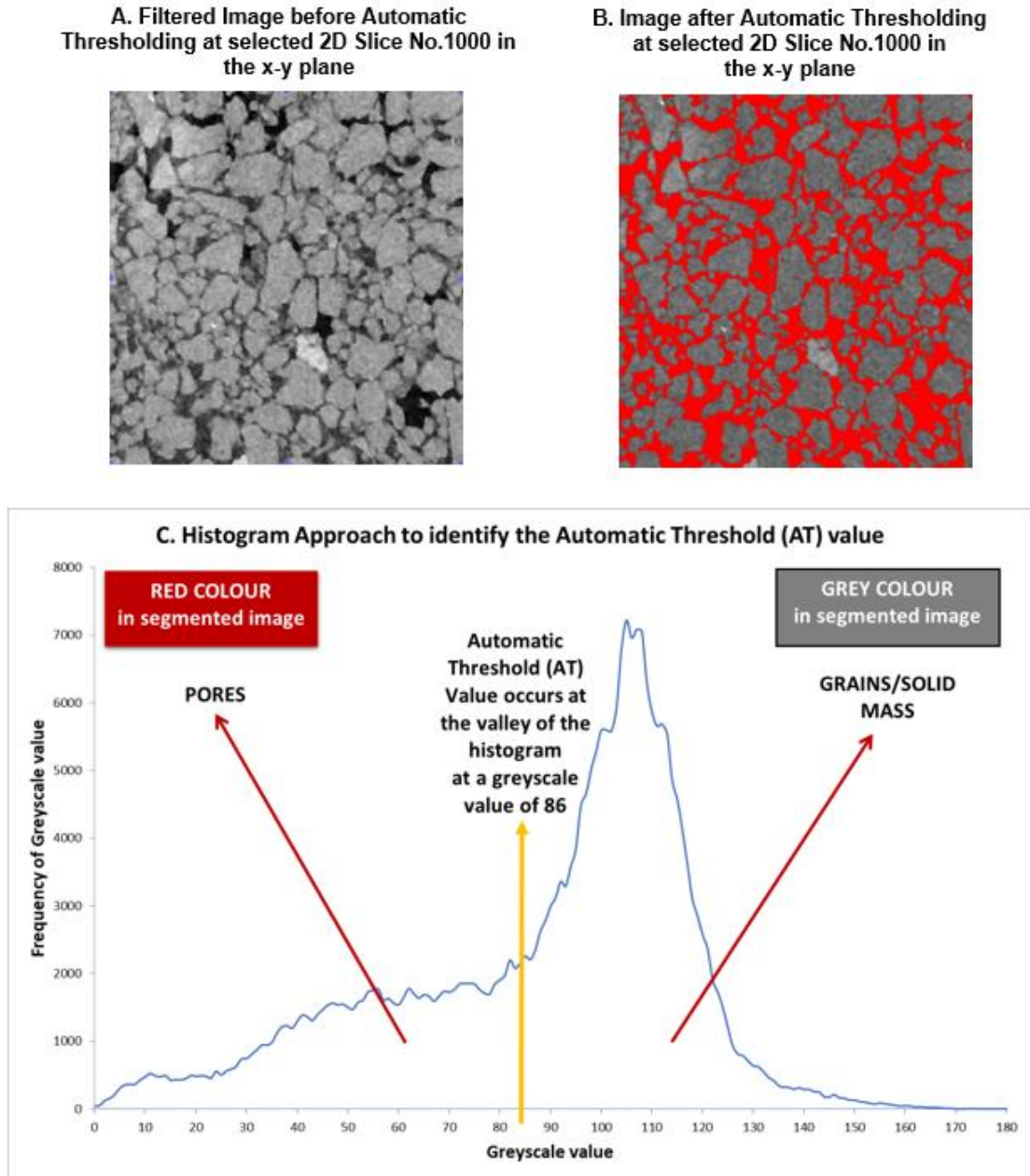
Figure 6-4: Threshold Identification and Segmentation Results at the MROI for the AOS Sample

As outlined in Section 4.2.4.1, Step 5 involves sectioning the 2000-voxel MROI cube into 20 ROIs. An initial cube of length 100 voxels (0.5 mm) is chosen as the first ROI with this volume being increased by 100 voxels in all directions until the 2000 voxel MROI of

(~ 10mm) was reached. Figures 4-7B and 4-7C show the 27 orientations which were chosen as the starting locations of the first 100-voxel ROI.

Once the ROIs were identified, Step 6 provides the ROI porosity for each incremented ROI. Figure 6-5 shows the porosity distribution across the 540 ROIs investigated and indicates that the PNM porosity of the AOS sample was 29.1%. Step 7 then involves calculating the percent porosity change at each ROI increment which is shown in Figure 6-6.
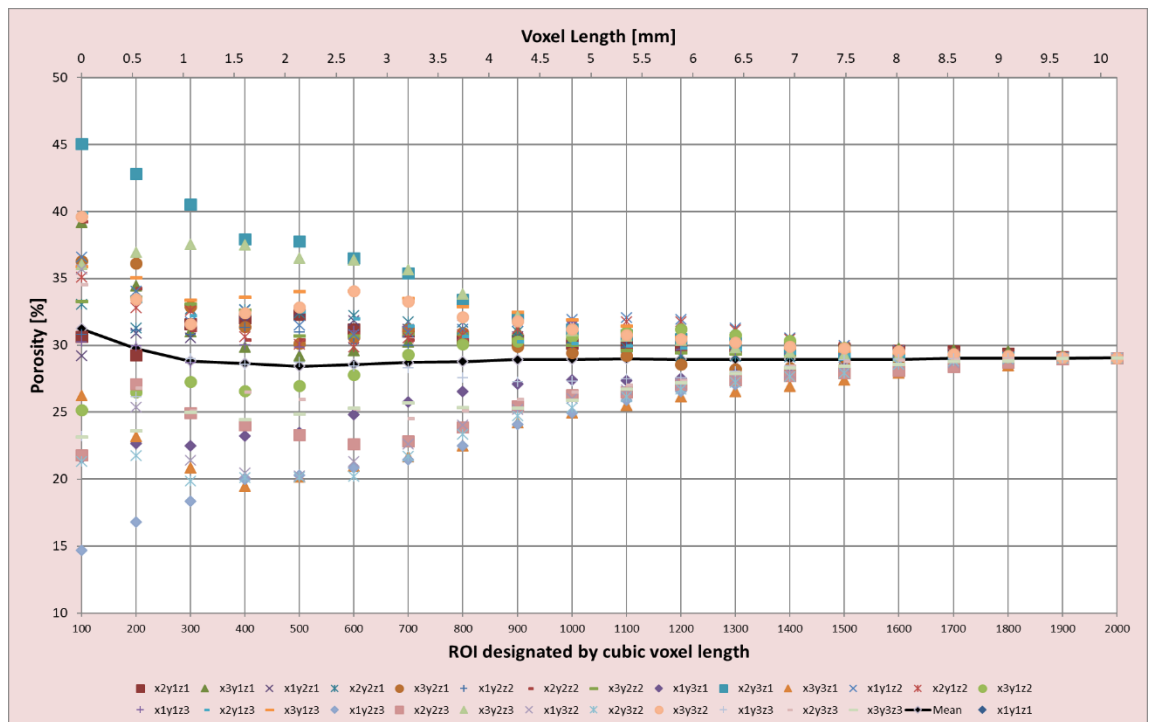
Figure 6-5: ROI Porosity Evaluation for the AOS Sample at the Automatic Threshold

Step 8 involves selecting the REV when the percent porosity change is consistent at ±5% for successive ROIs. This occurred at a 900-voxel ROI as shown in Figure 6-6 indicating that the REV was found at 900 voxels (4.5 mm^3).

The last step of the recommended practice, Step 10, involves extracting the pore network and obtaining the PSD. Figure 6-7 shows the resulting PSD of the 40,853 pores which were identified within the REV of the AOS sample during the PNM process. Further statistical analysis of this PSD is provided in Chapter 7 (Section 7.2) which also shows the PSD results of the MICP and NMR Testing of the AOS sample from Sections 6.2 and 6.4 respectively.
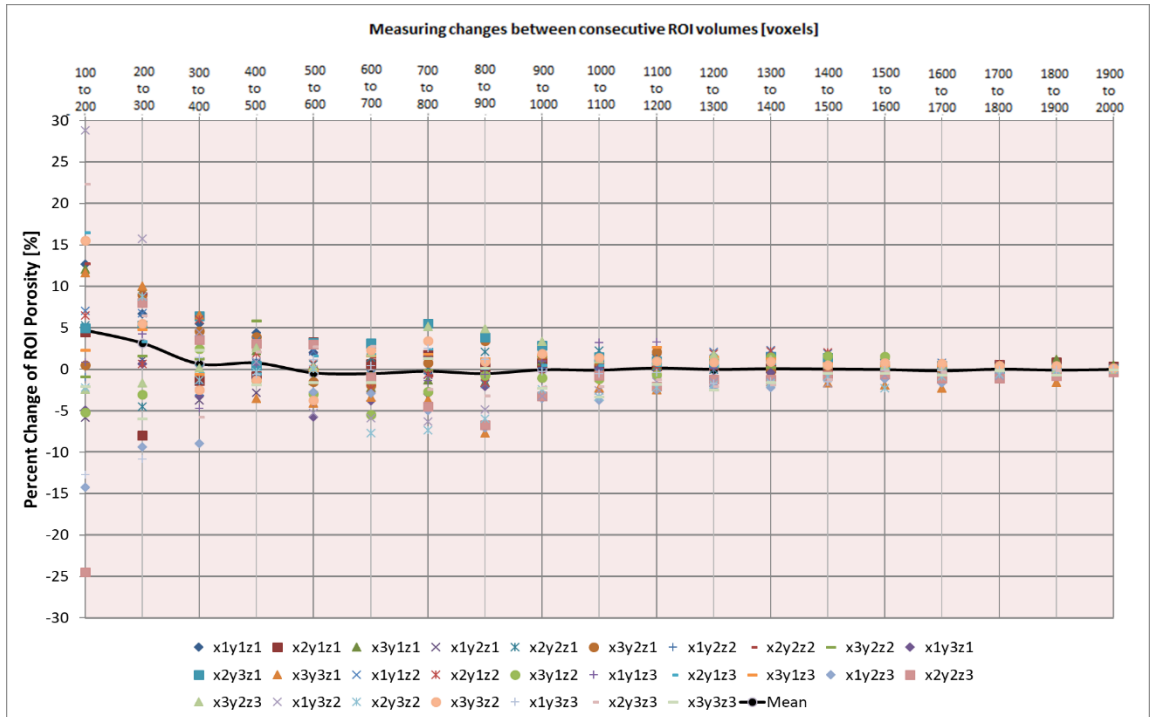
Figure 6-6: Identifying the REV at the Automatic Threshold Value for the AOS Sample
using a Percent Change Approach
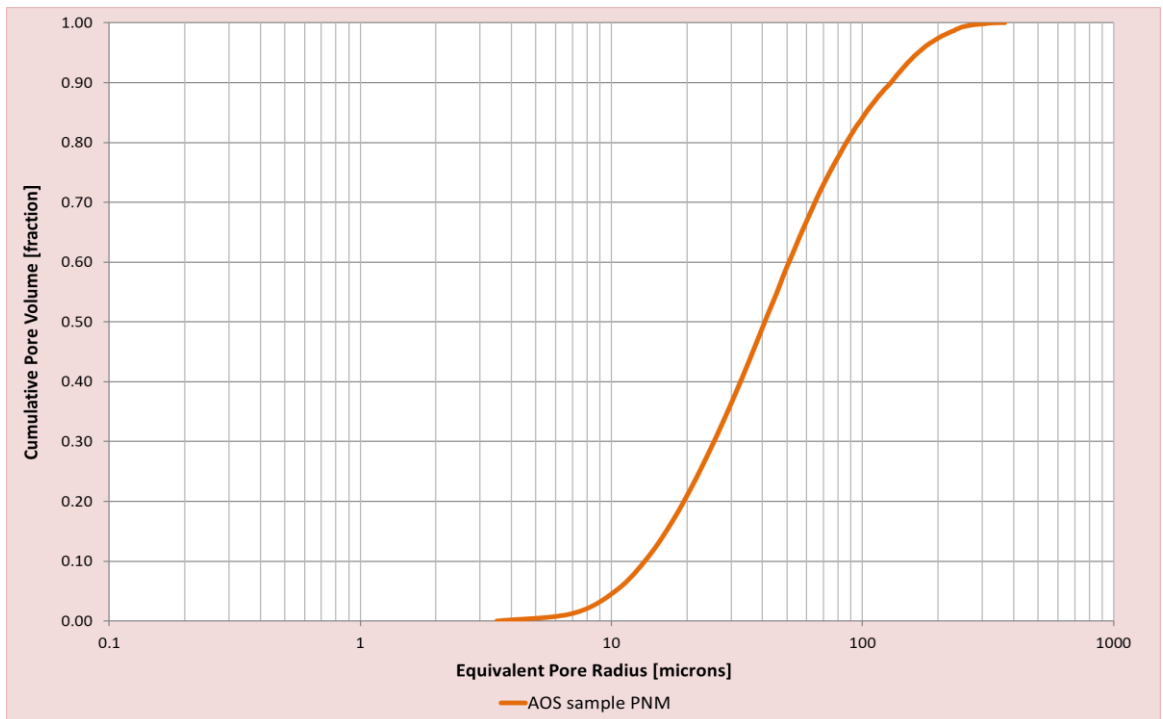
Figure 6-7: The Cumulative PSD from PNM for the AOS sample

170

6.3.2 Pore Shape Characteristics of the AOS from PNM

As outlined in Section 5.4.3, the PNM approach is also able to identify a shape factor (F_s) and an average surface area to volume $\left(\overline{\dfrac{S}{V}}\right)$ value independently from the NMR testing. This is useful in situations when PGSTE testing cannot be performed or when there are uncertainties regarding the use of a spherical pore to obtain NMR PSDs. Figures 6-8 and 6-9 show the F_s and $\left(\dfrac{S}{V}\right)$ distributions of the 40,853 pores identified in 900 REV of the AOS sample.
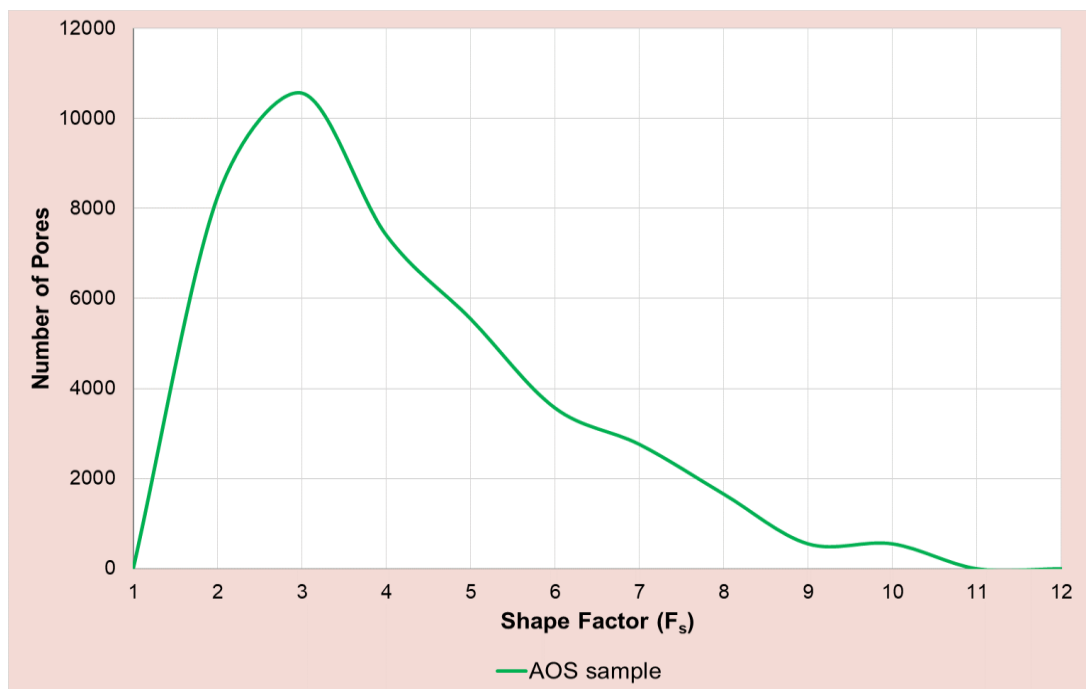
Figure 6-8: Shape Factor Analysis of the pores within the REVs for AOS sample

The weighted average F_s was found to be 3.3 indicating that a majority of the pores tended towards sphericity. This allows equations 4-11 and 5-5 to be refined as shown below for the AOS sample to use a more realistic and representative pore shape factor to derive the PSD.

NMR PSD equation for the AOS sample:
$$\frac{1}{T2} = \rho_2 \left(\frac{3.3}{r}\right) \qquad \text{[6-1]}$$

The $\overline{\left(\dfrac{S}{V}\right)}$ was found to be 177,157 m^{-1} which is reflective of the larger pores when compared to the Berea and Bentheimer samples. No similar $\overline{\left(\dfrac{S}{V}\right)}$ data could be found in the literature to substantiate the value found from PNM.
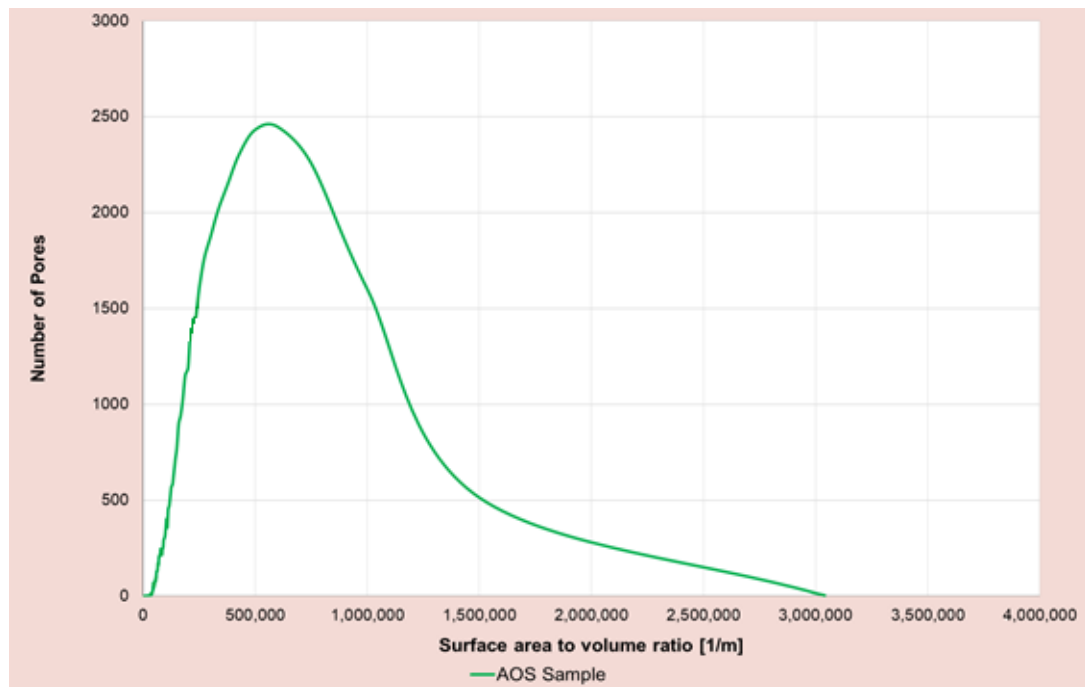
Figure 6-9: The distribution of the surface area to volume ratio of the pores within the AOS sample REV

6.4   NMR Testing of the AOS sample

A modified approach for obtaining the PSDs of samples which are saturated with fluids having viscosities higher than that of water is outlined in Section 5.4.4. This attempts to extend the NMR-PSD approach provided in Section 4.3.4 which is limited to the use of low viscous fluids (like water and brine) since these minimise the contribution of the bulk fluid relaxation and simplify the overall T2 signal as a sole function of the surface relaxation.

Obtaining NMR PSDs on formations and cores that still contain their in-situ fluids (which may not necessarily be comprised of low viscous fluids) is valuable to the petroleum

industry and in particular for NMR logging and other applications in which it is easier to test samples with their in-situ fluids such an unconsolidated oil sand material.

This forms the rationale for this section and the AOS sample was therefore subjected to NMR testing with its in-situ fluids. The sample was wrapped in plastic film and then subjected to T2 and PGSTE NMR testing using a 2 MHz NMR Rock Core Analyzer Magritek instrument. All tests were performed at temperatures between 20 – 25°C.

Figure 6-10 shows the T2 distribution of the AOS sample from the T2 NMR testing. Unfortunately a sample of the bulk bitumen fluid contained in this AOS sample was not available for testing. From email correspondence however (Al-Wahaib, 2012), this bulk bitumen was reported to have a viscosity of 10870 cP at 25°C.

At this viscosity, it is expected that the bulk bitumen will typically relax at less than 10ms and have an average weighted-harmonic T2 relaxation ($\overline{T2}$) of around 1ms (Kantzas, 2009). This is a low when compared to a bulk water signal and is a result of the restriction of the hydrogen nuclei within the high viscous bitumen mass leading to very fast T2 relaxation times.
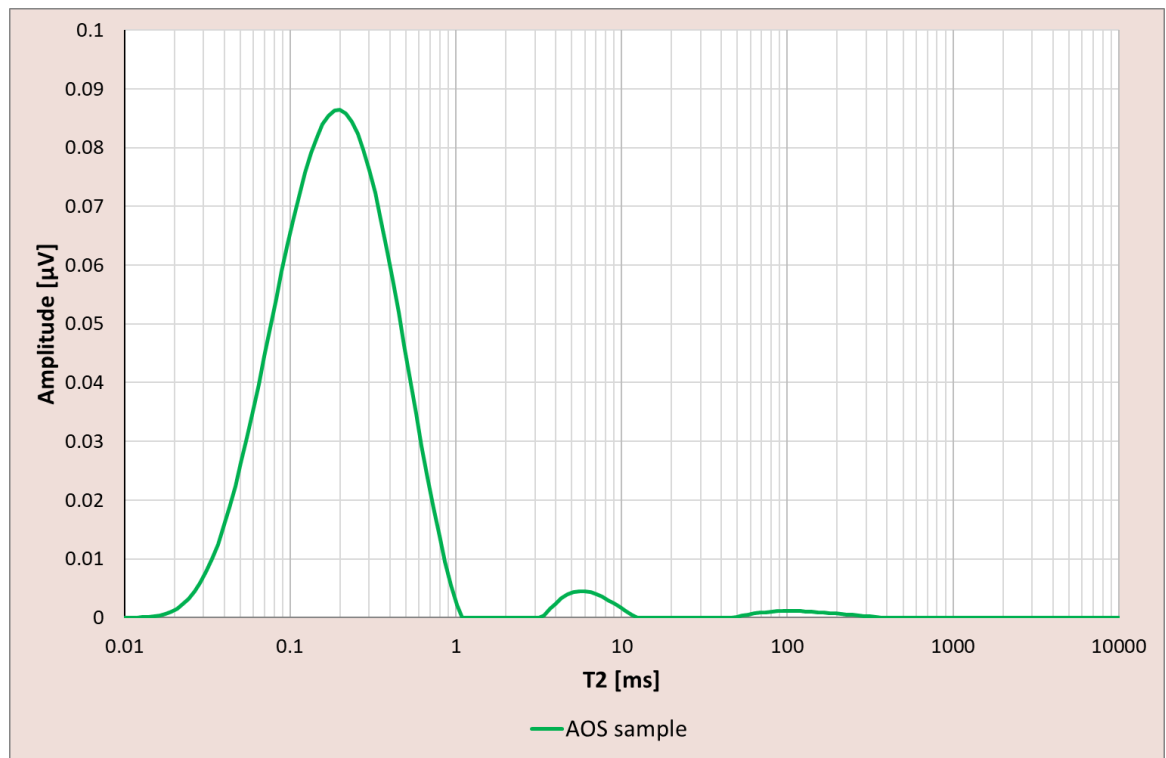
Figure 6-10: The T2 distribution of the AOS sample

Figure 6-10 shows that there are three peaks associated with the NMR relaxation of the AOS sample. The first peak relaxes before 1ms, the second peak between 3 – 10ms and the last peak between 50 – 300ms. The presence of three peaks indicates that there are three fluid subgroups within the sample with varying viscosities.

The portion of the spectra that takes place between 0.01 – 1ms denotes a typical bitumen response (Cabrera, 2008; Kantzas, 2008) where due to its higher viscosity, the bitumen in the pores undergoes a very fast relaxation due to bulk relaxation processes. Bryan *et al.* (2008) conducted experiments which show that the relaxation times for bulk bitumen generally occur at approximately the same T2 locations whether the fluid exists in bulk or in porous media (shown in Figure 2-3). This is attributed to the high bitumen viscosity and implies that the relaxation due to surface effects for these oil sands is negligible. The second peak indicates that the AOS sample is perhaps associated with lighter hydrocarbon elements and suggests the presence of a gaseous phase from gas exsolution. The third is attributed to a water signal arising from connate water in the pores.

The amplitude distribution of the signal associated with each peak can provide an idea of the amounts of hydrogen-bearing fluid in place (Kantzas, 2008). In terms of the three subgroups observed, the largest peak represents approximately 95% by volume of the entire sample (which is assumed to be bitumen) while the other two peaks represent a combined 5% amount by volume.

The value of $\overline{(T2)}$ for the AOS sample from Figure 6-10 was found to be 0.2ms. This $\overline{(T2)}$ value was used to calculate the surface relaxivity (ρ_2) using the $\overline{\left(\dfrac{S}{V}\right)}$ value from the PNM as shown in Table 6-2.

Although no similar data regarding the ρ_2 of the AOS could be found in the literature, it is expected that the calculated ρ_2 value in Table 6-2 is much lower than the true ρ_2 since the $\overline{(T2)}$ value used comes from the AOS sample being saturated with high-viscous bitumen. This results in a much shorter T2 distribution and hence a much lower $\overline{(T2)}$ value than if the sample were saturated with low-viscous water or brine.

Table 6-2: The calculated surface relaxivity for the AOS sample

	AOS Sample
$\overline{(T2)}$ [ms]	0.2
$\overline{\left(\dfrac{1}{T2}\right)}$ [1/s]	5.0
$\overline{\left(\dfrac{S}{V}\right)}$ [1/m]	177,157
ρ_2 [µm/s]	0.028

Despite this, the ρ_2 from Table 6-2 was used to convert the T2 distribution shown in Figure 6-10 into a PSD as described in Section 5.4.4.1. The resulting PSD is shown in Figure 6-11 (curve A). This PSD is very small when compared to the PSDs from the MICP and PNM testing due to the small value of ρ_2 used. This PSD was then shifted using the transform developed in Section 5.4.4.1 (Equation 5-9) with the final NMR PSD for the AOS sample being denoted by the curve labelled B in Figure 6-11.

Although a more detailed discussion is provided in Chapter 7, the transformed NMR PSD compares very well to those obtained from the PNM and MICP approaches particularly in the pore radii range of 10 – 100 microns.

The transformed NMR PSD distribution however shows that very large pore radii within the range of 1,000 – 100,000 exist. This anomaly is due to the T2 distribution shown in Figure 6-10 having a small peak ranging from 50 – 300ms. This is attributable to connate water in the pores. The amplitude of this water signal is small as the connate water comprises less than 2% of the fluid in the pore space (deduced from the amplitude of the overall T2 signal as described earlier).

Although water exists in the pore space, the $\overline{(T2)}$ value of the entire distribution is small (being 0.2ms which is far removed from the 50 – 300ms water signal) and is due to the large percentage of bulk bitumen (~95% deduced from the amplitude of the overall T2 signal as described earlier) in the sample which skews the T2 distribution towards shorter

relaxation times. This small $\overline{(T2)}$ value causes the calculated surface relaxivity to be small (Table 6-2) which results in a large transform value to shift the bitumen-saturated NMR PSD towards more representative pore size values.
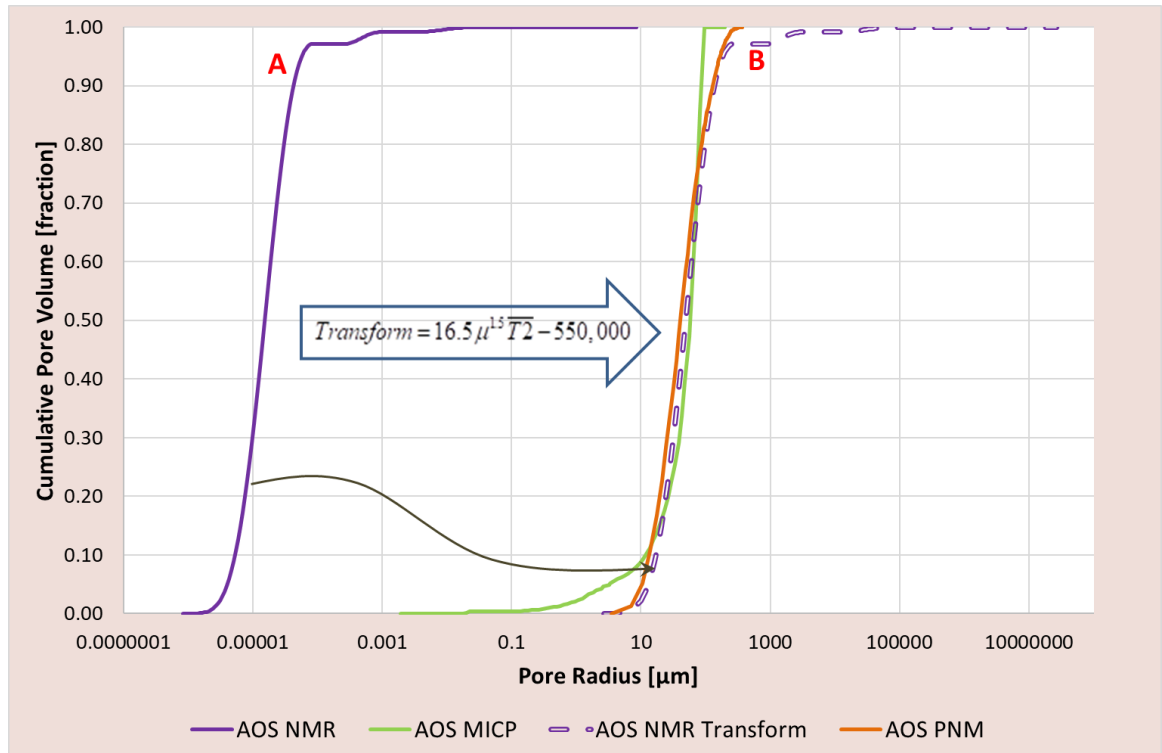
Figure 6-11: The Cumulative PSDs of the AOS sample from the PNM and MICP approaches, from the NMR testing before being transformed (Curve A) and from the NMR testing after transformation (Curve B)

Water-filled pores will however reflect the '*true*' pore size as the signal will be attributable to only T2S surface relaxation. Given that the transform was developed to shift bitumen-filled pores, applying the transform to water-filled pores will therefore exaggerate the pore size of these pores as seen in Figure 6-11. This leads to pore radii of 1,000 – 100,000 which do not exist.

This, as well as a more detailed comparison of all three methods, are discussed in Chapter 7.

DISCUSSION AND CONCLUSIONS

7.1   Introduction

The general objective of this work was to evaluate the pore space of selected sandstone samples using the methods of MICP, PNM and NMR.   These methods generally measure varying aspects of the pore space with regards to the fluid type which should saturate the pore space, pore dimension measurements (i.e. measures of pore throat versus pore body), the destructive nature of the test as well as the resolution and connectivity of the pore space.   A consideration of these aspects was needed to have confidence in the use of each method to determine porosity and PSD as well as to inform the choice of one method over another for petroleum engineering applications.

This chapter presents, summarises and discusses the key findings from Chapters 5 and 6 which relate to the testing of the Berea, Bentheimer and AOS samples using the MICP, PNM and NMR approaches.   The main objective of this chapter is to establish the capability of each method to derive independent and robust representative measures of porosity and PSD of the porous media under study.

7.2   Collating the porosity and PSD information from the MICP, PNM and NMR approaches from Chapters 5 and 6

The PSDs for the Berea, Bentheimer and AOS samples have been presented individually in the earlier chapters of this thesis.   Figures 7-1 to 7-3 collate these in order to provide an easier comparison of the PSDs across each method.   The PSDs in the figures have been obtained using:

- MICP testing;
- the PNM approach;
- water-saturated NMR testing using a spherical pore shape factor of 3;
- water-saturated and bitumen-saturated NMR testing using the pore shape factor derived from PNM (from Equations 5-7A and 5-7B and 7-1); and

- the empirical NMR transform developed in this work (Equation 5-9) to transform glycerol-saturated Berea and Bentheimer PSDs as well as the bitumen-saturated AOS PSDs. Both these transformed NMR PSDs have assumed a spherical shape factor of 3.

The PSDs in Figure 7-1 to 7-3 were then subjected to statistical analysis using the approaches outlined in Section 4.1.4 with the results shown in Tables 7-1 to 7-3 for the Berea, Bentheimer and AOS samples. These are discussed below in tandem in the following sections and form the basis of assessing the capability of each method to derive independent and robust measures of porosity and PSD.
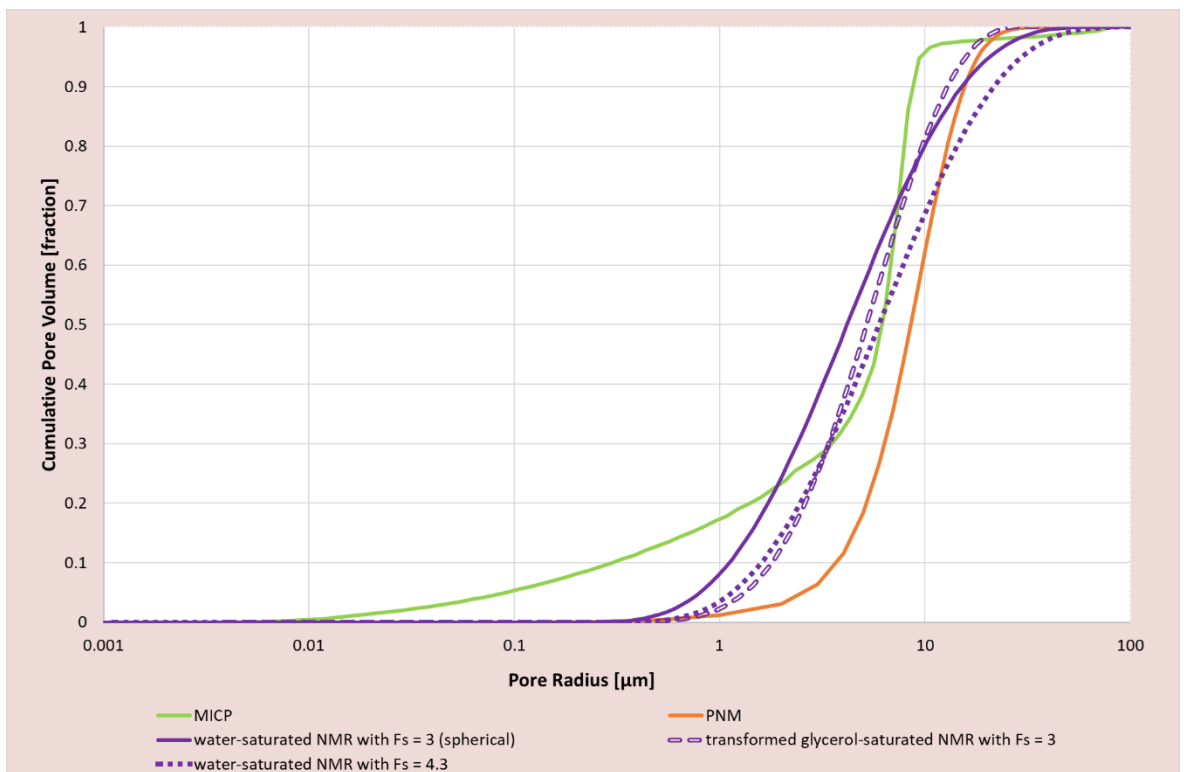
Figure 7-1: The Cumulative PSDs of the Berea sample from the MICP Testing, PNM and NMR approaches
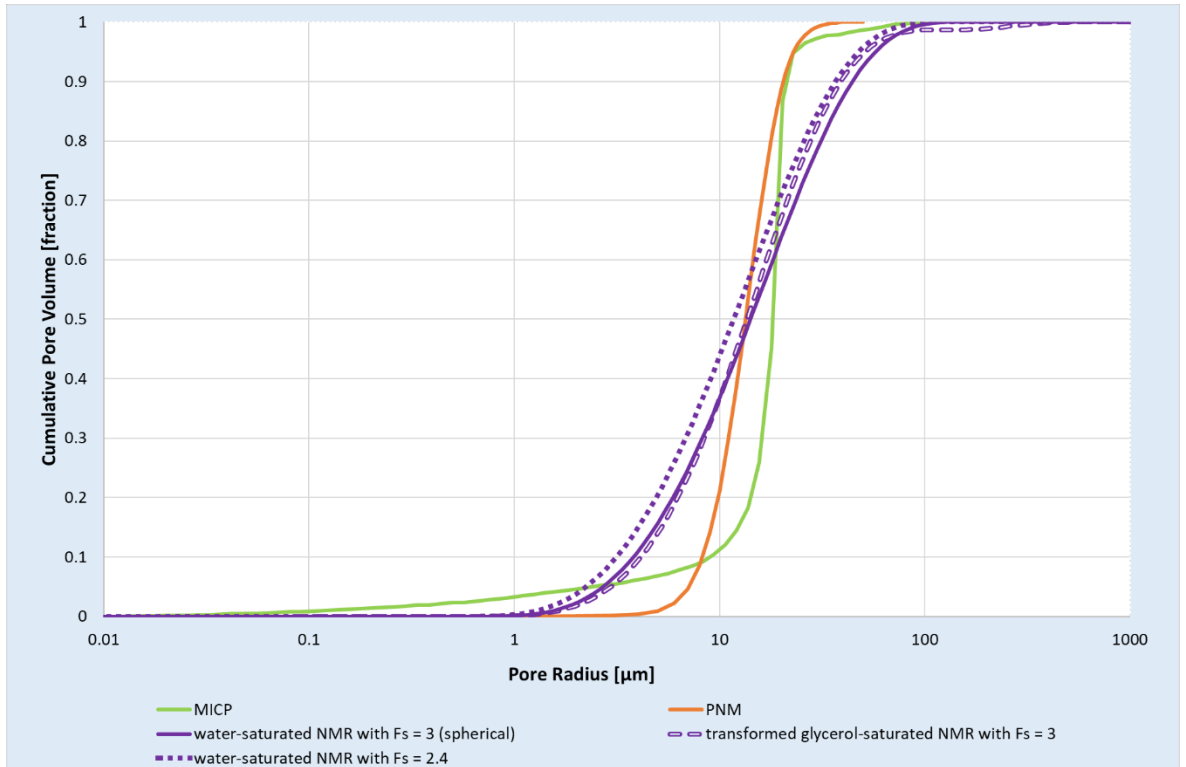
Figure 7-2: The Cumulative PSDs of the Bentheimer sample from the MICP Testing, PNM and NMR approaches
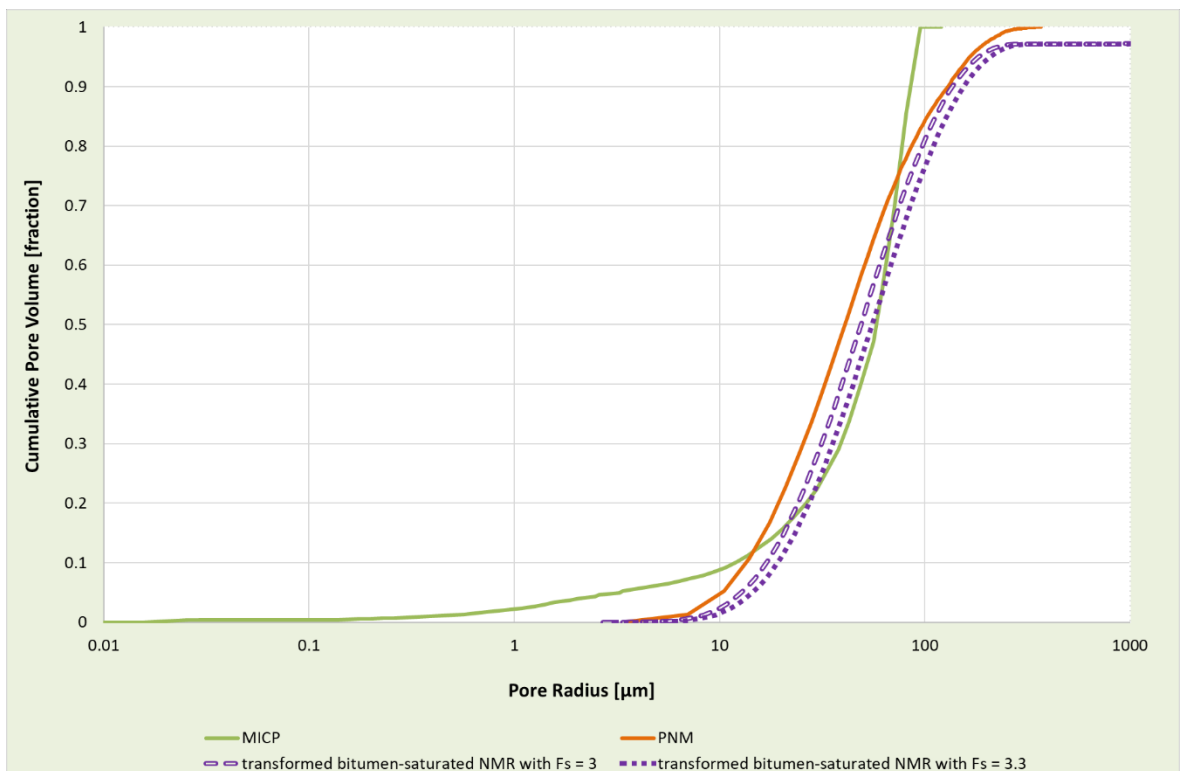
Figure 7-3: The Cumulative PSDs of AOS sample from the MICP Testing, PNM and NMR* approaches (*truncated to 1000 microns)

179

Table 7-1: Analysis of the PSDs of the Berea sample across all methods

	MICP Testing	PNM	Water-saturated NMR testing using a Fs = 3	Water-saturated NMR testing using the Fs = 4.3 from PNM	NMR transformed glycerol-saturated sample using a Fs = 3
Porosity [%]	13.6	15.0	12.8	12.8	12.8
Statistical Measures:					
Pore Size Range [μm]	0.003 - 100	0 - 40	0.2 - 100	0.3 - 110	0.3 - 30
Median (r_{50}) [μm]	6.1	8.7	4.2	6	5.3
Mean (r_m) [μm]	6.8	9.6	4.3	6.2	5.2
Pore Sorting (S_p)	3.2	4.8	5.7	6.8	3.3
Skewness (Sk_p)	-0.38	0.13	0.6	4.9	3.9
Kurtosis (K_p)	0.69	1.1	1.3	0.0	-0.1
Pore Classification:					
Micropore (≤ 1 μm) [%]	17	3	8	4	3
Mesopore (1 < r ≤ 25 μm) [%]	80	96	89	88	97
Macropore (> 25 μm) [%]	3	1	3	8	~0

Table 7-2: Analysis of the PSDs of the Bentheimer sample across all methods

	MICP Testing	PNM	Water-saturated NMR testing using a Fs = 3	water-saturated NMR testing using the Fs = 2.4 from PNM	NMR transformed glycerol-saturated sample using a Fs = 3
Porosity [%]	18.2	19.1	18.5	18.5	18.5
Statistical Measures:					
Pore Size Range [μm]	0.015 - 200	0 - 50	1 - 120	0.6 - 125	0.6 - 700
Median (r_{50}) [μm]	18.2	13.3	14.8	11.8	13.6
Mean (r_m) [μm]	18.5	14.3	14.6	11.6	13.8
Pore Sorting (S_p)	4.9	4.7	16.3	10.4	10.8
Skewness (Sk_p)	-0.56	0.18	0.5	5.0	4.4
Kurtosis (K_p)	2.35	1.0	1.1	0.0	-0.1
Pore Classification:					
Micropore (≤ 1 μm) [%]	3	0	0	0	0
Mesopore (1 < r ≤ 25 μm) [%]	95	97	70	79	75
Macropore (> 25 μm) [%]	2	3	30	21	25

Table 7-3: Analysis of the PSDs of the AOS sample across all methods

	MICP Testing	PNM	NMR transformed **bitumen**-saturated sample using a **Fs = 3**	NMR transformed **bitumen**-saturated sample using a **Fs = 3.3** from PNM
Porosity [%]	32.0	29.1	29.6	29.6
Statistical Measures:				
Pore Size Range [µm]	0.02 – 100	3.5 – 360	2.7 – 100,000	3.4 – 130,000
Median (r_{50}) [µm]	59	41.8	49.4	54.5
Mean (r_m) [µm]	56.5	43.2	51.2	56.8
Pore Sorting (S_p)	18.2	36.0	38.2	43.3
Skewness (Sk_p)	17.4	3.8	3.5	3.6
Kurtosis (K_p)	0.0	-0.1	-0.1	-0.1
Pore Classification:				
Micropore (≤ 1 µm) [%]	2	0	0	0
Mesopore (1 < r ≤ 25 µm) [%]	18	29	22	17
Macropore (> 25 µm) [%]	80	71	78	83

7.3 The influence of resolution and porosity type on porosity and pore size classification

In terms of the pore size classification, Table 7-1 shows that the MICP PSD for the Berea contain micropores (less than 1 µm) that account for approximately 17% of the pore space which is not reflected in any of the other methods. The largest disparity arises from the PNM PSD where only 3% of the distribution is attributed to micropores. This indicates that the PNM PSD does not capture the heterogeneity which exists with respect to small pores for this sample. This is also the case for the Bentheimer and AOS samples although differences between the MICP results to these other methods are much lower.

For all samples, Figures 7-1 to 7-3 shows that the PNM approach does not readily provide pore radii information below 1µm which is not entirely unexpected given that micro-CT is generally limited to resolutions of 1 micron or higher (Table 2-1). This is low when compared to a similar resolution from MICP testing which is capable of injecting

mercury into samples at pressures up to 70,000 psi that can characterise very small pores within the sample within the sub-micron range (Honarpour, 2004).

Misrepresenting the smaller size fractions within the PSD can yield incomplete information regarding the location of fluids within the pore space. The wetting phase generally tends to occupy the smaller pores of the rock and the non-wetting phase occupies the more open channels. For an oil-wet rock, the oil will have the tendency to occupy the smaller pores and as such may lead to inefficient recovery if the smaller fraction of pores is not fully represented in the PSD. This will affect applications relating to catalysis and enhanced oil recovery (EOR) as the injection of nanoparticles, surfactants and other solvents (as well as the duration time of the EOR process) depends on pore-related measures like capillary pressures and pore space volumes.

Peng *et al.* (2012) suggests that some of these limitations can be overcome by imaging the porous media at higher resolutions. This is because lower resolutions may lead to an overestimation of pore size and connectivity which tends to amplify pore volumes leading to a lower representation of microporous volumes. These authors go on to state that higher resolutions can reduce this effect but that this may lead to smaller samples being studied due to the increased processing and computational power required which may provide results that are not representative of the overall microstructure.

In terms of porosity, Tables 7-1 and 7-2 show that the PNM porosities of the Berea and Bentheimer are higher than those quoted for the MICP testing. This is a consequence of both resolution and porosity type. As outlined in the paragraph above, the (lower) resolution of the micro-CT images can amplify pore spaces so that small sizes are not readily identified during PNM; this can result higher porosities which may not be entirely reflective of the porous medium.

Porosity type is also a contributing factor. PNM derives porosity and PSD by first extracting the topological skeleton running through the centre of the pore network and then identifies individual pore diameters by partitioning the skeleton and fitting ellipsoids into local minima. This typically provides a measurement of both the pore bodies and throats regardless of whether these are connected. In essence, PNM provides a measure of the total porosity (both effective and isolated) which is different to the MICP testing in which only the pore throat radii of connected pores are measured since the forced intrusion of mercury must take place through interconnected pores.

For NMR testing, samples are typically saturated with water or brine since the response to water and brine correlates well with surface measurements of the pore space (Sorland *et al.*, 2007). This requires that samples be cleaned of all in-situ fluids and replaced with either water or brine. The introduction of water (or brine) into the pore space must take place through interconnected pores and accordingly the PSD from NMR measurements typically reflect only effective porosity. Additionally, high enough pressures must be used to ensure that the water or brine contacts the smaller pores. If the water or brine is not introduced to these small pores due to insufficient saturating pressures, then these pores will not contribute to the NMR signal as they will not contain hydrogen nuclei.

The NMR porosity for Bentheimer sample is comparable to the MICP porosity. MICP also requires the injection of mercury at high pressures which must fill interconnected pore spaces. However, NMR porosity of the Berea sample is lower to that of MICP and this is perhaps due to Berea having a much smaller pore size than Bentheimer which suggests that possibly the ranges of pressures used to saturate the sample with water during NMR testing (Section 4.3.5) may have been insufficient to introduce water into smaller pores.

For the AOS sample, Table 7-3 shows that the NMR and PNM porosities compare well. These samples have been tested with the in-situ bitumen which implies that during the NMR testing, the hydrogen response will come from both isolated and connected pores since no removal of in-situ fluid has taken place. In this way, when cores samples from producing formations are subjected to NMR testing without having gone through any cleaning or processing, the T2 signal will typically reflect the total porosity. This makes PNM and NMR exceedingly similar in terms of porosity type measured. They are also similar as both measure the pore body and throat radii when producing PSDs.

Although the PNM and NMR porosities of the AOS sample are comparable, the MICP porosity is higher. This is perhaps due to changes in the pore space due to the pre-requisite cleaning and the introduction of mercury into the sample at high pressures.

7.4   The influence of varying pore aspect measures across methods

In terms of the pore aspects measured, PNM and NMR typically provide the size of both the pore bodies and throats which is different to MICP testing in which only the pore

throat radii of connected pores are measured. This might suggest that a convergence of the results across these approaches may not always be possible.

The pore throat radius measured during the MICP test refers to the largest throat through which the pore body can be accessed (Comisky *et al.*, 2007 and Vavra *et al.*, 1992). The results of the MICP test, although more accurately representing a pore throat size, are very often used to describe the pore (body) size distribution (Mao *et al.*, 2005; Vavra *et al.*, 1992 and Volokitin *et al.*, 2001).

This assumption is often made for several reasons; one of which includes the existence of a relationship between the radii of pore bodies and the radii of pore throats. Volokitin *et al.* (2001) maintain that this relationship exists since the radius of the grains in a porous medium governs both the pore size and the pore throat size. It can then be assumed that if the pore size is proportional to the pore throat size, then these two quantities reflect the same distribution. Vavra *et al.*, 1992 go on to state that the fluid entering through a pore throat is assumed to immediately fill the adjoining pore body and as such the volumes accessed by both pore body and throat are proportional and echo similar distributions.

The above assumptions suggest that although pore throats are measured during MICP testing while both pore bodies and throats are measured during PNM and NMR, this difference in pore aspect measurements should not affect the PSDs from the MICP, PNM and NMR and that these should be equivalent in terms of pore aspect. Within this context, it is expected that variations in the PSDs across these methods arise from other criteria.

One such criteria is the challenge of interpreting large pores from MICP measurements that tend to understate the true nature of the material under study. This arises from a consideration that the mercury intrusion of larger pores may be hindered if these are accessed through smaller neighbouring pores which require larger injection pressures. When these larger pores are eventually accessed, they may be interpreted in the PSD incorrectly as an amplified quantity of smaller pores (Morrow and Heller, 1985).

If this reasoning is applied to the MICP data obtained here, then it suggests that the quantity of macropores may be excessively misrepresented (lower) as they are being accessed through smaller pores. Figures 7-1 to 7-3 shows that the PNM and MICP PSDs at larger pores tend to have the same shape and follow the same distribution

leading to a high confidence that the challenge of misrepresenting larger pores as outlined above in the MICP PSD is minimised. However, a similar comparison for the AOS sample shows that the PNM and NMR PSDs have similar shapes which are far-removed from the MICP PSD at larger pores. This could be due to the low displacement pressures typically associated with unconsolidated sands due to the high permeabilities which exist. This may cause the surface pores of the AOS sample to be flooded with mercury quite easily regardless of the pore size.

While there is a good general agreement between the PSDs of the PNM and MICP at larger pore sizes for the Berea and Bentheimer samples, the corresponding NMR results are much larger. This can be due to the hydrogen nuclei in very large pores requiring longer times to reach the pore wall surface which may tend to exaggerate the pore size at the macropore level resulting in data which is not reflective of the inherent PSD.

7.5   The influence of fluid viscosity on the PSD from NMR testing

Both MICP and NMR require specific fluids to be contained in the pore space prior to testing. For MICP and NMR, these fluids are air and water (or brine) respectively. This generally impedes the MICP and NMR testing of samples imbued with their original fluids. Micro-CT scanning requires little to no prior sample preparation (Ketcham and Carlson, 2001) and so can be used when any fluid is contained within the pore space.

During this work, the effect of varying the fluid viscosity on NMR PSD tests was examined since many new exploits within the petroleum industry focus on heavy oil and bitumen reservoirs (Hein, 2016). These reservoirs tend to be unconsolidated and are often imbued with native fluids which when removed from core samples, have the capacity to alter the inherent pore structure. The development of techniques which allow for the robust pore space testing of these kinds of materials without the cleaning or removal of their native fluids will therefore be valuable to the petroleum industry.

Glycerol, having a viscosity of 1,412cP at 20°C, was introduced into water-wet Berea and Bentheimer samples. This resulted in the average $\overline{(T2)}$ being reduced from 87 and 311ms for water-saturated samples to values of 0.68 and 1.65ms respectively for the glycerol-saturated Berea and Bentheimer samples. This reduction is due to the

predominance of bulk relaxation over surface relaxation due to the high viscous glycerol fluid.

The lower $\overline{(T2)}$ values further result in very low calculated surface relaxivities (Table 5-20) which causes the PSDs from the glycerol-saturated NMR testing to be very low (almost 100,000 times lower than their corresponding water-saturated NMR PSDs) as shown in Figure 5-33. Although lower, the similarity in PSD shape spurred the development of a novel transform based on $\overline{(T2)}$ and viscosity which was used to convert glycerol-saturated NMR PSDs (Equation 5-9).

Figures 7-1 and 7-2 show that this empirical transform can result in robust PSDs which are comparable to the benchmark water-saturated PSDs for Berea and Bentheimer. This information is particularly useful for NMR logging and for other applications in which it is easier to test samples with their in-situ fluids which may not necessarily have low viscosities.

For the Bentheimer sample, the water-saturated and transformed glycerol-saturated PSDs compare exceedingly well across the entire distribution. However, for the Berea sample, there is a noticeable disparity between the water-saturated and glycerol-saturated PSDs at both small and large pore sizes. At smaller pore sizes, the transformed glycerol-saturated PSD is larger than the corresponding water-saturated PSD with the difference becoming increasingly smaller as the pore size increases. This is attributed to the dominance of surface relaxation for smaller pores in which the hydrogen nuclei will have a longer relaxation time to reach the pore walls when compared to water. This implies that the surface relaxation contributes more towards the overall T2 signal than the bulk relaxation; this may tend to overestimate the pore size at the micropore level resulting in data which is not reflective of the in-situ PSD.

At larger pores however, the transformed glycerol-saturated PSD is smaller than the corresponding water-saturated PSD with the difference becoming increasingly larger as the pore size increases. This is attributed to larger pores containing larger amounts of glycerol and the increasing tendency for the bulk relaxation rate of this glycerol to progressively contribute to the overall T2 signal. This minimises the contribution of the surface relaxation of the hydrogen nuclei resulting in T2 times which may tend to underestimate the pore size at the macropore level resulting in data which is not reflective of the in-situ PSD.

186

The NMR testing on the AOS sample was performed with only its in-situ bitumen contained within the pores. As such, no water-saturated NMR PSD is available for comparison with the transformed bitumen-saturated NMR PSD. However, the PNM PSD compares very well to transformed bitumen-saturated NMR PSD as shown in Figure 7-3. These both measure the size of the pores contributing to total porosity (as outlined in Section 7.3) and reflect both the pore body and throat. Small variations between these PSDs exist but this is marginal (where, for example the median pore size from PNM is 13.3µm and that from transformed NMR is 13.6 µm).

It is important to note that the empirical transform requires a value of the average surface area to volume ratio $\overline{\left(\dfrac{S}{V}\right)}$ to calculate the surface relaxivity (Equation 4-14). During the NMR testing of water-saturated samples, this value is obtained from the PGSTE testing (as outlined in Section 4.3.3). The NMR testing of water-saturated samples is therefore a stand-alone or independent means of acquiring PSD. However, when in-situ or other fluids are present, another method is needed to find the $\overline{\left(\dfrac{S}{V}\right)}$. This work used PNM to find the $\overline{\left(\dfrac{S}{V}\right)}$ which indicates that the NMR testing of samples containing their in-situ fluids is do not provide an independent or stand-alone means of acquiring PSDs.

It is also important to note that Figure 7-3 is truncated to 1000µm. Figure 6-11 however shows the PSDs in their entirety and indicates that the transformed NMR PSD has very large pore radii within the range of 1,000 – 100,000. This is an anomaly due to the T2 distribution shown in Figure 6-10 having a small peak ranging from 50 – 300ms which is attributable to connate water in the pores. Although water exists in the pore space, the $\overline{(T2)}$ value of the entire distribution is small (being 0.2ms which is far removed from the 50 – 300ms water signal) due to the large percentage of bulk bitumen (~95%) in the sample which skews the T2 distribution towards shorter relaxation times. This small $\overline{(T2)}$ value causes the calculated surface relaxivity to be small (Table 6-2) which results in a large transform value to shift the bitumen-saturated NMR PSD towards more representative pore size values.

Water-filled pores will however reflect the '*true*' pore size as the signal will be attributable to only T2S surface relaxation. Given that the transform was developed to shift bitumen-

filled pores, applying the transform to water-filled pores will therefore exaggerate the pore size of these pores as seen in Figure 6-11 which leads to pore radii of 1,000 – 100,000 which do not exist.

Although the empirical transform has been successful in shifting the glycerol-saturated PSDs towards the more representative water-saturated PSDs, it is important to recognise that this transform has been developed under the limited conditions of one fluid type and one viscosity and may therefore not be applicable to samples having varying fluid characteristics.

7.6   The influence of pore shape on NMR PSD

The determination of pore throat radii using the MICP method assumes that the pore throats have a cylindrical geometry. In PNM, individual pores are identified by partitioning and fitting ellipsoids into local minima with the pore diameter taken as the minimum Feret diameter. In NMR, pores are commonly assumed to be spherical (Anovitz and Cole, 2015; Brownstein and Tarr, 1979; Coates *et al.*, 1999) resulting in the use of a generic shape factor of 3 during NMR testing.

In real porous media, the pore and throats form a complex assortment of shapes and geometries (Vavra *et al.*, 1992). The assumption of a pre-set geometry can therefore simplify this complexity and tend to misrepresent the actual morphology which exists.

Although NMR can be used as an independent method for deriving robust PSDs for water-saturated samples, an opportunity to strengthen this approach lies in the identification of a more representative pore shape factor. The use of micro-CT and PNM approaches presents a viable means of exploring more realistic shape factors.

An examination of the pore space using PNM approaches shows that the average pore shape factor (F_s) for the Berea, Bentheimer and AOS samples are 4.3, 2.4 and 3.3 respectively. This implies that many of the pores with the Berea sample tend to be cubic in shape with rounded corners, that the pores of the Bentheimer sample tend to be either tubular or capsular in shape and that the pores of the AOS tend towards sphericity (Table 4-3). These pore shape factors were used to modify Equation 4-10 and derive NMR

PSDs more reflective of the pore shapes identified in the PNM (using equations 5-7A, 5-7B and 6-1).

The resulting F_s-derived PSDs will have an almost identical shape to that from the water-saturated and transformed bitumen-saturated NMR testing which would have used a pore shape factor of 3. If the factor used is less than 3, then the PSD will shift to the left resulting in a smaller PSD. Conversely, if the factor used is greater than 3, a shift to the right will occur leading to larger pore sizes.

For the Berea sample, Figure 7-1 shows that the F_s-derived PSD is shifted to the right (as an Fs of 4.3 is greater than the spherical value of 3). When compared to the MICP PSD, this further underestimates the small pores which exist and subsequently further amplifies the larger pores. While the true nature of the pore structure is unknown, MICP testing is usually taken as the benchmark within the petroleum industry (Comisky *et al.*, 2007). When compared with this benchmark, it would appear that the F_s-derived PSD for Berea will not reflect the benchmark results leading to a low confidence in the results.

This is also true for the Bentheimer sample. Figure 7-2 shows that the F_s-derived PSD is shifted to the left (as an F_s of 2.4 is less than the spherical value of 3). This shift is small compared to the water-saturated NMR and so the differences between the PSDs are marginal. Nevertheless, when compared to the MICP PSD, the F_s-derived PSD also underestimates the small pores which exist and subsequently further amplifies the larger pores leading to a low confidence in the results.

For the AOS sample, the F_s-derived PSD is exceedingly comparable to the transformed bitumen-saturated NMR which is a result of the F_s of 3.3 is being very close to the spherical value of 3. As indicated before, both NMR PSDs are particularly comparable to the PNM PSD which is encouraging given that the MICP testing for unconsolidated material is subjected to several challenges.

7.7   Choosing the '*right*' method to determine porosity and PSD

The porosity of reservoir material can be determined using several methods which include core analysis and well-logging (Jozanikohan *et al.*, 2014). However, MICP

testing is usually taken as the benchmark for determining PSD within the petroleum industry (Comisky *et al.*, 2007).

The above results show that the derived PSDs across all methods are somewhat comparable and provide porosity and PSD results within a similar range. Variations across these PSDs are as a result of the influence of resolution, porosity type, pore aspect measures, fluid viscosity and pore shape. Choosing the '*right*' method from among MICP, PNM and NMR testing must therefore be a function of the application.

Although several challenges can exist, Figures 7-1 to 7-3 show that MICP testing can provide a measure of the small pores (particularly micropores) which exist. These small pores are not recognised during PNM due to resolutions being limited to the micron level and above. Resolution limitations can be overcome using methods which have higher resolutions. A good example is the use of Focused Ion Beam nano-tomography (FIB-nt) which has a resolution of approximately 10 nm that can image materials whose pore spaces are within the nanometre range, such as shale (Peng *et al.*, 2012).

The identification of small pores during NMR testing is also limited by the use of sufficient and relatively high pressures during the saturation of water or brine into the pore space. High pressures will ensure that these small pores are fully saturated and contain hydrogen nuclei leading to a subsequent NMR response.

Misrepresenting the smaller size fractions within the PSD can yield incomplete information regarding the location of fluids within the pore space. The wetting phase generally tends to occupy the smaller pores of the rock and the non-wetting phase occupies the more open channels. For an oil-wet rock, the oil will have the tendency to occupy the smaller pores and as such may lead to inefficient recovery if the smaller fraction of pores is not fully represented in the PSD. This will affect applications relating to catalysis and enhanced oil recovery (EOR) as the injection of nanoparticles, surfactants and other solvents (as well as the duration time of the EOR process) depends on pore-related measures like capillary pressures and pore space volumes.

Conversely, the NMR and PNM PSDs show the existence of large pores which are not reflected in the MICP results. The mercury intrusion of larger pores may be hindered if these are accessed through smaller neighbouring pores which require larger injection pressures. When these larger pores are eventually accessed, they may be interpreted in the PSD incorrectly as an amplified quantity of smaller pores (Morrow and Heller,

1985). If this reasoning is applied to the MICP data obtained here, then it suggests that the quantity of macropores may be excessively misrepresented (lower) as they are being accessed through smaller pores.

Misrepresenting the larger size fractions within the PSD can also affect applications relating to enhanced oil recovery (EOR) operations. This will be particularly important when injecting surfactants and other solvents in terms of the amount of fluids injected and their interactions with the grain surfaces.

PNM and NMR approaches will also be preferred when core samples are limited given that MICP testing is destructive. This will be challenging when samples are expensive to obtain and are limited in quantity. Both PNM and NMR are non-destructive allowing for the repeatability of measurements which overcomes these limitations.

PNM can also test samples having their in-situ or native fluids. This is a marked advantage over NMR and MICP which both require specific fluids to be contained in the pore space prior to testing. This generally requires the removal and replacement of all original fluids with air for MICP and with water (or brine) for the NMR method which typically impedes the testing of samples imbued with their original fluids using these methods. PNM requires little to no sample preparation prior to testing (Ketcham and Carlson, 2001) and so is ideal for studying samples containing their in-situ fluids.

With specific reference to unconsolidated Athabasca oil sand material, the in-situ bitumen acts as a cohesive agent binding the grains together (Schmitt, 2005). Removal of this bitumen can lead to a rearrangement of the pore structure unless meticulous care is taken to preserve the pore integrity during the cleaning process. Techniques such as the Modified Dean-Stark method (the AOSI-3573 technique) have been developed specifically for these kinds of material but it is important to recognise that the removal of the original fluids can ultimately change the inherent pore structure and may not readily provide consistent and robust pore information for these kinds of materials. The development of techniques which allow for the robust pore space testing of these kinds of materials without the cleaning or removal of their native fluids will therefore be valuable to the petroleum industry.

Based on these ideas, this work developed a novel empirical transform which could apply NMR tests to samples containing viscous fluids and their in-situ fluids, specifically glycerol and bitumen. This empirical transform has been successful in obtaining PSDs

which are comparable to the MICP and PNM approaches leading to a high confidence in its use. This empirical transform overcomes the limitations of NMR testing involving the stipulated use of water or brine to obtain PSDs.

In light of the above, this work proposes that any of the methods of MICP, PNM and NMR can be used to derive robust PSDs but that care and a consideration the final application is needed when choosing one method over the other. Table 7-4 summarises most of the above and provides a ranking of the preference of each method for a broad range of applications and situations.

Table 7-4: Ranking the preference of the MICP, PNM and NMR methods for a broad range of applications and situations

Broad Application/Situation	MICP Testing	PNM	NMR
Testing a limited quantity of core samples	low preference	high preference	high preference
Testing partially consolidated or unconsolidated material	low preference	high preference	low preference (if water-saturated tested) high preference (if in-situ fluid tested)
In-situ fluid core analysis	not applicable	high preference	high preference
Testing samples having a large percentage of micropores	high preference	low preference	low preference
Testing samples having a wide range of pore size (high pore sorting)	low preference	high preference	high preference

7.8 A consideration of the objectives of this work

The general objective of this work was to determine and compare the porosity and PSD of selected sandstone samples obtained from the three methods of MICP, PNM and NMR approaches. This was done in order:

1. to gauge whether the PNM and NMR approaches can provide comparable results to conventional MICP testing
2. to assess the use of the PNM and NMR methods as stand-alone techniques for evaluating the pore space and
3. to determine whether PNM and NMR can provide a robust measurement of porosity and PSD for samples imbued with their native hydrocarbon fluids.

When considering the above, it was important to recognise that the PSDs from the MICP, PNM and NMR approaches varied due to the fluid type contained in the pore space, the pore dimension measured (i.e. measures of pore throat versus pore body) as well as the resolution and connectivity of the pore space. These differences suggested that a convergence of the results across these approaches was not always be possible.

A good example of this is where the lower resolution of the micro-CT images used in this work (limited to 1µm or higher) did not identify the existence of micropores during the PNM testing of the Berea and Bentheimer samples. These micropores were also not identified during the water-saturated NMR testing as there was the possibility that the saturation pressures were not high enough for water to contact the smaller pores of the sample. These micropores however were easily identifiable during the MICP testing due to the high injection pressures.

Several other examples exist which are summarised in Section 7.7. A careful consideration of these is therefore needed to have confidence in the use of each method to determine porosity and PSD as well as to inform the choice of one method over another for petroleum engineering applications. The choice of one method over another is a function of the application. Broad application classifications to inform the choice of method include:

- the testing of a limited quantity of core samples
- the testing of partially consolidated or unconsolidated material
- the testing of samples imbued with their original fluids (in-situ fluid core analysis)
- the testing samples having a large percentage of micropores

- the testing samples having a wide range of pore size (high pore sorting)

Table 7-4 ranks the preference of the use the MICP, PNM and NMR methods within these broad categories.

Considering the above within the context of the broad objectives of this work shows that:

1. Yes, PNM and NMR testing do provide comparable results to conventional MICP testing but that these approaches are more suited when the testing involves limited quantities of core samples, partially consolidated and unconsolidated materials and when samples contain their original fluids.

2. Yes, PNM and the water-saturated NMR approaches can be used as stand-alone methods when deriving PSDs. However, when fluids other than water or brine are contained in the pore space, NMR testing requires the $\overline{\left(\dfrac{S}{V}\right)}$ to be found externally which impedes its use as an independent means of PSD determination.

3. Yes, both PNM and NMR testing can derive robust pore space information for samples containing their original fluids. PNM generally requires little to no sample preparation and so is ideal to the testing of samples imbued with their in-situ fluids. In terms of NMR, the developed empirical transform can transform the PSDs of viscous fluid-saturated samples into representative PSDs which show a good general agreement with the MICP and PNM approaches.

7.9   Contribution to the Body of Knowledge and Future Work

Based on the above, this work has contributed to the literature by adding important information regarding the use and applicability of the MICP, PNM and NMR methods for the testing of conventional and unconventional samples.

Two significant contributions have been made which include:

1. The development of a Recommended PNM Practice for Homogenous and Heterogenous samples. This can reduce the uncertainties surrounding the segmentation and REV processes during PNM and has been shown to produce porosity and PSD results in a robust and time-effective manner for both conventional and unconventional samples.

2. The development of a novel empirical transform which allow the NMR testing of samples containing viscous or in-situ fluids. This overcomes the limitations of the stipulated use of water or brine in the pore space during NMR testing. This transform has been shown to successfully obtain robust PSDs when two viscous fluids (bitumen and glycerol) are contained in the pore space.

Future work to strengthen these two contributions include:

1. Using a wider use of sandstone samples to test the Recommended PNM Practice for homogeneous and heterogeneous sandstone samples which was developed and outlined in Table 5-11. This can result in a further refinement of steps leading to an even greater confidence in the results.

2. Testing the empirical transform with a wider range of samples containing a greater variety of fluids. Although the empirical transform (Equation 5-9) has been successful in obtaining PSDs which are comparable to the MICP and PNM approaches, it is important to recognise that this transform has been developed under the limited conditions of one fluid type and one viscosity and therefore may not be applicable to samples having varying fluid characteristics. This would prove valuable to the petroleum industry by extending the results obtained from NMR logging as well as testing samples with their in-situ fluids without any pre-requisite cleaning or removal of original fluids.

REFERENCES

Adebayo, A., Kandila, M., Okasha, T. and Sanni, M. (2017) Measurements of electrical resistivity, NMR pore size and distribution, and x-ray CT-scan for performance evaluation of CO2 injection in carbonate rocks: A pilot study, *International Journal of Greenhouse Gas Control*, 63, pp. 1 – 11.

Ahmed, T. (2019) Chapter 4: Fundamentals of Rock Properties, in: Ahmed, T. (ed.) *Reservoir Engineering Handbook*. 5th ed. Houston: Gulf Professional Publishing, pp. 167 – 281.

Al-Raoush, R. and Papadopoulos, A. (2010) Representative elementary volume analysis of porous media using X-ray computed tomography, *Powder Technology*, 200, pp. 69–77.

Al-Wahaib, I. (2012) *RE: Athabasca bitumen fluid properties*. Personal e-mail to: M. Maraj, 18 November.

Alberta Oil Sands Technology and Research Authority AOSTRA Information Centre (1974) *Alberta Oil Sands Index (AOSI)-3573: Round Robin Study of Analytical Procedures of Various Laboratories on Assay Analysis of Athabasca Tar Sands*. Edmonton, Alberta: Canadian Petroleum Association Oil Sands and Heavy Oil Committee.

Aligizaki, K. (2006) *Pore structure of cement-based materials: Testing, interpretation and requirements*. New York: Taylor and Francis.

American Petroleum Institute (1998) *RP40: Recommended practices for core analysis*. Washington: API Publishing Services.

Anderson, W. (1986) Wettability Literature Survey - Part 1: Rock/Oil/Brine Interactions and the Effects of Core Handling on Wettability, *Journal of Petroleum Technology*, pp. 1125 – 1144. [Online]. Available from: http://faculty.ksu.edu.sa/aalfayfi/363%20PGE/Wettability%201.pdf [Accessed 20 September 2011].

Andra, H., Combaret, N., Dvorkin, J., Glatt, E., Han, J., Kabel, M., Keehm, Y., Krzikalla, F., Lee, M., Madonna, C., Mrsh, M., Mukerji, T., Saenger, E., Sain, R., Saxena, N., Ricker, S., Wiegmann, A. and Zhan, X. (2013) Digital rock physics benchmarks – Part I: Imaging and segmentation, *Computers and Geosciences*, 50, pp. 25 – 32.

Anovitz, L. and Cole, D. (2015) Characterization and analysis of porosity and pore structures, *Reviews in Mineralogy & Geochemistry*, 8, pp. 61 – 164.

Arfi, A., Heliot, D., Zhan, J. and Allen, D. (2006) A new porosity partitioning-based methodology for permeability and texture analysis in Abu Dhabi carbonates, in: *The Abu Dhabi International Petroleum Exhibition and Conference*, Abu Dhabi, UAE, 5 – 8 November 2006, [Online]. Available from https://www.onepetro.org/download/conference-paper/SPE-101176-MS?id=conference-paper%2FSPE-101176-MS [Accessed: 20th June 2014].

Balhoff, M. and Wheeler, M. (2007) A Predictive Pore-Scale Model for Non-Darcy Flow in Anisotropic Media, in: *The SPE Annual Technical Conference and Exhibition*, California, U.S.A., 11 - 14 November, [Online]. Available from: https://www.onepetro.org/download/conference-paper/SPE-110838-MS?id=conference-paper%2FSPE-110838-MS [Accessed: 20th June 2012].

Banavar, R. and Schwartz, L. (1989) Probing porous media with nuclear magnetic resonance, in: Klafter, J. and Drake, J. (eds.) *Molecular Dynamics in Restricted Geometries*. New York: Wiley, pp. 273 – 309.

Bateman, R. (2012) *Openhole log analysis and formation evaluation*. Houston: Society of Petroleum Engineers.

Bear, J. (1972) *Dynamics of fluids in porous media*. New York: Elsevier.

Bear, J. and Bachmat, Y. (1990) *Introduction to Modelling of Transport Phenomena in Porous Media*. London: Kluwer.

Bell, J., Eruteya, O. and Oono, O. (2012) Application of Petrographic Image Analysis and Multivariate Statistical Techniques for Textural Studies of Oil Sand Samples, in: *The AAPG Annual Convention and Exhibition*, California, USA, 22 – 25 April, [Online]. Available from:

http://www.searchanddiscovery.com/documents/2012/80212bell/ndx_bell.pdf
[Accessed: 20th June 2012].

Bennion, D. and Bachu, S. (2006) The impact of interfacial tension and pore size distribution/capillary pressure character on CO_2 relative permeability at reservoir conditions in CO_2-brine systems, in: The SPE/DOE Symposium on Improved Oil Recovery, Oklahoma, USA, 22-26 April, [Online]. Available from: http://www.weatherfordlabs.com/media/34869/the_impact_of_interfacial_tension_and_pore_size_distribuitio.pdf [Accessed 21 June 2011].

Bera, B., Mitra, S. and Vick, D. (2011) Understanding the micro structure of Berea Sandstone by the simultaneous use of micro-computed tomography (micro-CT) and focused ion beam-scanning electron microscopy (FIB-SEM), *Micron*, 42, pp. 412–418.

Bird, M. (2013) Numerical calculation of transport properties of rock with geometry obtained using synchrotron x-ray computed microtomography, MSc Dissertation, University of Saskatchewan. [Online]. Available from: www.ecommons.usask.ca/bitstream/handle/10388/ETD-2013-11-1288/BIRD-THESIS.pdf?sequence=4 formation resistivity avizo [Accessed 21 May 2015].

Bliefnick, D. and Kaldi, J. (1996) Pore geometry: Control on reservoir properties, Walker Creek Field, Columbia and Lafayette Counties, Arkansas, *American Association of Petroleum Geologists Bulletin*, 8 (7), pp. 1027 – 1044.

Blunt, M. (2001) Flow in porous media - pore-network models and multiphase flow. *Colloid and Interface Science*, 6 (3), pp. 197–207.

Blunt, M., Bijeljic, B., Dong, H., Gharbi, O., Iglauer, S., Mostaghimi, P., Paluszny, A and Pentland, C. (2013) Pore-scale imaging and modelling, Advances in Water Resources, 51, pp. 197 – 216.

Boek, E. (2010) Pore Scale Simulation of Flow in Porous Media using Lattice-Boltzmann Computer Simulations, in: *The SPE Annual Technical Conference and Exhibition*, Florence, Italy, 19 - 22 September, [Online]. Available from: https://www.onepetro.org/download/conference-paper/SPE-135506-MS?id=conference-paper%2FSPE-135506-MS [Accessed 21 June 2011].

Borgia, G., Bortolotti, V., Brown, R. and Fantazzani, P. (1996) A robust method for calculating geometric mean times from multiexponential data, using only a few data points and a few elementary operations, *Magnetic Resonance Imaging*, 14 (7/8), pp. 895 – 897.

Brewer, R. and Sleeman, J. (1960) Soil structure and fabric their definition and description, *Journal of Soil Science*, 11, pp. 172-185.

Brown, R. and Gamson, B. (1960) Nuclear magnetism logging*, AIME Pet. Trans.*, 219, pp. 201 - 209.

Brownstein, K. and Tarr, C. (1979), Importance of classical diffusion in NMR studies of water in biological cells, *Physical Review A*, 19 (6).

Bryan, J., Mirotchnik, K. and Kantzas, A. (2003) Viscosity determination of heavy oil and bitumen using NMR relaxometry, *Journal of Canadian Petroleum Technology*, 42 (7), pp. 29 – 34.

Bryan, J., Kantzas, A., Badry, R., Emmerson, J. and Hancsicsak, T. (2007) In situ viscosity of heavy oil: Core and log calibrations, *Journal of Canadian Petroleum Technology*, 46 (11), pp. 47 – 55.

Bryan, J., Kantzas, A. and Mai, A. (2008) Heavy oil reservoir characterization using low-field, in: The CSPG/CSEG/CWLS GeoConvention 2008, Alberta, Canada, 12 – 15 May, [Online]. Available from: http://www.searchanddiscovery.com/abstracts/pdf/2013/90170cspg/abstracts/ndx_byran.pdf [Accessed 3 March 2014].

Butler, J., Reeds, J. and Dawson, S. (1981) Estimating Solutions of First Kind Integral Equations with Nonnegative Constraints and Optimal Smoothing, *SIAM Journal on Numerical Analysis*, 18 (3), 99. 381 – 397.

Cabrera, S. (2008) Characterization of oil sands tailings using low field nuclear magnetic resonance (NMR) technique. MSc dissertation, University of Calgary. [Online]. Available   from:

http://www.collectionscanada.gc.ca/obj/thesescanada/vol2/002/MR44621.PDF
[Accessed 21 December 2013]

Carr, H. and Purcell, E. (1954) Effects of diffusion on free precession in Nuclear Magnetic Resonance experiments, *Physical Review*, 94.

Chekani, M. and Kharrat, R. (2009) Reservoir rock typing in a carbonate reservoir – Cooperation of core and log data: Case study, in: *The SPE/EAGE Reservoir Characterization and Simulation Conference*, Abu Dhabi, UAE, 19 – 21 October, [Online]. Available from: https://www.onepetro.org/download/conference-paper/SPE-123703-MS?id=conference-paper%2FSPE-123703-MS   [Accessed 21 January 2014].

Chen, Q. and Song, Y. (2002) What is the shape of pores in natural rocks?, *Journal of Chemical Physics*, 116 (19), pp. 8247 – 8250.

Chen, X. and Zhou, Y. (2017) Applications of digital core analysis and hydraulic flow units in petrophysical characterization, *Advances in Geo-Energy Research*, 1 (1), pp. 18 – 30.

Chilingarian, G., Mazzullo, S. and Rieke, H. (1992) Chapter 1: Introduction, in: Mazzullo, S., Dominguez, G., Rieke, H. Samaiego, F. and Chilingarian, G. (eds.) *Volume 30: Carbonate reservoir characterization: A geologic-engineering analysis, Part I.* Los Angeles: Elsevier Print, pp. 1 – 58.

Choquette, P. and Pray, L. (1970) Geologic nomenclature and classification of porosity in sedimentary carbonates, *American Association of Petroleum Geologists Bulletin*, 54, pp. 207 – 250.

Coates, G., Xiao, L. and Prammer, M. (1999) *NMR logging: principle and applications.* USA: Halliburton Energy Services. [Online]. Available from: http://www.halliburton.com/public/lp/contents/Books_and_Catalogs/web/Nmr_textbook/H02308.pdf [Accessed 12 June 2012].

Collins, P. (2005) Geomechanical effects on the SAGD Process, in: *SPE International Thermal Operations and Heavy Oil Symposium*, Calgary, Canada, 1 – 3 November, pp. 1 - 12. [Online]. Available from:

http://www.petroleumgeomechanics.com/papers/SAGD%20Geomechanics%20SPE 97905.pdf [Accessed 22nd March 2015].

Comisky, J., Newsham, K., Rushing, J. and Blasingame, T. (2007) A comparative study of capillary-pressure-based empirical models for estimating absolute permeability in tight gas sands, in the SPE Annual Technical Conference and Exhibition, 11 – 14 November, Anaheim, California, pp. 1 - 18. [Online]. Available from: https://www.onepetro.org/download/conference-paper/SPE-110050-MS?id=conference-paper%2FSPE-110050-MS [Accessed 1 March 2012].

Corder, G and Foreman, D. (2014) Non-parametric Statistics: A Step-By-Step Approach. New Jersey: John Wiley & Sons Inc.

Corps, N. (2013) *RE: B100 and B500 microCT images*. Personal e-mail to: M. Maraj, 12 July.

Cotts, R., Hoch, M., Sun, T. and Marker, J. (1989) Pulsed field gradient stimulated echo methods for improved NMR diffusion measurements in heterogeneous systems, *Journal of Magnetic Resonance*, 83, pp. 252 – 266.

Cowan, B. (2005) Nuclear magnetic resonance and relaxation. Cambridge: Cambridge Press. [Online]. Available from: http://books.google.co.uk/books?id=a3t_ysBNwD4C&printsec=frontcover&dq=cowan+nmr&hl=en&sa=X&ei=XqkfU7KbCo7whQenzIC4Cw&ved=0CC8Q6AEwAA#v=onepage&q=carr&f=false [Accessed 12 December 2013].

Craig, F. (1976) *Reservoir Engineering Aspects of Water Flooding*. SPE Monograph Series Vol. Richardson: ASM International.

Czarnecki, J., Radoev, B., Schramm, L. and Slavchev, R. (2005) On the nature of Athabasca Oil Sands. *Advances in Colloid and Interface Science*, 114 -115, pp. 53 – 60.

Diamond, S. (1970). Pore size distributions in clays. Clays and clay minerals, 18, pp. 7 – 23.

Dong, H. and Blunt, M. (2009) Pore-network extraction from micro-computerised tomography images, *Physical Review E,* 80, pp. 1 – 11.

Dufresne, T., Chemielewski, P., Borah, B. and Laib, A. (2004) Microcomputed tomography and its applications, in: Bowlin, G. and Wnek, G. (eds.) *Encyclopedia of biomaterials and biomedical engineering*, New York: CRC Press, pp. 1850 – 1859.

Dullien, F. (1991) *Porous Media: fluid transport and pore structure*. New York: Academic Press.

Dunn, K., Bergman, D. and LaTorraca, G. (2002) *Nuclear magnetic resonance: Petrophysical and logging application.* New York: Pergamon. [Online]. Available from: http://books.google.co.uk/books?id=7OmAcL2qi0C&pg=PA89&dq=surface+relaxivity+nmr&hl=en&sa=X&ei=PWkfU5f4KoTxhQe_xYDwBw&ved=0CFcQ6AEwCA#v=onepage&q=surface%20relaxivity%20nmr&f=false [Accessed 11 March 2014].

Dusseault, M. (1980) Sample disturbance in Athabasca oil sand, *Journal of Canadian Petroleum Technology*, 19 (4), pp. 85 – 92.

Dusseault, M. and Morgenstern, N. (1978) Shear strength of Athabasca Oil Sands, *Canadian Geotechnical Journal*, 15 (2), pp. 216 – 238.

Dusseault, M. and van Domselaar, H. (1982) Unconsolidated sand sampling in Canadian and Venezuelan waters, *Revista Tecnica Intevep*, 2 (2), pp. 165–174.

Eisinga, R., Heskes, T., Pelzer, B. and Te Grotenhuis, M. (2017) Exact p-values for pairwise comparison of Friedman rank sums, with application to comparing classifiers, *BMC Bioinformatics*, 18 (68), pp. 1 – 18.

Elshahawi, H., Fathy, K. and Hiekal, S. (1999) Capillary measurements and rock wettability effects on wireline formation tester measurements, in the SPE Annual Technical Conference and Exhibition, 3 – 6 October, Houston, Texas, pp. 1 - 16. [Online]. Available from: https://www.onepetro.org/download/conference-paper/SPE-56712-MS?id=conference-paper%2FSPE-56712-MS [Accessed 1 March 2012].

Energy Resources Conservation Board (2011) *ST98-2011: Alberta's energy reserves 2010 and supply/demand outlook 2011 – 2020.* Edmonton: Energy Resources

Conservation Board. [Online]. Available from: http://www.ercb.ca/docs/products/STs/st98_current.pdf [Accessed 4th November 2011]

FEI Company (2013) Avizo® Fire for Semiconductor Analysis, [Online]. Available from: http://www.fei.com/software/avizo3d/ [Accessed 21 January 2014].

Feldkamp, L., Davis, L. and Kress, J. (1984) Practical cone beam algorithm, *Journal of the Optical Society of America*, A 1, pp. 612 – 619.

Fernandes, J., Appoloni, C. and Fernandes, C. (2012) Determination of the representative elementary volume for the study of sandstones and siltstones by X-ray microtomography, *Materials Research*, 15 (4), pp. 662 – 670.

Folk, R. and Ward, W. (1957) Brazos River bar, a study in the significance of grain size parameters, *Journal of Sedimentary Petrology*, 27.

Gelb, J., Gu, A., Fong, T., Hunter, L., Lau, S. and Yun, W. (2011) A closer look at shale: Representative elementary volume analysis with laboratory 3D X-ray computed microtomography and nanotomography, in: The *International Symposium of the Society of Core Analysts,* Texas, USA, 18 - 21 September, [Online]. Available from: https://www.yumpu.com/en/document/view/26049365/a-closer-look-at-shale-representative-elementary-scaweb [Accessed 21 January 2014].

Ghous, A., Arns, C., Sheppard, A., Sok, R., Knackstedt, M., Kumar, M., Senden, T., latham, S., Jones, A., Averdunk, H. and Pinczewski, W. (2008) 3D Imaging of reservoir core at multiple scales: Correlations to petrophysical properties and pore scale fluid distributions, in: *The International Petroleum Technical Conference*, Kuala Lumpur, Malaysia, 3 – 5 December, [Online]. Available from: https://www.onepetro.org/download/conference-paper/IPTC-12767-MS?id=conference-paper%2FIPTC-12767-MS [Accessed 6 March 2011].

Gillen, K., Douglass, D. and Hoch, M. (1972) Self-Diffusion in Liquid Water to -31°C, *The Journal of Chemical Physics*, 57 (12), pp. 5117 – 5119.

Glover, P. (2014) *Chapter 7: Wettability (Formation Evaluation MSc Course Notes).* [Online]. Available from:

http://homepages.see.leeds.ac.uk/~earpwjg/PG_EN/CD%20Contents/Formation%20Evaluation%20English/Chapter%207.PDF [Accessed 14 February 2014].

Golparvar, A., Zhou, Y., Wu, K., Ma, J. and Yu, Z. (2018) A comprehensive review of pore scale modelling methodologies for multiphase flow in porous media, *Advances in Geo-Energy Research*, 2 (4), pp. 418 – 440.

Grachev, N. (2012) Digital core analysis - the future of petrophysics, in: SPE Russian Oil and Gas Exploration and Production Technical Conference and Exhibition, Moscow, Russia, 16 – 18 October, [Online]. Available from: https://www.onepetro.org/conference-paper/SPE-160499-MS [Accessed 26 June 2017]

Gregg, S. and Sing, K. (1983) Adsorption, Surface Area, and Porosity. 2nd ed. New York: Academic Press.

Groen, J., Peffer, L., and Pérez-RamíÂŋrez, J. (2002) Incorporation of appropriate contact angles in textural characterization by mercury porosimetry, in: Rodriguez-Reinoso, J., McEnaney, B. and Unger, K. (eds.) *Characterization of Porous Solids VI Proceedings of the 6th International Symposium on the Characterization of Porous Solids (COPS-VI)* (pp. 91 – 98). Elsevier volume 144 of Studies in Surface Science and Catalysis.

Guerrero-Aconcha, U. (2009) The Diffusion Coefficient of Liquid and Gaseous Solvents in Heavy Oil and Bitumen. MSc dissertation, University of Calgary.

Halisch, M. (2013) The REV challenge – estimating representative elementary volumes and porous rock inhomogeneity from high resolution micro-CT data sets, in: *The International Symposium of the Society of Core Analysis*, California, USA, 16 – 19 September, [Online]. Available from: http://www.researchgate.net/profile/Matthias_Halisch/publication/268066266_THE_REV_CHALLENGE__ESTIMATING_REPRESENTATIVE_ELEMENTARY_VOLUMES_AND_POROUS_ROCK_INHOMOGENEITY_FROM_HIGH_RESOLUTION_MICRO-CT_DATA_SETS_INTRODUCTION/links/54608a7b0cf2c1a63bfdf8f6.pdf [Accessed 21 January 2014].

Hein, F. (2016) Geology of Bitumen and Heavy Oil: An Overview, *Journal of Petroleum Science and Engineering*, 154.

Honarpour, M., Djabbarah, N. and Kralik, J. (2004) Expert-based methodology for primary drainage capillary pressure measurements and modelling, in: *Abu Dhabi International Petroleum Exhibition and Conference*, Abu Dhabi, UAE, 10 – 13 October, pp. 1 - 16. [Online]. Available from: https://www.onepetro.org/download/conference-paper/SPE-88709-MS?id=conference-paper%2FSPE-88709-MS [Accessed 1 March 2012].

Hulea, I. and Nicholls, C. (2012) Carbonate rock characterization and modeling: Capillary pressure and permeability in multimodal rocks – a look beyond sample specific heterogeneity, *American Association of Petroleum Geologists Bulletin*, 96, pp. 1627 – 1642.

Iassonov, P., Gebrenegus, T. and Tuller, M. (2009) Segmentation of X-ray computed tomography images of porous materials: A crucial step for characterization and quantitative analysis of pore structures, *Water Resources Research*, 45, pp. 1 – 12.

Ioannidis, M., Kwiecien, M. and Chatzis, I. (1996) Statistical analysis of the porous microstructure as a method for estimating reservoir permeability, *Journal of Petroleum Science and Engineering*, 16, pp. 251 – 261.

Jensen, S., Samanta, S., Chakrabarti-Bell, S., Lieb-Regenauer, K., Siddique, K. and Wang, S. (2014) Automated thresholding and analysis of microCT scanned bread dough, *Journal of Microscopy*, 256 (2), pp. 100 – 110.

Jerauld, G. and Salter, S. (1990) The effect of pore-structure on hysteresis in relative permeability and capillary pressure: pore level modelling, *Transport in Porous Media,* 5, pp. 103 – 151.

Jin, G., Torres-Verdín, C. and Toumelin, E. (2009) Comparison of NMR simulations of porous media derived from analytical and voxelized representations, *Journal of Magnetic Resonance*, 200, pp. 313 – 320.

Jozanikohan, G., Norouzi, G., Moshiri, B., Sahabi, F. and Razi, J. (2014) Porosity Estimation from Well Log and Core Data, Case Study: Shurijeh Formation in one of

non-producing wells of Eastern Kopet-Dagh, in: The Fifth Iranian Mining Engineering Conference, MINEX 2014, Tehran, Iran, 3 - 4 November, [Online]. Available from: https://www.researchgate.net/publication/268079182_Porosity_Estimation_From_Well_Log_and_Core_Data_Case_Study_Shurijeh_Formation_in_One_of_Non-producing_Wells_of_Eastern_Kopet-Dagh [Accessed 7 January 2018]

Kalam, M. (2012) Digital Rock Physics for Fast and Accurate Special Core Analysis in Carbonates, in Gomes, J., ed. New Technologies in the Oil and Gas Industry: London, InTech Open, pp. 201 – 226.

Kalender, W. (2011) *Computed Tomography: Fundamentals, System Technology, Image Quality, Applications*. London: Wiley.

Kantzas, A. (2009) Advances in magnetic resonance relaxometry for heavy oil and bitumen characterization, *Journal of Canadian Petroleum Technology*, 48 (3), pp. 15 – 23.

Keehm, Y. and Lee, M. (2007) Artifact in 3D pore-microstructure from X-ray tomogram and its impacts on physical property simulations, in: 77th SEG International Exposition and Annual Meeting, Texas, USA, 23 - 26 September, [Online]. Available from: https://www.onepetro.org/download/conference-paper/SEG-2007-1706?id=conference-paper%2FSEG-2007-1706 [Accessed 7 January 2013]

Kenyon, W. (1997) Petrophysical principles of applications of NMR logging, *The Log Analyst*. 38 (2), pp. 21 - 43.

Ketcham, R. and Carlson, W. (2001) Acquisition, optimization and interpretation of X-ray computed tomographic imagery: applications to the geosciences, *Computers and Geosciences*, 27, pp. 381 – 400.

Kimmich, R. (2001) *NMR: Tomography, Diffusometry, Relaxometry.* London: Springer.

Kleinberg, R. (1996) Utility of NMR T2 distributions, connection with capillary pressure, clay effect, and determination of the surface relaxivity parameter ρ_2, *Magnetic Resonance Imaging*, 14 (7/8), pp. 761 - 767.

Kokeb, A., Manahiloh, K. and Nejad, M. (2017) The effectiveness of global thresholding techniques in segmenting two-phase porous media, *Construction and Building Materials*, 142, pp. 256 – 267.

Krumbein, W. (1940) Flood gravels of San Gabriel Canyon, California, *Geological Society of America Bulletin*, 5, pp. 639 – 676.

Krygowski, D. (2004) *Basic well-log analysis.* Houston: American Association of Petroleum Geologists.

Langheinrich, A., Kampschulte, M., Cröβmann, C., Moritz, R., Rau, W., Bohle, R. and Ritman, E. (2009) Role of Computed Tomography Voxel Size in Detection and Discrimination of Calcium and Iron Deposits in Atherosclerotic Human Coronary Artery Specimens, *Journal of Computer Assisted Tomography*, 33 (4), pp. 517 – 522.

Lide, D. (1994) *CRC Handbook of Data on Organic Compounds.* Boca Raton, Florida: CRC Press. pp. 4386.

Lindquist, W., Lee, S., Coker, D., Jones K. and Spanne P. (1996) Medial axis analysis of void structure in three-dimensional tomographic images of porous media, *Journal of Geophysical Research (Solid Earth)*, 101(B4), pp. 8297–8310.

Ling, K., Han, G., Shen, Z., Ghalambor, A, He, J. and Pei, P. (2014) Calculating pore size distribution by using capillary pressure, in: The SPE International Symposium and Exhibition on Formation Damage Control, Louisiana, USA 26 - 28 February, [Online]. Available from: https://www.onepetro.org/download/conference-paper/SPE-168183-MS?id=conference-paper%2FSPE-168183-MS [Accessed 7 January 2015]

Lonnes, S., Guzman-Garcia, A. and Holland, R. (2003). NMR Petrophysical Predictions on Cores, in: 44th SPWLA Annual Logging Symposium, Galveston, Texas, 22-25 June, pp. 1-14. [Online]. Available from: https://www.onepetro.org/conference-paper/SPWLA-2003-DDD [Accessed: 12 January 2017].

Loskutov, V. (2012) Empirical time dependence of liquid self-diffusion coefficient in porous media, *Journal of Magnetic Resonance*, 216, pp. 192 – 196.

Lyu, C., Ning, Z., Wang, Q. and Chen, M. (2018) Application of NMR T2 to Pore Size Distribution and Movable Fluid Distribution in Tight Sandstones, *Energy Fuels*, 32 (2), pp. 1395 – 1405.

Magritek (2013) *Routine core analysis - Porosity measurement: Application Note 1*. [Online]. Available from: http://www.magritek.com/wp-content/uploads/2013/12/Magritek-App-Note-001-Porosity-09-   678   2013.pdf [Accessed 1 February 2014].

Mao, Z., He,Y. and Ren, X. (2005) An improved method of using NMR T2 distribution to evaluate pore size distribution, *Chinese Journal of Geophysics*, 48 (2), pp. 412 – 418.

Marschal, D., Gardner, J., Mardon, D. and Coates, G. (1995). Method for correlating NMR relaxometry and mercury injection data. [Online]. Available from: http://www.ux.uis.no/~s-skj/ipt/Proceedings/SCA.1987-2004/1-SCA1995-11.pdf [Accessed: 22 January 2017]

Marzouk, I., Takezaki, H. and Miwa, M. (1995) Geologic controls on wettability of carbonate reservoirs, Abu Dhabi, U.A.E., in: *The SPE Middle East Oil Show*, Bahrain, Manama, 11 – 14 March, [Online]. Available from: https://www.onepetro.org/download/conference-paper/SPE-29883-MS?id=conference-paper%2FSPE-29883-MS [Accessed 8 April 2014].

Matrecano, M. (2010) *Porous media characterisation by micro-tomographic image processing*. PhD dissertation, Università Degli Studi Di Napoli. [Online]. Available from: http://www.fedoa.unina.it/8518/1/Matrecano.pdf [Accessed 2 May 2013].

Mattax, C., McKinley, R. and Clothier, A. (1975) Core Analysis of Unconsolidated and Friable Sands, *Journal of Petroleum Technology*, pp. 1423 – 1432.

Maze, G. and Wagner, U. (2009) A Note on the Weighted Harmonic-Geomteric-Arithmetic Means Inequalities, *Mathematical Inequalities and Applications*, 15 (1).

Medellín, D., Ravi, V. and Torres-Verdín, C. (2016) Multidimensional NMR Inversion without Kronecker Products: Multilinear Inversion, *Journal of Magnetic Resonance*, 269, pp. 24 – 35.

Meyer, R., Attanasi, E. and Freeman, P. (2007) Heavy Oil and Natural Bitumen Resources in Geological Basins of the World. United States Geological Survey. Available from: http://pubs.usgs.gov/of/2007/1084/OF2007-1084v1.pdf [Accessed 24 October 2011]

Mills, R. (1973) Self-Diffusion in Normal and Heavy Water, *The Journal of Physical Chemistry*, 77 (5), pp. 685 – 688.

Mitra, P., Sen, P. and Schwartz, L. (1993) Short-time behaviour of the diffusion coefficient as a geometrical probe of porous media, *Physical Review B*, 47, pp. 8565 – 8574.

Morrow, N. and Heller, J. (1985) Fundamentals of enhanced recovery, in: Donaldson, E., Chillingarian, G. and Yen, T.F. (eds.). *Enhanced Oil Recovery, I: Fundamentals and Analysis.* New York: Elsevier, pp. 47 – 74.

Narsilio, G., Buzzi, O., Fityus, S., Sup Yun, T. and Smith, D. (2009) Upscaling of Navier–Stokes equations in porous media: Theoretical, numerical and experimental approach, *Computers and Geotechnics*, 36, pp. 1200 – 1206.

Ng, H., Jargalsaikhan, D., Tsai, H and Lin, C. (2013) An improved method for Image Thresholding based on the Valley-Emphasis method, in: Signal and Information Processing Association Annual Summit and Conference (APSIPA), 2013 Asia-Pacific, Kaohsiung, China, 29 Oct – 1 Nov, pp. 1 – 4. [Online]. Available from: http://ieeexplore.ieee.org/xpls/abs_all.jsp?arnumber=6694261&tag=1 [Accessed 12 March 2015]

Nicot, B., Fleury, M. and Leblond, J. (2006) A new methodology for better viscosity prediction using NMR relaxation, in: SPWLA 47th Annual Logging Symposium, Veracruz, Mexico, 4 – 7 June, pp. 1 – 12. [Online]. Available from: https://www.onepetro.org/download/conference-paper/SPWLA-2006-Z?id=conference-paper%2FSPWLA-2006-Z [Accessed 12 March 2013]

Nimmo, J. (2004) Porosity and Pore Size Distribution, in Hillel, D., ed. Encyclopedia of Soils in the Environment: London, Elsevier, v. 3, p. 295-303.

Niu, Y., Kantzas, A. and Bryan, J. (2008) Determining bitumen, water and solids in oil sands ore by using low-field NMR, *Journal of Canadian Petroleum Technology*, 47 (7), pp. 40 – 47.

Pal, N. and Pal, S. (1993) A review of image segmentation techniques, *Pattern Recognition*, 6, pp. 1277 – 1294.

Passchier, C. and Trouw, R. (2005) *Microtectonics.* 2nd Edition. Berlin: Springer Verlag.

Peksa, A., Wolf, K. and Zitha P. (2015) Bentheimer Sandstone Revisited for Experimental Purposes, *Marine and Petroleum Geology*, 67, pp. 701-719.

Peng, S., Hu, Q., Dultz, S. and Zhang, M. (2012) Using X-ray computed tomography in pore structure characterization for a Berea sandstone: Resolution effect, *Journal of Hydrology*, 473 – 473, pp. 254 – 261.

Peszyńska, M., Trykozko, A. and Sobieski, W. (2010) Forchheimer law in computational and experimental studies of flow through porous media at porescale and mesoscale, *GAKUTO International Series, Mathematical Sciences and Applications*, 32, pp. 463 - 482.

Pittman, E. (1992) Relationship of porosity and permeability to various parameters derived from mercury injection-capillary pressure curves for sandstones, *American Association of Petroleum Geologists Bulletin*, 76 (2), pp. 191 – 198.

Porras, J. and Campos, O. (2001) Rock typing: A key approach for petrophysical characterization and definition of flow units, Santa Barbara Field, Eastern Venezuela Basin, in: The SPE Latin American and Caribbean Petroleum Engineering Conference, Buenos Aires, Argentina, 25–28 March, [Online]. Available from: https://www.onepetro.org/download/conference-paper/SPE-69458-MS?id=conference-paper%2FSPE-69458-MS [Accessed 10 April 2014].

Prodanovic, M., Lindquist, W. and Seright, R. (2007) 3D image-based characterization of fluid displacement in a Berea core, *Advances in Water Resources*, 30 (2), pp. 214–226.

Radke, C., Kovscek, A. and Wong, H. (1992) A pore-level scenario for the development of mixed wettability in oil reservoirs, in: SPE 67th Annual Technical Conference and Exhibition, Washington, D.C., USA, 4 – 7 October, pp. 163 – 177. [Online]. Available from: https://www.onepetro.org/download/conference-paper/SPE-24880-MS?id=conference-paper%2FSPE-24880-MS [Accessed 22 March 2011].

Rosen, R., Mickelson, B., Fry, J, Hill, G. Knabe, B. and Sharf-Aldin, M. (2007) Recent experience with unconsolidated core analysis, in: *The International Symposium of the Society of Core Analysis*, Calgary, Canada, 10 – 12 September, [Online]. Available from: https://www.yumpu.com/en/document/view/26049269/recent-experience-with-unconsolidated-core-analysis-scaweb [Accessed 8 April 2013].

Rouquerol, J., Avnir, D., Fairbridge, C., Everett, D., Haynes, J., Pernicone, N., Ramsay, J., Sing, K. and Unger, K. Recommendations for the characterization of porous solids, *Pure and Applied Chemistry*, 66, pp. 1739 – 1758.

Rozenbaum, O. and Rolland du Roscoat, S. (2014) Representative elementary volume assessment of three-dimensional x-ray microtomograpgy images of hetertogenous material: Application to limestones, *Physical Review E,* 89, pp. 1 – 11.

Sarker, M. and Siddiqui, S. (2009) Advances in micro-CT based evaluation of reservoir rocks, in: The SPE Saudi Arabia Section Technical Symposium and Exhibition, Al Khobar, Saudi Arabia, 9 – 11 May, [Online]. Available from: https://www.onepetro.org/download/conference-paper/SPE-126039-MS?id=conference-paper%2FSPE-126039-MS [Accessed 13 August 2011].

Schmitt, D. (2005). Rock physics and time-lapse monitoring of heavy-oil reservoirs, in *Proceedings of the International Thermal Operations and Heavy Oil Symposium*, Calgary, Alberta, Canada, 1 - 3 November, Online]. Available from: https://www.onepetro.org/conference-paper/SPE-98075-MS [Accessed 8 April 2014].

Sezgin, C. and Weaver, W. (2004) Survey over image thresholding techniques and quantitative performance evaluation, *Journal of Electronic Imaging*, 13, pp. 146 – 165.

Shafer, J., Mardon, D. and Gardner, J. (1999) Diffusion Effects on NMR Response of Oil & Water in Rock: Impact of Internal Gradients, in: *The International Symposium of the*

Society of Core Analysis, Colorado, USA, 1 – 4 August, [Online]. Available from: http://www.ux.uis.no/~s-skj/ipt/Proceedings/SCA.1987-2004/1-SCA1999-16.pdf [Accessed 21 January 2014].

Sheppard, A., Sok, R. and Averdunk, H. (2004) Techniques for image enhancement and segmentation of tomographic images for porous media, *Physica A*, 339, pp. 145 – 151.

Silin, D., Jin, G. and Patzek, T. (2003) Robust determination of the pore space morphology in sedimentary rocks, in: The SPE Annual Technical Conference and Exhibition, Colorado, USA, 5 – 8 October, [Online]. Available from: https://www.onepetro.org/download/conference-paper/SPE-84296-MS?id=conference-paper%2FSPE-84296-MS [Accessed 3 July 2013].

Skalinski, M. and Kenter, J. (2014) Carbonate petrophysical rock typing: integrating geological attributes and petrophysical properties while linking with dynamic behaviour, Geological Society London Special Publications, 406 (1), pp. 229 - 259. Available from: http://sp.lyellcollection.org/content/early/2014/05/28/SP406.6.full.pdf+html [Accessed 3 March 2015].

Skalinski, M., Kenter, J. and Jenkins, S. (2009) Rock type definition and pore type classification of a carbonate platform, Tengiz Field, Republic of Kazakhstan, in: *The SPWLA 50th Annual Logging Symposium*, Texas, USA, 21–24 June 2009, [Online]. Available from: https://www.onepetro.org/conferences/SPWLA/SPWLA09 [Accessed 8 April 2014].

Slijkerman, W. and Hofman, J. (1998) Determination of surface relaxivity from NMR diffusion measurements, *Magnetic Resonance Imaging*, 16 (5/6), pp. 541 – 544.

Sok, R., Varslot, T., Ghous, A., Latham, S., Sheppard, A. and Knackstedt, M. (2010) Pore scale characterization of carbonates at multiple scales: integration of micro-CT, BSEM and FIBSEM, *Petrophysics*, 51 (6), pp. 379 – 387.

Song, Y., Lisitza, N., Allen, D. and Kenyon, W. (2002) Pore geometry and its geological evolution in carbonate rocks, *Petrophysics*, 43 (5), pp. 420 – 424.

Sorland, G., Djurhuus, K., Wideroe, H., Lien, J. and Skauge, A. (2007) Absolute Pore Size Distributions from NMR, Diffusion Fundamentals, 5, pp. 4.1 – 4.15. [Online] Available from: http://www.uni-leipzig.de/~diff/pdf/volume5/diff_fund_5(2007)4.pdf [Accessed 4 March 2014].

Straley, C., Rossini, D., Vinegar, H., Tutunjian, P. and Morriss, C. (1997) Core analysis by low field NMR, *The Log Analyst*, 38, pp. 84 - 94.

Suicmez, V. and Touati, M. (2008) Pore Network Modelling: A new technology for SCAL predictions and interpretations. *Saudi Arabia Oil & Gas*, 5, pp. 64 – 70. [Online] Available from: http://www.numericalrocks.com/images/stories/News/saogissue5_p64-70.pdf [Accessed 16th November 2011].

Takamura.K. (1982). Microscopic Structure of Athabasca Oil Sands. *The Canadian Journal of Chemical Engineering*, 60, pp. 538-545.

Taud, H., Martinez-Angeles, R, Parrot, J and Hernandez-Escobedo, L. (2005) Porosity estimation method by X-ray computed tomography, *Journal of Petroleum Science and Engineering*, 47, pp. 209 – 217.

Testamanti, M. and Rezaee, R. (2019) Considerations for the acquisition and inversion of NMR T2 data in shales, *Journal of Petroleum Science and Engineering*. 174, pp. 177 – 188.

Tofts, P., Lloyd, D., Clark, C., Barker, G., Parker, G., McConville, P., Baldock, C. and Pope, J. (2000) Test Liquids for Quantitative MRI Measurements of Self-Diffusion Coefficients in Vivo, *Magnetic Resonance in Medicine*, 43 (3), pp. 368 – 374.

Tomlinson, D. (1972) Temperature dependent self-diffusion coefficient measurements of glycerol by the pulsed N.M.R. technique, Molecular Physics, 25 (3), pp. 735 – 738.

Tucker, M. (1991) *Sedimentary petrology.* 2nd Edition. Oxford: Blackwell.

Van Geet, M., Swennen, R. and Wevers, M. (2000) Quantitative analysis of reservoir rocks by microfocus X-ray computerised tomography, Sedimentary Geology, 132, pp. 25 – 36.

Varloteaux, C., Békri, S. and Adler, P. (2013) Pore network modelling to determine the transport properties in presence of a reactive fluid: From pore to reservoir scale, *Advances in Water Resources*, 53, pp. 87 -100.

Vavra, C., Kaldi, J. and Sneider, R. (1992) Geological applications of capillary pressure: A review, American Association of Petroleum Geologists Bulletin, 76 (6), pp. 840 – 850.

Verges, E., Tost, D., Ayala, D., Ramos, E. and Grau, S. (2011) 3D pore analysis of sedimentary rocks, *Sedimentary Geology*, 234, pp. 109 – 115.

Vogt, C., Galvosas, P., Klitzsch, N. and Stallmach, F. (2002) Self-diffusion studies of pore fluids in unconsolidated sediments by PFG NMR, *Journal of Applied Geophysics*, 50, pp. 455 – 467.

Volokitin, Y., Looyestijn, W., Slijkerman, W. and Hofman, J. (2001) A practical approach to obtain primary drainage capillary pressure curves from NMR core and log data, *Petrophysics*, 42 (4), pp. 334 – 343.

Wadell, H. (1932) Volume, shape, and roundness of rock particles, *Journal of Geology*, 40, pp. 443 – 451.

Washburn, K., Anderssen, E., Vogt, S., Seymour, J., Birdwell, J., Kirkland, C. and Codd, S. (2015) Simultaneous Gaussian and exponential inversion for improved analysis of shales by NMR relaxometry, *Journal of Magnetic Resonance*, 250, pp. 7 – 16.

Westphal, H., Surholt, I., Kiesl, C., Thern, H and Kruspe, T. (2005) NMR Measurements in Carbonate Rocks: Problems and an Approach to a Solution, *Pure Applied Geophysics*, 162, pp. 549 – 570.

Wildenschild, D., Hopmans, J., Vaz, C., Rivers, M., Rikard, D. and Christensen, B. (2002) Using X-ray computed tomography in hydrology: Systems, resolutions, and limitations, *Journal of Hydrology*, 267, pp. 285 – 297.

Wilson, O. (2004) *The influence of porous plates on effective drainage and imbibition rates.* PhD dissertation, NTNU Norwegian University of Science and Technology. [Online]. Available from: http://www.diva-portal.org/smash/get/diva2:126203/FULLTEXT01.pdf [Accessed 4 May 2015].

Winkelmann J. (2017) Self-diffusion coefficient of water, in: Lechner M.D. (eds) *Diffusion in Gases, Liquids and Electrolytes. Physical Chemistry, vol 15B1*. Berlin: Springer.

Wong, R. (2005) Effect of oil sands core disturbance induced by gas exsolution on geotechnical and hydraulic properties measurements, *Journal of Canadian Petroleum Technology*, 44 (9), pp. 44 – 50.

Wong, R., Ko, L. and Movassagh, R. (2004) A study of flow tortuosity in locked oil sand, *Journal of Canadian Petroleum Technology*, 43 (1), pp. 35 – 40.

World Energy Council (2007) Natural Bitumen and Extra-Heavy Oil. 2007 Survey of Energy Resources. [online] Available from: http://www.worldenergy.org/publications/survey_of_energy_resources_2007/natural_bitumen_and_extraheavy_oil/654.asp [Accessed 21st September 2011]

Xiong, Q., Baychev, T. and Jivkov, A. (2016) Review of pore network modelling of porous media: Experimental characterisations, network constructions and applications to reactive transport, *Journal of Contaminant Hydrology*, 192, pp. 101 – 117.

Yang, Z., Ma, Z, Luo, Y, Zhang, Y, Guo, H and Lin, W. (2018) A Measured Method for In Situ Viscosity of Fluid in Porous Media by Nuclear Magnetic Resonance, Geofluids, 2018, pp. 1 – 8.

NMR Principles and Fundamentals

A1.1 Introduction

NMR analysis and interpretation rely upon a good understanding of several key terms related to nuclear magnetism, polarization, relaxation times, spin echoes and pulse sequences. These concepts are presented briefly here to provide a sufficient background. Further reviews and a more comprehensive framework of NMR physics can be found in Coates et al. (1999), Cowan (2005), Dunn et al. (2002) and Kimmich (2001).

NMR measurements are based upon the response of selected atomic nuclei to applied magnetic fields. These nuclei must possess an odd mass number (sum of protons and neutrons) as this gives rise to an angular momentum or spin. This spin generates a magnetic field (or net magnetic moment) which has north and south poles aligned in the direction of the spin axes as shown in Figure A1 (Coates *et al.*, 1999). The concepts of magnetic moment and spin are essential to NMR measurements.
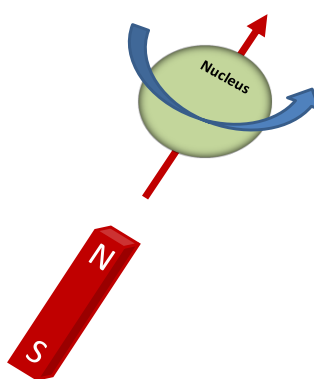

Figure A1-1: The spin and magnetic moment of a nucleus with an odd mass number
(after Coates et al., 1999)

Hydrogen nuclei, having a mass number of one (one proton and no neutrons), possess a relatively large magnetic moment and produce a strong NMR response. Hydrogen is a primary component of the fluids present in petroleum reservoirs (water and

hydrocarbons) and almost all NMR measurements related to the petroleum industry are based on the response of hydrogen nuclei (Coates *et al.*, 1999).

The initial step in the NMR process is to apply an external magnetic field, B_o. Prior to the application of B_o, the spin axes of the hydrogen nuclei are randomly oriented. When B_o is applied, it exerts a torque which *polarises* or aligns the spin axes in the direction of B_o. This causes the axes of the nuclei to *precess* or move perpendicularly to the applied torque (and magnetic field direction). This precession is characterised by the Larmor frequency, f which is given by:

$$f = \frac{\gamma B_o}{2\pi} \qquad \text{[A1-1]}$$

where γ is the gyromagnetic ratio (which is a measure of the strength of the nuclear magnetism) and is species dependent.

The next step is in the NMR process is to apply a pulsed oscillating magnetic field, B_1. B_1 is in a direction that is perpendicular to B_o. This causes the magnetisation of the nuclei to be tipped from the longitudinal direction to a transverse plane. The angle through which the magnetisation is tipped is denoted by θ and given by:

$$\theta = \gamma B_1 \delta \qquad \text{[A1-2]}$$

where θ is the tip angle (degrees) and δ is the time over which B_1 is applied.

Angular-pulse terms are also used to refer to the angle through which magnetisation has been tipped by B_1. Tipping the magnetisation from the longitudinal direction to the transverse plane requires the application of a $\pi/2$ pulse or 90° pulse. This causes the nuclei to now precess about B_1.

The precession of the hydrogen nuclei about B_1 forms a bulk magnetisation denoted by M_o. This provides the amplitude signal measured in the NMR process. M_o is related to a time constant taken to polarise or align the nuclei to B_1. This time constant is termed the transverse relaxation time, T2.

$$M_x(t) = M_o\left(1 - e^{\frac{-t}{T2}}\right) \qquad \text{[A1-3]}$$

where t is the time the nuclei are exposed to B_1, M_o is the final and maximum magnetisation (also called bulk magnetisation) and $M_x(t)$ is the magnitude of the transverse magnetisation at time t.

The application of the 90° B_1 pulse takes place only for a short time. When B_1 ceases to be applied, the nuclei no longer tend to wholly precess in the transverse direction and they begin to lose phase coherency (also called de-phasing). This leads a decrease in the net magnetisation caused by B_1 and results in exponential decay in amplitude. This decay is termed the free induction decay (FID) and the decaying signal is detected via a receiver coil that measures the magnetisation in the transverse plane.

De-phasing can be reduced if a 180° or π B_1 pulse is applied. This causes the nuclei to be re-phased in the transverse plane. This process of de-phasing and re-phasing is associated with a signal called the spin echo. The peak of this signal (the peak of the spin echo) indicates that the nuclei have been re-phased in the transverse plane. The de-phasing time, τ is equal to the re-phasing time. This implies that the spin echo takes place over a 2τ interval. This 2τ interval is also referred to as the inter-echo time, TE.
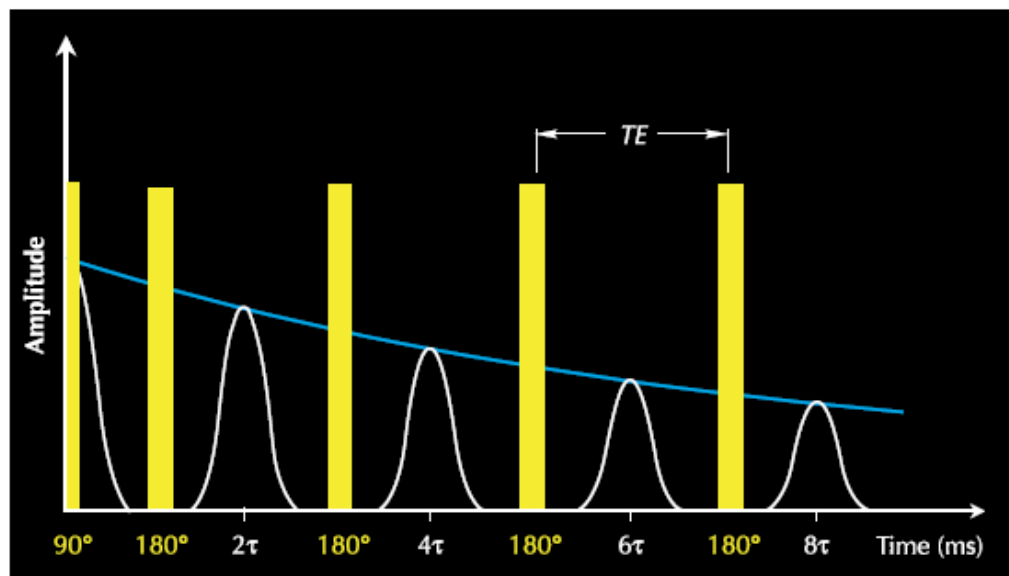

Figure A1-2: Generation of a spin echo train using a CPMG sequence
(after Coates et al., 1999)

A single spin echo (re-phasing followed by de-phasing) takes place very rapidly. Continued re-phasing of the nuclei requires the application of repeated 180° pulses in intervals of 2τ. This is termed a spin echo train and is illustrated in Figure A1-2. The

entire pulse sequence of a 90° pulse followed by repeated 180° pulses is called a CPMG sequence after its inventors - Carr, Purcell, Meiboom and Gill (Cowan, 2005).

Figure A1-2 shows that the individual spin echoes which occur between successive 180° pulses take place with decreasing amplitude. This is due because the de-phasing associated with molecular interactions and diffusion is inevitable and over time, leads to an eventual decay in the CPMG spin echo train. The amplitudes of the spin echo peaks are used to monitor the decay in transverse magnetisation. These amplitudes at time t denote the transverse magnetisation, $M_x(t)$.

A1.2 Multi-Exponential Decay

Reservoir rocks are generally heterogeneous in nature and usually have both a variety of pore sizes as well as varying fluid types. The spin echo train (transverse-magnetization measurements) therefore does not decay with a single T2 value but instead with a distribution of T2 values given by:

$$M_x\left(t\right) = \sum M_{o,i}\left(1 - e^{-\frac{t}{T2_i}}\right) \quad \text{[A1-4]}$$

where t is the time the nuclei are exposed to B_1, $M_{o,i}$ is the initial magnetisation from the ith component of relaxation, $M_x(t)$ is the magnitude of the transverse magnetisation at time t and T$_{2i}$ is the decay constant of the ith component of transverse relaxation

The summation in equation A1.4 is across the entire sample therefore captures data from all pores and all different types of fluid. The summation is across the entire sample therefore captures data from all pores and all different types of fluid. Figure A1-3 further illustrates this concept and shows a system with three distinct pore sizes. The micropores and mesopores each comprise about roughly a quarter of the pore volume while the macropores account for the other half. The micropores due to their size have the highest surface to volume which is reflected in the NMR as the shortest T2 value, the mesopores have an intermediate T2 value and macropores (lowest surface to volume) have the longest T2 value.

The initial NMR signal amplitude and T2 distribution peak height reflect the respective volumes with the micro and mesopores containing a quarter of the volume each and the

macropores containing the other half. The NMR signals from the pores of each size add together and are observed simultaneously, as the sum of the relaxation curves as outlined in equation A1-4.
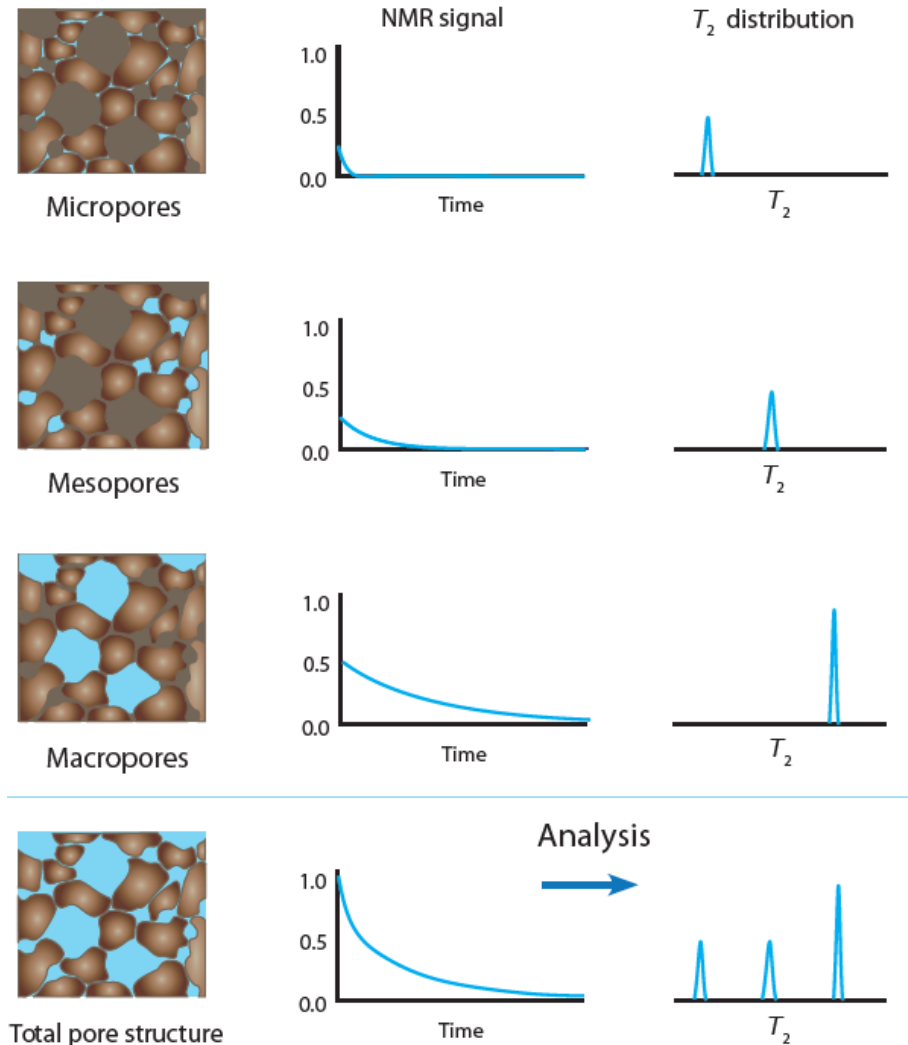

Figure A1-3: A heterogeneous pore system showing the individual pore and combined system raw NMR data and T2 spectra (after Magritek, 2013)

A1.3 Generating a T2 Spectrum using mathematical inversion

The resultant echo train as shown in Figure A1-2 (blue line) represents the raw data of a T2 test and is essentially a series of spin-echo amplitudes as a function of time recorded at fixed time increments. This raw data is converted is mathematically inverted (mapped) by use of a best-fit curve to produce a distribution of T2 values as a function of relaxation time (Figure A1-3).

Multi-exponential mathematical models are commonly used for inverting the data (Dunn et al., 2002). Four mathematical inversion models are provided with the 2 MHz NMR Rock Core Analyzer Magritek instrument used in this work. These include an exponential fit (*exp*), a bi-exponential fit (*bi-exp*), the *Lexus* method based on the Butler-Reeds – Dawson algorithm and a non-negative least square fit, *NNLS* (also based on Butler-Reid-Dawson). More information on these inversion models can be found in Medellin *et al.* (2016).

For this study, the *Lexus* method was used as it provided logarithmic binning on data points which allowed a wider range of relaxation times (both short and long) to be considered.
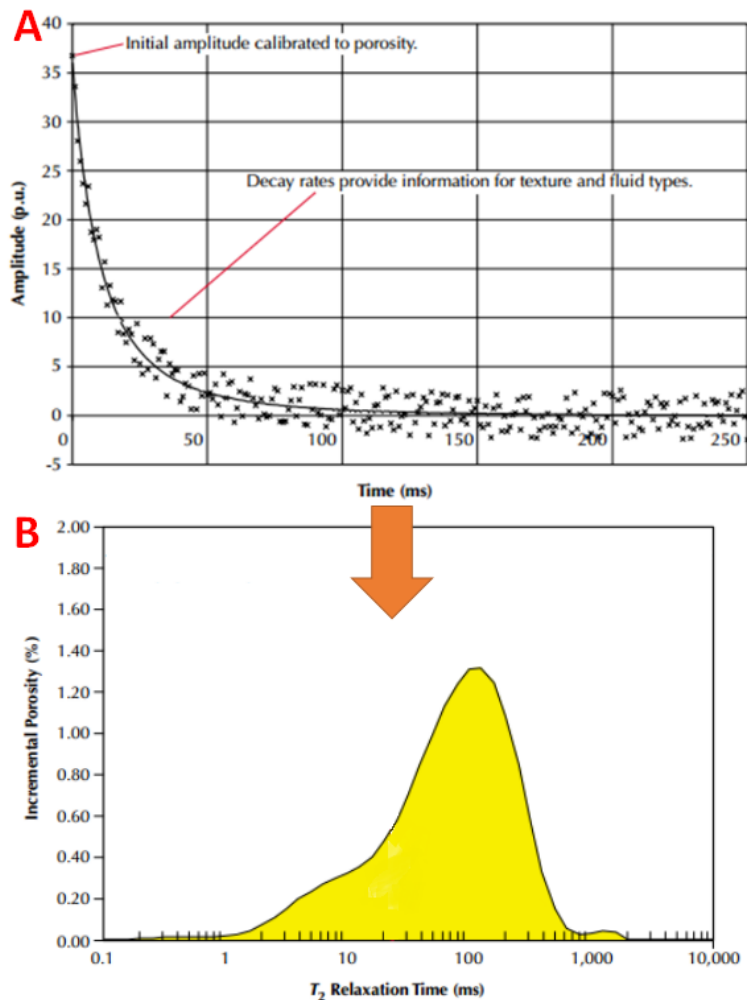

Figure A1-3: (A) Example of the '*raw data*' of a spin echo train and (B) the generation of a T2 spectrum after mathematical inversion (after Coates *et al.*, 1999)

NMR T2 and PGSTE Testing

A2.1 The Magritek 2MHz NMR Rock Core Analyzer

The NMR T2 and PGSTE testing in this work used a 2 MHz NMR Rock Core Analyzer Magritek instrument which is shown in Figure A2-1. All tests were performed at temperatures between 20 – 25°C.

Figure A2-1: Magritek 2MHz NMR Rock Core Analyzer

A2.2 NMR T2 Testing

An NMR T2 test initially records an echo train (raw data) which is then converted to T2 spectrum using an appropriate mathematical inversion. The Prospa® software package controls the operation of the Rock Core Analyzer Magritek instrument. A T2 test is carried out by selecting the T2 tab off the Parameters section as shown in Figure A2-2. This T2 tab has several acquisition parameters which control the form of the T2 test. These include the dummy scans, points per echo, number of echoes, echo shift, *tau* and dwell time.

Of these, the *tau* and number of echoes (NE) were the only parameters which affected the T2 testing in this work. *Tau* is the delay between the 90 and 180 pulses (where 2×*tau*

provides a measure of the inter-echo time, TE). The number of echoes (NE) determines the number of 180 pulses and therefore quantity of echoes which will be measured.

The *x*-axis or time (in ms) of the raw echo train from T2 testing is obtained from:

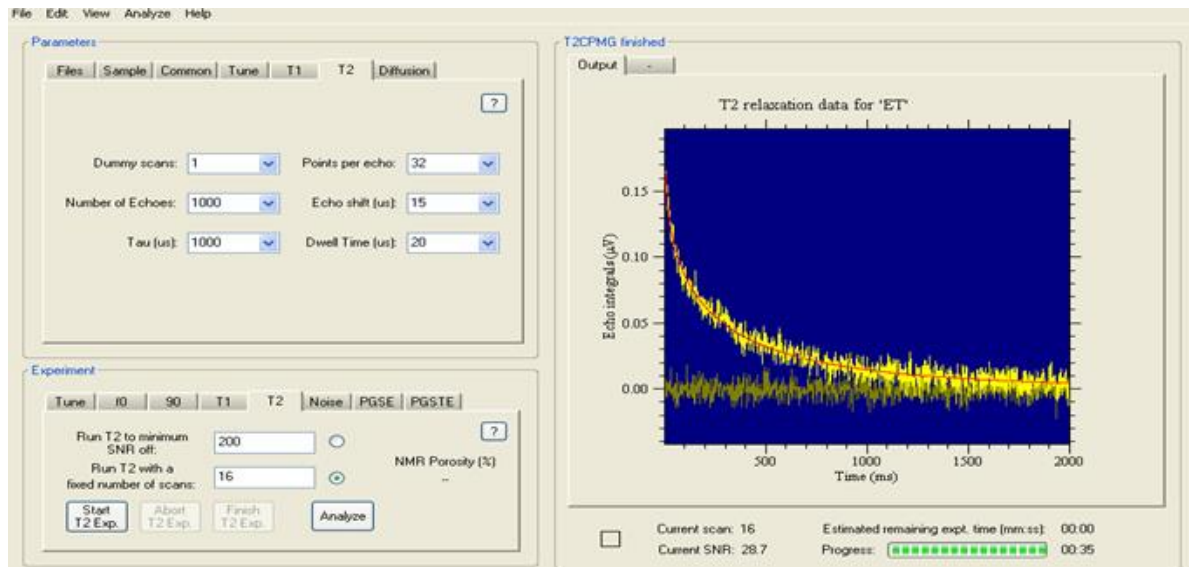$$Time = \frac{2tau}{1000} xNE = \frac{TE}{1000} xNE \qquad [A2\text{-}1]$$

Figure A2-2: An example of the T2 experimental parameters and exponential decaying curve

During this work, tau values were kept constant at 1000μs (indicating that the inter-echo times were fixed at 2ms) while the number of echoes was varied between 2000 – 4500 echoes.

A2.3 NMR PGSTE Testing

A PGSTE test is carried out by selecting the *Diffusion* tab off the Parameters section as shown in Figure A2-3. This *Diffusion* tab has several acquisition parameters which control the form of the PGSTE test.

Of these, the *grad separation* was the only parameter which affected the PGSTE testing in this work. This is the observation time for diffusion [*t*] which was varied from 16 – 64s

with the resultant time-dependent restricted diffusion coefficient [*D(t)*] being measured as shown in Table 5-13.
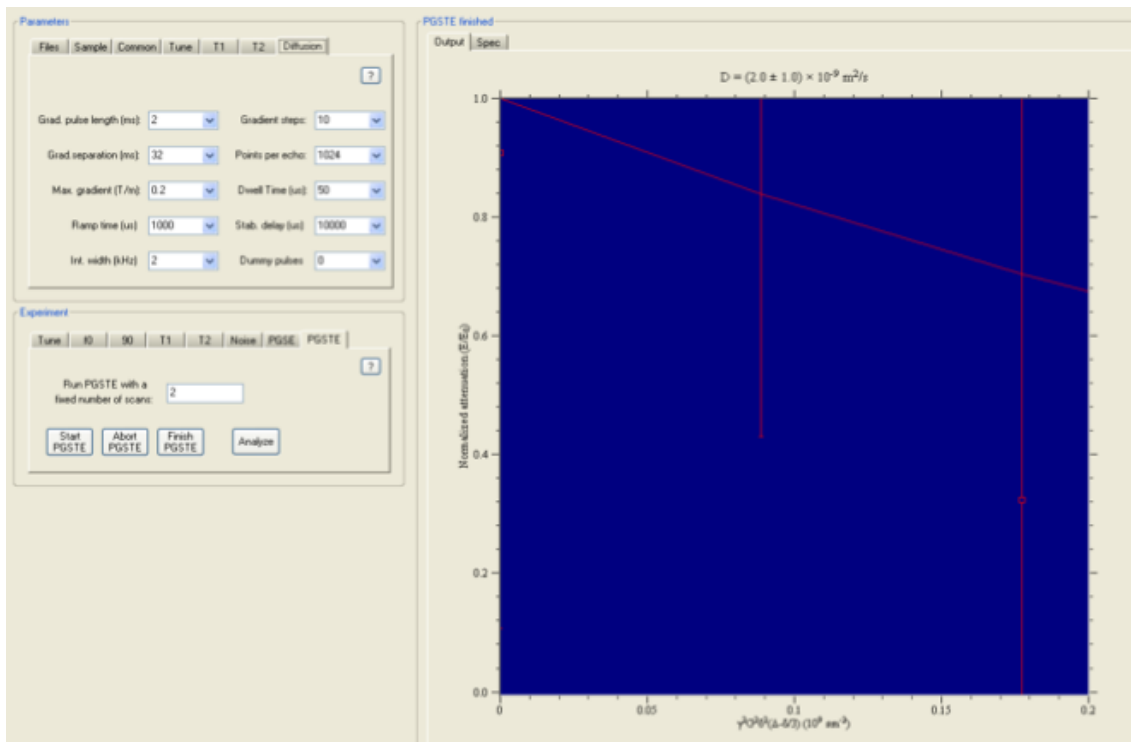

Figure A2-3: An example of the PGSTE experimental parameters and resulting *D(t)*